# Enhanced emission of a single quantum emitter coupled to a microcavity and a nanocavity

**Dissertation**

der Mathematisch-Naturwissenschaftlichen Fakultät

der Eberhard Karls Universität Tübingen

zur Erlangung des Grades eines

Doktors der Naturwissenschaften

(Dr. rer. nat.)

vorgelegt von

Quan LIU

aus Jiangxi/China

Tübingen

2021

Gedruckt mit Genehmigung der Mathematisch-Naturwissenschaftlichen Fakultät der Eberhard Karls Universität Tübingen.

| | |
|---|---|
| Tag der mündlichen Qualifikation: | 29.09.2021 |
| Dekan: | Prof. Dr. Thilo Stehle |
| 1. Berichterstatterin: | Prof. Dr. Agnès Maître |
| 2. Berichterstatter: | Prof. Dr. Thomas Huser |
| 3. Berichterstatter: | Prof. Dr. Erik Schäffer |

# Université de Technologie de Troyes

Light, Nanomaterials, Nanotechnologies (L2N)

Spécialité: Matériaux, Mécanique, Optique, Nanotechnologie

*In cotutelle with*

# Eberhard Karls Universität Tübingen

Institute of Physical and Theoretical Chemistry

Spécialité: Physics


Thesis presented for obtention of the Title Ph.D.


Quan LIU


# Enhanced emission of a single quantum emitter coupled to a microcavity and a nanocavity

Jury

| | | |
|---|---|---|
| MAITRE Agnès | Professeure des universités | Examinateur |
| HUSER Thomas | Professor | Examinateur |
| KERN Dieter | Professor | Rapporteur |
| BACHELOT Renaud | Professeure des universités | Rapporteur |
| ADAM Pierre-Michel | Professeure des universités | Directeur de thèse |
| MEIXNER Alfred J. | Professor | Directeur de thèse |

I would like to dedicate this thesis to my loving parents …

I gratefully acknowledge the financial support of China Scholarship Council (CSC).

https://www.csc.edu.cn

The financial support of the Franco-German University (FGU) is also gratefully acknowledged.

https://www.dfh-ufa.org/en/

# Acknowledgements

I am sincerely grateful for my supervisors, Prof. Dr. Alfred J. Meixner, Prof. Dr. Pierre-Michel Adam and Prof. Dr. Marc Brecht. If not for their efforts, this great journey between Troyes and Tübingen will never happen.

I am thankful to Dr. Frank Wackenhut for fruitful discussions during my work. And I would like to express special gratitude to him for helping with my writing skills and proofreading my early drafts.

I would like to thank Otto Hauler, Liangxuan Wang and Prof. Dr. Johannes Gierschner for the solid theoretical support with their beautiful simulations.

I would like to give my grateful thanks to Prof. Dr. Monika Fleischer for providing the access to her lab and various experimental facilities. I would further like to thank Sergei Kostcheev, Regis Deturche and Jeremie Beal for their professional guidance. I extend my thanks to Dr. Kai Braun and Dr. Dai Zhang for their excellent guidance on various experimental equipment and social life as well.

Special thanks to Achim Junginger, Lin Pan, Saeed Nosrati, Tim Rammler and YuTing Chen. I had good time working with them and enjoyable time in Tübingen. I am thankful to all my colleagues from L2n and AK Meixner for the nice working atmosphere.

I am grateful to China Scholarship Council for funding my PhD study.

Finally, my eternal gratitude to my parents, my sister and my partner Dandan for their support and love.

# Abstract

The development of single molecule-based techniques in the last decades has enabled directly selecting, tracking, and measuring an individual molecule. Single molecule spectroscopy can directly observe the properties of individual molecules usually hidden in ensemble averages. In this thesis, the structural dynamics of a single quantum emitter, served by hypericin, is characterized. Hypericin, isolated from St. John's wort, does not only have large potential in modern medicine but also exhibits fascinating structural dynamics, such as dissociation, conformation and tautomerism.

By using confocal scanning microscopy combined with radially/azimuthally polarized laser modes, three-dimensional reorientation of the transition dipole moment of a single molecule, due to the charge redistribution during tautomerism, is observed. The transient reorientation is detected in a fluorescence time trace as a sudden fluctuation. To quantify the temporal properties of the tautomerism, photon autocorrelation function is used to extract the intensity fluctuations. The results show the distinct influence of the local environment, such as PVA matrix and deuteration effect.

The local photonic environment of a molecule is modified by the microcavity/nanocavity. The theoretical principles and experimental results are presented for a coupled molecule. A significant change of the radiative emission rate and of the fluorescence spectra is discussed. It allows us to measure the absolute quantum yield by using a tunable microcavity. The results show the possibility of controlling tautomerization by changing the photonic environment.

Subsequently, molecular dissociation is discussed by single molecule surface-enhanced Raman spectra profiting from near field enhancement of nanocavity. Furthermore, the theoretical model reveals the importance of the radius of the nanoparticles and the gap distance between them in order to achieve maximum emission enhancement. A fast experimental optimization strategy towards optimal fluorescence enhancement is outlined.

**Key words:** Single molecule, Fluorescence, Hypericin, Fabry-Perot interferometers, Surface plasmon resonance, Raman effect, Surface enhanced

# Résumé

Le développement de techniques basées sur une seule molécule au cours des dernières décennies a permis de sélectionner, de suivre et de mesurer directement une molécule individuelle. La spectroscopie à une seule molécule permet d'observer directement les propriétés de molécules individuelles généralement cachées dans les moyennes d'ensemble. Dans cette thèse, la dynamique structurelle d'un seul émetteur quantique, servi par l'hypéricine, est caractérisée. L'hypericine, isolée du millepertuis, n'a pas seulement un grand potentiel en médecine moderne, mais présente également une dynamique structurelle fascinante, comme la dissociation, la conformation et la tautomérie.

En utilisant la microscopie à balayage confocale combinée à des modes laser polarisés radialement / azimutalement, on observe une réorientation tridimensionnelle du moment dipolaire de transition d'une seule molécule, en raison de la redistribution de charge pendant la tautomérie. La réorientation transitoire est détectée dans une trace temporelle de fluorescence comme une fluctuation soudaine. Pour quantifier les propriétés temporelles de la tautomérie, la fonction d'autocorrélation des photons est utilisée pour extraire les fluctuations d'intensité. Les résultats montrent l'influence distincte de l'environnement local, comme la matrice PVA et l'effet de deutération.

L'environnement photonique local d'une molécule est modifié par la microcavité / nanocavité. Les principes théoriques et les résultats expérimentaux sont présentés pour une molécule couplée. Un changement significatif du taux d'émission radiatif et des spectres de fluorescence est discuté. Il nous permet de mesurer le rendement quantique absolu en utilisant une microcavité accordable. Les résultats montrent la possibilité de contrôler la tautomérisation en modifiant l'environnement photonique.

Par la suite, la dissociation moléculaire est discutée par des spectres Raman améliorés en surface à molécule unique bénéficiant de l'amélioration en champ proche de la nanocavité. De plus, le modèle théorique révèle l'importance du rayon des nanoparticules et de la distance entre elles afin d'obtenir une amélioration maximale des émissions. Une stratégie d'optimisation expérimentale rapide vers une amélioration optimale de la fluorescence est décrite.

**Mots-clés:** Molécule unique, Fluorescence, Hypéricine, Fabry-Pérot, Interféromètres de, Résonance plasmonique de surface, Raman, Effet augmenté en surface

# Zusammenfassung

Die Entwicklung von Einzelmolekül-basierten Techniken in den letzten Jahrzehnten ermöglichte die direkte Auswahl, Verfolgung und Messung eines einzelnen Moleküls. Einzelmolekülspektroskopie kann direkt die Eigenschaften einzelner Moleküle beobachten, die normalerweise in Ensemble-Durchschnittswerten verborgen sind. In dieser Arbeit wird die Strukturdynamik eines einzelnen Quantenemitters charakterisiert, der von Hypericin bedient wird. Hypericin, isoliert aus Johanniskraut, hat nicht nur ein großes Potenzial in der modernen Medizin, sondern zeigt auch faszinierende strukturelle Dynamiken wie Dissoziation, Konformation und Tautomerie.

Durch konfokale Rastermikroskopie in Kombination mit radial / azimutal polarisierten Lasermoden wird eine dreidimensionale Neuorientierung des Übergangsdipolmoments eines einzelnen Moleküls aufgrund der Ladungsumverteilung während der Tautomerie beobachtet. Die vorübergehende Neuorientierung wird in einer Fluoreszenzzeitspur als plötzliche Fluktuation erfasst. Um die zeitlichen Eigenschaften der Tautomerie zu quantifizieren, wird die Photonenautokorrelationsfunktion verwendet, um die Intensitätsschwankungen zu extrahieren. Die Ergebnisse zeigen den deutlichen Einfluss der lokalen Umgebung wie PVA-Matrix und Deuterierungseffekt.

Die lokale photonische Umgebung eines Moleküls wird durch die Mikrokavität / Nanokavität modifiziert. Die theoretischen Prinzipien und experimentellen Ergebnisse werden für ein gekoppeltes Molekül vorgestellt. Eine signifikante Änderung der Strahlungsemissionsrate und der Fluoreszenzspektren wird diskutiert. Es ermöglicht uns, die absolute Quantenausbeute unter Verwendung einer einstellbaren Mikrokavität zu messen. Die Ergebnisse zeigen die Möglichkeit, die Tautomerisierung durch Veränderung der photonischen Umgebung zu steuern.

Anschließend wird die molekulare Dissoziation durch oberflächenverstärkte Einzelmolekül-Raman-Spektren diskutiert, die von der Nahfeldverstärkung der Nanokavität profitieren. Darüber hinaus zeigt das theoretische Modell die Bedeutung des Radius der Nanopartikel und des Spaltabstands zwischen ihnen, um eine maximale Emissionsverbesserung zu erreichen. Eine schnelle experimentelle Optimierungsstrategie zur optimalen Fluoreszenzverstärkung wird skizziert.

# Contents

# List of Figures

# List of Tables

# Nomenclature

| | |
|---|---|
| TCSPC | time-correlated single photon counting |
| FLIM | fluorescence lifetime imaging spectroscopy |
| FCS | fluorescence correlation spectroscopy |
| FLCS | fluorescence lifetime correlation spectroscopy |
| DBR | distributed Bragg reflectors |
| TD-DFT | Time-dependent density functional theory |
| PVA | Poly (vinyl alcohol) |
| SERS | Surface enhanced Raman scattering |
| RWA | rotating-wave approximation |
| TDM | Transition dipole moment |
| HOMO | Highest Occupied Molecular Orbital |
| LUMO | Lowest Unoccupied Molecular Orbital |
| ISC | Intersystem crossing |
| TMM | Transfer Matrix Method |
| LSPR | localized surface plasmon resonance |
| SPR | surface plasmon resonance |
| CW | continuous-wave |
| RPDM | radially polarized doughnut mode |
| APDM | azimuthally polarized doughnut mode |
| IRF | instrument response function |
| LP | lower polariton |
| UP | upper polariton |
| SM | single molecule |
| FWHM | full width at half maxima |

| | |
|---|---|
| PS II | Photosystem II |
| SEM | scanning electron microscopy |

# Chapter 1 Introduction

Since the first time Stokes[1,2] uses the word *fluorescence* to describe the emission of light following absorption of light, numerous efforts have been made to build up the experimental methods and theoretical understandings of fluorescence. Historically, fluorescence and phosphorescence are not distinguished until Lewis and Kasha[3] prove the phosphorescent state is the triplet state. A more reasonable term, *photoluminescence,* describes a clear picture on the interaction of light and matter ends with new emitted light.

With the advances in the laser light sources and photon detectors, fluorescence spectroscopy[4,5] has become a very successful investigative tool with high sensitivity. Advanced time-correlated single photon counting (TCSPC) techniques[6–8] provide temporal information of fluorescence with amazing sensitivity and accuracy. Prominent applications like fluorescence lifetime imaging spectroscopy[9–11] (FLIM), fluorescence correlation spectroscopy[12–14] (FCS), fluorescence lifetime correlation spectroscopy[15–17] (FLCS) in biophysics and coincidence correlation measurements in quantum optics[18–20] heavily rely on TCSPC. On demand of analytical, material and biological sciences, fluorescence-based[21] single molecule experiments are booming after the first detection of a single molecule in an optical absorption based[22] experiment. The impressive progress of electronics and laser techniques[23–28] over the last decades have removed some challenges in single molecule fluorescence spectroscopy. Increased processing speed and detection efficiency, as well as the repetition rate and power of pulsed light sources, improve detection sensitive and reduce acquisition time. Unlike the bulk measurements, single molecule fluorescence spectroscopy offers the most important advantage, i.e., observing the properties of individual molecules usually hidden in ensemble averages.[29–31] These new techniques open up the possibility of directly selecting, tracking, and measuring an individual molecule. Super-resolution microscopy, such as stochastic optical reconstruction microscopy (STORM),[32] photo activated localization microscopy (PALM),[33] and fluorescence photo-activation localization microscopy (FPALM)[34] is a class of successful techniques based on single molecule localization. Different routes focused on the new insights into physical, chemical and biological phenomena, such as molecular diffusion,[35] spectral diffusion,[36] triplet lifetime variations,[37] DNA conformational fluctuations,[38] and intramolecular proton transfer,[30] just to name a few.

Today, new nanofabrication technology enables us to fabricate and manipulate individual structures on nanometre scale.[39–41] Instead of just observing, more interest is now focused on the possibility of controlling the interaction of light and matter in microscopic scale, even to achieve controlled interaction between a single photons and single emitters. Single molecule fluorescence spectroscopy is, of course, still one of the most common and most intuitional investigative tool.

Well established quantum electrodynamics[42–44] (QED) have described how light and matter interact and predicts plenty of phenomenon. A main challenge to manifest the quantum theory in the 'real world,' the interaction of a single photon and a single electronic excitation, is very weak. An efficient approach is to confine light and electronic excitation in a high-finesse cavity. Purcell[45] described an emitting system coupled to a resonant cavity, where the spontaneous emission probability is thereby increased, and the relaxation time reduced by a factor, i.e., Purcell factor, $F=3Q\lambda^3/4\pi^2V$. As the interaction between the emitter and the cavity field increase, a so-called strong coupling regime can be achieved, where energy is coherently exchanged between the emitter and the cavity mode field. Strong coupling results in bosonic quasiparticles called exciton-polariton (or polariton for short), which is a superposition of photons and excitons.

Carefully designed cavities, such as micropillar cavities,[46] Whispering-Gallery mode cavities,[47] and photonic crystal cavities[48] have been widely used to investigate the strong interaction of light with atoms[49] and quantum dots.[46,48] However, the low binding energy typical of Wannier–Mott excitons in semiconductors make them only suitable at low temperature[50,51] (below ~20 K). In addition, complicated fabrication processes for those cavities have limited their wide applications.

The Fabry–Pérot (F-P) type microcavity formed by two distributed Bragg reflectors (DBR) or even simple metallic mirrors with subwavelength spacing is a great alternative. By changing the reflection of the mirrors, the quality factor (Q-factor, the ratio of a resonance frequency to the linewidth of the cavity mode) can vary over the range of 10 ~ 100000. Additionally, the resonance is tuneable by changing the mirrors' separation. The most attractive property of an open F-P microcavity is that they can easily incorporate organic materials (amorphous and crystalline dye molecules), typical of Frenkel exciton systems, with large binding energy. This has made it possible to experimentally observe strong coupling at room temperature. Strong light-matter interactions have been demonstrated in F-P type microcavity with many different emitting systems at room temperature and in ambient conditions.[52,53] The possibility of modifying the emission properties of molecules,[54–56] influence light-driven reactions,[57] change molecular vibrational transition,[55,58,59] enhance intermolecular energy transfer,[54,60] realize room temperature polariton lasing[61] and Bose–Einstein

condensation[62,63] have been explored extensively. Single molecules can also be observed in a F-P microcavity.[64–66] The results show a notable enhancement of spontaneous emission rate[65] and significant changes of the emission spectrum[64] of an individual molecule by the Purcell effect. Taking advantage of the tunability, the wavelength dependence of the Förster resonance energy transfer (FRET) rate of single donor-acceptor pairs inside the cavity was investigated.[67] In a different work,[68] the coherent coupling of a single molecule to a tunable DBR-based F-P cavity with a quality factor up to $2.3\times10^5$ is achieved at low temperature ($T < 4K$).

While room temperature strong coupling of a single emitter is not achieved in an F-P cavity yet, plasmonic nanocavity[69] realize a Rabi splitting of 90 meV for single methylene-blue molecules at room temperature and ambient conditions. The advantages arise due to the extreme localization and fast decay rate of the particle plasmon in the nanocavity. The surface plasmon resonance[70] (SPR) is a resonant coherent oscillation of the conduction band electrons at the interface between a metal and a dielectric stimulated by an electromagnetic light field. SPR in metallic nanoparticles is confined inside the nanoparticle. Large varieties of materials and shapes of nanoparticles contribute to the optimization possibilities of the SPR, leading to diverse applications. The evanescent property[71] of the SPR along a normal nanoparticle interface ensures the localization of an electric field and give rise to significant near-field enhancement. Surface-enhanced Raman scattering[72] (SERS) is one of the most spectacular applications that benefit from the large field enhancement of plasmonic and have been recorded on a single molecule[73,74] regime. The fast damping rate[75] of SPR, mainly due to the large imaginary permittivity of metal, gives a broad linewidth of the resonance, which, however, suppresses parts of the non-radiative processes, like phonon-induced relaxation at ambient conditions. Adapting the same description for a normal resonant cavity, a small quality factor (broad resonance linewidth) and a small mode volume (near-field enhancement) could eventually give a reasonable Purcell factor to emitters. The fluorescence enhancement of single molecule[76,77] near plasmonic nanoparticles have also been investigated experimentally and theoretically.

The experiments presented in this thesis make use of resonance tunability and fabrication facility of F-P type microcavities and plasmonic nanocavities to explore efficient light-matter interaction towards the single molecule regime. The hypericin molecule was characterized using single fluorescence spectroscopy. Without ensemble averaging, the tautomerization of a single hypericin molecule fixed in a Poly (vinyl alcohol) (PVA) matrix is observed. The TCSPC technique can reveal unusual molecular dynamics with high temporal precision. Variations of the spontaneous emission rate of a single hypericin molecule is measured in a tunable F-P microcavity. The impact of cavity mode on the tautomerization rate is also investigated.

In order to profit from the large near-field enhancement of plasmonic nanocavities for efficient interaction, a major challenge is to align a single emitter to the vicinity of 'hot spot.' We use a fast thermal annealing approach for metallic films,[78,79] which has already been proven to be efficient and successful.[31] This method creates plenty[31,78] of 'hot spots,' so sparse distributed emitters could easily locate in a preferred position. A multiplexing optimization protocol based on plasmonic nanocavity towards single molecule enhanced fluorescence is developed.

The thesis is organized as follows. First, there is an outline of the general theoretical background of the interaction of light and matter in Chapter 2. The concept and general properties of single quantum emitter are introduced, followed by the basic descriptions of optical resonators. Shared properties and significant difference between a F-P microcavity and a plasmonic nanocavity are addressed. At the end of the chapter, quantum theory and a semi-classical description of the interaction of a two-level system with a monochromatic electromagnetic field is reviewed. Special focus is put on the coupled mode theory of emission enhancement by nanocavities.

Chapter 3 describes the related experimental techniques. A home-built confocal scanning microscopy is introduced, as well as the preparation procedures of the molecule samples used in this work. In addition, the realization of a tuneable F-P microcavity and plasmonic nanocavity is well-documented.

The properties of single quantum emitters are characterized in Chapter 4. We stress the usefulness of confocal scanning microscopy, combined with higher order laser modes to characterize single molecules. Observed single hypericin molecule dynamics are carefully analysed. The results from time-dependent density functional theory (TD-DFT) calculations are used for cross confirmation that tautomerization is observed. Furthermore, the temporal dynamics of the triplet state blinking and the tautomerization of hypericin are described by photon autocorrelation model.

The interaction of the cavity and quantum emitters is demonstrated in Chapter 5. The spontaneous emission rate of hypericin molecules is altered in a tunable F-P microcavity, and a quantitative model is presented, which enable the spontaneous emission rate and emission spectra at certain cavity thickness to be predicted. The absolute quantum yield of the emitter can be calculated by tuning the cavity. Besides, a single molecule SERS experiment is presented for nanocavity. Finally, the experimental realization of strong coupling with J-aggregated dye molecules is presented. Coupling strength and emission properties at different cavity thicknesses are investigated.

A fast optimization strategy based on plasmonic nanocavity towards the enhanced fluorescence of a single photosystem II is introduced in the following Chapter 6. Optimal enhancement can be

achieved from a radius continuously increased plasmonic sample prepared in a simple one-step evaporation. The final Chapter 7 gives a summary of the thesis and an outlook on possible future experiments.

# Chapter 2 Theoretical foundations

This chapter is focused on the theoretical description of light-matter interaction. More detailed descriptions and discussions can be found in [5,42,43]. In the first section, the excitation and emission of a quantum emitter similar to a hydrogen atom is introduced in a quantum mechanical picture. Next the electronic excitation and emission of organic fluorescent molecules is addressed. A general characterization of a Fabry–Pérot (F-P) microcavity and a plasmonic nanocavity is given in the second section. In the next section, the quantum theory of light-matter interaction is outlined. We will consider the spontaneous emission properties of a single emitter in the cavity from the weak coupling to the strong coupling regime. A classical description is also introduced for an intuitive discussion of the impact of damping. In addition, an analytic description, allowing fast optimization of the emission enhancement, is presented for a plasmonic nanocavity.

## 2.1 Single quantum emitter

A quantum emitter is an emitting system dominated by the laws of quantum mechanics. To precisely describe a fluorescent molecule or a semiconductor quantum dot is extremely complex and not always necessary. For simplicity, we start our discussion with the interaction of a two-level atom and a single mode of the electromagnetic field, which allows us to characterize essential features of a single quantum emitter.

Within the dipole approximation[43], the interaction Hamiltonian of the radiation field $\boldsymbol{E}$ with a single-electron atom is:

$$H = H_F + H_a - e\boldsymbol{r} \cdot \boldsymbol{E}, \tag{2.1}$$

where $H_a$ and $H_F$ are the energies of the atom and the radiation field without interaction. $-e\boldsymbol{r} \cdot \boldsymbol{E}$ is the interaction energy and $\boldsymbol{r}$ describes the position of the electron, and $\boldsymbol{E}$ is the external electric field.

Considering a single mode field of angular frequency $\omega = 2\pi\nu$ and a two-level atom represented by ground state $|b\rangle$ and excited state $|a\rangle$ with energy eigenvalues of $E_b = \hbar\omega_b$ and $E_a = \hbar\omega_a$ (sketched in Figure 2-1 a)). After omitting the zero-point energy, the interaction of the

atom with the field, including the unperturbed Hamiltonian of the atom $\frac{1}{2}\hbar\omega_0\sigma_z$ and the field $\hbar\omega a^\dagger a$, is described by:

$$H = H_0 + H_1 = \left(\hbar\omega a^\dagger a + \frac{1}{2}\hbar\omega_0\sigma_z\right) + \hbar g(\sigma_+ a + a^\dagger\sigma_-). \tag{2.2}$$

Here, $\omega_0 = \omega_a - \omega_b$ is the atomic transition frequency and $\sigma_z = \sigma_+\sigma_- - \sigma_-\sigma_+$. The bosonic creation operator $a^\dagger$ emits a photon and annihilation operator $a$ absorbs a photon, whereas the fermionic creation operator $\sigma_+$ excites the atom to the excited state $|a\rangle$ and the annihilation $\sigma_-$ operator relaxes the atom back to the ground state $|b\rangle$. The interaction terms can be understood by considering that $\sigma_+ a$ corresponds to the absorption of a photon and the excitation of the atom from $|b\rangle$ to $|a\rangle$, and $a^\dagger\sigma_-$ corresponds to the emission of a photon and the de-excitation of the atom. Noting the interaction terms including fast rotating terms proportional to $exp[\pm i(\omega + \omega_0)t]$ are ignored under the rotating-wave approximation (RWA). The interaction rate is:

$$g = -\frac{\hat{\wp}\cdot\hat{\epsilon}_k\mathcal{E}_k}{\hbar}, \tag{2.3}$$

where $\hat{\epsilon}_k$ is a unit polarization vector, and $\hat{\wp}$ is electronic transition dipole moment defined in equation (2.5) and

$$\mathcal{E}_k = \left(\frac{2\hbar\omega_k}{\varepsilon_0 V}\right)^{1/2} \tag{2.4}$$

is the quantity of quantized electric field with the mode volume $V$. An induced dipole moment during the transition between two states, so called transition dipole moment (TDM) of the atom, is:

$$\hat{\wp}_{ij} = e\langle i|\boldsymbol{r}|j\rangle, \tag{2.5}$$

with $\hat{\wp} = \hat{\wp}_{ij} = \hat{\wp}_{ji}$.

The Hamiltonian in the interaction picture is given by:

$$\Upsilon = \hbar g\left(\sigma_+ a e^{i\Delta t} + a^\dagger\sigma_- e^{-i\Delta t}\right), \tag{2.6}$$

where $\Delta = \omega_0 - \omega$. Then we obtain the time dependent Schrödinger equation

$$i\hbar\frac{\partial|\varphi\rangle}{\partial t} = \Upsilon|\varphi\rangle, \tag{2.7}$$

in which $|\varphi\rangle$ is a linear combination of the states $|a,n\rangle$ and $|b,n\rangle$ of the two-level system and the field. And $|a,n\rangle$ ($|b,n\rangle$) means that the atom is in the excited (ground) state, while $n$ photons exist for the field. We can write the state:

$$|\varphi\rangle = \sum_n \left[c_{a,n}(t)|a,n\rangle + c_{b,n}(t)|b,n\rangle\right]. \tag{2.8}$$

The interaction Hamiltonian (2.6) will only cause transition between $|a,n\rangle$ and $|b,n+1\rangle$. Therefore the other terms can be omitted in the sum and we may only consider the time dependent probability amplitudes $c_{a,n}(t)$ and $c_{b,n+1}(t)$. Substituting equation (2.6) and (2.8) into (2.7), then projecting it to $\langle a,n|$ and $\langle b,n+1|$ we obtain the time-derivatives of the probability amplitudes:

$$\dot{c}_{a,n} = -ig\sqrt{n+1}e^{i\Delta t}c_{b,n+1}, \tag{2.9}$$

$$\dot{c}_{b,n+1} = -ig\sqrt{n+1}e^{-i\Delta t}c_{a,n}. \tag{2.10}$$

A general solution for equations (2.9) and (2.10) is given by

$$c_{a,n}(t) = \left\{c_{a,n}(0)\left[\cos\left(\frac{\Omega_n t}{2}\right) - \frac{i\Delta}{\Omega_n}\sin\left(\frac{\Omega_n t}{2}\right)\right] - \frac{2ig\sqrt{n+1}}{\Omega_n}c_{b,n+1}(0)\sin\left(\frac{\Omega_n t}{2}\right)\right\}e^{i\Delta t/2}, \tag{2.11}$$

$$c_{b,n+1}(t) = \left\{c_{b,n+1}(0)\left[\cos\left(\frac{\Omega_n t}{2}\right) + \frac{i\Delta}{\Omega_n}\sin\left(\frac{\Omega_n t}{2}\right)\right] - \frac{2ig\sqrt{n+1}}{\Omega_n}c_{a,n}(0)\sin\left(\frac{\Omega_n t}{2}\right)\right\}e^{i\Delta t/2}, \tag{2.12}$$

where $\Omega_n^2 = \Delta^2 + 4g^2(n+1)$. The normalization condition is satisfied for different initial value of $c_{a,n}(0)$ and $c_{b,n}(0)$.

The population inversion, i.e. the difference between the population in the excited and in the ground state, is:

$$W(t) = \sum_n \left[ \left| c_{a,n-1}(t) \right|^2 - \left| c_{b,n}(t) \right|^2 \right]. \tag{2.13}$$

In a weak field limit, assuming the photon number $n = 1$. If the field is on resonance with the atom and the atom is initially in the ground state $|b, 2\rangle$, i.e. $c_{a,0}(0) = 0$, $c_{b,1}(0) = 1$ and $\Delta = 0$, then

$$\left| c_{a,0}(t) \right|^2 = \sin^2\left(\frac{\Omega_n t}{2}\right), \tag{2.14}$$

$$\left| c_{b,1}(t) \right|^2 = \cos^2\left(\frac{\Omega_n t}{2}\right), \tag{2.15}$$

$$W(t) = \left| c_{a,0}(t) \right|^2 - \left| c_{b,1}(t) \right|^2 = -\cos(\Omega_n t) = -\cos(2g(1+1)t). \tag{2.16}$$

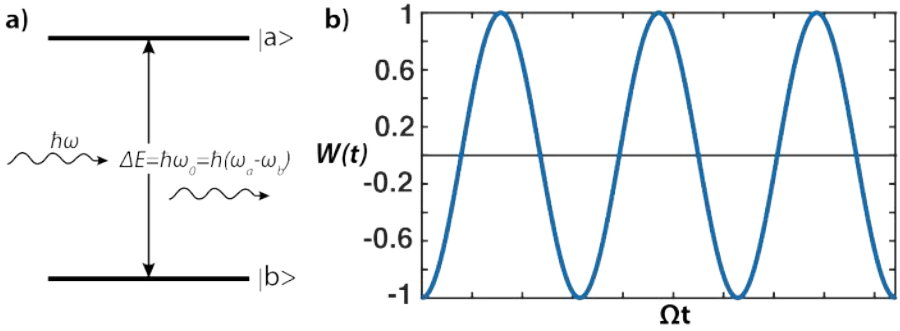


Figure 2-1 a) Energy diagram of a two-level atom. The photon energy of incident field is $\hbar\omega$. b) The inversion shows the atom oscillates between ground state and excited state.

Equation (2.16) as plotted in Figure 2-1 b) shows that the inversion oscillates back and forth between -1 and 1 with the Rabi frequency $\Omega_n$. This phenomenon is called Rabi oscillation which is reproduced here for a two-level system resonant with a single mode field. It is interesting to note that the Rabi oscillation takes place even for a vacuum field ($n = 0$). This is due to the spontaneous emission of the two-level system in excited state, which is not explained in classical and semiclassical theory. However, the continuous oscillation between ground and excited state is not experimentally consistent, since only one mode of the field is considered. A detailed analysis of spontaneous emission under Weisskopf-Wigner approximation is given in section 2.1.1.

### 2.1.1 Spontaneous emission

In semiclassical theory, spontaneous emission is added phenomenologically[5]. As explained above, in order to correctly address spontaneous emission, a continuum of modes in all directions, describing the free space, needs to be taken into account. The Hamiltonian in the interaction picture is now given by:

$$\Upsilon = \hbar \sum_{\boldsymbol{k}} g_{\boldsymbol{k}} e^{-i\boldsymbol{k}\cdot\boldsymbol{r_0}} \left(\sigma_+ a e^{i\Delta t} + a^\dagger \sigma_- e^{-i\Delta t}\right). \tag{2.17}$$

Here, the wave vector $\boldsymbol{k}$ also indicates the mode index. The summation over $\boldsymbol{k}$ indicates the multiple summation in all directions. The spatial dependence is included with $\boldsymbol{r_0}$ describing the location of the electron in the two-level atom. Same as the discussion presented above, assuming that field is on resonance with the atom and the atom is initially in the excited state $|a, 0\rangle$, then state vector is:

$$|\varphi\rangle = c_a(t)|a, 0\rangle + \sum_{\boldsymbol{k}} c_{b,\boldsymbol{k}}(t)|b, 1_{\boldsymbol{k}}\rangle. \tag{2.18}$$

Still we are interested in the population of states. Substitute equation (2.17) and (2.18) into (2.7), then projecting it to $\langle a, n|$ and $\langle b, n+1|$ to obtain:

$$\dot{c}_a(t) = -i \sum_{\boldsymbol{k}} g_{\boldsymbol{k}} e^{-i\boldsymbol{k}\cdot\boldsymbol{r_0}} e^{i\Delta t} c_{b,\boldsymbol{k}}(t), \tag{2.19}$$

$$\dot{c}_{b,\boldsymbol{k}}(t) = -i g_{\boldsymbol{k}} e^{-i\boldsymbol{k}\cdot\boldsymbol{r_0}} e^{-i\Delta t} c_a(t). \tag{2.20}$$

After integrating of equation (2.20) and substituting into (2.19), we have:

$$\dot{c}_a(t) = -\sum_{\boldsymbol{k}} \left| g_{\boldsymbol{k}} e^{-i\boldsymbol{k}\cdot\boldsymbol{r_0}} \right|^2 \int_0^t dt' e^{i\Delta(t-t')} c_a(t'). \tag{2.21}$$

The first assumption in the Weisskopf-Wigner approximation is the summation over $\boldsymbol{k}$ can be replaced by an integral over full space,

$$\sum_{\boldsymbol{k}} \rightarrow 2 \frac{V}{(2\pi)^3} \int_0^{2\pi} d\phi \int_0^{\pi} \sin\theta \, d\theta \int_0^{\infty} k^2 dk. \tag{2.22}$$

Here, $\theta$ is the angle between the TDM $\hat{\wp}$ and the electric field polarization vector $\hat{\epsilon}_k$. After performing integrations over $\phi$ and $\theta$ and using $k = \nu_k/c$, equation (2.21) is now:

$$\dot{c}_a(t) = -\frac{4\hat{\wp}_{ab}^2}{(2\pi)^2 6\hbar\epsilon_0 c^3}\int_0^\infty \nu_k^3 d\nu_k \int_0^t dt' e^{i\Delta(t-t')} c_a(t'). \tag{2.23}$$

Another important idea of the Weisskopf-Wigner approximation is that the emission spectrum is centred at the atomic transition frequency $\omega_0$, and the integration over $\omega_k$ deviating far from $\omega_0$ is negligible. We can replace $\omega_k$ by $\omega$, and the lower limit 0 to -∞. Utilizing the equation

$$\int_{-\infty}^{\infty} e^{i\Delta(t-t')} d\nu_k = 2\pi\delta(t-t'), \tag{2.24}$$

we obtain the time derivative of the probability amplitude $c_a(t)$,

$$\dot{c}_a(t) = -\frac{\Gamma}{2} c_a(t), \tag{2.25}$$

where the decay constant is,

$$\Gamma = \frac{1}{4\pi\epsilon_0}\frac{4\omega^3\hat{\wp}_{ab}^2}{3\hbar c^3}. \tag{2.26}$$

A solution of equation (2.25) reveals the population in excited state as:

$$\rho_{aa} \equiv |c_a(t)|^2 = exp(-\Gamma t). \tag{2.27}$$

This tells that an excited atom decays exponentially with the lifetime

$$\tau = 1/\Gamma. \tag{2.28}$$

Rewrite equation (2.26) to

$$\Gamma = 2\pi\langle g^2(\omega)\rangle D(\omega), \tag{2.29}$$

and

$$D(\omega) \equiv \frac{V\omega^2}{\pi^2 c^3}. \tag{2.30}$$

$g(\omega)$ is defined in equation (2.3) and the angle brackets in equation (2.29) represent an angular average. It should be stressed that $D(\omega)$, called the mode density, is the same as the one obtained in the quantization of the field. And equation (2.29) is same as the Fermi's golden rule[42] derived

from perturbation theory, which describes the transition rate from one energy eigenstate of a quantum system to another energy eigenstates.

### 2.1.2 Excitation of the emitter

In the following we derive the single photon excitation probability of an atomic system consisting of a lower state $|b\rangle$ and a set of excited states $|a_j\rangle$ as shown in Figure 2-2 considering the interaction with linearly polarized light following the notation of [43]. Assuming the atom starts at state $|b\rangle$ and the field state is $|i\rangle$, and applying the RAW, the interaction picture Hamiltonian is:

$$\Upsilon = -\sum_j \hat{\wp}_{a_j b}\sigma_{a_j b}E^{(+)}(\boldsymbol{r},t)e^{-i\omega_{a_j}t} + H.c.. \tag{2.31}$$

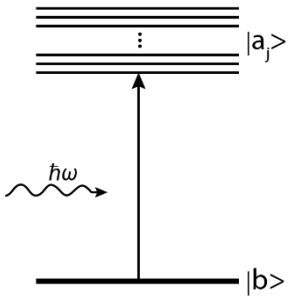


Figure 2-2 Energy diagram of an atom with a set of excited states. Adapted from [43]

$H.c.$ refers to the Hermitian conjugated Hamiltonian, and $E^{(+)}(\boldsymbol{r},t)$ and $E^{(-)}(\boldsymbol{r},t)$ are two conjugated operators, which compose the electric field operator

$$\begin{aligned} E(\boldsymbol{r},t) &= E^{(+)}(\boldsymbol{r},t) + E^{(-)}(\boldsymbol{r},t) \\ &= \sum_{\boldsymbol{k}} \hat{\epsilon}_{\boldsymbol{k}}\mathcal{E}_{\boldsymbol{k}}a_{\boldsymbol{k}}e^{-i\omega_{\boldsymbol{k}}t+i\boldsymbol{k}\cdot\boldsymbol{r}} + \sum_{\boldsymbol{k}} \hat{\epsilon}_{\boldsymbol{k}}\mathcal{E}_{\boldsymbol{k}}a_{\boldsymbol{k}}^{\dagger}e^{i\omega_{\boldsymbol{k}}t-i\boldsymbol{k}\cdot\boldsymbol{r}}. \end{aligned} \tag{2.32}$$

The probability of finding the atom in the excited state $|a_j\rangle$ is obtained by calculating the expectation value of the projection operator $|a_j\rangle\langle a_j|$. Assuming $\hat{\wp}_{a_j b}$ is independent of $j$, we get the probability of exciting the atom to any excited states $|a_j\rangle$ (detailed derivation can be found in [43])

$$P(t) = \kappa \hat{\wp}^2 \int_0^t dt_1 \left\langle i \middle| E^{(-)}(\boldsymbol{r}, t_1) + E^{(+)}(\boldsymbol{r}, t_1) \middle| i \right\rangle, \tag{2.33}$$

where $\kappa$ is constant. Normally, we are interested in the excitation rate $\gamma_{exc}$ for a stationary field which can be written as:

$$\gamma_{exc} \propto |\hat{\wp} \cdot \boldsymbol{E}|^2. \tag{2.34}$$

It is again the same as the equation of Fermi's golden rule.

### 2.1.3 Excitation patterns in the focal fields of radially/azimuthally polarized laser beams

In contrast to a linear polarized Gaussian laser beam, which is the lowest order Hermite-Gaussian (HG) mode[80], a combination of higher order HG modes can describe radially/azimuthally polarized laser beam where the polarization of the beam varies spatially. The HG modes $\boldsymbol{E}_{mn}^{H}$ can be described as[80]:

$$\boldsymbol{E}_{mn}^{H}(x, y, z) = w_0^{m+n} \frac{\partial^n}{\partial x^n} \frac{\partial^m}{\partial y^m} \boldsymbol{E}(x, y, z), \tag{2.35}$$

where $\boldsymbol{E}(x, y, z)$ is fundamental Gaussian mode and $w_0$ is the beam waist of Gaussian mode, $n$ and $m$ denote the order of the Hermite polynomials and account for the nodes of the beam, respectively.

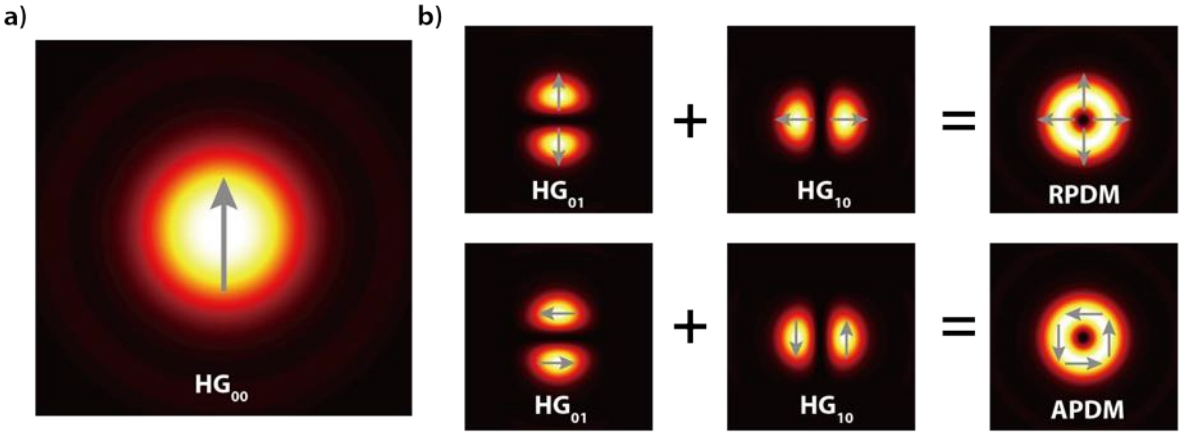


Figure 2-3 a) Electric intensity profile of zero order Hermite-Gaussian (HG) mode. b) Illustration of the

combination of higher order HG modes to form a radially/azimuthally (RPDM/APDM) polarized laser beam.

Figure 2-3 shows the intensity distribution $|\boldsymbol{E}|^2$ of the first three HG modes and illustrates the formation of radially/azimuthally polarized laser beam. Both radially and azimuthally polarized laser beams have intensity profiles in the collimated beam that look like a doughnut[81,82], and are therefore called radially polarized doughnut mode (RPDM) and azimuthally polarized doughnut mode (APDM).

Focal fields formed with excitation laser beams with APDM and RPDM polarization[83] are used to monitor the orientation of the molecular TDM. The image coordinate system **XYZ** is illustrated in Figure 2-4 a). In the focus, electric field of APDM is only transversally polarized in the **X-Y** plane (in-plane,), while the field of RPDM contains both transversal (in-plane) and longitudinal (out-of-plane) polarizations[82–84]. The intensity profiles of APDM and RPDM in the focus are shown in Figure 2-4 b)-d).

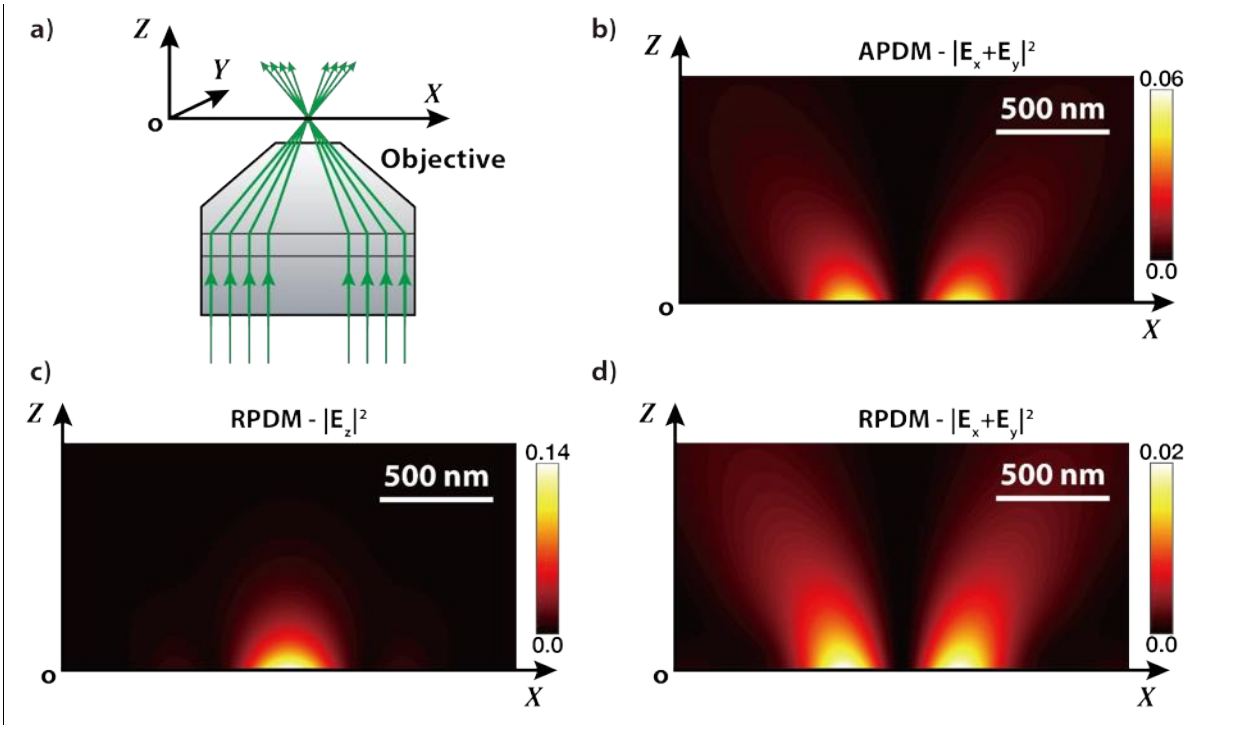


Figure 2-4 a) The image coordinate system **XYZ**. The focus is defined at $z = 0$. b) In-plane intensity profile of the APDM in the X-Z plane. Out-of-plane c) and in-plane d) intensity profile of the RPDM in the X-Z plane. The numerical aperture of the objective lens is set to 1.46, and simulation range is 2 μm×1 μm with excitation wavelength at 532 nm.

Figure 2-5 b) are simulated excitation patterns of a single TDM, which has different spatial orientations that are defined by the azimuthal $\Phi$ and polar $\Theta$ angle in the image coordinate system **XYZ** shown in Figure 2-5 a). All patterns acquired with the APDM have a double lobed shape,

where the pattern orientation directly indicates the orientation of the TDM in the **X-Y** plane (indicated by the grey arrows, referred to in-plane dipole). Excitation with the RPDM results in patterns ranging from dot-like to asymmetric double lobe to symmetric shapes. These different pattern shapes are caused by the interaction of in-plane and out-of-plane polarizations with the three dimensionally oriented TDM that allows determining the full three-dimensional orientation of the TDM.

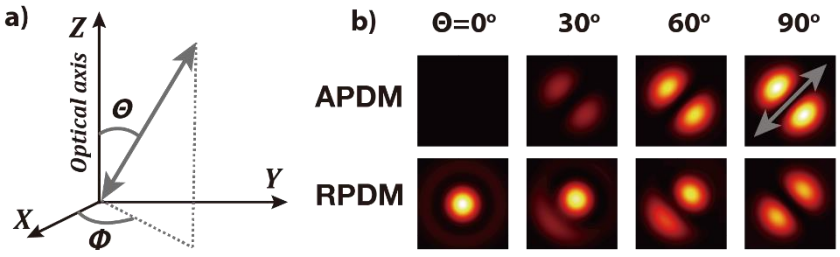


Figure 2-5 a) The image coordinate system **XYZ**. b) Simulated fluorescence excitation patterns for different TDM orientations. The polar angle $\Theta$ and azimuthal angle $\Phi$ are defined in the image coordinate system **XYZ** ($0° \leq \Phi \leq 360°$, $0° \leq \Theta \leq 180°$) shown in a).

### 2.1.4 Antibunching

The statistical properties of light in the quantum regime, which are often investigated via the photon correlation function, behave different than in the classical regime. The most often used correlation function is the second-order correlation function, which is defined as the joint probability of photon detection, which can be understood as the probability to detect a photon at time $t+\tau$ after one was detected at the time point $t$. The normalized second correlation function can be written as:

$$g^2(\tau) = \frac{\langle I(t)I(t+\tau)\rangle}{\langle I(t)\rangle^2}. \tag{2.36}$$

If $g^2(\tau) > g^2(0)$ is observed for a light source, it means fewer photon pairs are detected close together than further apart. It is hence called photon antibunching. For a stationary classical light source, the photon distribution obeys the Schwarz inequality,

$$|\langle I(t)I(t+\tau)\rangle|^2 \leq \langle I^2(t)\rangle\langle I^2(t+\tau)\rangle. \tag{2.37}$$

Thus, we have $g^2(\tau) \leq g^2(0)$ for a classical field. Photon antibunching is a purely quantum-mechanical effect.

Exact antibunching behaviour of a single two-level atom under resonance excitation was discussed by Carmichael and Walls[85]. Kitson et al.[86] provided an analysis of $g^2(\tau)$ for different number of emitters under excitation using a semiclassical approach, which gives a result for $N$ molecules with fluorescence decay rate $\gamma$:

$$g^2(\tau) = 1 - \frac{1}{N} e^{-|\gamma\tau|}. \tag{2.38}$$

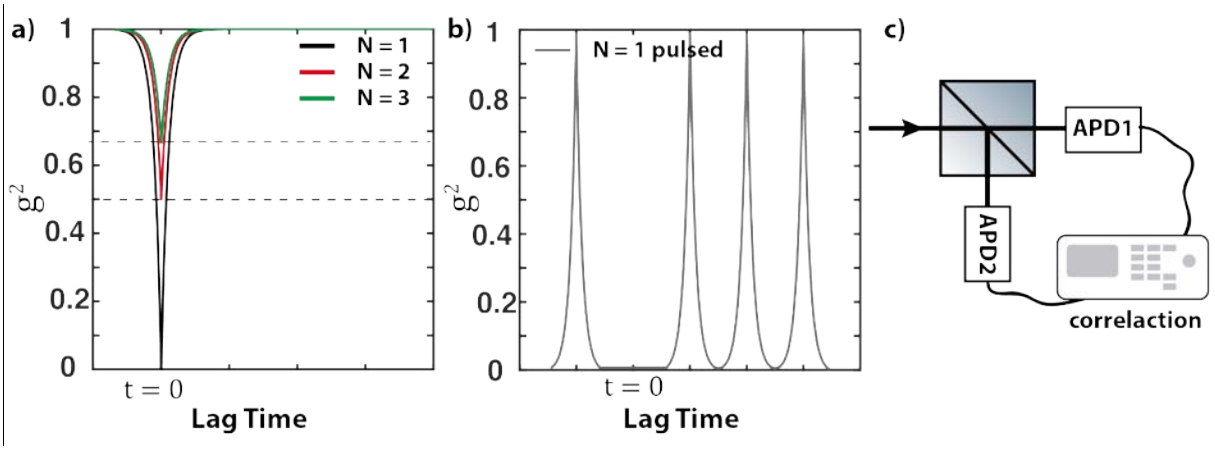


Figure 2-6 a) Second-order correlation function for N emitters under continuous-wave (CW) and b) pulsed excitation. c) Sketch of Hanbury Brown and Twiss interferometer.

Equation (2.38) is plotted in Figure 2-6 a) and b) for different $N$. $g^2(0)$ is zero if only one emitter is excited, and increase to 0.5 if two emitters are excited. Hence, it can be determined if single photon emitter is observed via photon antibunching. The second-order correlation function measurement can be implemented using a Hanbury Brown and Twiss interferometer[87] (Figure 2-6 c). Two detectors are required to overcome the long dead-time, i.e. the period of the detector to go back to the initial state after the detection of one photon.

### 2.1.5 Organic fluorescent molecule

We have introduced a theoretical framework describing some essential features of a single fluorescent atom. The main conclusions drawn above are also valid for a fluorescent molecule, since it can be reduced to an effective two-level system in many situations. Although, a complete quantum description of a fluorescent molecule is extremely complicated, transcendent progresses have been achieved with the efforts of several generations of scientists.

In this section, we will state general features and important principles of the excitation and emission process of fluorescent molecules consisting of several atoms so called polyatomic

molecules. The first step towards understanding a realistic molecule is to include larger nuclei consisting of several protons and neutrons, multiple electrons and their interactions. The Born-Oppenheimer approximation is assuming that the movement of nuclei can be neglected in the context of discussing the movement of electrons, since the electron mass is about 2000 times lighter than that of a proton mass, hence the electrons can respond to an externally applied electric field much faster than nuclei. The electronic wave functions of polyatomic molecules are called molecular orbitals and are constructed from the respective atomic orbitals and can spread over the entire molecule. Their energy eigen values can be obtained from solving the time-independent Schrödinger equation. Following Hund's rule of maximum multiplicity for the electron spin and Pauli's exclusion principle, the electrons occupy the energy states starting from the lowest energy state to reach the molecular ground state $\Psi_0(\boldsymbol{r})$. Here, $\boldsymbol{r}$ is the collection coordinate of spatial orbitals and spin orbitals of all electrons, i.e., $\boldsymbol{r} \equiv (\boldsymbol{r_1}, \boldsymbol{s_1}, \boldsymbol{r_2}, \boldsymbol{s_2}, \dots, \boldsymbol{r_N}, \boldsymbol{s_N}, \dots)$.

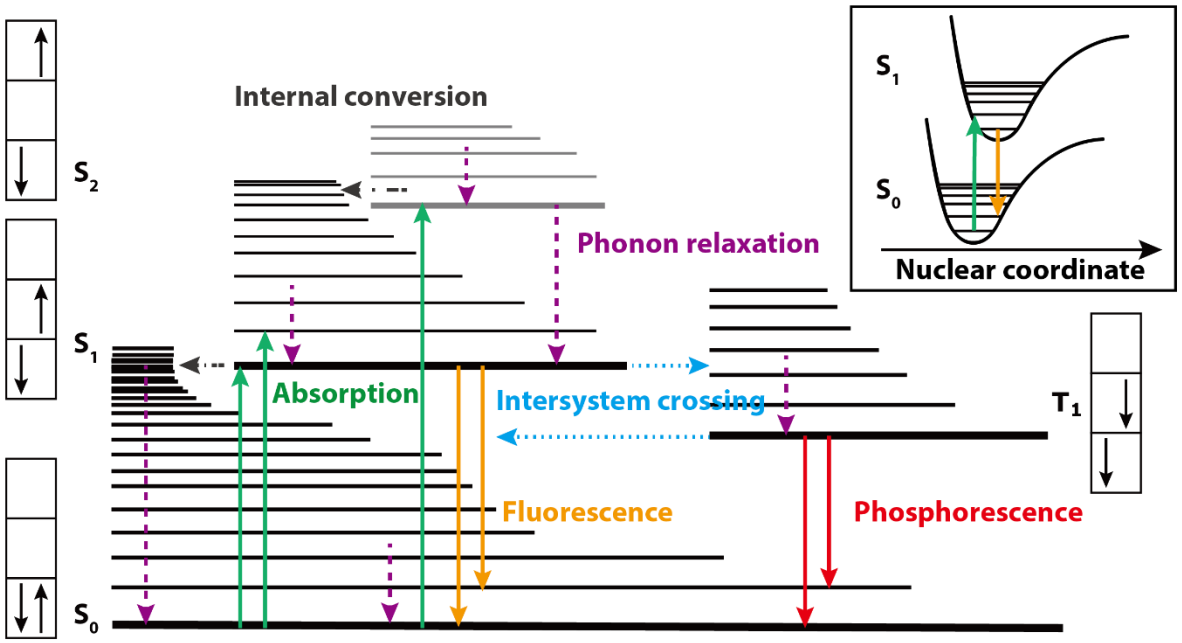


Figure 2-7 The Jablonski diagram of a fluorescent molecule. The inset in top-right is a simplified Morse potential energy diagram of a two atomic molecule including the nuclear coordinate. Adapted from [5].

Upon electromagnetic excitation, the molecule can undergo an electronic transition from the electronic ground state $S_0$ to the first electronic excited state $S_1$ and higher excited state $S_n$ described by the wave function $\Psi_n(\boldsymbol{r})$. The transition probability, hence, the absorption spectra, is determined with equation (2.34). With a broadband stationary excitation field, the TDM defined in equation (2.5) determines full absorption spectrum. For molecules that absorb and emit in the

visible range, the main electronic transition $\Psi_0(\boldsymbol{r}) \rightarrow \Psi_n(\boldsymbol{r})$ is the electron at HOMO (Highest Occupied Molecular Orbital) been lifted to LUMO (Lowest Unoccupied Molecular Orbital).

For most of the cases, molecular ground state $\Psi_0(\boldsymbol{r})$ is a singlet state, where all electrons are paired with an overall spin quantum number $S = 0$. Ignoring spin–orbit coupling, the molecule wavefunction can be separated into a spatial part $\psi_0(\boldsymbol{r})$ and spin part $\chi_0(\boldsymbol{s})$,

$$\Psi_0(\boldsymbol{r}) = \psi_0(\boldsymbol{r})\chi_0(\boldsymbol{s}). \tag{2.39}$$

We consider the hydrogen molecule for simplicity. The ground state corresponds to bounding orbital $\psi_0(\boldsymbol{r})$, which is symmetric. There is only one allowed value of the spin component $m_S = 0$ while $S = 0$, then

$$\chi_0(\boldsymbol{s}) = \frac{1}{\sqrt{2}}\big(\uparrow(s_1)\downarrow(s_2) - \downarrow(s_1)\uparrow(s_2)\big). \tag{2.40}$$

The antisymmetric property, i.e., the interchange of $s_1$ and $s_2$ leads to a $-\chi_0(\boldsymbol{s})$ and is a requirement of Pauli's exclusion principle ensures that the probability to find two electrons with same quantum numbers is zero.

For the excited state, the overall spin can be 0 or 1. $S = 0$ is again a singlet state with symmetric $\psi_1(\boldsymbol{r})$ and antisymmetric $\chi_1(\boldsymbol{s})$. While for $S = 1$, the spin multiplicity $2S + 1 = 3$ corresponds to three spin wavefunctions with allowed values of the spin component $m_S = -1, 0$, and 1,

$$\chi_1(\boldsymbol{s}) = \begin{cases} \uparrow(s_1)\uparrow(s_2) \\ \dfrac{1}{\sqrt{2}}(\uparrow(s_1)\downarrow(s_2) + \downarrow(s_1)\uparrow(s_2)). \\ \downarrow(s_1)\downarrow(s_2) \end{cases} \tag{2.41}$$

The energy of the state is mainly determined by the spatial wavefunction, hence the energies of three possible electronic states with different spins are equal. This is called a triplet state. Noticing the spin components are symmetric now, it is required that spatial components are antisymmetric. Now consider the electronic transition probability for a singlet-singlet and singlet-triplet using equation(2.5), it is proportional to

$$\widehat{\wp}_{01} = e\langle\psi_1(\boldsymbol{r})|\boldsymbol{r}|\psi_0(\boldsymbol{r})\rangle\langle\chi_1(\boldsymbol{s})\chi_0(\boldsymbol{s})\rangle. \tag{2.42}$$

$\downarrow(s)$ and $\uparrow(s)$ are mutual orthogonal, thus, only the spatial wavefunction matters. Considering the symmetric wavefunction of the singlet state and the antisymmetric wavefunction of the triplet

state, it can be concluded that electronic transition between singlet state and triplet state is forbidden.

If spin–orbit coupling is invoked[88], intersystem crossing (ISC), referring to the nonradiative transition between two electronic states of different multiplicity, is possible as a rare event. As an example, a typical fluorescent dye possesses a fluorescence lifetime of several nanoseconds and a phosphorescence lifetime of several milliseconds.

The nuclear movement has been ignored in the discussions above. In a fixed electronic state, introducing the vibration and rotation of the nuclei give rise to series of vibrational and rotational states with different associated energy. The rotational energy levels are closer compared to the vibrational energy levels, and they are neglected here. The energy diagram in Figure 2-7 shows the lowest electronic levels and series of superimposed vibrational energy levels. Inelastic scattering of optical photons from vibrating molecules is called Raman scattering[89], named after Indian scientist C.V. Raman. In this process, the scattered photon losses or gains vibrational energy

$$h\nu' = h\nu \pm \Delta E, \tag{2.43}$$

which is called Stokes Raman or anti-Stokes Raman scattering, respectively.

A transition that involves simultaneous changes of the electronic states and the vibrational states is a vibronic transition. The nuclear vibration can be described by molecular wavefunction of the form of equation (2.44) where $\boldsymbol{R}$ stands for the nuclear coordinates and $\boldsymbol{r}$ for the electron coordinate,

$$\Psi_n(\boldsymbol{R},\boldsymbol{r}) = \psi_{v,n}(\boldsymbol{R})\psi_{e,n}(\boldsymbol{r})\chi_n(\boldsymbol{s}). \tag{2.44}$$

The vibronic transition probability is then proportional to

$$\widehat{\wp}_{ij} = e\langle\psi_{v,i}(\boldsymbol{R})\psi_{v,i}(\boldsymbol{R})\rangle\langle\psi_{e,j}(\boldsymbol{r})|\boldsymbol{r}|\psi_{e,i}(\boldsymbol{r})\rangle\langle\chi_j(\boldsymbol{s})\chi_i(\boldsymbol{s})\rangle. \tag{2.45}$$

The first term $\langle\psi_{v,i}(\boldsymbol{R})\psi_{v,i}(\boldsymbol{R})\rangle$ is called Franck-Condon factor and depends on the nuclear coordinates $\boldsymbol{R}$. The Franck-Condon principle explains that a vibronic transition is more likely to happen, if the two vibrational wavefunctions have a larger overlap. A direct consequence of Franck-Condon principle is Kasha's Rule[90], which states that '*the emitting level of a given multiplicity is the lowest excited level of that multiplicity*'.

Thus, a molecule at ground state can be excited to higher energy level by absorbing a photon. After a fast relaxation process to the lowest vibrational state in the first electronic excited state, the molecule can emit a photon with longer wavelength or go through non-radiative internal conversion to return back to ground state. ISC can also happen from $S_1$ to $T_1$ followed by phosphorescence emission. All possible relaxation paths are sketched in Figure 2-7.

## 2.2 Optical Resonator

Optical resonator, also called optical cavity, is the term for devices that can confine light. Plenty of cavity configurations with different realization schemes for the confinement have been proposed, such as micropillar cavities, whispering-gallery mode cavities, and photonic crystal cavities. In this section, we give an overview on two types of cavities: the Fabry–Pérot (F-P) microcavity and the plasmonic nanocavity. Here, micro- and nanometre dimensions characterize the cavity.

### 2.2.1 Fabry–Pérot microcavity

A Fabry–Pérot microcavity, consisting of two parallel mirrors, is one of the simplest optical resonator configurations. To function effectively in the visible wavelength range, especially when the medium loss inside the cavity cannot be neglected, the distance $L$ of the mirrors should be less than a few wavelengths of light. Reflection allows constructive and destructive interference. For a cavity filled with a medium of refractive index $n$, as shown in Figure 2-8, the resonance condition requires the wavevector component $k_\perp = k\cos\theta$ perpendicular to the mirror surface to fulfil:

$$k_\perp \times 2L = 2m\pi. \tag{2.46}$$

Here, $m$ is a positive integer, $\theta$ is the incident angle. The resonance frequency is:

$$\omega_c = \frac{m\pi c/L}{\sqrt{n^2 - \sin^2\theta}}. \tag{2.47}$$

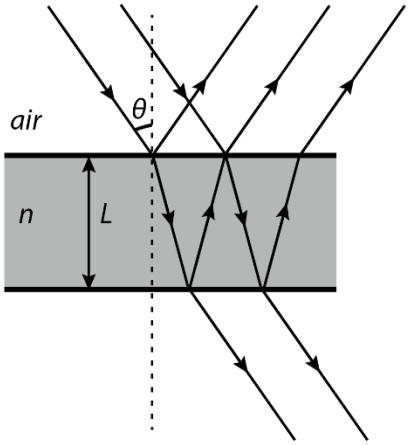


Figure 2-8 Schematic diagram of the F-P cavity. The opitcal path difference between each adjacent beam is $\delta = 2L\sqrt{n^2 - \sin^2\theta}$.

In the following we assume a two-layer structure, and the mirror thickness is not included. A numerical method, for example the Transfer Matrix Method[91] (TMM), can be used for the calculation of multilayer structures to obtain the resonance spectrum.

The quality-factor (or Q-factor) is defined as the ratio of the stored energy inside the cavity to the energy lost per oscillation cycle of the electromagnetic field:

$$Q = 2\pi \frac{stored\ energy\ (W)}{energy\ lost\ per\ cycle\ (\Delta W)} = 2\pi \frac{storage\ time\ (\tau_c)}{optical\ period\ \left(\frac{2\pi}{\omega_c}\right)}. \tag{2.48}$$

The lineshape of the resonance mode is given by a Lorentzian:

$$L_l(\omega) = \frac{\gamma/2\pi}{(\omega - \omega_c)^2 + \gamma^2/4}, \tag{2.49}$$

since the energy inside the cavity decays exponentially $W \propto |E|^2 \propto e^{-\gamma t}$. Where $\gamma$ is the damping rate that defines the linewidth $\delta\omega_c = \gamma$ and the energy storage time is $\tau_c = 1/\gamma$. Rewriting (2.48) and (2.49) we obtain

$$\begin{aligned} Q &= \frac{\omega_c}{\delta\omega_c}, \\ L_l(\omega) &= \frac{1}{\pi}\frac{\omega_c/2Q}{(\omega - \omega_c)^2 + (\omega_c/2Q)^2} \end{aligned}. \tag{2.50}$$

$L_l(\omega)$ determines the density of optical states inside the cavity. The cavity finesse is another important parameter for characterizing a F-P cavity and is defined as the ratio of the frequency separation between successive resonance modes $\Delta\omega_c$ to the linewidth $\delta\omega_c$:

$$F = \frac{\Delta\omega_c}{\delta\omega_c} \tag{2.51}$$

Q-factor and finesse are almost equal for a F-P cavity with small distance $L$, while they are quite different for a large $L$ or for cavity where the main loss does not come from the finite reflectivity R of the mirrors.

### 2.2.2 Plasmonic nanocavity

Gustav Mie[92] discussed the absorption and scattering of a plane electromagnetic wave by a spherical particle in 1908. His results, now called Mie theory, allow to calculate the exact scattering cross section $Q_{sca}$ and absorption cross section $Q_{abs}$ of a spherical particle. A summation quantity named extinction $Q_{ext} = Q_{sca} + Q_{abs}$ is more often used.

A prominent application of Mie theory is calculating the scattering of spherical noble metal particles with a radius close to or smaller than the wavelength of the incident light, where distinct peaks appear in the extinction spectrum. It is now understood that the peaks arise from the resonance of incident light and electromagnetic eigenmodes of the sphere, i.e., the collective oscillations of free electrons excited by the electric field component of the light. Combined with boundary conditions Mie theory can reveal the confinement of the resonance normal modes around the particle. Due to the localization property, the resonance is termed as localized surface plasmon resonance (LSPR).

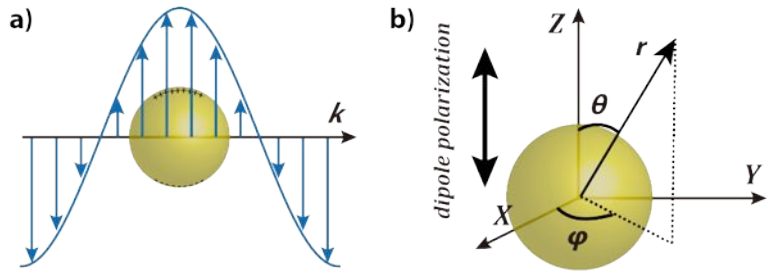


Figure 2-9 a) Schematic diagram of metal nanosphere interacting with light. b) The spherical coordinate system

used to describe the metal nanosphere polarized along $z$ axis.

In the electrostatic approximation the spherical particle is assumed to be small enough compared to the wavelength, such that the electric field can be treated uniform over the diameter of the sphere (Figure 2-9 a)) and the response of the particle to the electromagnetic wave can be approximated using electrostatic equations. Considering a single metal nanosphere with a radius of $a$ and a homogeneous, isotropic, frequency dependent complex dielectric constant $\varepsilon_M$ being placed in a dielectric medium with a real dielectric constant $\varepsilon_D$. Figure 2-9 b) shows a spherical coordinate system with the $z$ axis parallel to the dipole polarization of the nanosphere. The eigenmodes satisfy the Laplace equation $\nabla^2\Phi = 0$ for the scalar potential $\Phi$ in the absence of external charges. Considering rotation symmetry of the sphere, a solution of the $l$th mode is[93]:

$$\Phi = \begin{cases} C\left(\frac{r}{a}\right)^l P_l(\cos\theta), & r < a \\ C\left(\frac{a}{r}\right)^{l+1} P_l(\cos\theta), & r \geq a \end{cases}, \tag{2.52}$$

where $C$ is constant and $P_l(\cos\theta)$ is the Legendre polynomial of degree $l$ = 0, 1, 2,…. Noting that we have omitted the asymmetric solutions related to associated Legendre polynomials since an incident field will break the symmetry immediately.

At $r = a$, the continuity of the tangential electric field $E_\theta = -\partial\Phi_l/r\partial\theta$ is satisfied, while the continuity of the normal component of the electrical displacement $D_r = -\varepsilon\partial\Phi_l/\partial r$ requires that dielectric functions of the metal $\varepsilon_M(\omega)$ and the dielectric medium $\varepsilon_D(\omega)$ must meet:

$$l\varepsilon_M(\omega) + (l+1)\varepsilon_D(\omega) = 0, \tag{2.53}$$

i.e., only certain optical frequency $\omega_l$ can satisfy the continuity conditions, and these solutions are referred to the resonance frequency of the $l$th mode.

As shown later in equation (2.59), the higher order ($l > 1$) modes have zero dipole moment and can normally not be excited by an external electromagnetic field. If a nanosphere is placed in a uniform external electric field, only the dipole mode ($l = 1$) need to be considered, and the resonance condition given by (2.53) is:

$$\varepsilon_M(\omega_1) + 2\varepsilon_D(\omega_1) = 0. \tag{2.54}$$

This is the Fröhlich condition, and the associated mode is usually referred to the localized surface plasmon of a nanosphere.

The resonance frequency can be determined using Drude model for the metal dielectric function:

$$\varepsilon_M = 1 - \frac{\omega_p^2}{\omega^2 + i\gamma\omega}, \tag{2.55}$$

where $\omega_p$ is the plasmon frequency and $\gamma$ is the damping of the metal. Since the damping $\gamma$ is small compared to the optical frequency and the dielectric constant $\varepsilon_D$ of the medium only varies slowly with the angular frequency of the incident field, the resonance frequency of the eigenmodes is obtained by substituting (2.54) in (2.55):

$$\omega_l = \omega_p \sqrt{\frac{l}{l + (l+1)\varepsilon_D}}. \tag{2.56}$$

The electric field of the $l$th mode can be calculated using $\boldsymbol{E} = -\nabla\Phi$ and equation (2.52),

$$E_l(r,\theta) = \begin{matrix} E_{in,l}(r,\theta) \\ E_{out,l}(r,\theta) \end{matrix} \tag{2.57}$$
$$= \begin{cases} E_{max,l}\left(\frac{r}{a}\right)^{l-1}\left[-\frac{l}{l+1}P_l(\cos\theta)\hat{r} + \frac{1}{\sin\theta}[P_{l+1}(\cos\theta) - \cos\theta\, P_l(\cos\theta)]\hat{\theta}, \quad r < a \\ E_{max,l}\left(\frac{a}{r}\right)^{l+2}\left[P_l(\cos\theta)\hat{r} + \frac{1}{\sin\theta}[P_{l+1}(\cos\theta) - \cos\theta\, P_l(\cos\theta)]\hat{\theta}, \quad r \geq a \end{cases}.$$

$E_{max,l} = C(l+1)/a$ is the maximum field just outside of the metal sphere. $\hat{r}$ and $\hat{\theta}$ are radial and polar unit vector respectively. The surface charge density $\sigma_l(\theta)$ can be calculated at $r = a$,

$$\sigma_l(\theta) = \varepsilon_0(\varepsilon_M - 1)E_{in,l}^{\hat{r}}(a,\theta) - \varepsilon_0(\varepsilon_D - 1)E_{out,l}^{\hat{r}}(a,\theta) = \frac{2l+1}{l+1}\varepsilon_0 E_{max,l}P_l(\cos\theta). \tag{2.58}$$

The dipole moment can then be evaluated by:

$$p_l = q\hat{r} = \int a\cos\theta\, \sigma_l(\theta)ds = 2\pi a^3 \int_0^\pi \sigma_l(\theta)\cos\theta\sin\theta\, d\theta. \tag{2.59}$$

Only $l = 1$ produces a non-zero dipole moment $p_1 = 2\pi a^3\varepsilon_0 E_{max,1}$. The electric field distribution of the first four order modes is plotted for a sphere $a = 50$ nm in Figure 2-10. It clearly shows that the field is confined around the surface of the nanosphere. To get an efficient resonance at visible range, the sphere radius should be around several nanometres to hundreds of nanometres and thus the term nanocavity. The characterization for a microcavity described in 2.2.1 can be directly adapted to the nanocavity once the extinction spectrum is obtained.

Mie theory gives exact solution only for a spherical particle. For a non-spherical structure, numerical calculations of Maxwell's equations work efficiently. However, in comparison to an analytic model, numerical calculations fail to give a direct physical meaning of the results. Besides, it is time consuming if one wants to have a broad view of a certain nanostructure.

In the following, we introduce an analytic model developed by Khurgin and Sun[94–96]. The model is based on the effective volume method pioneered by Maier[97], and allows one to optimize the structures for the largest possible field enhancements. The concept of effective volume with single nanosphere is introduced and will be used for more complex systems in 2.3.4.

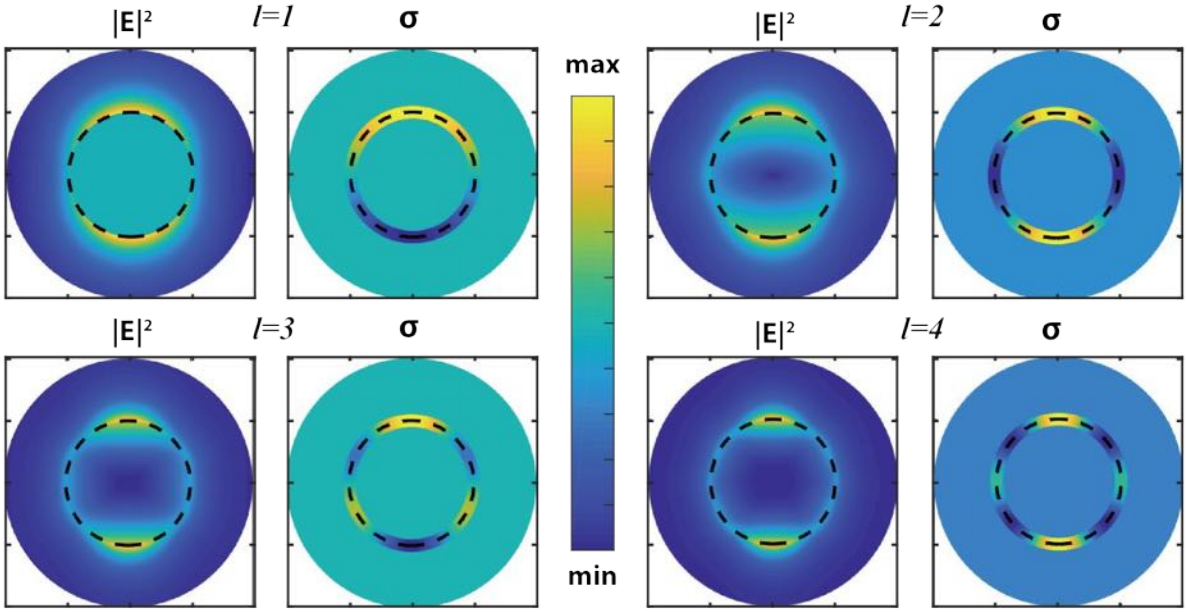


Figure 2-10 Optical intensity $|E|^2$ and surface charge density $\sigma$ of different order modes for a nanosphere $a = 50\ nm$. Black dash line outlined boundary of the sphere.

Begin with the $l$th mode energy[70], which is the summation of the energy inside and outside of the sphere:

$$U_l = U_{in,l} + U_{out,l}, \tag{2.60}$$

$$U_{in,l} = \frac{1}{4}\varepsilon_0 \frac{\partial \omega \varepsilon_M}{\partial \omega} \int_{r<a} |E_{in}|^2 d^3r = \frac{1}{4}\varepsilon_0 \varepsilon_D E_{max,l}^2 \frac{8\pi a^3}{(l+2)^2(2l+1)} \left(\frac{l}{\varepsilon_D} + \frac{l+1}{2}\right).$$

$$U_{out,l} = \frac{1}{4}\varepsilon_0 \varepsilon_D \int_{r>a} |E_{out}|^2 d^3r = \frac{1}{4}\varepsilon_0 \varepsilon_D E_{max,l}^2 \frac{4\pi a^3}{(l+2)(2l+1)}$$

The effective volume of the $l$th mode is defined as $U_l = 1/4\varepsilon_0 \varepsilon_D E_{max,l}^2 V_{eff,l}$, substituting in equation (2.60) to get

$$V_{eff,l} = \frac{8\pi a^3}{(l+1)(2l+1)}\left[1 + \frac{1}{(l+1)\varepsilon_D}\right]. \tag{2.61}$$

This suggests the field localization increases for higher order modes, which is consistent with Figure 2-10. Upon introducing $V_{eff,l}$, the effective density of states in the mode is:

$$\rho_l(\omega, d) = L_l(\omega)\frac{(1 + d/a)^{-2l-4}}{V_{eff,l}}. \tag{2.62}$$

The first term $L_l(\omega) = \frac{\gamma_l/2\pi}{(\omega-\omega_l)^2+\gamma_l^2/4}$, which describes the mode distribution over frequency, is the normalized Lorentzian linewidth factor depending on decay rate $\gamma_l$ of the mode, and the second term describes the spatial distribution of the mode. For $l > 1$, the decay rate is pure damping that depends on the materials (i.e., non-radiative decay), hence we assume they are same for all the modes i.e., $\gamma_l = \gamma$. But for $l = 1$, the decay rate is a summation of damping and radiative decay of a dipole[98] $\gamma_1 = \gamma + \gamma_{rad}$, in which

$$\gamma_{rad} = \frac{2\omega_{dp}}{1 + \varepsilon_D}\left(\frac{2\pi a}{\lambda_{dp}}\right)^3. \tag{2.63}$$

## 2.3 Interaction of cavity mode and emitter

We have discussed the interaction of a two-level atom with a single mode of the electromagnetic field in section 2.1. The focus was on the general properties of the emitter. Since a single electromagnetic field mode is a perfect approximation of a cavity resonance mode, the same methodology can be used for the discussion of cavity mode and emitter. It is shown that the cavity and emitter will evolve to a hybrid system as interaction strength increases.

### 2.3.1 Weak coupling

We first analyse the decay rate of the emitter weakly interacting with cavity mode. Recall that the spontaneous emission rate of an emitter in free space is given by equation (2.29), therefore it is proportional to the density of states $D(\omega)$. It is intuitive to replace $D(\omega)$ by equation (2.50), which gives the decay rate in cavity:

$$\Gamma_c = 2\pi\langle g^2(\omega)\rangle D_c(\omega). \tag{2.64}$$

For a resonance situation ($\Delta = \omega - \omega_c = 0$), it gives:

$$\Gamma_c = \Gamma Q\left(\frac{2\pi c^3}{V\omega^3}\right). \tag{2.65}$$

In a rigorous derivation[43] where the cavity damping is treated as the interactions with oscillator reservoir, the decay rate in cavity is same as (2.65) except for a trivial factor of 3. Introducing the Purcell factor $F$,

$$F = \frac{\Gamma_c}{\Gamma} = 3Q\left(\frac{2\pi c^3}{V\omega^3}\right) = \frac{3Q\lambda^3}{4\pi^2 V}. \tag{2.66}$$

Thus, the spontaneous emission rate can be enhanced or inhibited by the Purcell factor $F$.

### 2.3.2 Strong coupling

Next let us find the eigenstates of the system using a vector basis[42] where the excited state $|a,n\rangle = \begin{pmatrix}1\\0\end{pmatrix}$ and ground state $|b,n+1\rangle = \begin{pmatrix}0\\1\end{pmatrix}$. Also, operators are provided by the matrix $\sigma_z = \begin{pmatrix}1 & 0\\0 & -1\end{pmatrix}$ and $a^\dagger a = \begin{pmatrix}1 & 0\\0 & 1\end{pmatrix}$. The eigenenergies of three terms in equation (2.2) are quantum oscillator $\hbar\omega\left(n+\frac{1}{2}\right)$, field energy $\hbar\Delta$ (omitting the zero-point energy) and interaction energy $\hbar g\sqrt{n+1}$, respectively. In order to calculate the energy eigenstates, the Hamiltonian in equation (2.2) can be written as $H = \sum_n H_n$, where $H_n$ is the Hamiltonian of the $n$ photon state:

$$H_n = \hbar\omega\left(n+\frac{1}{2}\right)\begin{pmatrix}1 & 0\\0 & 1\end{pmatrix} + \frac{\hbar}{2}\begin{pmatrix}-\Delta & 2g\sqrt{n+1}\\2g\sqrt{n+1} & \Delta\end{pmatrix}. \tag{2.67}$$

After diagonalization one obtains eigenvalues as follow:

$$\begin{aligned} E_{1n} &= \hbar\omega\left(n+\frac{1}{2}\right) - \frac{1}{2}\hbar\sqrt{\Delta^2 + 4g^2(n+1)}\\ E_{2n} &= \hbar\omega\left(n+\frac{1}{2}\right) + \frac{1}{2}\hbar\sqrt{\Delta^2 + 4g^2(n+1)}\end{aligned}. \tag{2.68}$$

The corresponding eigenstates (so called dressed states) are:

$$\begin{aligned} |1n\rangle &= -\sin\theta_n|a,n\rangle + \cos\theta_n\,|b,n+1\rangle \\ |2n\rangle &= \cos\theta_n\,|a,n\rangle + \sin\theta_n\,|b,n+1\rangle \end{aligned}' \tag{2.69}$$

in which, $\sin\theta_n = \frac{2g\sqrt{n+1}}{\sqrt{\left(\sqrt{\Delta^2+4g^2(n+1)}-\Delta\right)^2+4g^2(n+1)}}$ and $\cos\theta_n = \sqrt{1-\sin^2\theta_n}$.

When the cavity mode and emitter are on resonance, i.e. $\Delta = 0$, we have

$$\begin{aligned} |1n\rangle &= \frac{\sqrt{2}}{2}[-|a,n\rangle + |b,n+1\rangle] \\ |2n\rangle &= \frac{\sqrt{2}}{2}[|a,n\rangle + |b,n+1\rangle] \\ E_{1n} &= \hbar\omega\left(n+\frac{1}{2}\right) - \hbar g\sqrt{n+1} \\ E_{2n} &= \hbar\omega\left(n+\frac{1}{2}\right) + \hbar g\sqrt{n+1} \end{aligned}. \tag{2.70}$$

Equations (2.70) tell us that the eigenstates of the system are a superposition of ground state and excited state, i.e., a hybrid of emitter exciton and cavity photon. The difference between eigen energies indicate a splitting in the spectrum, which is due to coherent exchange of energy between two systems. This phenomenon is known as strong coupling.

Interestingly, the energy splitting is conserved even if $n = 0$. This is called vacuum Rabi splitting and it is only predicted in quantum theory since a semiclassical model cannot describe the electromagnetic vacuum fluctuations. We note that the splitting degenerates if the coupling strength $g$ is zero. The eigenstates also degenerate to $|b,n+1\rangle$ where the emitter is at the ground state with one extra photon.

### 2.3.3 Classical model accounts for damping in microcavity

In the strong coupling discussion above, we have neglected the damping of the cavity and the emitter. A rigorous quantum model including the cavity damping can be found in [43]. Although the quantum description is obligatory for a microscopic system, a classical model is often sufficient for a quantitative description of experimental results. Especially for the macroscopic observations that are far beyond the quantum regime, a classical description is more suitable and intuitive.

Hence, a classical description of the strong coupling between a F-P microcavity and emitters, where a classical emitter is treated as a Lorentzian oscillator with the damping rate $\gamma$, is introduced. The permittivity $\varepsilon(\omega)$ is obtained as:

$$\varepsilon(\omega) = 1 + \frac{A}{\omega_0^2 - \omega^2 - i\gamma\omega}, \tag{2.71}$$

where $A = \frac{Ne^2}{V\varepsilon_0 m}$ characters oscillation strength. $N/\mathrm{V}$ is the density of the emitters, $m$ is the mass of an electron and $\omega_0$ is the resonance frequency. According to equation (2.46) and (2.71), the cavity dispersion is now:

$$\kappa^2 = \omega^2\left(1 + \frac{A}{\omega_0^2 - \omega^2 - i\gamma\omega}\right). \tag{2.72}$$

The moment has been scaled to $\kappa = c\left(k_{\parallel} + \frac{\pi}{L}\right)$. Assuming $\omega \approx \omega_0$, then $\kappa + \omega \approx 2\omega_0$ and $\omega_0 + \omega \approx 2\omega_0$. The dispersion becomes:

$$(\kappa - \omega)(\omega_0 - \omega - i\gamma/2) = \frac{A}{4}. \tag{2.73}$$

The solutions are:

$$\omega_{\pm} = \frac{\kappa}{2} + \frac{\omega_o}{2} - i\frac{\gamma}{4} \pm \frac{1}{2}\sqrt{A + \left(\kappa - \omega_0 + i\frac{\gamma}{2}\right)^2}. \tag{2.74}$$

This gives two normal modes with a splitting $\Omega = \sqrt{A + \left(\kappa - \omega_0 + i\frac{\gamma}{2}\right)^2}$. At resonance, the splitting is

$$\Omega = \sqrt{A - \frac{\gamma^2}{4}}, \tag{2.75}$$

i.e., the damping decreases the normal mode splitting. If the damping can be ignored ($\gamma = 0$), the mode splitting ($\Omega = \sqrt{A} \propto \sqrt{\frac{N}{\mathrm{V}}}$) is proportional to the density of the emitters, which is also deduced from semiclassical and fully quantum descriptions[42]. Equation (2.74) is plotted in Figure 2-11 with $\gamma = 0$. The two branches are usually called lower polariton (LP) and upper polariton (UP), respectively.

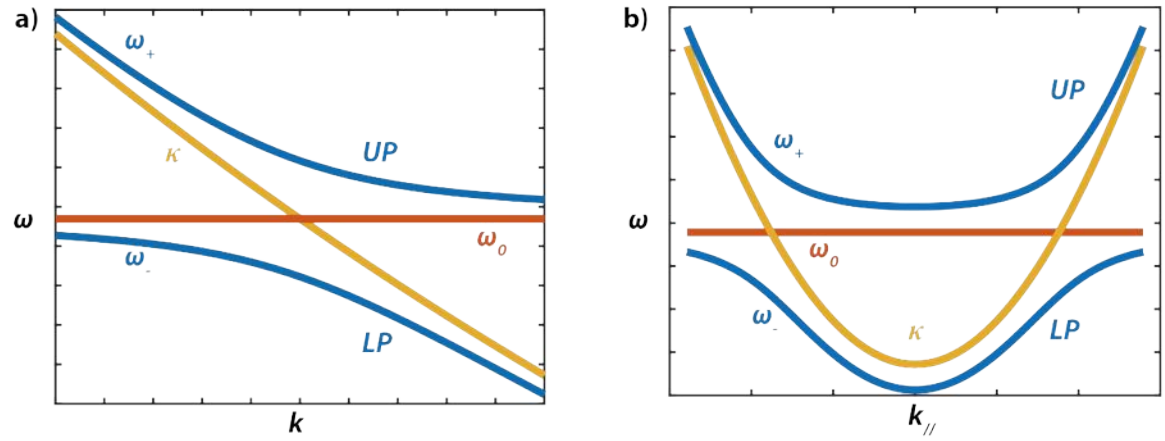


Figure 2-11 Dispersion curves of cavity mode (yellow) and emitter (or exciton, red) under weak coupling, and polaritons (blue) under strong coupling. a) $\omega - k$ dispersion, which is often used in a measurement with normal incident. Cavity mode is tuned by changing cavity thickness; b) $\omega - k_{//}$ dispersion, which is common for the fixed cavity in angle resolved measurements.

For a F-P cavity with a linewidth defined by equation (2.49), damping of the cavity can be incorporated by replacing $\kappa$ with $\kappa - i\frac{\gamma_c}{2}$. Then the normal mode splitting at resonance is:

$$\omega_{\pm} = \omega_0 - i\frac{\gamma_c}{4} - i\frac{\gamma}{4} \pm \frac{1}{2}\sqrt{A - \left(\frac{\gamma}{2} - \frac{\gamma_c}{2}\right)^2}. \tag{2.76}$$

This equation gives complicate criterions for strong coupling. The core idea is the splitting should not be overwhelmed by the damping. A strict criterion is:

$$A > \frac{\gamma^2}{2} + \frac{\gamma_c^2}{2}, \tag{2.77}$$

i.e., a large oscillation strength is helpful to achieve strong coupling. Thus, J-aggregate dye molecules, which possess large collective oscillation strength and narrow absorption, are most often implemented for strong coupling.

### 2.3.4 Coupled mode theory of emission enhancement by nanocavity

In this section, we introduce an analytic coupled mode theory[95,96,99] to optimize the plasmonic nanostructures in order to have the largest possible emission enhancements, which is determined together by the excitation enhancement and quantum yield enhancement[76], that is $F = F_{exc}F_{em}$. For a fluorescent emitter placed near a nanostructure with local field $\boldsymbol{E}$, excitation rate $\gamma_{exc}$ is

given by equation (2.34). Assuming the TDM of the emitter $\hat{\wp}$ is not altered by the environment, the excitation enhancement can be written as:

$$F_{exc} = \gamma_{exc}/\gamma_{exc}^{0} \propto |\hat{\wp} \cdot \boldsymbol{E}|^2/|\hat{\wp} \cdot \boldsymbol{E_0}|^2, \tag{2.78}$$

where $\gamma_{exc}^{0}$ and $\boldsymbol{E_0}$ are the excitation rate and electric field without nanostructure, respectively. Quantum yield enhancement is given by

$$F_{em} = \eta_{all}/\eta_{rad}, \tag{2.79}$$

in which $\eta_{all}$ is the emission efficiency of the emitter with the presence of nanostructure and $\eta_{rad}$ is the initial quantum yield.

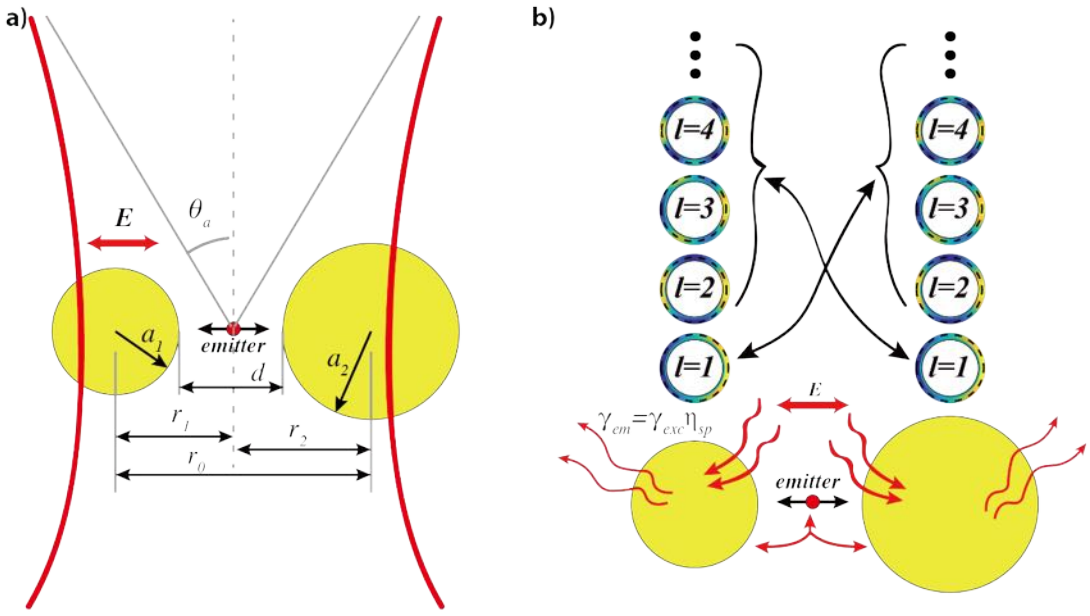


Figure 2-12 Illustration of a) an emitter placed in a line with two gold nanospheres which are illuminated by a Gaussian laser beam. Polarization of electric field is along the connecting line of the two spheres as well as the orientation of TDM of the emitter. b) coupling of dipole mode and higher order modes. The electric field is coupled into the dipole mode and then interacts with higher order modes of another sphere, then the emitter is excited. Emission of the emitter is also coupled to the dipole modes, then radiating or coupled with higher order modes subsequently. Adapted from [99].

An important advantage of plasmonic nanostructures is the near field enhancement provided by LSPR. For a single nanosphere as discussed in 2.2.2, higher order modes possess higher localization hence higher field enhancement, they cannot be excited externally or radiate to far-field, and therefore normally are not contributing to the emitter.

Considering a configuration of two gold nanospheres with the radius of $a_1$ and $a_2$, which are indexed by 1 and 2 as shown in Figure 2-12 a). An emitter is place in between them with the polarization of the transition dipole moment oriented along the connecting axis between the centres of the two spheres. The distances between the emitter and the sphere centres are $r_1$ and $r_2$, respectively. The excitation enhancement can be expressed as $F_{exc} = |\hat{\wp} \cdot \boldsymbol{E}|^2 / |\hat{\wp} \cdot \boldsymbol{E_0}|^2 = |E/E_0|^2 = F_{field}^2$.

Starting with the discussion of the field enhancement. The two-sphere configuration, where the dipole mode of one sphere is coupled with the higher order modes of another, could provide extra field enhancement[100] (sketched in Figure 2-12 b)). A linear polarized Gaussian laser beam along the connecting line of the sphere centres is focused on the particles, and the beam radius at the waist is:

$$w_0 = \frac{\lambda_{ex}}{\pi \theta_a}, \tag{2.80}$$

in which $\lambda_{ex}$ is the laser wavelength, $\theta_a$ is far-field half-angle of the numerical aperture of the focused beam.

In the absence of nanospheres, the power $|s_+|^2$ carried by the incident wave that possess a electric field $E_{foc}$ in the focus is[101]:

$$|s_+|^2 = \frac{\sqrt{\varepsilon_D}}{Z_0} \pi \left(\frac{w_0}{2}\right)^2 E_{foc}^2. \tag{2.81}$$

And $Z_0$ is the impedance of free space. Using the notation in [99], we can write the rate equations of the amplitude $A_l = \sqrt{U_l} = \sqrt{\frac{1}{4}\varepsilon_0 \varepsilon_D V_{eff,l}} E_{max,l}$ for excitation process as:

$$\begin{aligned} \frac{dA_1^{(m)}}{dt} &= i(\omega - \omega_1) A_1^{(m)} - i \sum_{l=1}^{\infty} \omega_{1l} \kappa_{1l}^{(mn)} A_l^{(n)} - \frac{1}{2} \gamma_1^{(m)} A_1^{(m)} + \kappa_{in}^{(m)} s_+ \\ \frac{dA_l^{(m)}}{dt} &= i(\omega - \omega_l) A_l^{(m)} - i\omega_{1l} \kappa_{1l}^{(nm)} A_1^{(n)} - \frac{1}{2} \gamma_l^{(m)} A_l^{(m)}, \quad l \geq 2 \end{aligned}, \tag{2.82}$$

where $\omega$ is the frequency of the excitation laser. $m, n = 1$ or 2 are sphere indexes. $\omega_l$ and $\gamma_l$ are the resonance frequency and decay rate of $l$th order plasmonic mode given by equation (2.56) and (2.63). $\omega_{1l} = \sqrt{\omega_1 \omega_l}$ is the reduced frequency. In addition, the coupling coefficient $\kappa_{in}^{(m)}$, which determines the laser energy coupled into nanospheres, is treated as a reciprocal process of

the radiative decay of the dipole mode. Following the discussion given by Haus in [101] to obtain $\kappa_{in}^{(m)} = \frac{\theta_a}{2}\sqrt{\frac{3\gamma_{rad}}{2}}$. Moreover, $\kappa_{1l}^{(mn)}$ is the coupling coefficient between the dipole mode in one sphere and all the other modes in another sphere, and is obtained as an integral of the electric potential $\phi_1^{(m)}$ times the surface charge density $\sigma_l^{(n)}$ evaluated over the surface of sphere $m$,

$$U_{1l}^{(mn)} = \oiint \phi_1^{(m)} \sigma_l^{(n)} ds^{(n)} = -\kappa_{1l}^{(mn)} A_1^{(m)} A_l^{(n)}, \tag{2.83}$$

which can be solved analytically,

$$\kappa_{1l}^{(mn)} = \left(\frac{a_m}{r_0}\right)^{\frac{3}{2}} \left(\frac{a_n}{r_0}\right)^{l+\frac{1}{2}} \left(1 + \left(\frac{a_n}{r_0}\right)^2 \frac{2(l+1)}{2l+3}\right). \tag{2.84}$$

The first term on the right side of equation (2.82) is the detuning term. The second term is the coupling between the dipole mode and higher order modes. Decay term are also included for energy loss. Since only the dipole mode is coupled to the external field, the coupling between plasmonic mode and external laser is only presence for dipole mode. At steady state, i.e., $\frac{dA_l}{dt} = 0$, equation (2.82) gives the connection between $E_{max,l}^{(n)}$ and $E_{max,1}^{(m)}$,

$$E_{max,l}^{(n)} = \frac{\omega_{1l}\kappa_{1l}^{(mn)}}{(\omega - \omega_l) + i\frac{\gamma}{2}} \frac{l+1}{2} \left(\frac{a_1}{a_2}\right)^{\frac{3}{2}} E_{max,1}^{(m)}, \quad m, n = 1,2. \tag{2.85}$$

After substituting (2.85) into (2.82), we can relate $E_{max,1}^{(n)}$ and $E_{foc}$,

$$\boldsymbol{M} \begin{pmatrix} E_{max,1}^{(1)} \\ E_{max,1}^{(2)} \end{pmatrix} = \frac{\omega}{\sqrt{2}} \begin{pmatrix} E_{foc} \\ E_{foc} \end{pmatrix}, \tag{2.86}$$

where the elements in the $2 \times 2$ matrix $\boldsymbol{M}$ are:

$$m_{11} = i(\omega - \omega_1) + \sum_{l=2}^{\infty} \frac{\omega_{1l}^2 [\kappa_{1l}^{12}]^2}{i(\omega - \omega_l) + \frac{\gamma}{2}} + \frac{1}{2}\gamma_1^{(1)}$$

$$m_{12} = i\omega_1 \kappa_{11} \left(\frac{a_2}{a_1}\right)^{3/2} = i\omega_1 \left(\frac{a_2}{r_0}\right)^3$$

$$m_{21} = i\omega_1 \kappa_{11} \left(\frac{a_1}{a_2}\right)^{3/2} = i\omega_1 \left(\frac{a_1}{r_0}\right)^3 \quad . \tag{2.87}$$

$$m_{22} = i(\omega - \omega_1) + \sum_{l=2}^{\infty} \frac{\omega_{1l}^2 \left[\kappa_{1l}^{(21)}\right]^2}{i(\omega - \omega_l) + \frac{\gamma}{2}} + \frac{1}{2}\gamma_1^{(2)}$$

The electric field at the location of the emitter is:

$$E(r_1) = E_{max,1}^{(1)} \left(\frac{a_1}{r_1}\right)^3 + E_{max,1}^{(1)} \sum_{l=2}^{\infty} \frac{\omega_{1l} \kappa_{1l}^{(mn)}}{(\omega - \omega_l) + i\frac{\gamma}{2}} \frac{l+1}{2} \left(\frac{a_1}{a_2}\right)^{\frac{3}{2}} \left(\frac{a_2}{r_2}\right)^{l+1}$$

$$+ E_{max,1}^{(2)} \left(\frac{a_2}{r_2}\right)^3 + E_{max,1}^{(2)} \sum_{l=2}^{\infty} \frac{\omega_{1l} \kappa_{1l}^{(mn)}}{(\omega - \omega_l) + i\frac{\gamma}{2}} \frac{l+1}{2} \left(\frac{a_2}{a_1}\right)^{\frac{3}{2}} \left(\frac{a_1}{r_1}\right)^{l+1} . \tag{2.88}$$

By substituting (2.88) into (2.86), the field enhancement factor, which is the ratio of solved field to the field in the absence of nanospheres, is given by:

$$F_{field} = \left|\frac{E(r_1)}{E_{foc}}\right|. \tag{2.89}$$

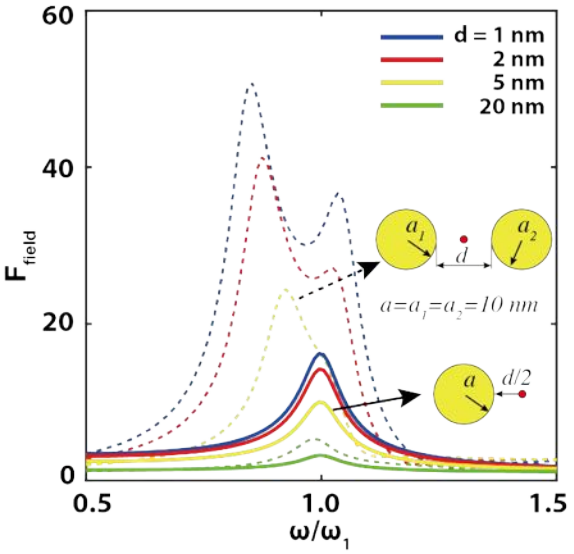


Figure 2-13 Excitation frequency dependence of the field enhancement (dashed line) at the centre of the gap for different gap sizes $d$. For single sphere, the enhancement (solid line) is calculated at a distance of $d/2$ to the sphere surface (red dot in the inset) along the excitation polarization. The enhancement of two spheres is larger than for a

single sphere due to mode coupling. The enhancement maximum is achieved at lower frequency than the dipole mode.

For a general impression of the model, we use equation (2.89) to evaluate the field enhancement by two gold spheres in air. The radii are $a_1 = a_2 = 10\ nm$, and the damping of gold is taken from Ref [99] ($\hbar\gamma \sim 0.2\ eV$). The higher order modes ($l \leq 100$) are considered, and the obtained excitation frequency dependence of the enhancement is plotted in Figure 2-13 for different gap distance $d$. The field enhancement is calculated at the centre of the gap, namely $r_1 - a_1 = r_2 - a_2 = d/2$. The field enhancement by a single gold sphere, which have been considered in [95], is also plotted for comparison. For the single sphere situation, the enhancement is calculated at a distance of $d/2$ to the sphere surface along the excitation polarization. The maximal enhancement of two spheres is dramatically increased compared to the single sphere due to the contribution of higher order modes. We note that our simulation reveals an excitation enhancement $F_{field}^2 \sim 2.5 \times 10^3$ at gap of $d = 1\ nm$, and the wavelength of LSPR is red shifted compared to single sphere. This is in good agreement (resonance red-shifted, $F_{field}^2 \sim 2 \times 10^3$ at $d = 1\ nm$) with the result obtained in [102] for a same dimer configuration.

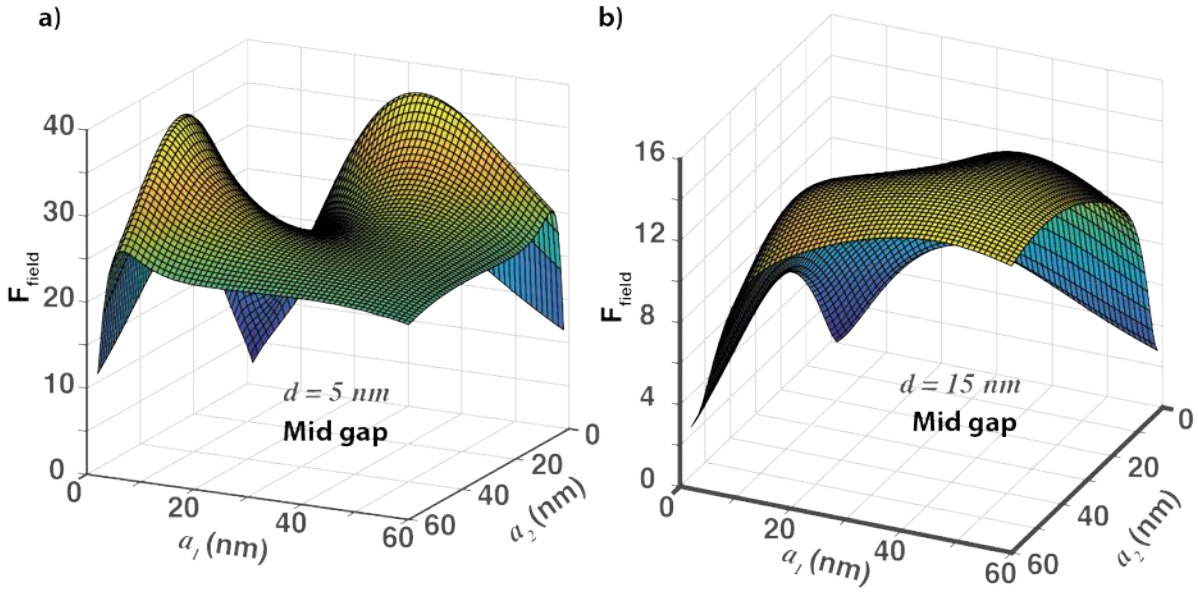


Figure 2-14 Dependence of field enhancement at the centre as a function of the gap on sphere radius. a) Two field enhancement maxima are observed for small gap $d = 5\ nm$, indicating a asymmetric configuation with one small sphere and a big sphere, while only one maximum peak is observed for larger gap $d = 15\ nm$ as shown in b) correspond to a symmetry configuration with two equal spheres. Adapted from [99].

The radius of two gold spheres is also optimized in order to obtain the optimized field enhancement at the centre of the gap. The radii of both spheres vary from 1 $nm$to 60 $nm$ while

the gap $d$ is limited between 2 $nm$ to 20 $nm$. 2D plots of the enhancement factor $d = 5\ nm$ and 15 $nm$ are shown in Figure 2-14 a) and b), respectively. For a small gap ($d = 5\ nm$), two spheres are intensely coupled, and two symmetric peaks of field enhancement appear for $a_1 = 5\ nm$ and $a_2 = 35\ nm$, and vice versa. In this case, as indicated by equation (2.63), the smaller sphere has a smaller dipole moment and hence smaller radiative rate. The small sphere acts like a cavity that conserves energy while the bigger sphere acts as an antenna. This is called nanolens[103] in literature. When the gap is large ($d = 15\ nm$) the coupling strength is smaller as well as the maximal enhancement, and only one enhancement maximum is observed for $a_1 = a_2 = 45\ nm$. A pair of optimized sphere radii together with optimized field enhancement factors are obtained for each gap distance. For a series of gap distances, optimized results are plotted in Figure 2-15 a). In order to balance the coupling efficiency and the radiative rate, the optimized radius of both spheres increase and tend to be equal when the gap increases. Figure 2-15 b) shows the result when the observation point is fixed at 2 $nm$ away from sphere 2. In this case, sphere 2 always has a smaller optimized radius to supress radiation and gain near field enhancement.

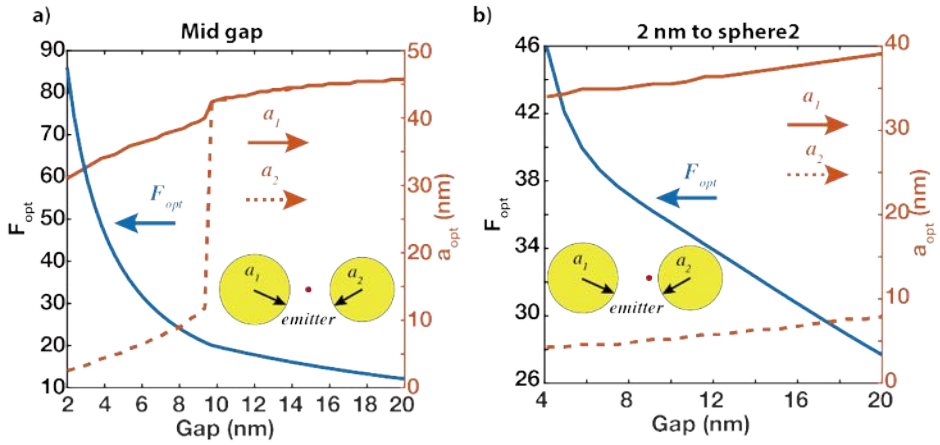


Figure 2-15 Optimized field enhancement and optimized radius for different gaps when the observation point is at the middle of the gap, a), and 2 $nm$ away from sphere 2, b), as indicated by a red dot in the inset. The maximum enhancement decreases when the gap increases. When observation point is at the mid gap, optimized radii of two spheres are different for small gap, and trend to be equal for large gap. When observation point is placed close to sphere 2, optimized radius is always smaller than sphere 1. Adapted from [99].

In the following, we discuss the quantum yield enhancement by introducing the emitter into the rate equations. In the same manner as foregoing, the rate equations are written as:

$$\begin{aligned}\frac{dA_1^{(m)}}{dt} &= i(\omega-\omega_1)A_1^{(m)} - i\sum_{l=1}^{\infty}\omega_{1l}\kappa_{1l}^{(mn)}A_l^{(n)} - \frac{1}{2}\gamma_1^{(m)}A_1^{(m)} - \frac{1}{2}\sqrt{\gamma_{rad}^{(m)}\gamma_{rad}^{(n)}}A_1^{(n)} - i\omega_{1B}\kappa_1^{(m)}B \\ \frac{dA_l^{(m)}}{dt} &= i(\omega-\omega_l)A_l^{(m)} - i\omega_{1l}\kappa_{1l}^{(nm)}A_1^{(n)} - \frac{1}{2}\gamma_l^{(m)}A_l^{(m)} - i\omega_{1B}\kappa_l^{(m)}B,\ \ l\geq 2 \\ \frac{dB}{dt} &= \frac{\sqrt{\gamma_m P}}{2} - \frac{1}{2}\gamma_m B - i\sum_{l=1}^{\infty}\omega_{lB}(\kappa_l^{(1)}A_l^{(1)} + \kappa_l^{(2)}A_l^{(2)})\end{aligned} \tag{2.90}$$

where $\omega_{1B}=\sqrt{\omega\omega_l}$ and $\omega_{1l}=\sqrt{\omega_1\omega_l}$ are reduced frequency. Comparing to equation (2.82), first difference is the presence of the rate equation for the emitter. It contains excitation term with pumping power $P$ (obtained by a reciprocal process[101]) that excites the emitter with a decay rate $\gamma_m=\tau_{rad}^{-1}+\tau_{nrad}^{-1}$. The external excitation term for spheres vanishes. The super-radiance term $\frac{1}{2}\sqrt{\gamma_{rad}^{(m)}\gamma_{rad}^{(n)}}A_1^{(n)}$ that accounts for the coherent character of emission by dipoles, as well as the coupling term between the emitter and plasmonic modes are included with a coupling constant $\kappa_l^{(m)}$,

$$\kappa_l^{(m)} = \left(\frac{a_0}{r_m}\right)^{\frac{3}{2}}\left(\frac{a_m}{r_m}\right)^{l+\frac{1}{2}}\left(1+\left(\frac{a_m}{r_m}\right)^2\frac{2(l+1)}{2l+3}\right). \tag{2.91}$$

The formula is similar to equation (2.84), but $r_m$ is the gap between the emitter and the sphere with $m=1,2$. And $a_0=\frac{\hat{\wp}}{q}$, in which $\hat{\wp}$ is the TDM of the emitter with the charges $q=ne$, is a characteristic radius of the emitter. For a general fluorescent molecule, the TDM is about $0\sim10\ Debye$, i.e., $a_0\approx(0\sim0.2)/n\ nm$.

Equation (2.90) is written in a matrix form at the steady state,

$$\boldsymbol{M}_{2N\times2N}\begin{bmatrix}\boldsymbol{A^{(1)}}\\ \boldsymbol{A^{(2)}}\end{bmatrix} = \begin{bmatrix}i\omega_{lB}\boldsymbol{\kappa^{(1)}}\\ i\omega_{lB}\boldsymbol{\kappa^{(2)}}\end{bmatrix}B, \tag{2.92}$$

in which $\boldsymbol{A^{(m)}}$ and $\boldsymbol{\kappa^{(m)}}$ are $N\times1$ vectors consisting of $A_l^{(m)}$ and $\kappa_l^{(m)}$ that $l=1,2,\dots,N$. Inverting $\boldsymbol{M}_{2N\times2N}$ to obtain $\boldsymbol{A^{(m)}}=i\omega_{lB}B\boldsymbol{M}_{2N\times2N}^{-1}\boldsymbol{\kappa^{(m)}}=i\omega_{lB}B\boldsymbol{T^{(m)}}$, where $\boldsymbol{T^{(m)}}$ is also a $N\times1$ vector. Thus, the radiating power of the system is obtained by solving (2.92),

$$P_{all} = P_{emitter} + P_{SP} = \frac{B^2}{\tau_{rad}} + \left|\sqrt{\gamma_{rad}^{(1)}}A_1^{(1)} + \sqrt{\gamma_{rad}^{(2)}}A_1^{(2)}\right|^2 = \frac{B^2}{\tau_{rad}} + \left|\sqrt{\gamma_{rad}^{(1)}}T_1^{(1)} + \sqrt{\gamma_{rad}^{(2)}}T_1^{(2)}\right|^2 \omega_{lB}^2 B^2. \tag{2.93}$$

The excitation power is obtained from (2.90) at steady state,

$$P = \left|\gamma_m - 2\sum_{l=1}^{\infty}\omega_{lB}^2(\kappa_l^{(1)}T_1^{(1)} + \kappa_l^{(2)}T_1^{(2)})\right|^2 \frac{B^2}{\gamma_m}. \tag{2.94}$$

Now analysing the enhancement of quantum yield $F_{em} = \eta_{all}/\eta_{rad}$. Here, $\eta_{all} = P_{all}/P$ is the emission efficiency of the coupled system. The quantum yield of the emitter is $\eta_{rad} = 1/(\tau_{rad}\gamma_m)$. Thus,

$$F_{em} = \frac{\eta_{all}}{\eta_{rad}} = \frac{1 + \left|\sqrt{\gamma_{rad}^{(1)}\tau_{rad}}T_1^{(1)} + \sqrt{\gamma_{rad}^{(2)}\tau_{rad}}T_1^{(2)}\right|^2 \omega_{lB}^2}{\left|1 - 2\sum_{l=1}^{\infty}\omega_{lB}^2(\kappa_l^{(1)}T_1^{(1)} + \kappa_l^{(2)}T_1^{(2)})/\gamma_m\right|^2}. \tag{2.95}$$

This equation can be used for any emitter placed in between two nanospheres. For very large gaps, the coupling rate $\boldsymbol{\kappa}^{(m)}$ and $\kappa_l^{(m)}$ can be ignored. Noticing $\boldsymbol{T}^{(m)} = \boldsymbol{M}_{2N\times 2N}^{-1}\boldsymbol{\kappa}^{(m)}$, we have $F_{em} = 1$, i.e., the emission efficiency is not changed. When the gap distance decreases, both $\boldsymbol{\kappa}^{(m)}$ and $\kappa_l^{(m)}$ increase, but the denominator increases faster than numerator since only $\boldsymbol{\kappa}^{(m)}$ is contained in the numerator. Hence, the emission efficiency $\eta_{all}$ will decrease eventually. Also note that a larger $\gamma_m$ could slow down the value rise of the denominator.

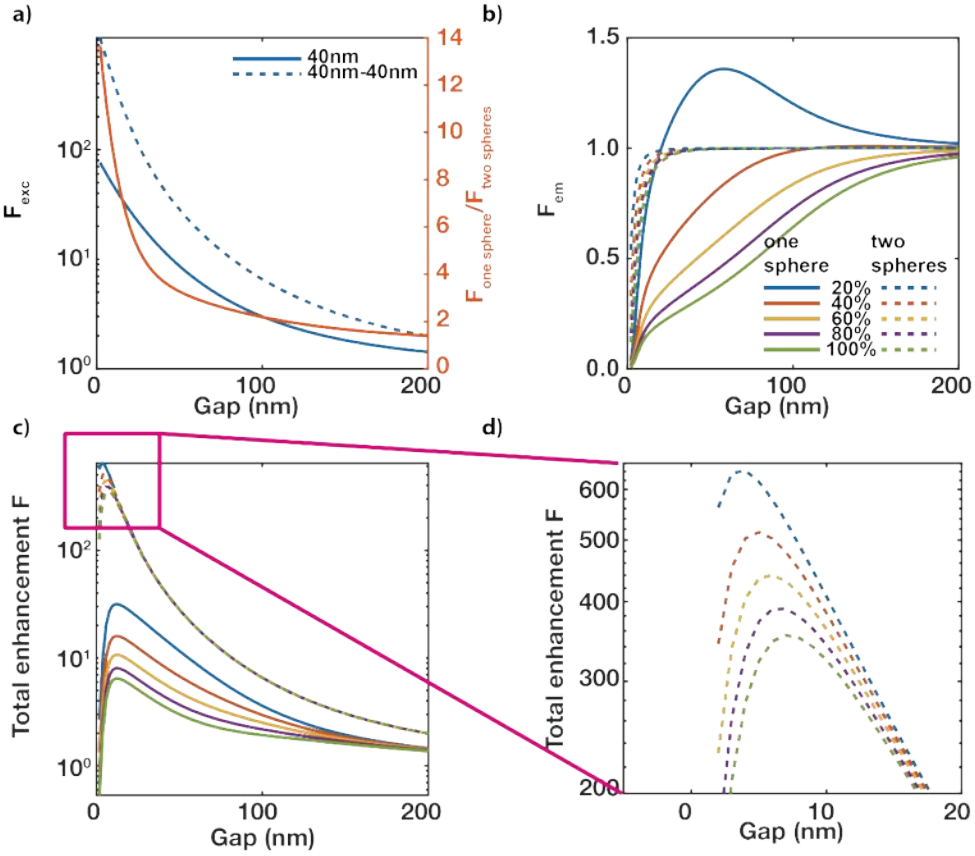


Figure 2-16 Dependence of a) excitation enhancement, b) quantum yield enhancement and c) emission enhancement on gap distance. Sphere radii are $a = a_1 = a_2 = 40\,nm$. Emitters are set to have a radiative lifetime $\tau_{rad} = 6\,ns$, $q = 10e$ is and TDM $\hat{\wp} = 5\,Debye$, i.e., $a_0 \approx 0.01\,nm$. Quantum yield $\eta_{rad}$, varies from 20% to 100%. The excitation enhancement of two spheres (dash line) is remarkably larger than for a single sphere (solid line) when the gap is small, and the difference diminish for a large gap. Compared to a single sphere, the emission efficiency is less altered for a large gap ($d \geq 30\,nm$). A dramatic decrease is observed for small gap ($d < 30\,nm$). The emission enhancement $F = F_{exc}F_{em}$ and partial zoom are plotted in c) and d).

Emission enhancement of the emitter $F = F_{exc}F_{em}$ can be calculated by evaluating equation (2.89) and equation (2.95) numerically. Considering two identical spheres $a_1 = a_2 = 40\,nm$ with an emitter placed in the middle of the gap. The dependence of excitation enhancement on the gap distance $d$ is shown in Figure 2-16 a). Enhancement by a single gold sphere, which is calculated at a distance $d/2$ to the sphere surface, is overlaid. Dividing the enhancement of two spheres by the enhancement of a single sphere, there is a difference of up to 14 times due to higher order mode coupling, which is far beyond a simple addition of two single spheres. The dependence of quantum yield enhancement on gap distance $d$, including the same simulation for a single sphere, is shown in Figure 2-16 b). Emitters are assumed to have a radiative lifetime $\tau_{rad} = 6\,ns$ with quantum yield $\eta_{rad}$ varies from 20% to 100%, charge and $q = 10e$ and TDM $\hat{\wp} = 5\,Debye$, i.e.,

$a_0 \approx 0.01\,nm$. Noticing quantum yield enhancement $F_{em}$ instead of emission efficiency $\eta_{all}$ is considered, hence it is possible to exceed one. The enhancement is equal to 1 for a large gap (i.e., $\eta_{all} = \eta_{rad}$), while a rapid descent presence at narrow gap ($\eta_{all} < \eta_{rad}$). This can be explained by an abrupt increase of the coupling of the dipole mode to the non-radiative higher order modes, as well as the coupling of emitter to all the plasmonic modes. When the rate of energy coupling into non-radiative modes exceeds the dipole mode radiative rate, energy is damped in higher order modes and the radiative efficiency of nanospheres starts to decrease, thus quenches emission. We have assumed the emitters have the same radiative decay rate $1/\tau_{rad}$ and different quantum yield, thus the emitter with higher quantum yield has smaller decay rate $\gamma_m$, so quenching starts at larger gap distance as shown in Figure 2-16 b).

The emission enhancement $F = F_{exc}F_{em}$ is plotted as a function of the gap distance $d$ in Figure 2-16 c). The enhancement reaches a maximum around $\frac{d}{2} \sim 8\,nm$ for single sphere which is same as in [76], while it is not decreasing for emitter in between two spheres until $d \sim 7\,nm$. The quenching appears at even narrower gaps for an emitter with smaller quantum yield (when $\eta_{rad}$ varies from 100% to 20%, the gap distance that has maxima enhancements varies from 7 $nm$ to 4 $nm$), and it eventually disappears[70,72,97] when $\eta_{rad} \sim 0$ ($\gamma_m \sim \infty$) which corresponds to SERS with an enhancement factor $F \sim |E|^4$.

# Chapter 3 Experimental setups and sample preparation

## 3.1 Confocal scanning microscope combined with higher order laser modes

All of the optical measurements in this work are performed with a home build confocal scanning microscope. A schematic of the setup is represented in Figure 3-1 that includes three main parts.

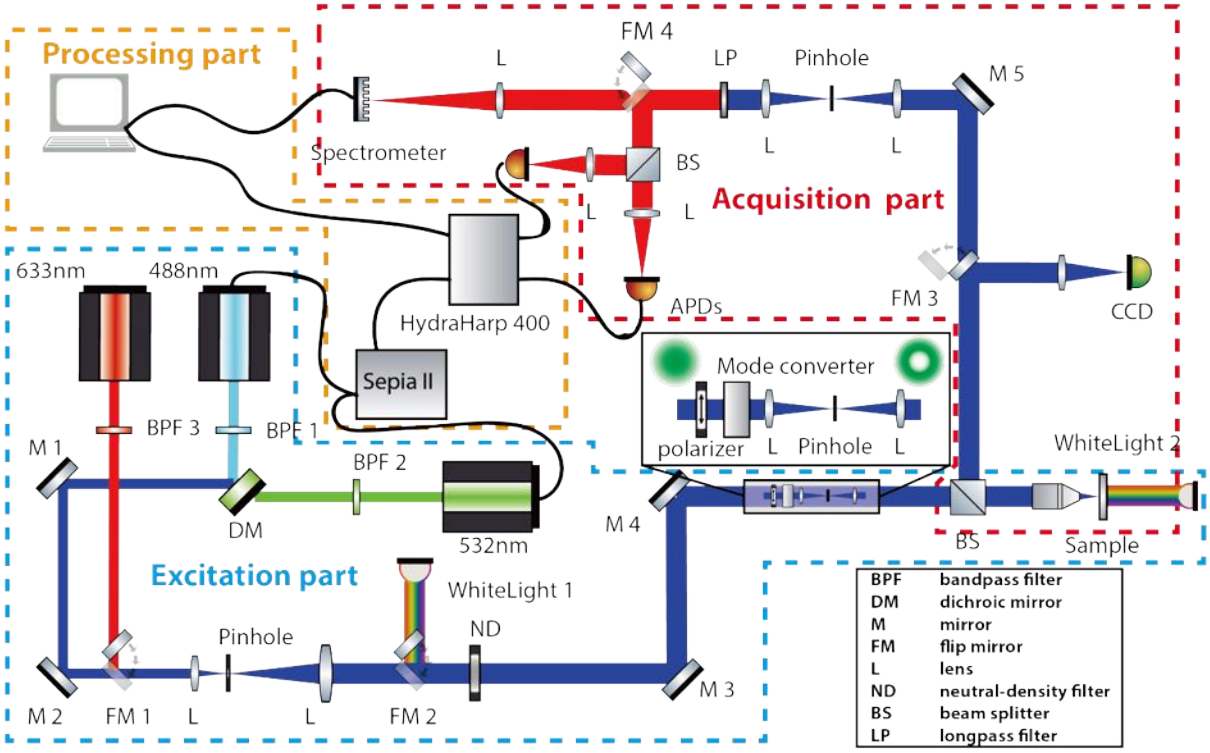


Figure 3-1 Schematic drawing of the experimental setup. Inset is the diagram of the mode converter, which can be introduced in the optical path if a doughnut mode is needed. Dashed lines mark three parts of the setup: excitation part, acquisition part, and processing part. CCD: charge coupled device camera. APD: avalanche photodiode. Optical components modified from ComponentLibrary created by Alexander Franzen.

A As indicated by the cyan dashed line, the excitation part contains three different lasers, 1) $\lambda = 488\ nm$, pulsed, D-C-485, PicoQuant; 2) $\lambda = 530\ nm$, pulsed/CW, LDH-P-FA-530L, PicoQuant; 3) $\lambda = 633\ nm$, CW) that are coupled into same optical path. Both pulsed diode lasers 1) and 2) with a pulse width (FWHM) $< 100\ ps$ are operated using a multichannel laser driver (PDL 828, Sepia II,

PicoQuant) with adjustable repetition rate from 1 MHz to 80 MHz. Laser 3) is a continuous wave HeNe laser operated at a wavelength of 632.8 nm. Laser beams are expanded before sending to the objective lens.

In general, the laser beam has a Gaussian intensity profile at any cross-section perpendicular to the optical axis as indicated in the inset of Figure 3-1. A mode-converting unit, including a linear polarizer, a mode converter (polarization converter, ARCoptix), a telescope system and a pinhole ($d = 15\ \mu m$), can be introduced in the optical path if doughnut mode[81,82] is demanded.

The mode converter contains two twisted nematic liquid crystal cells[104], where the first cell allows to rotate the polarization direction of the linear polarized incident laser beam by 90 $^{o}$ to switch between the RPDM/APDM, the second cell rotates the polarization direction of the linear polarized incident laser with respect to the cell axis to create the RPDM/APDM. The pinhole works as a spatial filter to select only donut mode.

The Gaussian/RPDM/APDM beams pass through a 50:50 non-polarizing beam splitter and are focused on the sample via an objective lens. Two different objectives are used for specified experiments: an oil immersion objective (NA = 1.46, 63×, Carl Zeiss) for single molecule related experiments and an air objective (NA = 0.6, 40×, Edmund Optics) for strong coupling experiments. The sample is fixed with magnets on a scanning piezo-stage (P-527.3CL, Physik Instrumente). Two white light sources can be used for reflection and transmission measurement, which will be described in detail in 0.

The fluorescence signal from the excitation spot is collected by the same objective lens and sent either to the spectrometer (SP-2500i, Princeton Instruments) or to two avalanche photodiodes (APDs, SPCM-AQR-14, PerkinElmer) via a 50/50 beam splitter. APDs are connected to a time-correlated single photon counting module (TCSPC, HydraHarp 400, PicoQuant). For each detected photon, a TTL (Transistor-Transistor-Logic) pulse is output from APD and recorded at HydraHarp 400 using Time-Tagged Time-Resolved (TTTR) acquisition mode[7] with a minimum timing resolution of 1 ps and a coarser timing (called time tag) performed. For a standard TCSPC, only one APD is used to have better signal to noise ratio. For fluorescence lifetime measurements, the timing resolution is set to 64 ps in order to have a larger time span. For antibunching measurements, the timing resolution is always 1 ps and two extra short-pass filters are inserted in front of the APDs to avoid the after-pulsing effect[8]. Collected TCSPC related data are processed using SymPhoTime 64 (PicoQuant). Spectra and scanning intensity images are processed using self-written MATLAB scripts.

## 3.2 Molecule sample preparation

Coverslips (22 mm × 22 mm, thickness 150 μm, Carl Roth) are cleaned in chromosulfuric acid solution for 4 hours, then rinsed with triply distilled water and finally dried in a nitrogen flow. These are used for single molecule experiments, or thermal/electron beam deposition of required materials.

Hypericin (Burg-Apotheke, Königstein) is dissolved in ethanol (Uvasol, Merck) and diluted to a certain concentration for further usage. Poly (vinyl alcohol) (PVA, Sigma-Aldrich) is dissolved in triply distilled water, and 2 μL of hypericin solution is added to a 2 wt. % PVA solution to obtain the required concentration. For deuteration experiments, hypericin is dissolved in methanol-$d_4$ (99 % atom D, Sigma-Aldrich) for H/D exchange. In addition, the solvent for PVA is changed to deuterium oxide (99 % atom D, Sigma-Aldrich). Due to the low p$K_a$ (1.8) at the *bay* hydroxyl groups[105–107], H/D exchange is easy to happen in the solution. All solutions are stocked in the fridge to minimize molecule bleaching.

Ensemble fluorescence spectra and fluorescence lifetime traces of hypericin were measured from samples consisting of clean coverslips covered by spin-coating 20 μL of a $10^{-5}$ M solution of hypericin with or without PVA. The same solution with PVA is spin coated (6k rpm, 30 s) on the flat mirror for the measurement in the microcavity. The ensemble absorption, which is recorded with an UV−Vis−NIR spectrophotometer (PerkinElmer Lambda 19), is measured with the same solution without PVA.

For single molecule measurements, 5 μL of the $10^{-10}$ M hypericin/ethanol solution is added directly on a cleaned glass coverslip or 20 μL of the $10^{-9}$ M hypericin/PVA solution is spin coated (6k rpm, 30 s) on the coverslip. Same amount of the $10^{-9}$ M hypericin/PVA solution is spin coated on the flat mirror for the measurement in microcavity. The polymer film is about 80 nm according to AFM measurement.

For the strong coupling experiment, TDBC (FEW Chemicals) is dissolved in triply distilled water and undergoes self-organization to form J-aggregates dye molecule then dispersed in 2 wt. % PVA matrix with a final concentration of 2.5×10-3 M. 100 μL of TDBC/PVA aqueous solution is injected into the cavity. The formation of J-aggregates in the aqueous solution leads to a decrease of the fluorescence emission from monomers. Furthermore, the J-aggregates are preserved in the aqueous solution and the PVA prevents water from drying out.

## 3.3 Tunable microcavity

The tunable microcavity used in this work consists of a flat mirror and a curved mirror that are assembled together in a cage system to form the cavity (Figure 3-2 a)). A photograph of the white light transmission patterns (Newton's rings) is shown in Figure 3-2 b). The curved mirror can be approached towards the flat mirror by a piezo actuator (Polaris® Kinematic Mirror Mounts KC1-T-PZ, Thorlabs). The flat mirror is prepared on a cleaned coverslip by first evaporating (Edwards EB3, $10^{-6}$ mbar, 0.1 nm/s) 1 nm chromium as adhesion layer and on top a 30 nm thick silver layer. The curved mirror is a plano-convex lens (f = 50 mm, radius of curvature 25.8 mm, Thorlabs) with 1 nm chromium and 50 nm silver evaporated on the curved surface. In addition, 50 nm silica is evaporated on top of the silver layers of both mirrors, serving as spacer to avoid quenching of the molecule on top of the silver film and to protect the two mirrors from mechanical damage. The fluorescence signal is collected from the flat mirror side, allowing for a thicker silver layer on curved mirror. The molecule sample is introduced on top of the flat mirror.

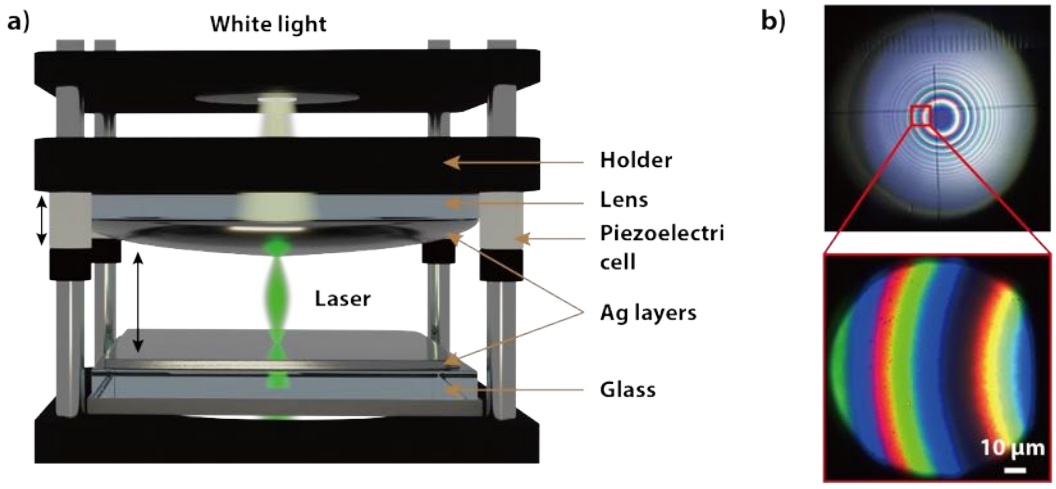


Figure 3-2 a) Scheme of the tunable microcavity. Courtesy of Frank Wackenhut. b) Photos of white light transmission patterns (Newton's rings) in the microcavity.

Reflection and transmission spectra of the cavity are measured with the white light source 1) or 2) shown in Figure 3-1, respectively. A reference spectrum is measured by using a broadband dielectric mirror (BB1-E02, Reflectance > 99%, Thorlabs) for reflection spectra or a glass coverslip for transmission spectra.

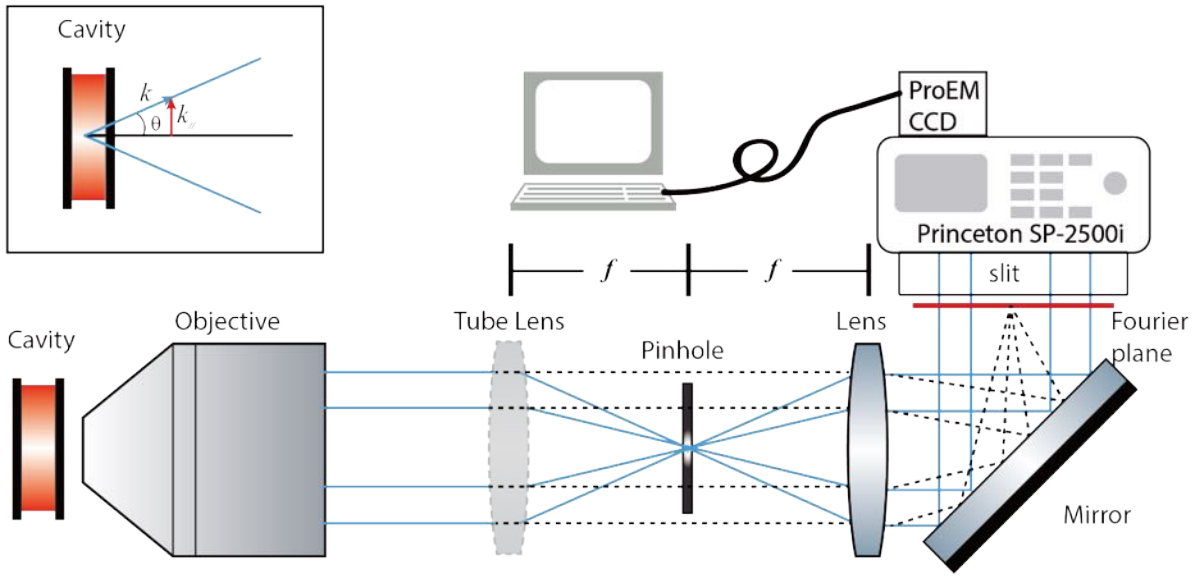


Figure 3-3 Schematic drawing of the 4f system for *k*-space dispersion measurement. Part of the cavity is imaged on the focus of the tube lens. After filtering stray light with a pinhole, the Fourier plane is imaged on the spectrometer via the second lens. The inset in the top left corner shows the sketch of the wave vector at incident angle $\theta$.

In order to obtain angle resolved reflection spectra, a tube lens is placed in front of the spectrometer to form a 4f system[108] as shown in Figure 3-3. The cavity is imaged on the focus of the tube lens. A pinhole is used to remove stray light, and the *k*-space dispersion is obtained by imaging the Fourier plane of the cavity image on the CCD of the spectrometer. The maximum collection angle for the wave vector is limited by the numerical aperture (NA) of the lens in front of the spectrometer instead of the objective lens. The lens (f=35 mm, d= 25.4 mm, Achromatic Doublets, Thorlabs) used in this work has a NA=0.35, which gives the maximum collection angle $\theta_{max}\sim 20^{o}$.

## 3.4 Plasmonic nanocavity

Two types of plasmonic nanocavities are used in this work. For single molecule SERS experiments, the substrate is prepared by evaporating (Edwards EB3, $10^{-6}$ mbar, 0.1 nm/s) a 4 nm thick silver layer on cleaned coverslips, resulting in nanoparticles after 12 hours of room-temperature annealing[109]. An example of this silver nanoparticle sample used for SERS is shown in Chapter 5. On this silver island film, a 5 µL droplet of $10^{-10}$ M hypericin ethanol solution is directly added to acquire single molecule SERS spectra. The same amount of $10^{-6}$ M hypericin ethanol solution is used to acquire ensemble SERS spectra for comparison.

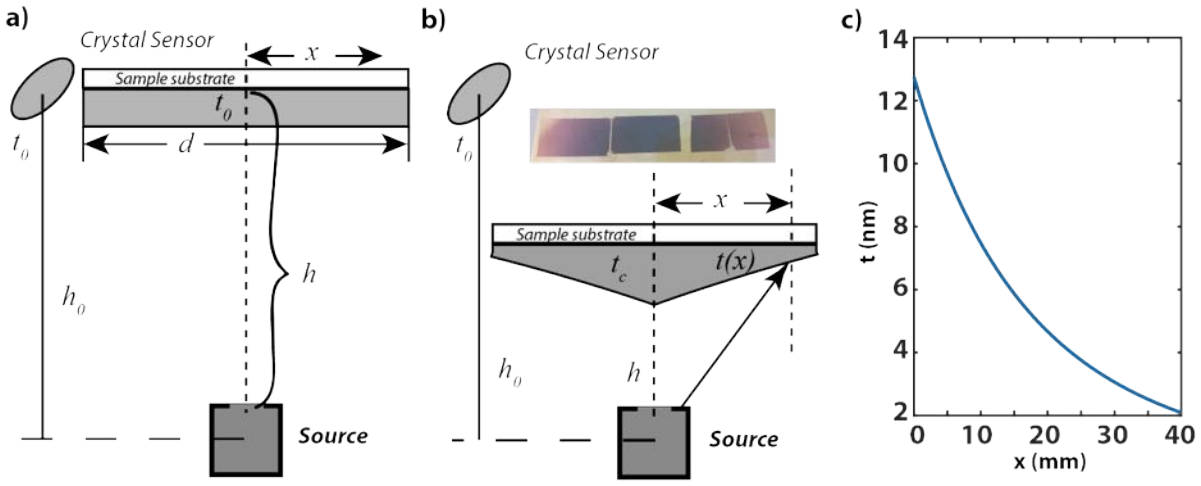


Figure 3-4 Schematic drawing to explain the evaporation process with a) sample in the normal height (~250 nm), b) sample in a lower height. A photo of non-uniform samples is shown on top. c) Evaporated film thickness at different position with $h_0 = 250\ mm, h = 70\ mm$ and $t_0 = 1\ nm$

Non-uniform gold nanoparticles are used for fluorescence enhancement experiments in Chapter 6. In the normal evaporation process (shown in Figure 3-4 a)), the detector and the sample substrate are at the same height ($h_0$), which is much larger than the size of sample substrate ($h_0 \gg d$). According to Knudsen's cosine law[110], an almost uniform film is deposited on the substrate:

$$t(x) = \frac{t_0}{\left(\left(1 + \frac{x}{h_0}\right)^2\right)^2}, \tag{3.1}$$

where $t_0$ is the thickness indicated by the crystal sensor, as well as the thickness at the centre of substrate. However, lowering the sample height to a smaller value ($h$), a film with non-uniform thickness will be obtained, as show in Figure 3-4 b). In addition, since the position of sensor is unchanged, there will be a difference between the thickness reading from sensor $t_0$ and the real thickness at the centre of sample $t_c$, which is deduced as:

$$\frac{t_c}{t_0} = \frac{h_0^2}{h^2}. \tag{3.2}$$

Thus, the real thickness of the evaporated film is

$$t(x) = \frac{\frac{h_0^2}{h^2} t_0}{\left(\left(1 + \frac{x}{h}\right)^2\right)^2}. \tag{3.3}$$

In this work, the sample is prepared by evaporating $t_0 = 1\ nm$ of gold (Plassys MEB400, $10^{-6}$ Torr, 0.05 nm/s) with $h_0 = 250\ mm, h = 70\ mm$ and $d = 40\ mm$. The sample have a film thickness varying from 2 nm to 13 nm as shown in Figure 3-4 c). Noting the thickness variation can be treated as a linear approximation when $x < 15\ mm$. Starting from the centre of the substrate, the film thickness can be evaluated. In order to obtain gold nanoparticles we follow a fast thermal annealing strategy[78,79] to heat the sample at 270°C for 30 s. The sample is then characterized with a scanning electron microscope (FEG 8030, Hitachi). Detailed results will be discussed later in Chapter 6.

# Chapter 4 Single quantum emitter characterization

Hypericin is one of the most efficient photosensitizers used in photodynamic tumor therapy (PDT) and many biochemical and medical research studies have focused on Hypericin during the last decades[111]. Hypericin is a natural active ingredient in *Hypericum perforatum* (St. John's Wort)[105],and a popular a multifunctional agent in drugs and medical applications, since it exhibits antidepressive, antineoplastic, antitumor and antiviral activitiy[111]. These are due to phototoxic reaction of hypericin, which can be exploited in photodynamic therapy applied for cancer treatment[111–114]. In photodynamic therapy, a photosensitizer is introduced into the tumour cells and excited with a suitable light source. The high triplet yield of photosensitizer creates singlet oxygen, which then destroys the tumor cell. Hypericin is a very promising candidate for such a therapy since it is the strongest natural photosensitizer. Besides, the red fluorescence emission of hypericin can be used to visualize tumor cells[115]. There are plenty of spectroscopic studies about the ensemble properties of hypericin[106,107,116–118], and covering the influence of different solvents and pH on the fluorescence spectrum and the excited state lifetimes,[107,119] excitation wavelength dependence of the Raman and SERS spectrum[117,118], excited state proton transfer[120,121], phototoxicity[113] and phosphorescence emission[122,123]. However, single molecule (SM) studies of hypericin were still missing. SM spectroscopy can provide a better understanding of its photophysical properties, since certain aspects, such as influence of the local environment or subpopulations, are hidden by ensemble averaging.[35,36,124–127] Furthermore, SM experiments allow to investigate dynamics caused by changes of the local environment or of the structure or orientation of the single molecule.[30,128–131]

We show that hypericin can be optically detected down to a single molecule at ambient conditions. Its photostability is large enough for single molecule experiments. We will show that the emission properties of hypericin are very sensitive to the local environment. Sudden fluorescence intensity fluctuation can be explained by the reorientation of TDMs that is directly observed using confocal microscopy combined with APDM and RPDM. TD-DFT calculations prove that the reorientation of TDMs is associated with tautomerization transition between four most stable tautomers of hypericin, which is a fast chemical reaction involving a relocation of a proton. If a hypericin molecule go through different tautomers during observation, we are able to assign the orientation of TDM to a specific tautomer and to determine the chemical structural in situ. In addition, fluorescence correlation

spectroscopy (FCS) is used to analyze temporal dynamics of hypericin tautomerization. Photon statistics in the fluorescence of single molecules reveal a transition rate of 1/8.4 $s^{-1}$ in PVA matrix.

Parts of this chapter and some figures have been published in the journal articles:

**Liu, Q.**; Wackenhut, F.; Hauler, O.; Scholz, M.; zur Oven-Krockhaus, S.; Ritz, R.; Adam, P.-M.; Brecht, M.; Meixner, A. J. *Hypericin: Single Molecule Spectroscopy of an Active Natural Drug*. J. Phys. Chem. A 2020, 124 (12), 2497–2504.

**Liu, Q.**; Wackenhut, F.; Wang, L.; Hauler, O.; Roldao, J. C.; Adam, P.-M.; Brecht, M.; Gierschner, J.; Meixner, A. J. Direct Observation of Structural Heterogeneity and Tautomerization of Single Hypericin Molecules. *J. Phys. Chem. Lett.* **2021**, 1025–1031.

Partial results of the presented work have been submitted at:

**Liu, Q.**; Wang, L.; Hauler, O.; Roldao, J. C.; Adam, P.-M.; Brecht, M.; Gierschner, J.; Wackenhut, F.; Meixner, A. J. Theoretical and experimental evidence of two-step tautomerization in hypericin.

All DFT and TD-DFT calculations in this work are performed by Liangxuan Wang, Prof. Johannes Gierschner and Otto Hauler.

## 4.1 Hypericin

In this work, we present SM experiments with hypericin and show that it is possible to study its optical properties, e.g. fluorescence blinking, fluorescence lifetimes and fluorescence photon statistics, despite its high triplet yield of 0.5-0.7.[105,116]

Hypericin is an anthraquinone derivative with its molecular structure depicted in Figure 4-1 a). Starting with the characterization of the optical properties of hypericin on the ensemble level, which is done by acquiring the absorption (blue line) and the fluorescence (black line) spectrum as shown in Figure 4-1 b). The absorption spectrum (blue line) can be roughly divided into three different domains, i.e. the absorption to the $S_1$ state between 490 nm and 600 nm (with the electronic transition $S_0 \rightarrow S_1$ at 591 nm and its vibronic manifold), the $S_2$ absorption between 400 nm and 490 nm (electronic transition $S_0 \rightarrow S_2$ at 480 nm) and the triplet-triplet absorption at 510 nm[107,122]. The

fluorescence spectrum is recorded with a pulsed excitation laser $\lambda_{ex}$=530 nm (Figure 4-1 b) green line). The ensemble fluorescence spectrum (black line) has mirror symmetry to the absorption spectrum with a Stokes shift of ~12 nm to 603 nm. The red line in Figure 4-1 b) displays an exemplary fluorescence spectrum of a single hypericin molecule showing the same emission bands like the ensemble spectrum, but with different intensity ratios. The concentration of hypericin in the SM experiment was adjusted such that the average spatial distance between single hypericin molecules was much larger than the diffraction limited focal spot of the confocal microscope to ensure that only one molecule was within the focal volume at a time.

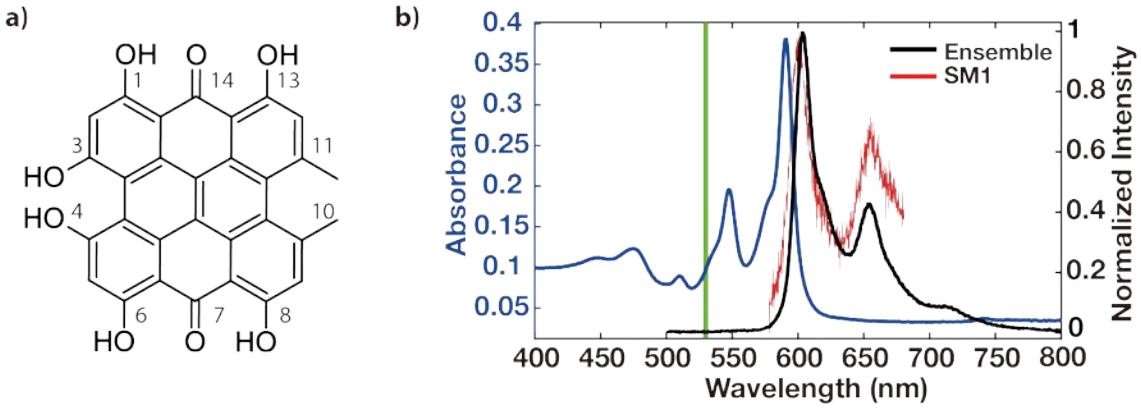


Figure 4-1 (a) Chemical structure of hypericin. (b) Ensemble absorption (blue line) and fluorescence (black line) spectra of hypericin in ethanol as well as an emission spectrum of a single hypericin molecule (red line) on a glass coverslip. The excitation wavelength is 530 nm for both emission spectra and is indicated by the green line.

## 4.2 Influence of the local environment on the emission properties

Two different types of samples are prepared in order to study the influence of the local environment on single hypericin molecules (for details see Section 3.2). Fluorescence intensity images of single hypericin molecules prepared from directly spin coating (for details see Section 3.2) on a carefully cleaned glass substrate (denoted as On Glass) and embedded in a 2 wt % PVA matrix (denoted as In PVA) are shown in Figure 4-2 a)/b), respectively. The fluorescence images are recorded with a pulsed excitation laser $\lambda_{ex}$=530 nm (1.4 µW, 20 MHz).

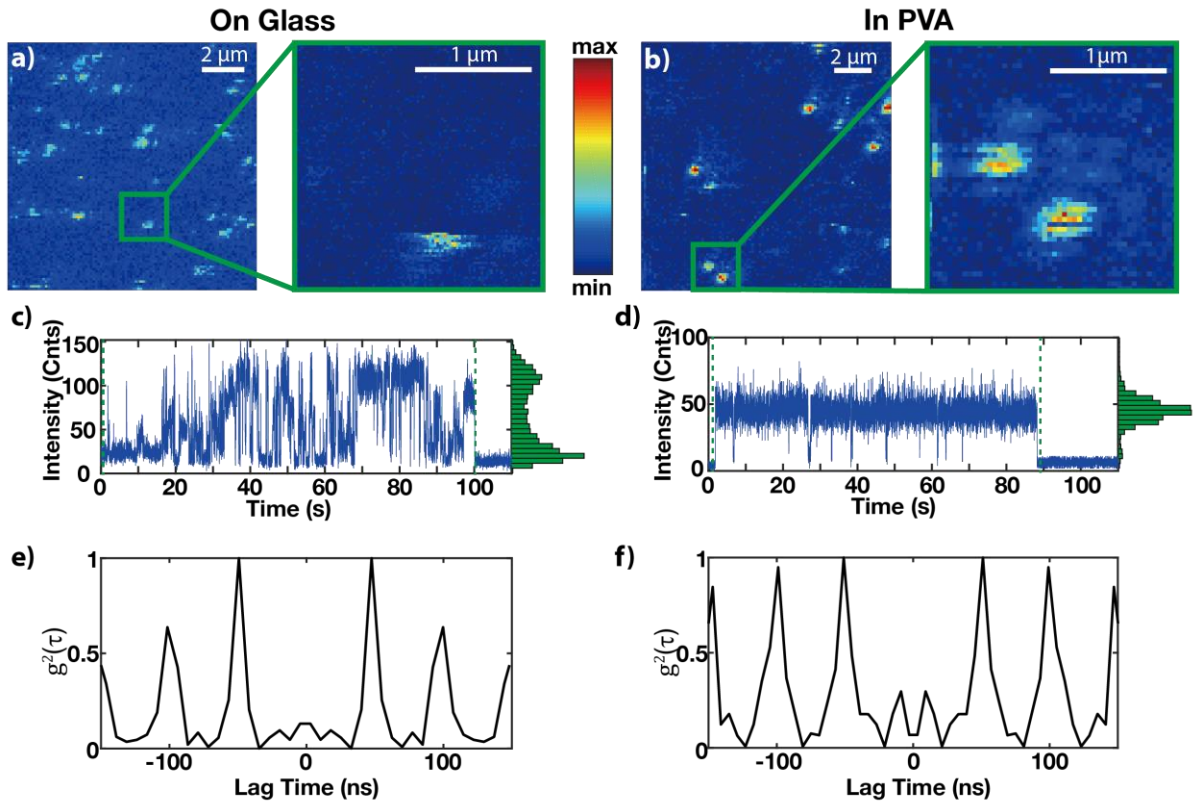


Figure 4-2 Fluorescence properties of single hypericin molecules. (a, b) Fluorescence images of single hypericin molecules on a glass coverslip and embedded in 2 wt % PVA. The inset is a close-up scan and shows the characteristic bleaching and blinking behaviour of single molecules. Scanning range is 10 µm × 10 µm/2 µm × 2 µm (100 pixels × 100 pixels, 5 ms per pixel). (c, d) shows two exemplary intensity time traces of single hypericin molecule on glass (c) and embedded in PVA (d), the corresponding histograms can be seen on the right side. (e, f) shows the second-order intensity correlation function calculated from the respective intensity time traces shown in (c, d). (Modified from [132] Figure 2)

The fluorescence images show isolated Gaussian shaped spots with a diffraction limited diameter, more details can be observed in the close up views on the right side of Figure 4-2 a)/b). Intensity fluctuations in the image patterns occur when the molecule is in a dark state for a certain amount of time, e.g. the triplet state or in another non-emissive states.[133–135] In order to investigate the blinking dynamics of hypericin, intensity time traces of SMs have been recorded. Two examples with a binning time of 10ms, which were recorded until no emission signal could be recorded after a total time of at least 20 s, are shown in the Figure 4-2 c)/d). The two exemplary intensity time traces show the characteristic on/off behaviour of a SM since it can be either in a bright or in a dark state, which is already observed in the images in Figure 4-2 a)/b). Furthermore, there are distinct differences between the two environments suggested by the two exemplary time traces, which becomes more obvious in the histograms shown on the right side of the corresponding time trace. The SM on glass is more often in the dark state, causing strong intensity fluctuations, while the SM in the PVA matrix is mainly

in the bright state until photo bleaching happens. The second-order photon correlation functions of the time traces shown in Figure 4-2 c)/d) are presented in Figure 4-2 e)/f), respectively. The absence of the peak at lag time $\tau = 0$ s, namely antibunching behaviour, confirms that the observed emission is indeed caused by a SM.

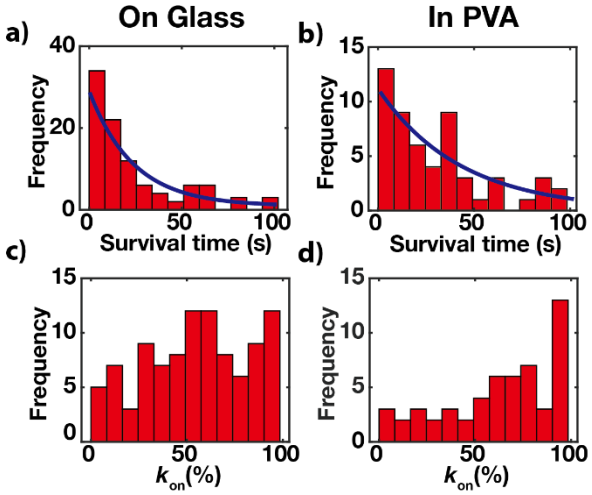


Figure 4-3 Statistics of single hypericin molecule fluorescence blinking behaviour. (a, b) show the histogram of the survival times of single hypericin molecules on a glass substrate (n=98) (a) and in a PVA matrix (n=54) (b). The blue line shows an exponential fit to the histograms and gives a bleaching time of 23.8 s on the glass substrate and 46.6 s in the PVA matrix. (c,d) On-ratio $k_{on}$ histogram of single hypericin molecules on a glass substrate (c) and in a PVA matrix (d). On the glass substrate the hypericin molecules show strong blinking, while it is suppressed in the PVA matrix.

The influence of the local environment provided by the matrices glass or PVA on the survival time and blinking dynamics are analysed statistically. The survival times of single hypericin molecules, i.e., the time before a molecule photo bleaches due to the repeated excitation, is presented in Figure 4-3 a)/b).

Figure 4-3 a) illustrates the survival time for 98 hypericin molecules directly deposited on a glass substrate, while the results shown in Figure 4-3 b) are based on 54 hypericin molecules in a PVA matrix. In both cases survival times reaching from a few seconds up to 100s can be observed. Fitting with an exponential function (blue line in Figure 4-3 a)/b)), we determine an average survival time of 23.8s on the glass substrate (Figure 4-3 a)) and 46.6s in the PVA matrix (Figure 4-3 b)). In consequence, due to this increase of the average survival time the portion of long living molecules is larger in PVA. The same intensity time traces were used to investigate the blinking dynamics by determining the on-ratio $k_{on}$, *i.e.* the ratio between the time when the molecule is in the bright state $t_{on}$ to the survival time $t_{surv}$. By setting a threshold of counts for each intensity time trace (binning time of 10ms), the molecule is considered to be in the bright state when the fluorescence intensity is

above this threshold. This allows one to determine $t_{on}$ and consequently $k_{on}$ can be calculated by $k_{on} = (t_{on}/t_{surv}) \times 100$. $k_{on}$ is almost evenly distributed from close to 0% up to 100% as presented in Figure 4-3 c) for the results of 98 molecules on the glass substrate and. The blinking dynamics changes when hypericin is embedded in the PVA matrix, which is shown for 54 SMs in Figure 4-3 d). Clearly, the amount of single hypericin molecules that hardly show any blinking increases with a significant amount of molecules having $k_{on}$ close to 100%.

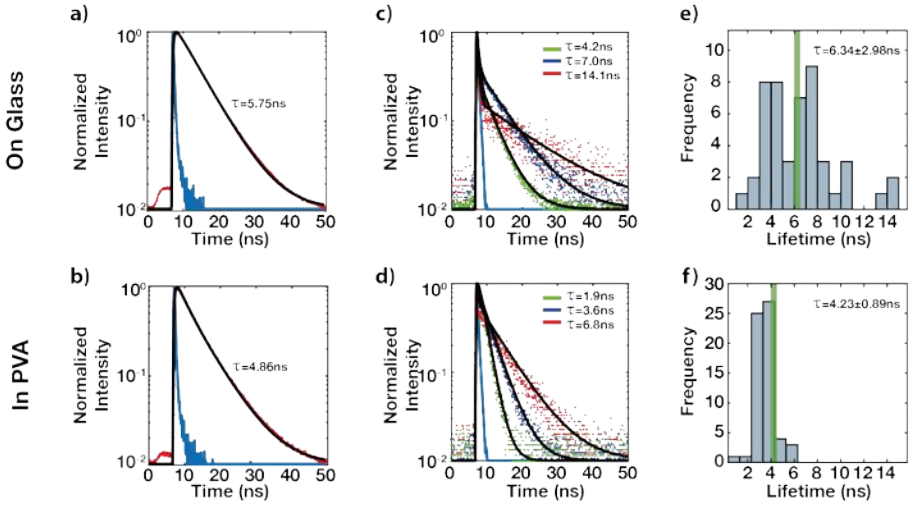


Figure 4-4 Fluorescence lifetime of hypericin. (a, b) show ensemble fluorescence decay of hypericin on a glass substrate (a) and in a PVA matrix (b). The experimental decay curves are shown in red together with the instrument response function (blue line). The excited state lifetimes determined from the exponential fit (black line) are 5.75 ns and 4.86 ns, respectively. (c, d) display decay traces and fitting results of three single hypericin molecule on glass (c) and in a PVA matrix (d). Lifetime histograms are presented in (e, f). The green line indicates the ensemble lifetime and the respective standard deviations are (6.34±2.98) ns (n=48) for the glass substrate and (4.23±0.89) ns (n=61) in the PVA matrix.

Changes in the blinking dynamics are often accompanied by changes in the fluorescence lifetime. Thus, TCSPC measurement for hypericin on glass and embedded in a PVA matrix are performed. Figure 4-4 a)/b) show fluorescence decay curves (red dots) of an ensemble of hypericin on a glass substrate a) and embedded in a PVA matrix b). Fluorescence lifetimes were obtained by fitting the decay curves with a double exponential function (black line), which is convoluted with the instrument response function (IRF, blue line). The amplitude averaged fluorescence lifetime on the glass substrate is 5.75ns and 4.86ns in the PVA matrix. These values are consistent with fluorescence lifetimes reported for ensemble hypericin in different solutions[44]. Three fluorescence decay curves of SMs and their exponential fitting functions (black lines) are displayed in Figure 4-4 c)/d). On the SM level, the fluorescence lifetimes are ranging from 1.65 ns to 14.65 ns on the glass substrate and from 1.91 ns to 6.95 ns in the PVA matrix. Corresponding histograms for molecules on the glass substrate

(n = 48) and in the PVA matrix (n = 61) are displayed in Figure 4-4 e)/f), respectively. An average fluorescence lifetime of $\tau = (6.34 \pm 2.98)$ ns on the glass substrate and of $\tau = (4.23 \pm 0.89)$ ns in the PVA matrix can be determined from these histograms. This coincides well with the ensemble fluorescence lifetime in Figure 4-4 a)/b), which is indicated by the green line in Figure 4-4 e)/f). However, the standard deviation reduces from 2.98 ns on the glass substrate to 0.89 ns in the PVA matrix. The shorter fluorescence lifetimes in the PVA matrix led to a larger radiative decay rate, which can also be observed by the higher brightness in the fluorescence images in Figure 4-2 a)/b). Additionally, a shorter fluorescence lifetime reduces the chance of a transition to the triplet state; and blinking and bleaching are reduced, which can be clearly observed in Figure 4-3.

Consequently, the results show that the PVA host matrix has a stabilizing effect and makes hypericin more suitable for fluorescence spectroscopy at the single molecule level.

## 4.3 Tautomerization transition of hypericin

Numerous theoretical studies have focused on the structural heterogeneity of hypericin concerning tautomerization, de-/protonation, and conformational (torsional), as well as possible association (dimerization) equilibria[105], while experimental difficulties prevent to clarify species related properties and equilibrium dynamics unambiguously in an ensemble. As shown above, it is possible to observe hypericin on the single molecule level, which opens up the possibility to discuss the heterogeneous dynamics of a single hypericin molecule.

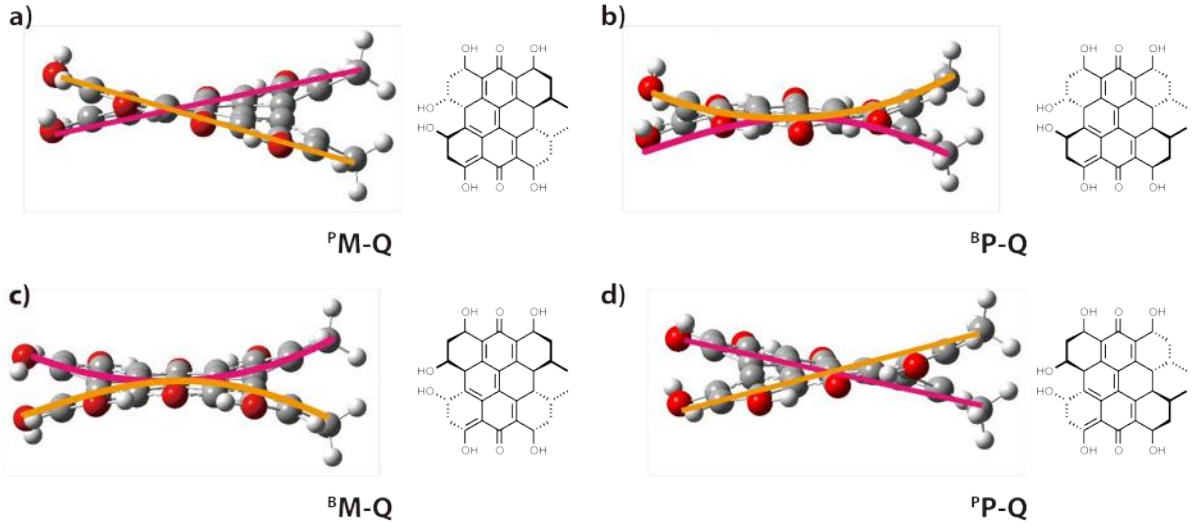


Figure 4-5 a), d) propeller (P) and b), c) butterfly (B) conformers of hypericin. The dihedral deformation of molecular

skeleton is guided with lines.

Hypericin exists in four stable conformers with different dihedral deformation, so called butterfly (B) and propeller (P) conformers. The dihedral deformation of molecular skeleton is a significant property of phenanthroperylene quinone family as sketched in Figure 4-5. The dihedral angles reported from X-ray crystallographic study[136] of the propeller conformers are 19° and 32°; DFT calculations by Liangxuan Wang and Johannes Gierschner of the free molecule gave 28° and 32°.

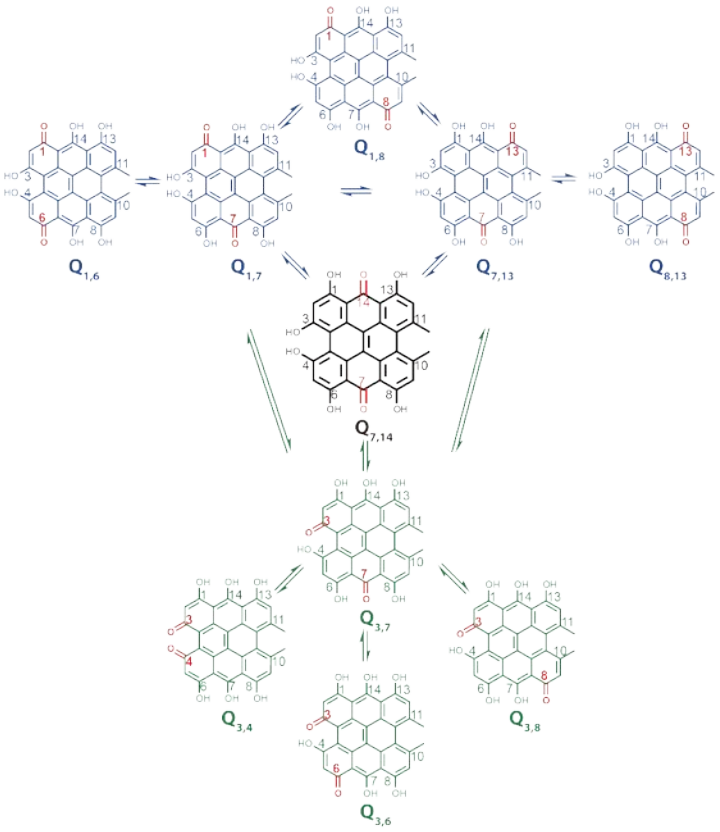


Figure 4-6 Tautomerization transition network. Two classes of tautomer that are accessible via *intra*- and *inter*-molecular proton transfer, which are sketched in blue and green.

According to [105], there are ten tautomers of hypericin, which are not affected by conformational isomerization. In the following the nomenclature from the literature [137] is used to describe the position of carbonyl groups, for instance **Q**$_{7,14}$ in Figure 4-1 a) denotes the tautomer with the carbonyl groups in positions 7 and 14. All of the interconversions shown in Figure 4-6 are further classified into *intra*- and *inter*- molecule tautomerization according to how the proton is transferred either internally or externally with respect to the molecular structure. Starting from the most stable tautomer **Q**$_{7,14}$, five tautomers are directly accessible by *intra*molecular proton transfer either in a one-step (**Q**$_{1,7}$**, Q**$_{7,13}$) or a two-step tautomerization (**Q**$_{1,6}$**, Q**$_{1,8}$**, Q**$_{8,13}$) or by *inter*molecular proton transfer in a one-step (**Q**$_{3,7}$) or two-step (**Q**$_{3,4}$**, Q**$_{3,6}$**, Q**$_{3,8}$) tautomerization. The four most stable tautomeric species,

(**$Q_{7,14}$, $Q_{1,7}$, $Q_{7,13}$, $Q_{3,7}$**), are tautomers with the lowest free energy. According to DFT calculations the activation energy barriers for single proton transfer in these tautomers are larger than the thermal energy *kT*. Therefore, quantum tunnelling[138] plays a dominant role for the tautomerization of hypericin. The other tautomeric species have higher energy barriers and demand for double proton transfer; therefore, they are unlikely to be observed under normal experimental conditions.

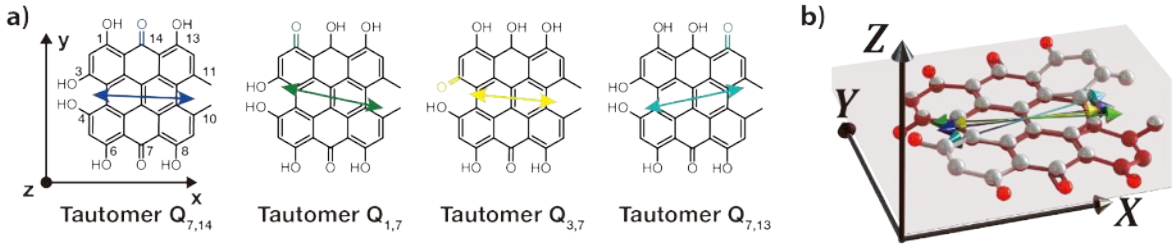


Figure 4-7 a) Chemical structure of hypericin tautomer **$Q_{7,14}$** and three other most stable tautomeric species. Coloured arrows indicate the orientation of $S_0 \rightarrow S_1$ electronic transition dipole moments (TDM). The molecular coordinate system **xyz** is fixed on the molecule. b) Three-dimensional molecular structure and TDMs when molecular coordinate system **xyz** is overlapped with image coordinate system **XYZ**.

Figure 4-7 a) shows the molecular structures of the four most stable tautomers. TDMs calculated by TD-DFT are shown by the coloured arrows (blue, yellow, green, cyan). The significant change of the carboxyl group position is accompanied with an electronic redistribution; hence, the $S_0 \rightarrow S_1$ electronic transition dipole moment (TDM) has a different orientation for the four tautomers. The exact three-dimensional orientation and relative strength of the TDMs is shown in Figure 4-7 b) together with the molecular structure. The molecular orientation is chosen in a way that the molecular coordinate system **xyz** is overlapping with the experimental image coordinate system **XYZ** (see Figure 2-5 b)). The colour of the TDM vectors corresponds to the tautomers in Figure 4-7 a). All TDMs lie almost in **X-Y** plane and the out-of-plane angles are less than $2^o$. For this orientation, the largest angle difference between TDMs from **$Q_{1,7}$** and **$Q_{7,13}$** is $24^o$ in the **X-Y** plane. It is worth to mention a transition between the conformations does not cause any change of the TDM orientation according to TD-DFT calculations. This can be explained by the small out-of-plane angles of the TDMs. Therefore, conformational transitions do not change the in-plane symmetry, as well as the TDMs. Besides, the energy barrier for a conformational transition is several times larger compared to a tautomer transition[105,137] and hence we can exclude conformational transitions in our experiment.

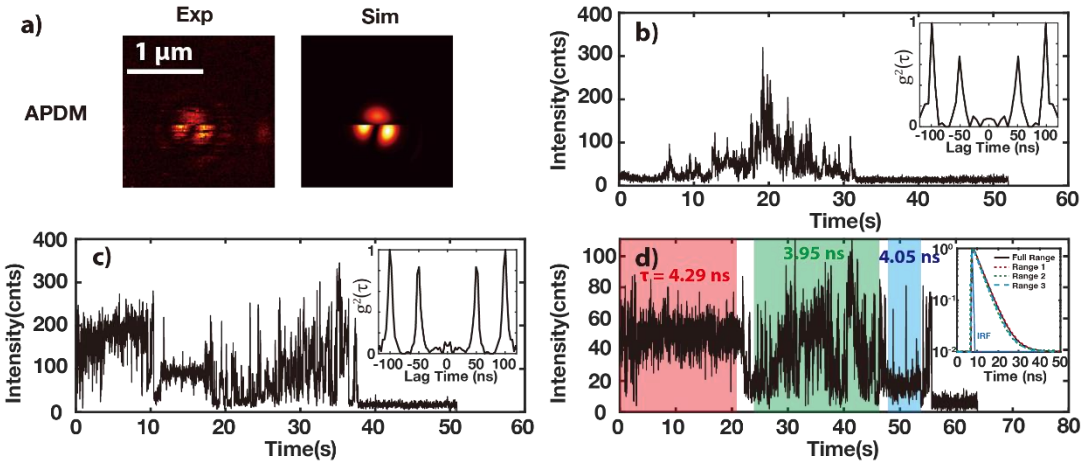


Figure 4-8 (a) Excitation images of a hypericin molecule acquired with the APDM and the simulation result. Scanning range is 2 µm × 2 µm (100 pixels × 100 pixels, 5 ms per pixel). Panel (b) and (c) show two intensity time traces of two different single hypericin molecules recorded with a binning time of 10 ms in coincidence mode. Inset figures are the second-order intensity correlation functions calculated from the respective time traces. Panel (d) shows an intensity time trace of a single hypericin molecule with a binning time of 10 ms in lifetime mode. Inset figure shows the normalized exponential decay of different emission states (red, green, blue). Single exponential fitting reveals that lifetimes range from 3.95 ns to 4.29 ns.

As explained in Section 2.1.3, the four tautomers of hypericin have a different orientation of the TDM and a transition between these tautomers can be observed by a change of the image pattern[30,139]. Figure 4-8 a) shows a scan image of a single hypericin molecule embedded in a PVA matrix acquired with APDM and simulation result, respectively

The double lobe pattern orientation and therefore the TDM in-plane orientation of the molecule rotate by 80° during the scan. A sudden flip of the excitation pattern orientation in company with intensity fluctuation suggests, that the tautomerization transition process can also be observed from the fluorescence intensity emitted by the molecule. Figure 4-8 b) and c) show intensity time traces of two different hypericin molecules. The total number of collected photons from each hypericin molecule are about $1.5 \times 10^5$ and $3.4 \times 10^5$, respectively. Both molecules show clear antibunching, which proves that the emission originates from a single molecule. Same multi-step behaviour is observed in the intensity time trace acquired during lifetime measurements, as shown in Figure 4-8 d). Remarkably, there is no significant lifetime difference between the coloured areas (4.29 ns for red, 3.95 ns for green, 4.05 ns for blue), even though the fluorescence intensity is different. This indicates that a grey state[140], i.e. an emission state with a different radiative rate, or association/dissociation[119] of hypericin are not the causes of the intensity fluctuations. We assume that the quantum yield of the same molecule and the collection efficiency of the system are the same for two reasons: first, there is

no difference in fluorescence lifetime and second the same confocal scanning microscope is used for all the measurements. Therefore, the intensity fluctuations arise from a tautomeric transition, since the orientation of electronic TDM relative to the excitation field changes and the excitation rate $\gamma_{exc}$ will be different, as indicated in Equation (2.34). From this temporal dynamic of the intensity time traces, it can be concluded that a single hypericin molecule can stay in the same tautomeric state for up to tens of seconds. This is consistent with the observation of a flipping double lobe pattern in Figure 4-8 a), which takes several seconds for the image acquisition.

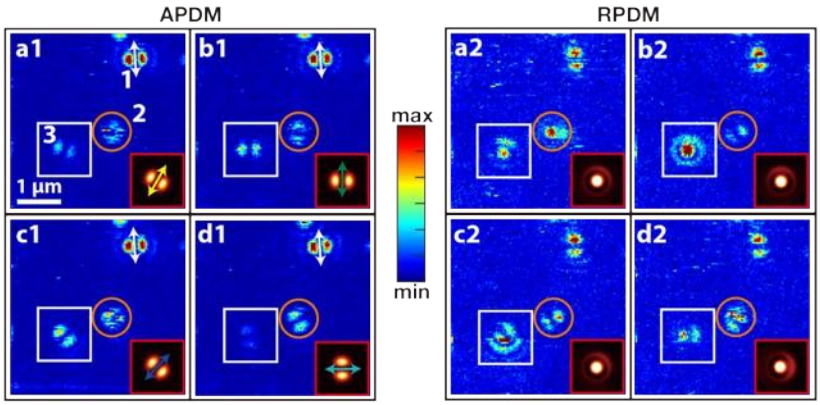


Figure 4-9 Eight exemplary images recorded at the same sample section showing the same three molecules excited in the focus of an APDM (left) and a RPDM (right). The scanning range is 4 µm × 4 µm (100 pixels × 100 pixels, 5 ms per pixel). Images are arranged in pairs (a1-a2, b1-b2, …) according to the transition dipole of the molecule. The TDM of molecule (1) has the same orientation in all four panels record with the same polarization. The difference of the patterns for molecule (1) between panels (a1-d1) and (a2-d2) is simply due to the perpendicular orientation of the in-plane electric field components of the focal fields for APDM and RPDM. The TDM of molecules (2) and (3) show an orientation change in consecutive scans. Inset images in red squares (1.2 µm × 1.2 µm) are simulation results. Coloured arrows correspond to the TDMs of the tautomers in Figure 4-5 c).

In order to further verify that the observed flipping of the TDM is caused by a tautomerization transition, scan images of the same spatial region are acquired until photo-bleaching to capture changes of TDM orientation. An exemplary image series of the same spatial area is shown in Figure 4-9.

Table 4-1 Calculated azimuthal and polar angle

| | Molecule 3 in Figure 4-9 | | | | Molecule in Figure 4-10 | | | |
|---|---|---|---|---|---|---|---|---|
| Tautomer | $Q_{7,14}$ | $Q_{1,7}$ | $Q_{3,7}$ | $Q_{7,13}$ | $Q_{7,14}$ | $Q_{1,7}$ | $Q_{3,7}$ | $Q_{7,13}$ |
| Φ | 46.8° | 89.0° | 60.2° | 0.8° | 72.9° | 125.0° | 88.3° | 41.2° |
| Θ | 167.1° | 166.0° | 167.6° | 160.0° | 11.1° | 11.0° | 10.2° | 22.6° |

Fluorescence patterns of three single molecules can be observed in Figure 4-9 and the images are arranged in pairs (a1-a2, b1-b2, …) according to the transition dipole orientation of molecule 3. The pattern orientation of molecule 1 (white arrow) is stable during all measurements, hence this molecule is always in the same tautomeric state and serves as reference. The orientation of molecule 2 (marked orange circle) changes faster than the image acquisition time, leading to a ring like pattern shape in a1 and c1. For molecule 3 (marked white square) four pairs of different excitation patterns can be distinguished representing four different TDM orientations. These are consistent with the four most stable tautomers of hypericin (see Figure 4-7 a)). The orientation of the double lobe pattern of molecule 3 in image a1 was first fitted with 2D Gaussian functions using a self-written MATLAB script, which gives an azimuthal angle $\Phi \approx 60^{o}$. Numerical simulations[141,142] are performed to compute a series of image patterns with fixed azimuthal angle $\Phi$, and varied polar angle $\Theta$ under RPDM excitation. Comparison between simulated image patterns and the experimental image in Figure 4-9 a2 allows to determine the polar angle to be $\Theta \approx 165^{o}$. Once the three-dimensional orientation of one TDM is known in the image coordinate system **XYZ**, and given that the macrocycle of the molecule cannot rotate in the solid matrix, the rotation of the TDM must be a consequence of the transition between different tautomers. Hence, the different orientations of the TDM of a given molecule must be consistent with the different tautomeric forms and the rotation matrix **R** from the image coordinate system to the molecular coordinate system **xyz** can be solved[143] as described in Appendix A.

The rotation matrix **R** times the TDM orientations in the molecular coordinate system obtained from the TD-DFT calculations yield the spatial orientation of the other three tautomers in the image coordinate system. The actual polar $\Theta$ and azimuthal $\Phi$ angles for all four dipoles in the image coordinate system are shown in Figure 4-11 a). The corresponding angles are summarized in Table 4-1. The inset images in red squares are respective image pattern calculated with the TDM orientations in Table 4-1. Please be aware that only the first image pattern in a1 is fitted to determine the orientation of one TDM. The pattern orientations of the other three tautomers is purely obtained from the relative TDM orientations obtained from TD-DFT calculations. It is worth to mention that the pattern of molecule 3 in Figure 4-9 c2) is an overlap of the tautomer $\mathbf{Q_{7,14}}$ and $\mathbf{Q_{1,7}}$. The excellent agreement between the experimental data and the TDM orientations obtained by TD-DFT calculations confirms that the observed flipping of the image patterns is caused by tautomerization transitions; and we can identify which tautomer is observed in the individual images.

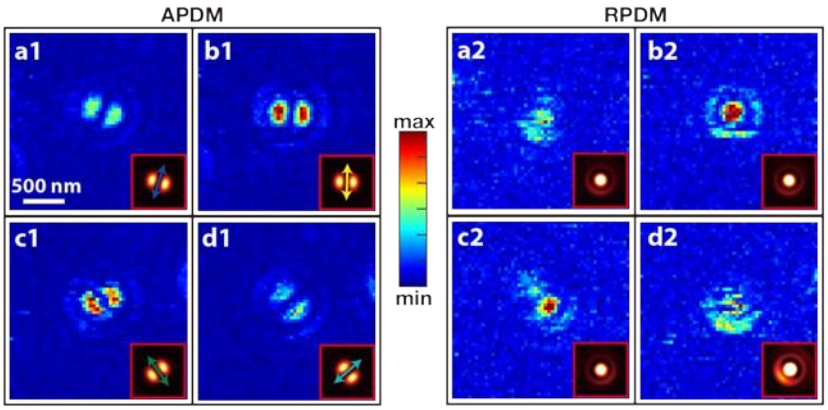


Figure 4-10 Series of successive images recorded at same spatial position. Eight exemplary images are picked from 25 scans. Scan range is 2 µm × 2 µm (50 pixels × 50 pixels, 5 ms acquisition time per pixel), (a1-d1) are excited with APDM and (a2-d2) are excited with RPDM. Inset images in red squares (1.2 µm × 1.2 µm) are simulation results. Coloured arrows (blue, yellow, green, cyan) correspond to the tautomers in Figure 4-5 c).

Another example is shown in Figure 4-10. The actual polar $\Theta$ and azimuthal $\Phi$ angles for all four dipole orientations in the image coordinate system are shown in Figure 4-11 b) and the corresponding angles are given in Table 4-1. Noting that the methyl groups of the molecule 3 shown in Figure 4-9 are pointing in negative z-direction (the polar angle is larger than 90°), while they are pointing in positive z-direction for the molecule in Figure 4-10 (the polar angle is smaller than 90°). This shows that the full 3D orientation of a single molecule can be determine. Additionally, these results prove that the same hypericin molecule cycles between all four stable tautomers and that imaging with higher order laser modes is suitable to directly image this three-dimensional structural change. These results give the first experimental prove for the coexistence of different tautomers of hypericin.

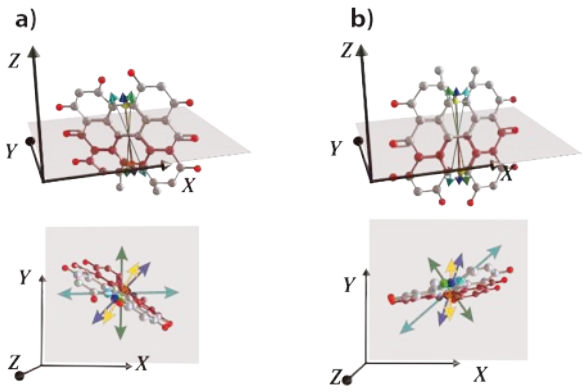


Figure 4-11 Respective orientations of the electronic transition dipole with respect to the molecular structure in the image coordinate system **XYZ**. a) represents results solved from the measurement of molecule 3 in Figure 4-9; b) represents results solved from the measurement in Figure 4-10. Top row shows the orientation of the transition dipoles in the image coordinate system at the same observation point of Figure 4-5 e). Bottom row illustrates the in-plane projection.

Coloured arrows correspond to the scaled projection length and the orientation of the transition dipoles in the **X-Y** plane

## 4.4 Temporal dynamics of hypericin tautomerization transition

As shown in the previous section 4.3, the tautomerization of hypericin can be observed as a flipping of the TDM. Limited to the time resolution of the confocal scanning method, doughnut mode scanning can only reveal the temporal dynamics of the TDMs reorientation as a sudden flipping. However, the fluorescence intensity fluctuation is also evident during tautomerization transition, hence additional information can be extracted from the intensity time trace.

Firstly, the connection between intensity fluctuations of time trace and tautomerization of hypericin should be discussed. Fluorescence Correlation Spectroscopy (FCS) gives a quantitative picture to discuss the origin of the intensity fluctuations using the autocorrelation function. It has been used to study kinetic processes with different timescales, such as molecular diffusion[144,145], singlet-triplet interactions[146], and conformational transition[147]. Depending on time resolution of the time trace, a quantitatively investigation of molecular dynamics ranging from nanoseconds to seconds are accessible.

In contrast to a standard FCS, which reflects the statistical analysis of equilibrium fluctuations, we focus on the fluctuation of a fixed single molecule (no rotation) following the discussion in [[148,149]]. Time traces *I(t)* acquired in Time-Tagged Time-Resolved experiment (see Section 3.1) can be treated as a series of photon events with a delay distribution $C(\tau)$, where $t$ is total time and $\tau$ is time delay between two photons. The timing resolution $\Delta t$ = 64 ps is set by the TTTR mode and minimum time delay $\Delta\tau \sim 100$ ns is limited by the dead-time of the detection device. Hence, the fluctuation dynamics from microseconds to seconds can be described by the autocorrelation function:

$$g^2(\tau) \cong Ae^{-\left(\frac{\tau}{\tau_1}\right)^{\beta_1}} + Be^{-\left(\frac{\tau}{\tau_2}\right)^{\beta_2}}, \tag{4.1}$$

where $A$ and $B$ are constants give the ratio of fast and slow fluctuations. $\tau_1$ and $\tau_2$ represent fast and slow fluctuation dynamics, which are corresponding to triplet state quenching and tautomerization, respectively. The stretch parameters $\beta_1$ and $\beta_2$ can describe a linear superposition of several exponential decays[150,151], giving a value of one if there is only a single exponential decay. Mean lifetimes for fast ($\langle\tau_1\rangle$) and slow ($\langle\tau_2\rangle$) fluctuation are calculated from stretched exponential decay. Detailed discussion can be found in Appendix B.

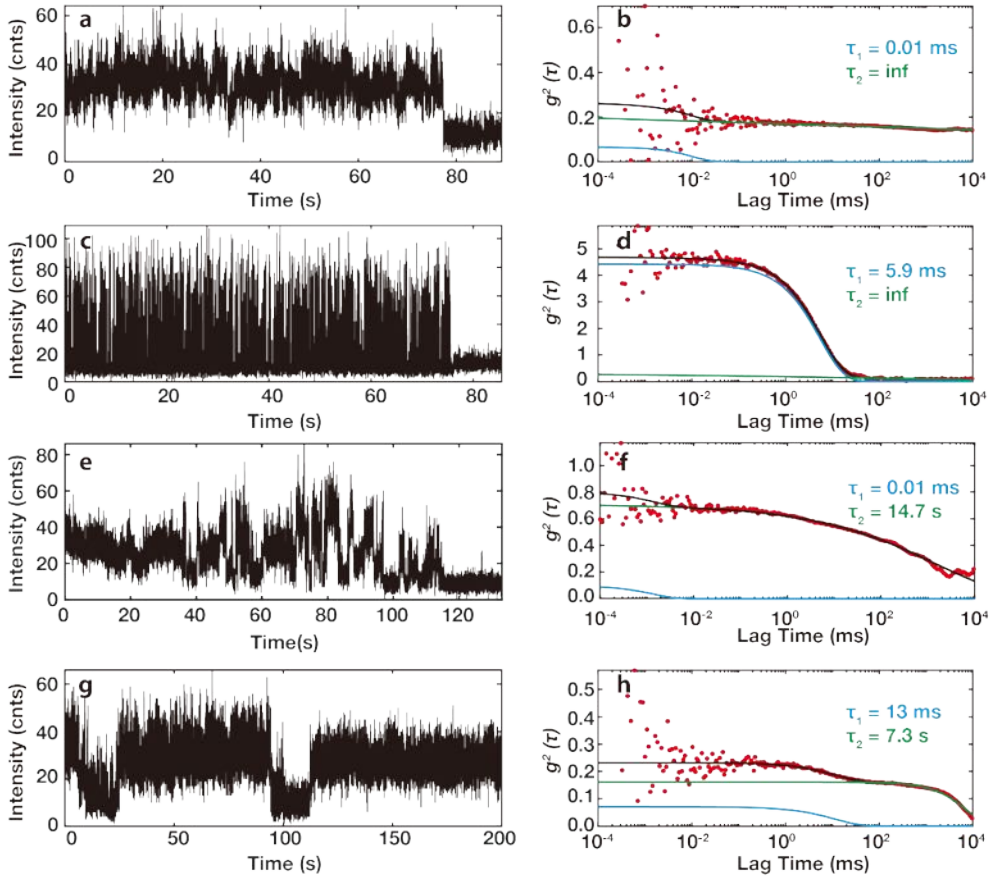


Figure 4-12 Four typical intensity time traces of single hypericin molecules (a, c, e, g) and corresponding autocorrelation function (b, d, f, h).

The dynamic parameters are obtained by calculating the autocorrelation function and fitting it with equation (4.1). Four typical intensity time traces of single hypericin molecules in PVA and corresponding autocorrelation function (detector afterpulsing effect is removed[27]) with fitting results are given in Figure 4-12. Time traces are binned in 10 ms for displaying. The molecule in a)/b) is stable over the whole collection time, i.e., there are no apparent long timescale dynamics, which is clearly shown in b) and the autocorrelation function is constant with $\langle\tau_2\rangle$ = inf. The small portion of short-timescale dynamic with $\langle\tau_1\rangle$ = 0.01 ms reveals very fast dynamics. Although it is not well resolved, the fitting results can capture the fast dynamics. The large fluctuation of autocorrelation function at small lag time is due to large standard deviation of the time traces with small binning time[152]. The second molecule in c)/d) shows fast blinking during the whole acquisition time due to fluorescence quenching by the triplet states and there is no long timescale intensity fluctuation. The autocorrelation function in d) gives a single exponential decay ($\beta_1$ = 1) with $\langle\tau_1\rangle$ = 5.9 ms. $\langle\tau_2\rangle$ = inf confirms that there is no long timescale dynamics. The molecule in e) exhibits large intensity fluctuation in long timescale, which is clearly revealed in f) with $\langle\tau_2\rangle$ = 14.7 s. The molecule in g) is

a perfect example showing both short-time blinking and long-time fluctuations. As expected, the autocorrelation curve in h) is a mixture of two decays with $\langle\tau_1\rangle$ = 13 ms and $\langle\tau_2\rangle$ = 7.3 s.

We have implied for the derivations shown in Appendix B that measurements are stationary, i.e. the survival time of single molecule is long enough for all states to be sampled in the time trace *I(t)* with their steady-state probability. This is a safe assumption in this work since hypericin normally stays in the same tautomer for several seconds (proved later), while the average survival time is much longer (Section 4.2). If the finite survival time $T$ is taken into account, the autocorrelation function will decrease to zero when the lag time is larger than the survival time. Assuming the finite survival time is the only dynamics in the time trace, the corresponding autocorrelation function will either be a single exponential decay ($\beta_2 = 1$) or a stretched exponential decay with $\langle\tau_2\rangle > T$. Therefore, we can exclude data only containing decays due to the finite survive al time by removing autocorrelation functions with $\beta_2 \geq 0.95$ and $\langle\tau_2\rangle > 40\ s$. ($\beta_2 < 0.95$ indicates superposition of several exponential decays, i.e. more intensity fluctuations. The average survival time is set to 40 s according to the results in Section 4.2). We note this is a strong exclusion condition since the cases with $\beta_2 \geq 0.95$ also contain the situations where tautomerization happens, for example, the fitting in Figure 4-12 h) yields $\beta_2 = 1$, while clear intensity fluctuation due to tautomerization can be observed in g).

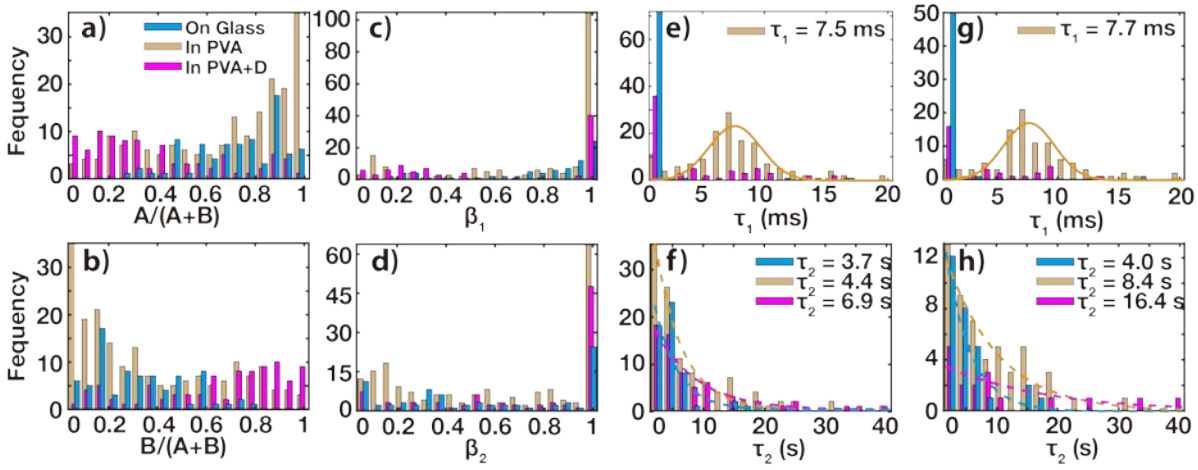


Figure 4-13 Histograms of the dynamic parameters for single hypericin on glass ($\sigma$ = 78), in PVA ($\sigma$ = 189) and deuterated in PVA ($\sigma$ = 89). a) Amplitude ratio of fast dynamic A/(A+B). b) Amplitude ratio of slow dynamic B/(A+B). c) and d) Stretch parameters of $\beta_1$ and $\beta_2$. e) and f) Histogram of mean lifetime $\langle\tau_1\rangle$ and $\langle\tau_2\rangle$. g) and h) Histogram of mean lifetime $\langle\tau_1\rangle$ and $\langle\tau_2\rangle$ by limiting $\beta_2$<0.95

Figure 4-13 shows the histograms of the dynamic parameters for single hypericin molecules on glass ($\sigma$ = 78, blue), in PVA ($\sigma$ = 189, orange) and deuterated in PVA ($\sigma$ = 89, magenta). Panel a) and b) show the distribution of the amplitude ratio of fast dynamic A/(A+B) and slow dynamic B/(A+B). Clearly, for both cases, on glass and in PVA, molecular dynamics are dominated by fast

fluctuations since the amplitude ratio of fast dynamic A/(A+B) is close to 1. However, fast dynamics in deuterated hypericin are suppressed leading an increased portion of amplitude ratios of the slow dynamics B/(A+B) close to 1. Although the mechanism of suppression needs further discussion, we give a possible explanation here. Due to the low p$K_a$ (1.8), H/D exchange is most likely to happen at the *bay* hydroxyl groups[105–107] (label 3 or 4 in Figure 4-1 a)). In addition, tautomerization transitions (network in Figure 4-6) enable multiple H/D exchanges, which can result in the prolongation of triplet state lifetime up to tens of times[153–155], thus the fast dynamics in millisecond scale are suppressed.

Most of the stretch parameters $\beta_1$ and $\beta_2$ are equal to 1 as shown in c) and d). It is reasonable for $\beta_1 = 1$ since triplet state quenching is the main reason of fast fluctuation, while $\beta_2 = 1$ indicates that molecules do not show obvious tautomerization or decreasing of the autocorrelation function is mainly due to a finite survival time.

Both fast lifetime $\tau_1$ and slow lifetime $\tau_2$ should follow a Poisson distribution[156,157]. In the present observation timescale (~60 s), fast fluctuations (~ms) occur many times and a normal distribution is an excellent approximation for $\langle\tau_1\rangle$, while slow fluctuation should still obey exponential decay. Histograms of mean lifetimes $\langle\tau_1\rangle$ and $\langle\tau_2\rangle$ are presented in e) and f). The distribution of $\langle\tau_1\rangle$ is cut at 20 ms and $\langle\tau_2\rangle$ is cut at 40 s to exclude data where the only long time scale dynamic is bleaching. For molecules on glass, most of $\langle\tau_1\rangle$ are very short and the average $\overline{\langle\tau_1\rangle}$ = 0.10 ms is in the range of the triplet-state lifetime of hypericin[122,123,158], while the distribution of $\langle\tau_1\rangle$ in PVA is fitted by a Gaussian function with an average $\overline{\langle\tau_1\rangle}$ = 7.5±1.2 ms. The longer triplet lifetime probably due to faster radiative decay rate suppresses the transition to the triplet state, and less oxygen in PVA reduce the possible nonradiative decay pathways in the triplet state[116,159]. The distribution of $\langle\tau_1\rangle$ for deuterated hypericin in PVA is different from the other two situations: many of molecules possess short $\langle\tau_1\rangle$ (<1 ms) and the rests are randomly distributed in longer time (>1 ms). This also can be explained by the possible multiple H/D exchanges, which give rise to the broad distribution of prolonged $\langle\tau_1\rangle$ and decrease the ratio of fast dynamics.

The distributions of $\langle\tau_2\rangle$ are similar for all three situations as shown in f). The histogram distributions are fitted by an exponential function $y = A\, e^{-b\tau}$, which gives average $\overline{\langle\tau_2\rangle}$ = 3.7 s 4.4 s and 6.9 s for hypericin on glass, in PVA and deuterated, respectively. Panels g) and h) show the histograms of $\langle\tau_1\rangle$ and $\langle\tau_2\rangle$ by limiting $\beta_2$<0.95, i.e. only molecules showing obvious tautomerization. The distribution of $\langle\tau_1\rangle$ in g) is barely changed compared to e), while the average $\overline{\langle\tau_2\rangle}$ = 4.0 s, 8.4 s and 16.4 s are significantly different, indicating the hypericin tautomerization rate ($1/\overline{\langle\tau_2\rangle}$) is altered by the PVA matrix and H/D exchange. We have explained tautomerization of hypericin as quantum

tunnelling. A ‘Freezing effect’ induced by a rigid polymer matrix on proton transfer is already reported[30]. And the tautomerization rate difference between hypericin in PVA and deuterated hypericin can be attributed to the modification of the tunnelling energy barrier and the mass difference of hydrogen and deuterium.

In conclusion, we have shown that hypericin is, despite its high triplet yield, excellently suited for fluorescence spectroscopy on the single molecule level. In particular, in-situ observation of single molecule tautomerization dynamic is presented, proving the coexistence of the four most stable tautomers of hypericin. TD-DFT calculations allow to determine relative orientation of the TDMs of the tautomeric species. This enables to determine the three-dimensional spatial orientation of the molecule and to identify the tautomeric state observed in a specific image. Additionally, fluctuation of the tautomerization rates depending on their local environment are analysed by FCS. We can determine that hypericin stays in the same tautomer for several to tens of seconds. A ‘Freezing effect’ induced by the polymer matrix and the isotope effect are also observed.

# Chapter 5 Coupling of cavity and quantum emitters

An optical cavity changes the optical mode density (see Section 2.3) with respect to free space. When the interaction between a cavity mode and a molecule is weak (unperturbed Hamiltonian $H_0 \gg$ interaction Hamiltonian $H_1$, see Section 2.3.2), the modification of the molecular spontaneous emission rate, emission spectrum, as well as the excitation rate can be discussed in a perturbative manner. In this scenario, the cavity and the molecules can be characterized separately, and then the perturbation is applied.

The following chapter will characterize the optical modes in a microcavity and demonstrate how it can change the photophysical properties of hypericin, which is weakly coupled to the microcavity. In addition, profiting from the large local field enhancement of plasmonic nanocavity, deprotonation of hypericin at ambient condition is confirmed via single molecule surface enhanced Raman spectroscopy (SERS).

When the interaction between the mode in the cavity and a molecule is strong enough, the cavity and the molecules are coherently coupled and have to be treated as hybrid system. Strongly coupled J-aggregate dye molecules in an optical microcavity are explored in the final section.

Partial results of the presented work have been submitted to:

**Liu, Q.**; Wang, L.; Hauler, O.; Roldao, J. C.; Adam, P.-M.; Brecht, M.; Gierschner, J.; Wackenhut, F.; Meixner, A. J. Theoretical and experimental evidence of two-step tautomerization in hypericin.

## 5.1 Characterization of microcavity

The schematic drawing in Figure 5-1 a) illustrates the structure of the microcavity used in this work. A detailed description can be found in Section 3.3. When the top lens approaches to the bottom mirror, Newton's rings are observed at the centre of the convex lens (Figure 5-1 b)). The transmission spectra of a representative microcavity (at $\lambda/2$ range) with different resonances are shown in Figure 5-1 c), where the motion of the plano-convex lens is controlled by a piezo actuator. Lorentzian functions

fitted to the transmission spectra give a full width at half maximum (FWHM) of approximately 27 nm corresponding to a Q-factor of around 20.

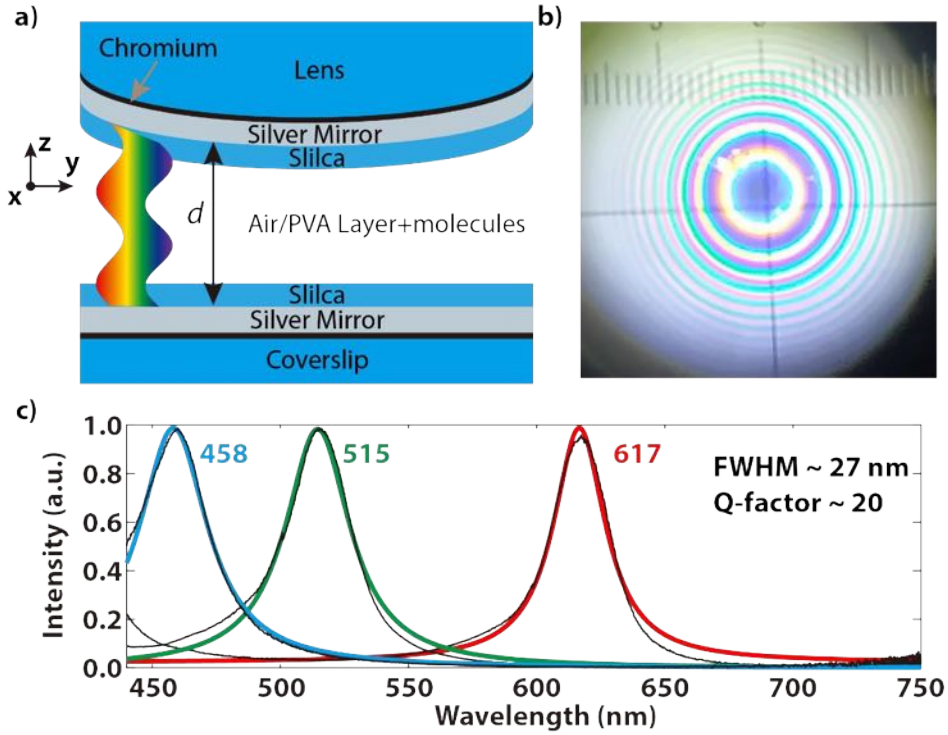


Figure 5-1 a) Schematic drawing of a microcavity. b) White light transmission patterns (Newton's rings) in the microcavity. c) Measured transmission spectra (black lines) of a representative microcavity (at $\lambda/2$ range) fitted with Lorentzians (coloured lines).

The resonance can also be tuned by lateral scanning the cavity in the xy plane (Figure 5-1 a)) as can be seen by a simple calculation: the radius of curvature of the top lens is 25.8 mm and xy plane scanning piezo-stage can travel 100 μm×100 μm, the movement of 100 μm starting from the centre of Newton's rings in xy plane corresponds to a displacement of the mirror spacing of about 200 nm in z direction. In contrast to a direct moving of the lens in z direction by a piezo actuator, the lateral scan provides a more accurate and more precise z control. In addition, this could avoid molecular photo-bleaching due to the long-time measurement at same spot. However, lateral scanning of the cavity has the drawback that always a different spot is in the focus, needing a homogenous sample.

Figure 5-2 a) shows the dispersion of reflection spectra obtained by laterally scanning at the direction indicated by the arrow in the inserted optical image. The cavity thickness (gap between silver layers) is obtained by fitting the spectra with a Fresnel model assuming that the cavity is filled with silica, where the cavity thickness is the only fit parameter. Angle resolved dispersion in Figure 5-2 b) is measured at the position indicated by the red circle in the insert optical image. Dispersions

obtained from Transfer Matrix Method (TMM) simulations are presented by the dashed lines. Excellent agreement between experimental data and the TMM simulation results proves the reliability of the tunable microcavity.

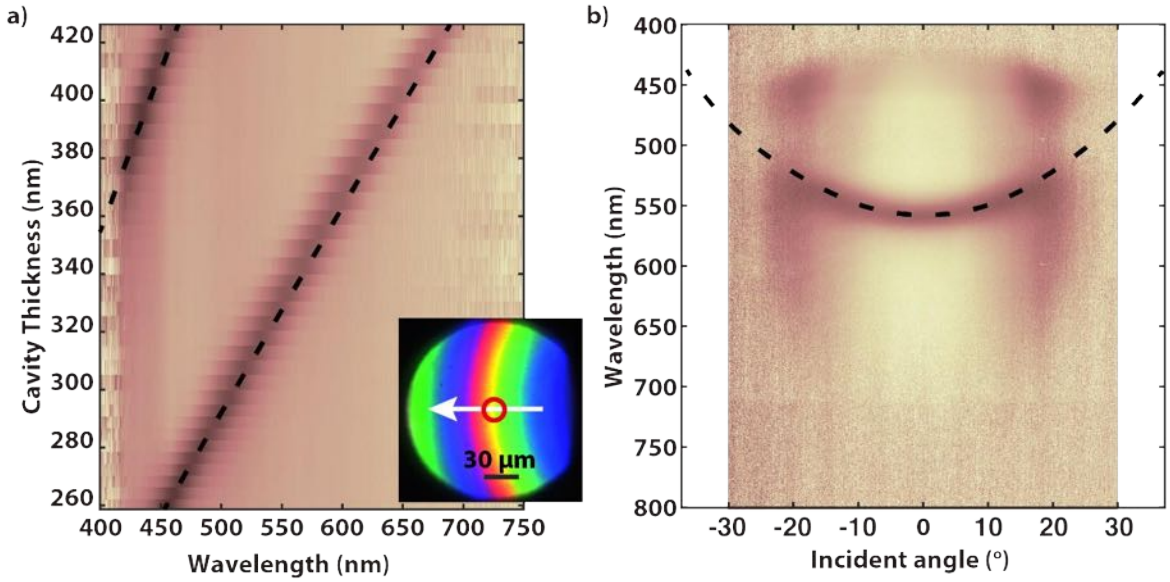


Figure 5-2 a) Dispersion of reflection spectra. The insert is an optical image of Newton's rings. The white arrow indicates the lateral scan direction and the red circle indicated the position for angle resolved dispersion measurement shown in b). Dashed lines represent TMM simulation results.

## 5.2 Microcavity – Tailoring hypericin fluorescence emission properties

As already shown in Section 2.3.1, the spontaneous emission rate of molecules in a cavity is altered by the Purcell factor. Several studies have investigated the emission properties of emitters inside a microcavity[160–162]. Experiments with single quantum dots[163,164], molecules[29,65], and nitrogen-vacancy centres[165,166] in nanodiamond are also reported. To study the emission properties of hypericin in a tunable microcavity, a theoretical framework for the calculation of radiative decay rate and detected fluorescence spectra is presented first.

Following the approach presented by Björk[167] assigning the variations of the spontaneous emission rate to the zero-point fluctuations associated with an electrical field entering the microcavity, which can be derived classically. When we discussed spontaneous emission in Section 2.1.1, the quantity of quantized electric field $\boldsymbol{\mathcal{E}_k}$ (equation (2.4)) is the same in all directions. However, the cavity breaks the isotropic property. Rewriting the quantized electric field as $\boldsymbol{\mathcal{E}_k^c}(\theta, \phi, z)$, it can be evaluated

numerically using the TMM method. The orientation of molecular TDM should also be taken into account. For ensemble measurement, the TDMs of molecules are randomly distributed in the cavity and can be represented by

$$\hat{\wp} = C \times [1,1,1]/\sqrt{3}, \tag{5.1}$$

here $C$ is constant. The frequency-dependent Purcell factor can be calculated:

$$P(\omega,z) = \frac{\Gamma_{sp}(\omega)}{\Gamma_{sp0}(\omega)} = \frac{\int_0^{2\pi} d\phi \int_0^{\pi} \sin\theta \, d\theta \, \omega^2 |\hat{\wp} \cdot \boldsymbol{\mathcal{E}}_{\boldsymbol{k}}^{c}(\theta,\phi,z)|^2}{\int_0^{2\pi} d\phi \int_0^{\pi} \sin\theta \, d\theta \, \omega^2 |\hat{\wp} \cdot \boldsymbol{\mathcal{E}}_{\boldsymbol{k}}|^2}. \tag{5.2}$$

where $z$ is the position of the molecule inside the cavity. Accounting for the influence of the line shape of the fluorescence spectrum $S(\omega)$, the average Purcell factor is obtained:

$$\bar{P}(z) = \frac{\bar{\Gamma}_{sp}}{\bar{\Gamma}_{sp0}} = \frac{\int_0^{2\pi} d\phi \int_0^{\pi} \sin\theta \, d\theta \int_0^{\infty} \omega^2 d\omega \, |\hat{\wp} \cdot \boldsymbol{\mathcal{E}}_{\boldsymbol{k}}^{c}(\theta,\phi,z)|^2 S(\omega)}{\int_0^{2\pi} d\phi \int_0^{\pi} \sin\theta \, d\theta \int_0^{\infty} \omega^2 d\omega \, |\hat{\wp} \cdot \boldsymbol{\mathcal{E}}_{\boldsymbol{k}}|^2 S(\omega)}. \tag{5.3}$$

The excited state lifetime inside the cavity is given by

$$\frac{1}{\tau_c} = \gamma_c + \gamma_n = \bar{P}\gamma_0 + \gamma_n = \frac{1}{\tau_0}(1 - \eta + \bar{P}\eta). \tag{5.4}$$

Here $\gamma_c$ and $\gamma_n$ are the radiative and nonradiative rate in the cavity, respectively. $\gamma_c$ equals to the free space radiative rate $\gamma_0$ times the average Purcell factor. $\tau_0$ and is the free space excited state lifetime, and $\eta$ is the quantum yield of the molecule.

Finally, the detected fluorescence spectra $S_{real}(\omega)$ depend on the position of the excited molecules and the limited numerical aperture of the objective lens. The excitation field distribution can be calculated as in [168]. For our experimental conditions (see Section 3.2), molecules are embedded in a thin PVA layer that is spatially separated from the silver layer. Setting $z = 90\,nm$ (silica layer + half of PVA film) yields an reasonable estimation of the average distance of the molecules to the mirror[169]. The impact of the limited numerical aperture can be treated as a reciprocal process for the discussion of the spontaneous emission rate, i.e. the electrical field exiting the microcavity. Consequently, $S_{real}(\omega)$ can be calculated by

$$S_{real}(\omega) = P_{NA}(\omega) \times S(\omega) \tag{5.5}$$

where $P_{NA}(\omega)$ is calculated by equation (5.2) limiting the integration within the angle of the numerical aperture.

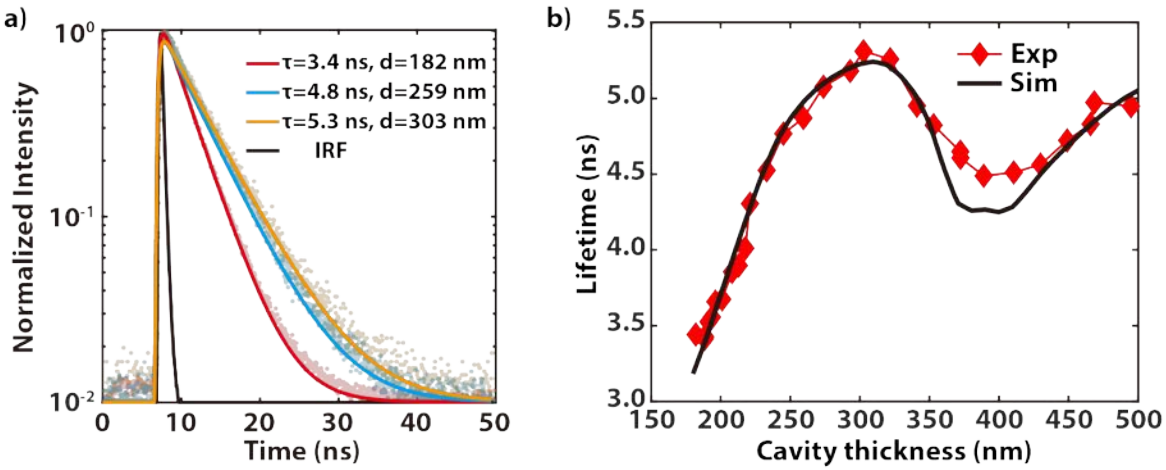


Figure 5-3 a) Fluorescence decays measured in the cavity for different cavity thickness. The experimental data are fitted with a single exponential decay. b) Lifetime as a function of the cavity thickness. The solid black line represents a fit of the theoretical model to the experimental data.

The film in the cavity is prepared by spin coating a layer of $10^{-5}$ M hypericin/PVA solution on the flat mirror (for details see Section 3.2). The cavity thickness is tuned from 180 nm to 500 nm as determined from the cavity transmission spectra. Figure 5-3 a) shows three representative fluorescence decays measured in the cavity, where the excited state lifetime is obtained by fitting with a single exponential decay. A significant influence of the cavity thickness on the excited state lifetime can be observed. Figure 5-3 b) shows the results of measured lifetime as a function of the cavity thickness. The solid black line represents a fit of the theoretical model to the experimental data. Noting only the free space excited state lifetime $\tau_0$ and the quantum yield $\eta$ are fitted according to equation (5.4), which are $\tau_0 = 4.8\,ns$ and $\eta = 13\,\%$. The free space excited state lifetime is in excellent agreement with experimental value,[132] while the quantum yield is slightly smaller than reported (20±3%).[170] The smaller quantum yield can be most likely caused by the contribution of the molecules at different $z$ position, which is neglected in the simulation.

Three cavity transmission spectra with maximum at 606 nm, 625 nm and 649 nm are presented in Figure 5-4 a), in which hypericin fluorescence spectrum is also shown. Corresponding emission spectra and simulated spectra computed on the basis of equation (5.5) are shown in Figure 5-4 b) and c), respectively. Compared to free space emission, the fluorescence spectra are altered dramatically, which demonstrates that the microcavity allows to control molecular vibronic transition probabilities. There is a good agreement between measured and calculated spectra proving that the semiclassical model is suitable for the description of the cavity-induced changes.

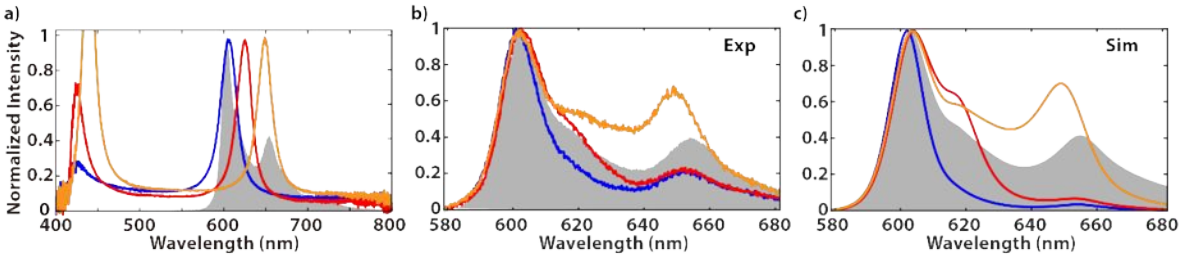


Figure 5-4 a) Transmission spectra with transmission maximum at 606 nm (blue), 625 nm (red) and 649 nm (orange). Free space fluorescence spectrum is shown in grey area. Emission spectra b) and simulated emission spectra c) with colours corresponding to the transmission in a)

## 5.3 Plasmonic Nanocavity – Single hypericin molecule Surface-Enhanced Raman scattering

Hypericin was additionally characterized with surface-enhanced Raman scattering (SERS). A silver island film is used as SERS substrate (for details see Section 3.4), which is depicted in the scanning electron microscopy (SEM) image shown in Figure 5-5 a).

The SEM image of the silver film is analysed with the software "ImageJ" and the radius distribution of the nanoparticles in Figure 5-5 b) is fitted by a Gaussian function with $R = (11.93 \pm 3.66)\ nm$. An extinction spectrum of the SERS substrate is presented in Figure 5-5 c) with a surface plasmon resonance at 482 nm.

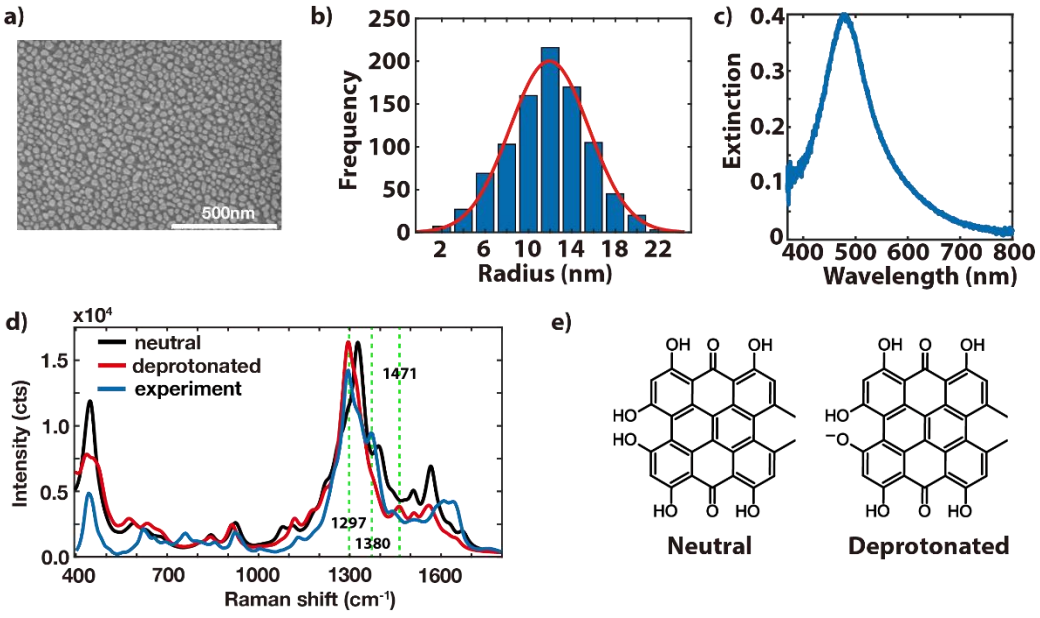


Figure 5-5 a) Scanning electron micrograph of the SERS substrate consisting of silver nanoparticles on a glass substrate.

b) The corresponding particle size distribution of the substrate. The radius fitted with Gaussian function is $R = 11.93 \pm 3.66\ nm$. c) Extinction spectrum of the substrate. d) Ensemble SERS spectra acquired with an excitation wavelength of $\lambda_{ex}$ = 633 nm (blue line) and DFT simulation of the neutral (black line) and deprotonated (red line) form of hypericin. e) Chemical structure of neutral and deprotonated hypericin.

5 µL of a 1 µM hypericin solution was dropped on such a substrate to acquire ensemble SERS spectra. A 633 nm excitation laser is used for the ensemble experiments to avoid fluorescence background. The SERS spectra shown in blue in Figure 5-5 d) are analysed with a self-written MATLAB script and the corresponding peak positions are listed in Table 5-1. They are consistent with values reported in literature for hypericin[117,106,107,171]. In addition, DFT calculations were performed and respective simulated spectra for the neutral and deprotonated form of hypericin are shown in black and red in Figure 5-5 d), respectively. The first deprotonation of hypericin occurs at the *bay* hydroxyl groups (as shown in Figure 5-5 e)), which have a low pKa of 1.8[106,107,105]. Comparing the calculated spectra with the experimental ensemble spectrum suggests that both the neutral and deprotonated species of hypericin are present in the ensemble experiment. The pronounced peaks in the SERS spectrum at 1297 $cm^{-1}$ and at 1471 $cm^{-1}$ are assigned to the deprotonated form of hypericin. On the other hand, the shoulder at ~1333 $cm^{-1}$ and the peak at 1380 $cm^{-1}$ in the ensemble SERS spectrum originate from the neutral species.

Table 5-1 SERS peak positions in $cm^{-1}$ and relative intensity (in brackets)

| **Ensemble** | **Exp. $Hyp^-$** | **Sim. $Hyp^-$** | **Exp. Hyp** | **Sim. Hyp** | **assignment[117]** |
|---|---|---|---|---|---|
| 309 (0.04) | | 319 (0.28) | | 321 (0.09) | |
| 358 (0.04) | | 342 (0.35) | | 349 (0.20) | |
| 450 (0.35) | 448 (0.19) | 438 (0.39) | 455 (0.19) | 459 (1.00) | Skeletal deformation |
| 476 (0.17) | | 465 (0.37) | | 490 (0.13) | Skeletal deformation |
| | 529 (0.18) | 518 (0.11) | 518 (0.10) | 510 (0.13) | Skeletal deformation |
| | | | 593 (0.08) | 600 (0.08) | Skeletal deformation |
| 630 (0.13) | 636 (0.32) | 639 (0.12) | 637 (0.15) | 636 (0.05) | |
| 665 (0.09) | | 667 (0.08) | 746 (0.09) | | |
| 699 (0.07) | | 682 (0.08) | | 700 (0.04) | |
| 763 (0.11) | | | | | |
| 816 (0.07) | 830 (0.47) | 808 (0.04) | 790 (0.14) | 814 (0.02) | |
| 862 (0.07) | 868 (0.56) | 848 (0.08) | 839 (0.14) | 850 (0.09) | |
| 933 (0.12) | 938 (0.13) | 918 (0.17) | 939 (0.13) | 936 (0.17) | |
| 1018 (0.03) | 1017 (0.10) | 1017 (0.02) | 1016 (0.12) | 1025 (0.02) | |
| 1134 (0.09) | 1129 (0.67) | 1122 (0.17) | 1125 (0.44) | 1119 (0.16) | C-H bending |
| 1189 (0.13) | 1168 (0.56) | 1177 (0.16) | | 1190 (0.12) | C-O stretching |
| 1251 (0.44) | 1232 (0.70) | 1223 (0.24) | 1230 (0.63) | 1225 (0.24) | Ring in plane |
| 1297 (1.00) | 1299 (1.00) | 1298 (1.00) | | 1298 (0.46) | Ring in plane |
| 1333 (0.77) | 1364 (0.82) | 1324 (0.69) | 1316 (0.76) | 1327 (0.97) | Ring in plane |

| | | | | | |
|---|---|---|---|---|---|
| 1380 (0.66) | 1405 (0.46) | 1380 (0.26) | 1398 (0.92) | 1395 (0.22) | Ring in plane |
| 1450 (0.24) | 1471 (0.33) | 1467 (0.20) | 1451 (0.39) | 1444 (0.20) | Ring in plane |
| 1514 (0.19) | 1525 (0.24) | 1514 (0.17) | 1480 (0.28) | 1514 (0.40) | |
| | 1589 (0.87) | 1564 (0.21) | 1545 (0.57) | 1571 (0.58) | Ring stretching with C=O |
| 1604 (0.30) | 1613 (0.49) | 1614 (0.07) | 1610 (1.00) | 1609 (0.05) | C=O stretching |
| 1648 (0.29) | | 1625 (0.07) | | 1633 (0.13) | |

SM SERS spectra of hypericin were acquired by using the same SERS substrates, but the concentration of the hypericin solution was reduced to 0.1 nM. Confocal scanning images recorded from pure substrates and from substrates doped with 1.0 nM and 0.1 nM hypericin solution are presented in Figure 5-6 a)-c), respectively. The SM SERS spectra were acquired from the intense hot spots with a 530nm laser, which is in resonance with the $S_0 \rightarrow S_1$ electronic transition of hypericin, enabling resonance Raman scattering. For comparison the ensemble resonance Raman spectrum is displayed by the grey area in Figure 5-6 d)/e). Two exemplary SM SERS spectra are shown in Figure 5-6 d). In general, the same SERS peaks as in the ensemble spectrum can be observed for SMs, but the full width at half maximum of the peaks is significantly reduced since there is no ensemble averaging. The SERS spectrum shown in Figure 5-6 d) in red exhibits strong peaks at 1589 $cm^{-1}$, 1471 $cm^{-1}$ and 1299 $cm^{-1}$. These peaks have been assigned to the deprotonated form of hypericin[106]. However, the peak positions shown in Figure 5-6 d) in black are shifted to 1610 $cm^{-1}$, 1451 $cm^{-1}$ and 1316 $cm^{-1}$, which can be attributed to the deprotonation of hypericin[10]. Therefore, SM SERS experiments allow to directly observe different hypericin subpopulations. The spectral peak positions of these SERS experiments are summarized in Table 5-1 for the deprotonated and the neutral SM together with the corresponding simulations.

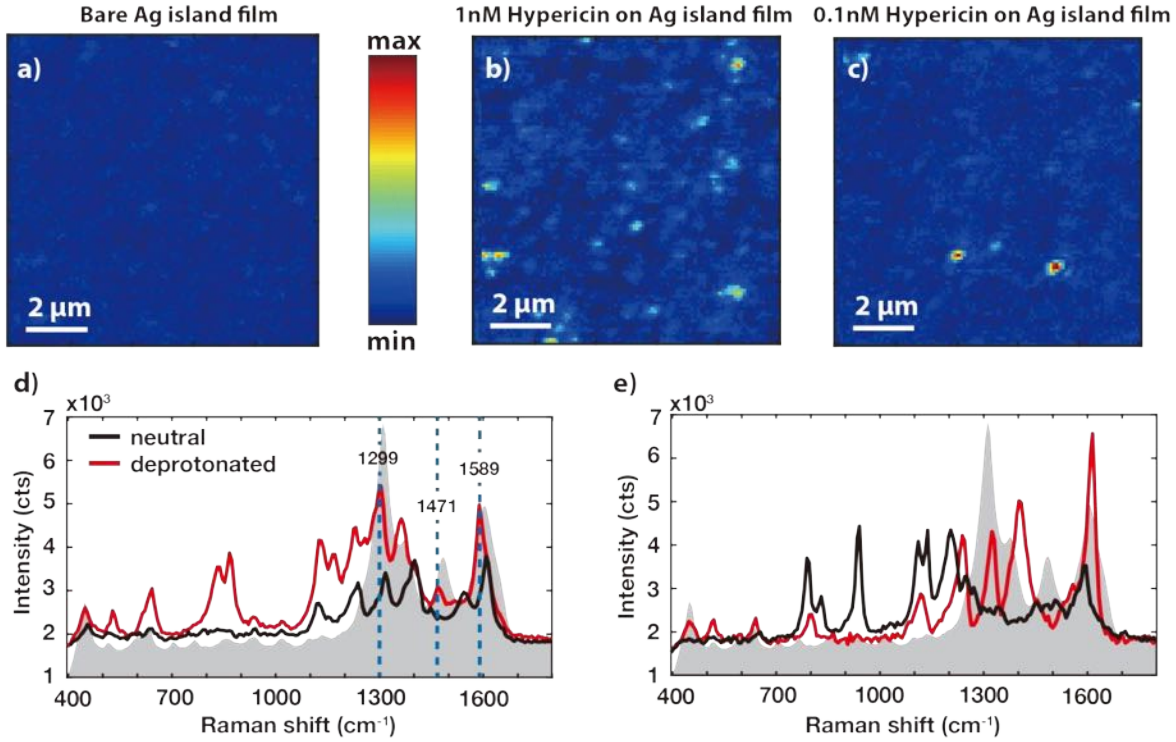


Figure 5-6 Confocal scanning images recorded from a) pure substrates and from substrates doped with b) 1.0 nM and c) 0.1 nM hypericin solution d) SM SERS spectra excited at $\lambda_{ex}$ = 530 nm. The black and red line show SM SERS spectra of the neutral and deprotonated form of hypericin, respectively. The blue dashed lines mark prominent peaks of deprotonated hypericin. The grey area displays the ensemble resonance Raman spectrum. e) SERS spectrum of the same neutral hypericin SM acquired at different times.

The SERS spectra presented in Figure 5-6 e) are obtained from the same SM at different times and strong intensity variations can be observed between the spectra shown in red and black. The strongest intensity differences occur between 1400-1600 $cm^{-1}$ and the peaks in this spectral region have an in plane character, which makes them very sensitive to the orientation of the SM on the nanoparticle surface[106,117]. The near field of the silver nanoparticle is oriented perpendicular to its surface and Raman modes with a Raman tensor component parallel to the field are enhanced[172]. This makes it possible to determine the orientation of the SM relative to the surface. The changes in the SERS intensities indicate that the same SM is first oriented almost parallel (black line in Figure 5-6 e)) and reorients perpendicularly or almost perpendicularly to the nanoparticle surface (red line in Figure 5-6 e)). Such a perpendicular orientation of hypericin on the silver surface is also proposed in ensemble SERS studies[117,118]. Altogether, SM SERS experiments show that both neutral and deprotonated form

of hypericin are adsorbed on the silver surface, and indicate that hypericin can reorient on the silver surface.

## 5.4 Strong coupling of J-aggregated TDBC molecule and microcavity

A J-aggregate can be treated as a chain of many dye molecules linked together that acts like a giant quantum oscillator[75,173,174]. A large oscillator strength of the molecule is helpful to achieve strong coupling. Strong coupling of molecules to a cavity mode has attracted lots of attention since it can influence light-driven chemical reactions[57], enhance intermolecular energy transfer[54,60], realize room-temperature polariton lasing[61,175] and Bose–Einstein condensation[62,63]. Recent results have been well documented in several reviews[52,53,75,176,177]. This section focuses on the demonstration of strong coupling of J-aggregated dye molecules and a tunable microcavity at room temperature.

TDBC (5,6-dichloro-2-[[5,6-dichloro-1-ethyl-3-(4-sulphobutyl)-benzimidazol-2-ylidene]-propenyl]-1-ethyl-3-(4-sulphobutyl)-benzimidazolium hydroxide, sodium salt, inner salt, FEW Chemicals)) is a cyanine dye that undergoes self-organization when dissolved in water to form J-aggregates. The absorption (black line) and the fluorescence (red line) spectra of TDBC are shown in Figure 5-7 with its molecular structure depicted in the insert. The spectrum is measured by spin-coating a TDBC/PVA film on top of a glass coverslip. Two different domains in the absorption spectrum can be observed, i.e. the absorption of the monomers between 450 nm and 550 nm and the sharp absorption of the J-aggregates with the maximum at 586 nm. The fluorescence spectrum is collected with excitation at 530 nm. The emission maximum is slightly red-shifted to the absorption maximum with a small Stokes shift of ~4 nm to 590 nm. Note the emission peak around 536 nm (according to the fluorescence spectrum excited at 488 nm, not shown here) that arises from the monomers vanishes if measured in solution. Therefore, aqueous solution of TDBC is filled in the microcavity (for details see Section 3.2).

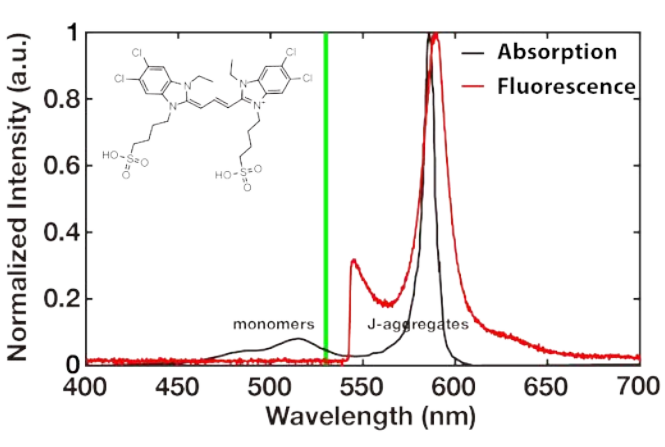


Figure 5-7 Absorption (black line) and fluorescence (red line) spectra of TDBC in PVA matrix spin coated on a glass coverslip. The excitation wavelength is 530 nm and is indicated by the green line. Insert depicts the chemical structure of TDBC.

Figure 5-8 a)-b) present transmission and reflection spectra recorded at the same spatial position for different cavity thickness. Clear anticrossing around molecular exciton (yellow dash line) indicates that the cavity mode (red dash lines) and the molecules are coherently coupled. The dispersions are fitted with the two-level model introduced in Section 2.3.3, where the molecular exciton and the cavity mode are plotted with yellow and red lines in Figure 5-8, respectively. The hybrid polaritons are plotted in blue (UP) and green (LP). The Rabi splitting extracted from transmission and reflection spectra in both cases is 150 meV.

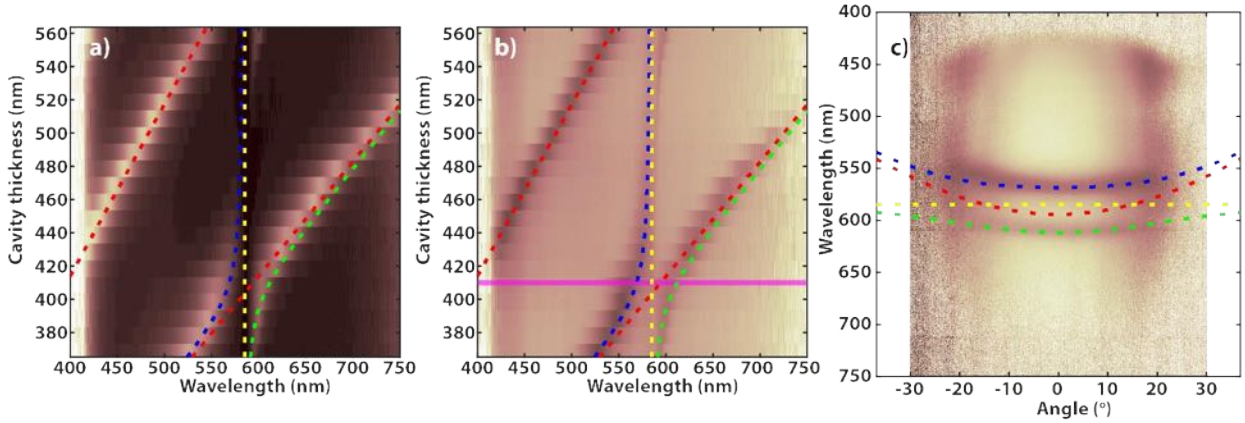


Figure 5-8 a) Transmission and b) reflection spectra recorded at the same position for different cavity thickness. c) Angle dependent dispersion of reflection. The spectra are recorded for cavity thickness $d = 410\ nm$ as indicated by the magenta line in b). Simulation results presented by dash lines. Molecular exciton, cavity mode, UP and LP are plotted with yellow, red, blue and green lines, respectively.

The angle dependent dispersion of the reflection in Figure 5-8 c) is recorded at for cavity thickness at $d = 410\ nm$ as indicated by the magenta line in Figure 5-8 b). The angle dependent dispersion

also shows a Rabi splitting of $\hbar\Omega$ =150 meV. We note the maximum collection angle $\theta_{max}$~$20^o$ is limited by the numerical aperture of the lens in front of the spectrometer (see Section 3.3 for details).

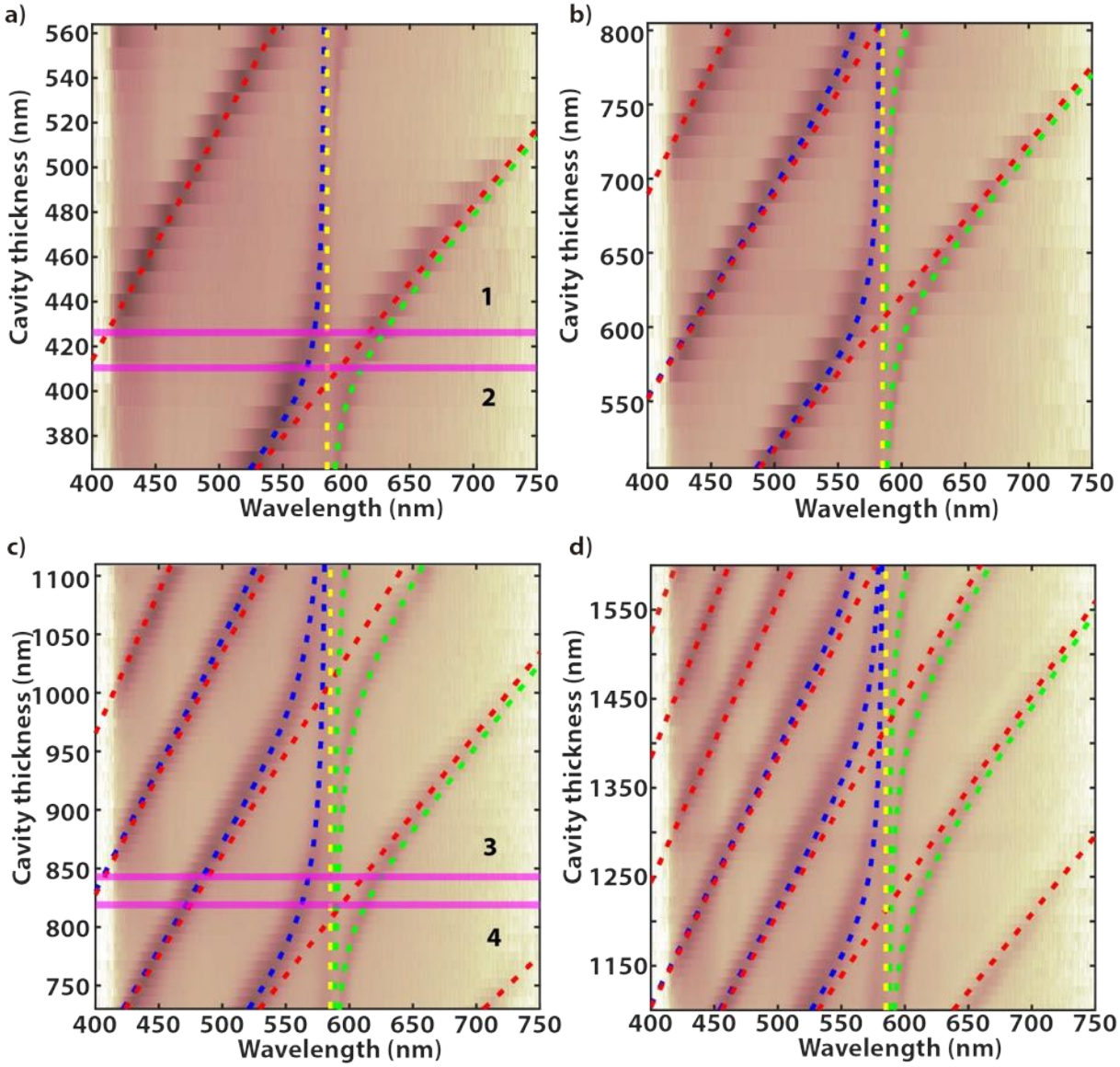


Figure 5-9 Panels a)-d) reflection spectra recorded at different cavity thickness. Simulation results presented by dash lines with the same colours as in Figure 5-8. Numbered magenta lines indicate the cavity thickness for angle resolved fluorescence measurement in Figure 5-10.

Figure 5-9 shows reflection spectra when the cavity thickness is varied from 365 nm to 1600 nm. Eight anticrossings are observed for different orders of the cavity mode. Fitting results with $\hbar\Omega$ =150 meV are plotted with coloured dash lines similar as in Figure 5-8. Interestingly, the Rabi splitting is almost the same when the cavity thickness increases, because the mode splitting is proportional to the density of the emitters in the cavity, i.e. $\Omega = \sqrt{A} \propto \sqrt{\frac{N}{V}}$. The density of aqueous

solution of TDBC inside the cavity is constant, and thus the mode splitting is the same. If the damping cannot be ignored ($\gamma \neq 0$), for example, when the cavity thickness is large enough, the splitting will start to decrease according to equation (2.75).

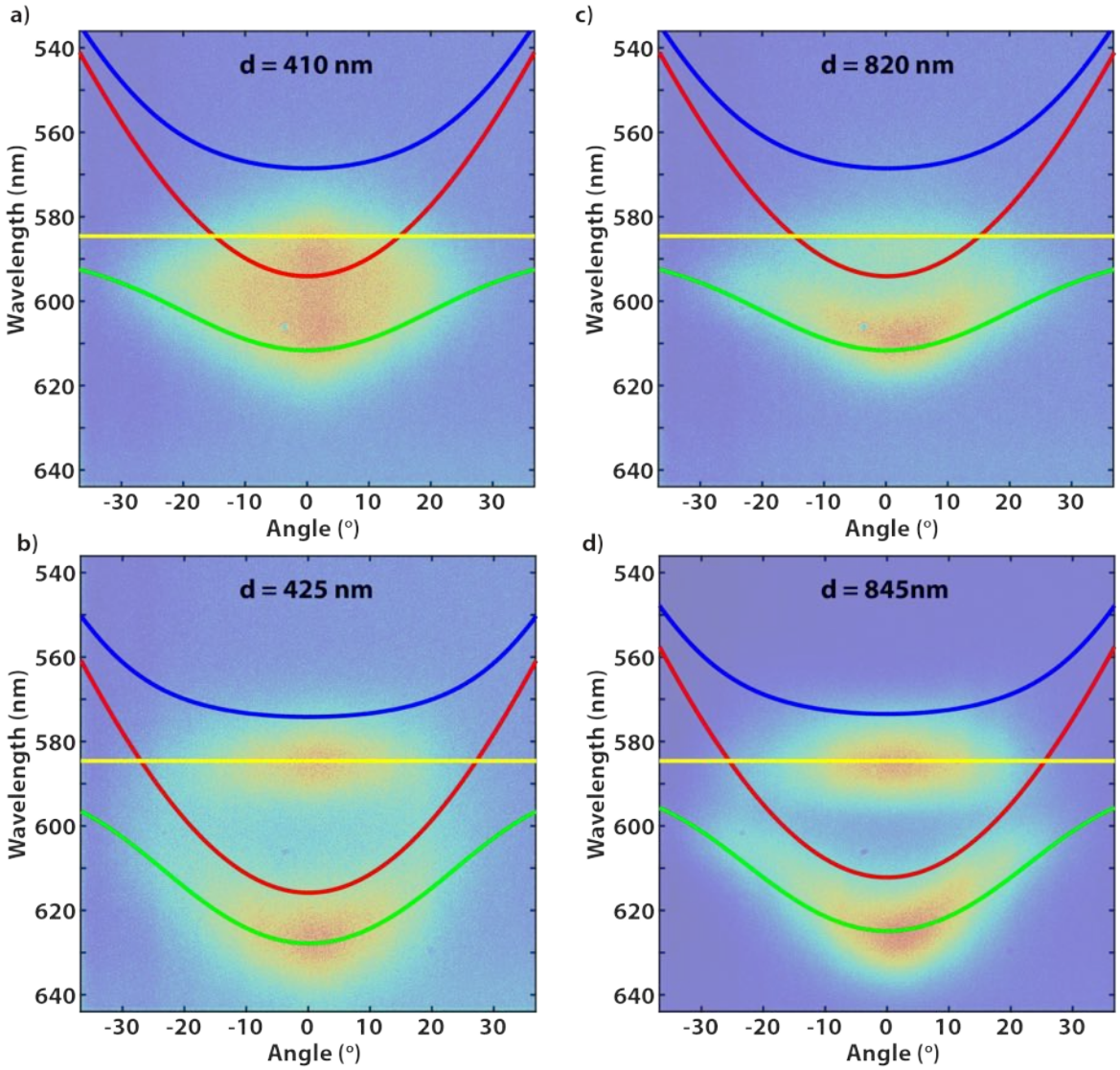


Figure 5-10 a)-d) Angle resolved fluorescence recorded at different cavity thickness indicated by numbered magenta lines 1-4 in Figure 5-9. Coloured lines are simulation results with parameters adapted from Figure 5-9 a)

We also recorded angle resolved fluorescence spectra. Figure 5-10 a)-d) show fluorescence spectra recorded at cavity thickness $d = 410\ nm, 425\ nm, 820\ nm$ and $845\ nm$ as indicated in Figure 5-9 with numbered magenta lines (1-4). Coloured lines are fitting results with parameters adapted from Figure 5-9 a). When the cavity mode and the molecular exciton are on resonance ($\Delta \sim 0$, Figure 5-10 a), magenta line 1 in Figure 5-9 a)), the fluorescence spectra are broadened and only the LP is observed. If the detuning is larger ($\Delta > 0$, Figure 5-10 b), magenta line 2 in Figure 5-9 a)), except for

LP which still follows the simulations, a leakage mode emitted by uncoupled molecules[173,174,178] is clearly observed. Same results are observed in Figure 5-10 c)-d) for larger cavity thicknesses.

The reason for the missing of the UP in fluorescence spectra is already discussed in literature[173,179,180]. In a strongly coupled organic molecule/microcavity system, a blue-detuned laser excites the molecule to an excited vibronic state of the S1 state, which is followed by a fast relaxation (shorter than 1 ps) to the lowest vibronic state. Excited excitons are accumulating due to bottleneck effect[56,174,181], so called exciton reservoir. They can be scattered to the LP and the UP in a timescale of 100 ps, which is much longer than the polariton lifetime (~50 fs). Therefore, they cannot lead to stable polariton population. The molecule in the UP can either emit (~100 fs) or are scattered back to exciton reservoir (~50 fs). These processes deplete the UP and thus no emission can be observed. The lifetime of the LP is shorter than the scattering process from exciton reservoir, and therefore emission from the LP is 'frozen'. In addition, excitons can relax directly to the ground state and emit photons (~300 ps), which forms the leakage mode.

## 5.5 Conclusions

The interaction of the optical modes in a tunable microcavity and enclosed molecules has been explored from the weak coupling to the strong coupling regime. In the weak coupling regime, the variation of the spontaneous emission rate of hypericin has been predicted. The absolute quantum yield of the molecule can be measured by varying the cavity thickness. The frequency dependent Purcell factor and angle dependent detection function are combined to evaluate the emission spectra. In addition, single molecule surface enhanced Raman spectroscopy (SM SERS) of hypericin is achieved profiting from the large near-field enhancement of the plasmonic nanostructures. Both the neutral and deprotonated form of hypericin can be distinguished by specific bands, and spectral variations of the same molecule over time indicate that hypericin can reorient on the silver surface.

Finally, strong coupling of J-aggregates to a microcavity is demonstrated. Both transmission and reflection spectra show the same anticrossing and the Rabi splitting are proportional to the molecule concentration. Angle resolved measurement indicate that fluorescence emission is only observed from the LP. The absence of UP is explained by the fast relaxation rate of the polariton

.

# Chapter 6 Plasmonic nanocavity multiplexing towards enhanced fluorescence of single photosystem II

Upon resonance excitation, metallic nanoparticles create highly localized electric fields leading to dramatic enhancement[70,126,182–184] of the molecular fluorescence. As discussed in Chapter 2, the enhancement is determined together by the excitation enhancement and emission enhancement via the increase of emission rate and the quantum yield[76]. Although lots of research was focused on achieving the largest fluorescence enhancement[182,183,185–188], complicated fabrication processes and limited quantity of 'hot spots' makes these approaches not suitable for general applications. A simple and low cost way of fabricating large area of nanoparticles, which makes use of a fast annealing process[78] have proven efficient to create substrates with a high density of 'hot spots' and have been successfully applied for the detection of single fluorescent photosystem complexes[189] and single molecule SERS[132].

Following the strategy presented in section 3.4, we introduce a fast optimization strategy based on plasmonic nanocavities towards maximum enhancement of single photosystem II fluorescence. Optimal enhancement is obtained from a plasmonic sample with continuously increasing particle radii, which is prepared in a one-step evaporation.

## 6.1 Photosystem II

Photosystem II (PS II) is a pigment-protein complexes for photosynthesis, in which pigments (mainly chlorophyll a (Chl a) and carotenoid molecules) are bound by a protein scaffold[190,191]. It widely exists in the thylakoid membranes of cyanobacteria, algae and higher plants. PS II functions as light harvesting unit that oxidize water and reduce plastoquinone[192–194]. The crystal structure of PS II reveals a dimension per unit of around 10 nm including two main proteins subunit CP43 and CP47[195,196], in which antenna molecules Chl a are bound. Chl a absorbs light and the excitation energy is transferred to the reaction centre (core pigment named P680 according to the absorption maximum), leading to charge separation (Figure 6-1 a)).

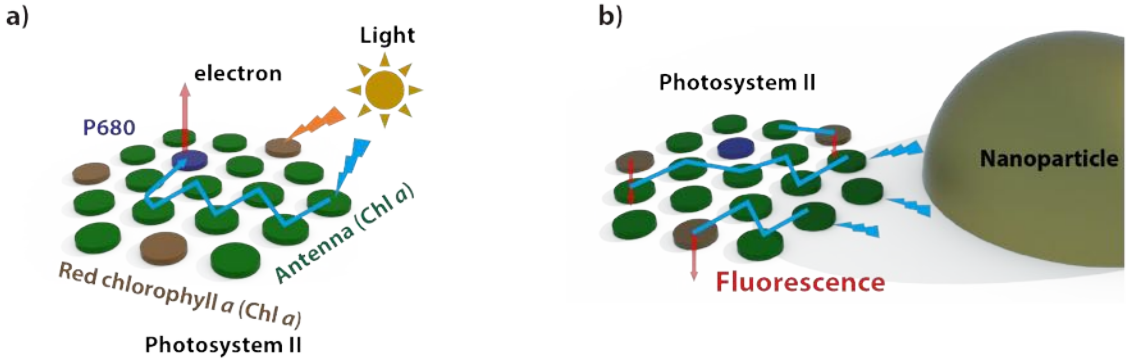


Figure 6-1 Diagram of photon absorption and exciton transfer pathways at room temperature a) and at low temperature with plasmonic nanoparticle in the vicinity b).

Absorption and emission spectra of PS II in solution are depicted in Figure 6-2. Pronounced peaks in absorption spectrum around 435 nm and 674 nm are due to Chl a, and the side band between 450 nm and 530 nm can be attributed to carotenoids[190].

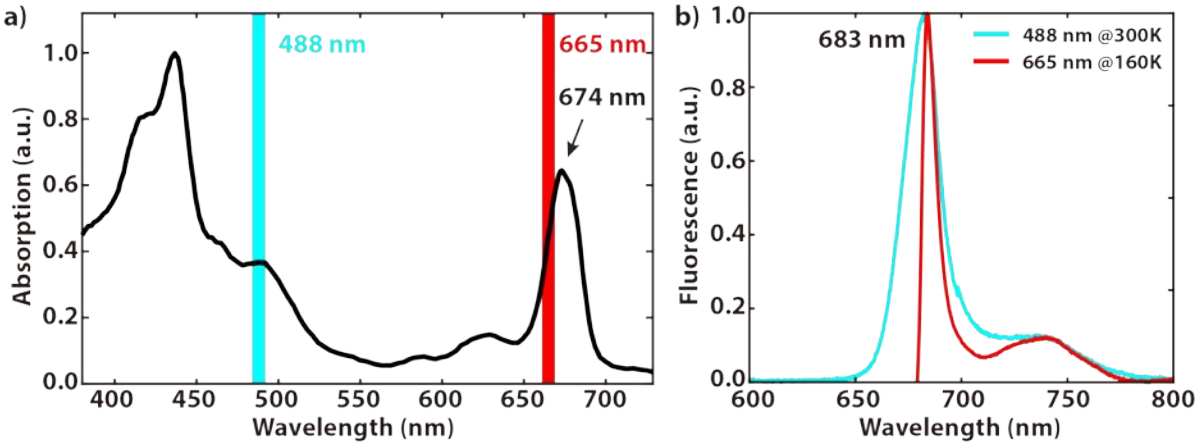


Figure 6-2 Absorption a) and emission b) spectra of PS II in solution. Excitation wavelengths of $\lambda_{ex}$=488 nm and 665 nm are indicated with cyan and red lines in a), and the emission spectra are plot in b) with the respective colours.

Fluorescence spectrum with the main emission peak at 683 nm and the weak side band around 740 nm is dominated by the emission of Chl a[190] when excited with $\lambda_{ex}$=488 nm laser radiation at room temperature, even though the carotenoids are mainly excited. When the temperature decreases to 160 K and the excitation laser tunes to 665 nm, the emission peaks stay the same. Noting that the fluorescence spectrum is partially blocked by the long-pass filter.

The emission efficiency of PS II is extremely low at room temperature. However, at low temperature or when excess excitation energy is present, more excitation energy is released through red Chl a as fluorescence[197,198] (Figure 6-1 b)), which can be used to analyse the energy transfer in

multichromophore systems. Plasmonic nanoparticles have been successfully used to enhance the emission of photosystem I[31,126,198], and enhancement factor up to 441-fold was reported for single photosystem I.

## 6.2 Non-uniform gold nanoparticles

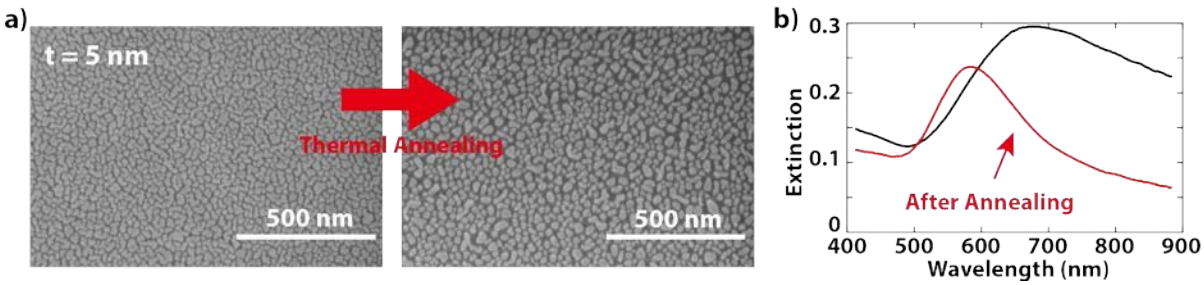


Figure 6-3 a) SEM images of 5 nm gold film before and after thermal annealing. b) Corresponding extinction spectra before and after annealing.

Figure 6-3 a) shows the SEM images of a 5 nm gold film evaporated on a glass coverslip before and after thermal annealing. A clear difference can be seen in the extinction spectra (Figure 6-3 b)) due to the transition from a large irregular island film to a more regular film with smaller nanoparticles. The extinction spectrum is related to the size and the shape of nanoparticles[199], decreasing the nanoparticle size leads to a blue shift of the LSPR. Size reduction also reduces scattering, hence narrowing extinction spectrum. Although the influence of the shape can be complex, a narrower size distribution will normally result in a sharper extinction spectrum[78].

The examples of non-uniform samples depicted in Figure 6-4 were prepared according to the description in Section 3.4. The size of the nanoparticles increases as the thickness $t$ of the evaporated gold film increase. When $t \leq 6\,nm$, the SEM images are analysed with the software "ImageJ" and the radius distribution of the nanoparticles in the insert of Figure 6-4 a)-c) are fitted by Gaussian functions with $R = 8.6\,nm$, $18.4\,nm$ and $20.5\,nm$, respectively. With increasing film thickness the surface convergence (the ratio of the area covered by gold with respect to the full area of the SEM image) decreases at first and starts to increase after an island film is obtained ($t \geq 7\,nm$).

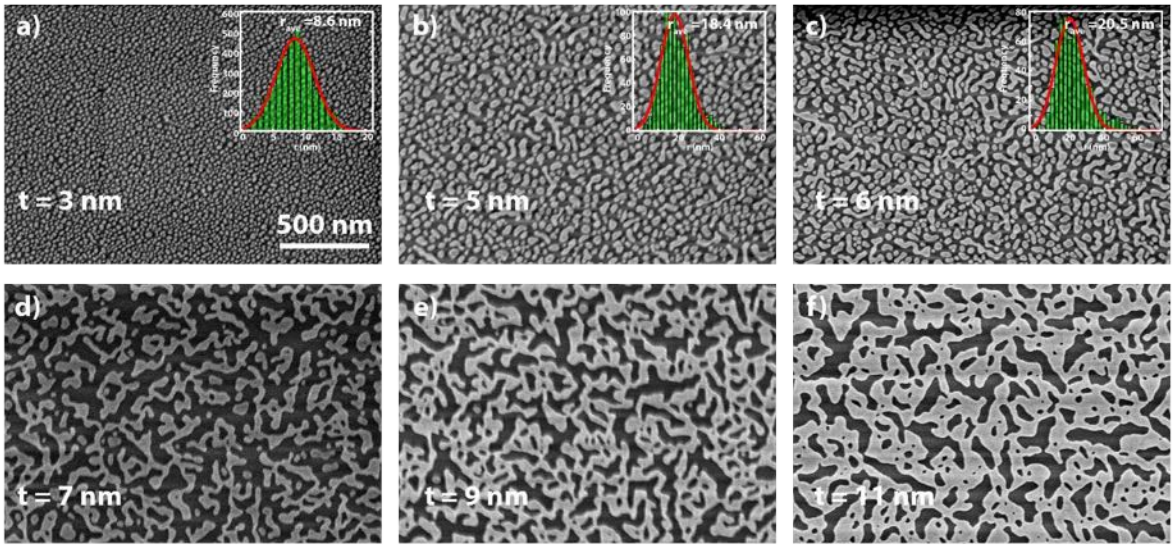


Figure 6-4 SEM images of non-uniform gold sample prepared from a one-step evaporation. Inserts in a)-c) are the radius distributions of the nanoparticles.

## 6.3 Fluorescence enhancement of photosystem II

The extinction spectra of the non-uniform sample are presented in Figure 6-5 a). The surface plasmon resonance is red-shifted from 560 nm for $t = 3\ nm$ to 580 nm for $t = 11\ nm$ according to Lorentzian fitting. The second peak around 750 nm is due to more elongated particle shapes for large thickness.

Monomer PS II from *Thermosynechococcus elongates* (*T. elongates*)[1] are purified following the procedure described in [200]. PS II is diluted to $10^{-9}$ M and 3 µL of the diluted solution is sandwiched between the gold nanoparticles and a bare coverslip (two bare coverslips for reference measurement). The sample is transferred into the cryostat (T = 160 K) using a fast sample exchange construction[201].

[1] PS II samples are provided by Prof. Athina Zouni, Humboldt-Universität zu Berlin.

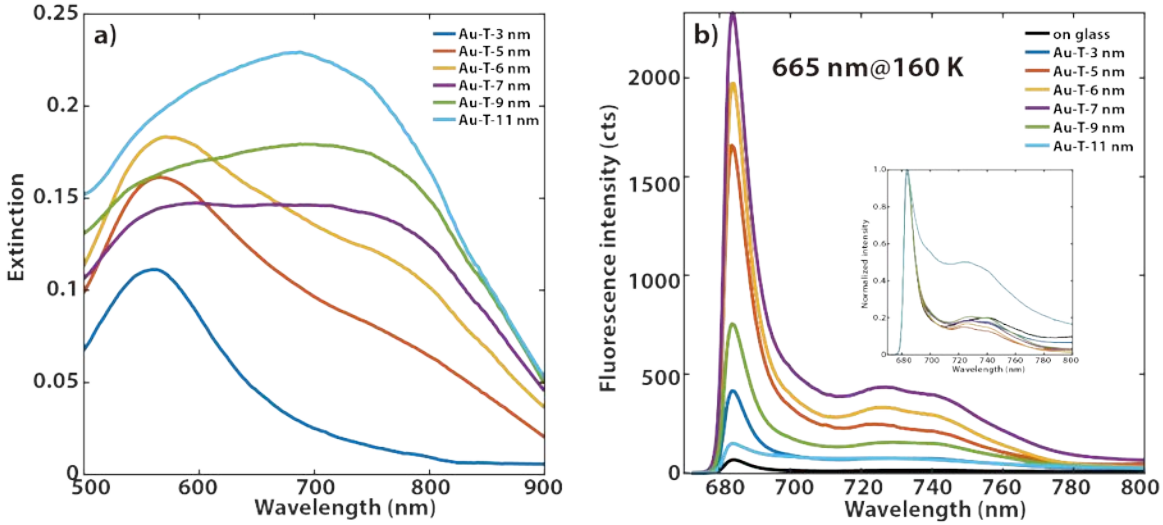


Figure 6-5 a) Extinction spectra of the non-uniform sample measured at different thickness. b) Corresponding averaged PS II fluorescence spectra. The insert shows the normalized spectra.

A 665 nm excitation laser wavelength is used for the emission enhancement measurements and the fluorescence is collected after a 680 nm long-pass filter. For each film thickness, 22 different positions in 100 μm×100 μm range are randomly selected, where 100 fluorescence spectra (one second per spectrum) are acquired for each position. Dramatic intensity differences can be observed from the averaged spectra for different thickness presented in Figure 6-5 b). Normalized spectra have the same line shape for the emission peak at 683 nm as shown in the insert of Figure 6-5 b), while the ratio of the side band around 740 nm varies slightly for difference thickness. The most significant difference appears for thickness $t = 11\ nm$, which leads to the strongest scattering.

Fluorescence enhancement is analysed by integrating in the full spectrum range then divided by the integration of the spectrum on glass. The distributions of the enhancement for each position are shown in Figure 6-6. The average enhancement (green diamonds) is plotted in Figure 6-6 b) together with box plots showing the variation.

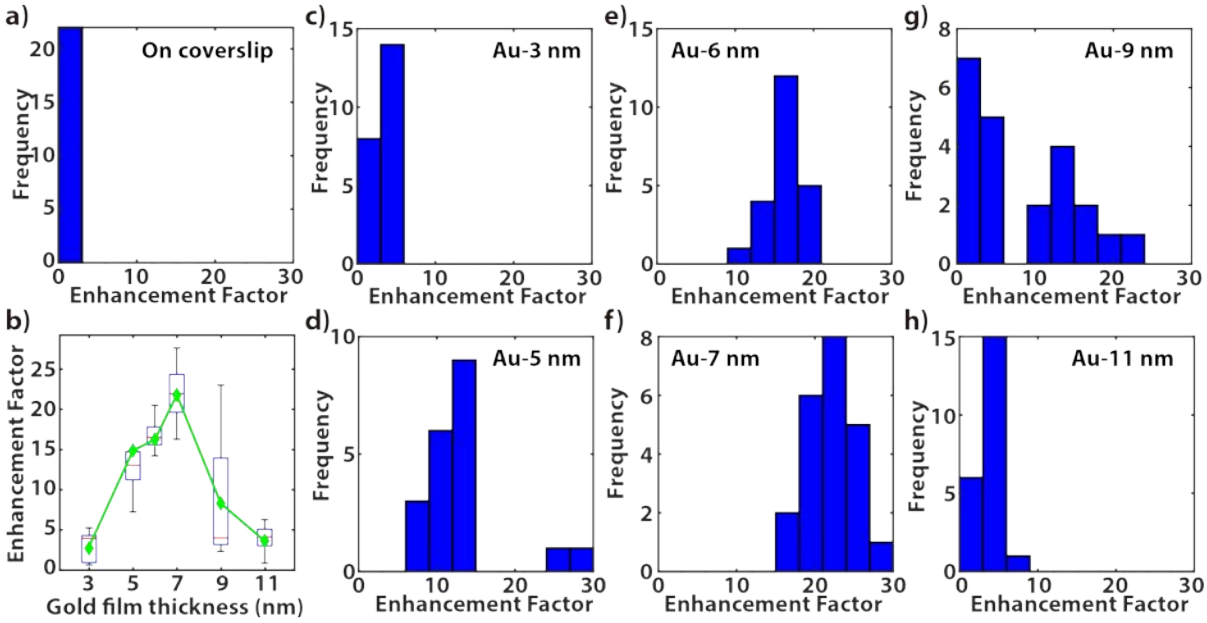


Figure 6-6 a) Distribution of fluorescence enhancement factor on bare coverslip. b) Average enhancement and box plots of the enhancement factors on gold nanoparticles. The whiskers indicate the minimum and maximum of the data points, the red line represents the middle value of the dataset, and the first and third quartiles are indicated by the lower and the upper boundary of the box. c)-h) Distributions of the fluorescence enhancement factor on gold nanoparticles.

The small variation of the fluorescence enhancement factor is due to the homogeneous particle distribution for a film thickness of $t \leq 6\,nm$. However, the island film ($t \geq 7\,nm$) result in large variation. The maximum enhancement factor $F_{max} = 21.8$ is achieved for $t = 7\,nm$ because the broad extinction spectrum of the island film is nearly on resonance with the excitation laser, which provides large excitation enhancement and the small surface convergence that leads to larger gaps between nanoparticles which is suitable for PS II that has a dimension around 10 nm to be located between two nanoparticles, i.e. in the nanocavities. For normal incident of a linear polarized laser radiation, the mode coupling between the nanoparticles can give rise to larger field enhancement for the emitter placed in between than single nanoparticle (see Section 2.3.4).

In order to confirm that the observed fluorescence mainly arises from single PS II, we decrease the temperature and measured spectra at a film thickness $t = 7\,nm$ for different temperatures as presented in Figure 6-7. The FWHM of the peaks is significantly reduced when temperature decreases to 86 K (Figure 6-7 d)). The emission peak is red-shifted to ~695 nm for temperature T=44 K and clear blinking and spectral diffusion[124,197,202] indicate that the emission originates from a single PS II. When the temperature decreases to 5 K, sharp zero-phonon lines appear as shown in Figure 6-7 c) and d). The complex behavior[203–205] is attributed to two distinct pools of chlorophylls, F685 and F695

(red Chls), where the numbers refer to the emission peak wavelength. At 5 K, the excitation energy transfer from red Chls to reaction centre is frozen out. Consequently, zero-phonon lines appear at both wavelengths. Excitation energy transfer of F695 is still frozen for T≤77 K, while F685 is quenched due to energy transfer followed with electron transfer. At higher temperature, the emission maximum moves to shorter wavelengths due to increased thermal population of higher exciton states.

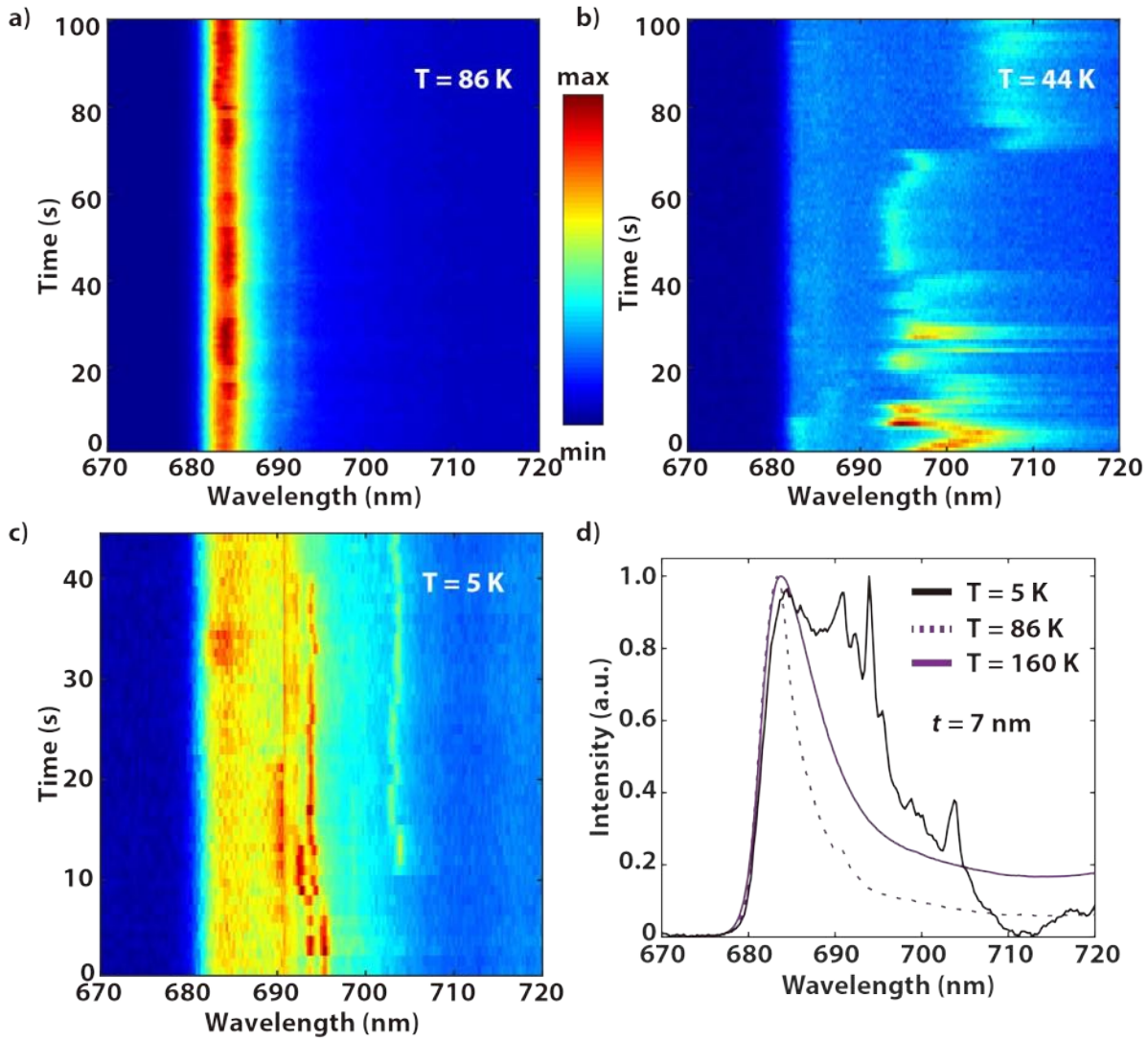


Figure 6-7 Sequence of fluorescence emission spectra recorded continuously at a) T = 86 K, b) T = 44 K and c) T = 5 K. The acquisition time of the single spectrum is 1 s. d) Averaged spectra recorded at different temperature.

In summary, we fabricated large-scale tunable nanoparticle substrates for plasmon enhanced fluorescence spectroscopy in a simple one-step evaporation process followed by thermal annealing. The size of the nanoparticles, as well as the extinction spectra is tuned due to the difference of the evaporated film thickness. The maximum emission enhancement factor $F_{max} = 21.8$ is achieved at film a thickness $t = 7\ nm$ because of the excitation enhancement and mode coupling effect. In the

fluorescence spectra of single PS II zero-phonon lines are observed at the optimal film thickness at low temperature. A similar multiplexing strategy can be quickly applied with different materials and for other molecules to achieve the optimal enhancement of fluorescence spectra or SERS.

# Chapter 7 Summary and Outlook

This thesis covers the characterization of a single hypericin molecule and the interaction of cavity mode with molecules. Hypericin is a natural drug in *Hypericum perforatum* (St. John's wort) that is very promising in modern medicine. It serves as a single quantum emitter that exhibits fascinating structural dynamics, such as dissociation, conformation and tautomerism, and enables the observation of single molecule dynamics and the impacts of a photonic environment.

In this work, the usefulness of confocal scanning microscopy, combined with higher order laser modes in characterizing the transient dynamics of single molecules, was demonstrated. The three-dimensional spatial orientation of a single molecule was determined, and the tautomeric state observed in a specific scanning image can be identified unambiguously. Extra efforts have been devoted to analysing the temporal properties of the dynamics by using photon autocorrelation, which reveals the distinct influence of the local environment and deuteration effect on molecules. Having established the photon autocorrelation model, a natural extension of this work is to study the impact of the broader context of the microscopic environment on the molecular probe. In addition, as hypericin is a promising drug in antidepressive, antitumor and antiviral treatment due to its phototoxic reaction, a deeper understanding of the mechanism can be obtained while exploring the photoinduced dynamics.

The coupling between microcavity/nanocavity and a quantum emitter was presented. The radiative rate is modulated by tuning the cavity resonance; hence, the local density of states is changed. Numerical simulations, which associate zero-point fluctuations with the electrical field entering the microcavity, allow to fully reproduce the local density of states and, therefore, predict the modification of the spontaneous emission. The same method is readily expanded to measure the radiative and nonradiative decay rates, as well as the intrinsic quantum yield.

Indeed, there are experimental investigations by placing the emitter close to a dielectric interface,[206] a movable silver mirror,[207] a metallic nanocavity[208,209] and a tunable microcavity.[210,211] In the latter case, the cavity length in the half-lambda range is required to achieve a tight confinement and thus the large modulation of the radiative rate. It is indeed effective when single emitter[29] is observed. However, the z-direction position dependent of the confinement and the directional emission pattern at this cavity length is undesired since they complicate the origin of the detected signal for an ensemble measurement and reduce the intensity of the collected signal for limited numerical aperture.

To overcome these restrictions, numerical simulations must include the field distribution inside the cavity, and special care should be given to the excitation field distribution in the focal spot.[168,169]

Strong coupling was achieved between a microcavity and J-aggregates in this work. A major task will be to explore the limitation in the coupling strength of a low Q-factor microcavity and single quantum emitter. An effective method is to extend the measurement to low temperature,[68] which decreases the dephasing of the emitter. Although distinct Rabi splitting might be hard to be observed, there are different aspects to be discussed. It has been pointed out in Section 4.4 that the tautomerization dynamics of hypericin are altered by the local environment. It should be possible to discuss the impact of the photonic environment with the use of the microcavity.

Large near field enhancement and high density of 'hot spots' of the annealing samples have enabled the creation of plasmonic nanocavities, which allow measuring single molecule SERS. Furthermore, a fast optimization strategy towards optimal fluorescence enhancement was validated with PS II. Coupled mode theory presented in Section 2.3.4 reveals the importance of the radius of the nanoparticles and the gap distance between them in order to achieve maximum emission enhancement. However, the thermal annealing sample is not a good representation of two coupled nanoparticles since both the radius of the nanoparticles and the gap distance change while tuning, and there is non-negligible coupling from other nanoparticles in the vicinity. Some methods are promising to validate the theory, namely DNA origami,[208,212–214] nanoimprint lithography,[188] and tip-enhanced microscopy with cylindrical vector beams,[215,216] to name a few. The latter is equipped with an apex tip, which is precisely driven by a shear-force tuning fork approaching the bottom substrate. A radially polarized laser beam is intensively polarized longitudinal (out-of-plane) in the focus. Therefore, a perfect representation of the description in Section 2.3.4 is achieved with intensive coupling between the tip and the bottom nanoparticle. The local field enhancement can be characterized by acquiring the fluorescence spectra and SERS simultaneously.

An apparent constraint of the coupled mode theory is that the nonlocal effect[102,217–219] and quantum effects,[186,220–222] such as electron tunnelling and screening, are not involved. However, these become significant when the gap is smaller than 5 nm. The nonlocal effect can be appropriately included[217] in a classical model, while quantum plasmonics[186] correction can be adopted if necessary. For a realistic implementation, e.g., an apex tip approaching the nanoparticle, extensive numerical simulations are necessary to reveal the features of the emission enhancement. It is still an open task to answer the limit of plasmonic-induced emission enhancement.

# References


(1) Stokes, G. G. XXX. On the Change of Refrangibility of Light. *Philosophical transactions of the Royal Society of London* **1852**, No. 142, 463–562.

(2) Stokes, G. G. XVI. On the Change of Refrangibility of Light.—No. II. *Philosophical Transactions of the Royal Society of London* **1853**, No. 143, 385–396.

(3) Lewis, G. N.; Kasha, M. Phosphorescence and the Triplet State. *Journal of the American Chemical Society* **1944**, *66* (12), 2100–2116.

(4) Lakowicz, J. R.; Masters, B. R. *Principles of Fluorescence Spectroscopy*; 2008; Vol. 13.

(5) Valeur, B.; Berberan-Santos, M. N. *Molecular Fluorescence: Principles and Applications*; John Wiley & Sons, 2012.

(6) O'Connor, D. V.; Phillips, D. *Time-Correlated Single Photon Counting*; Academic Press: London ; Orlando, 1984.

(7) Becker, W. *Advanced Time-Correlated Single Photon Counting Techniques*; Springer series in chemical physics; Springer: Berlin ; New York, 2005.

(8) *Advanced Time-Correlated Single Photon Counting Applications*; Becker, W., Ed.; Springer Series in Chemical Physics; Springer International Publishing: Cham, 2015; Vol. 111. https://doi.org/10.1007/978-3-319-14929-5.

(9) Niehörster, T.; Löschberger, A.; Gregor, I.; Krämer, B.; Rahn, H.-J.; Patting, M.; Koberling, F.; Enderlein, J.; Sauer, M. Multi-Target Spectrally Resolved Fluorescence Lifetime Imaging Microscopy. *Nature Methods* **2016**, *13* (3), 257–262. https://doi.org/10.1038/nmeth.3740.

(10) Bastiaens, P. I.; Squire, A. Fluorescence Lifetime Imaging Microscopy: Spatial Resolution of Biochemical Processes in the Cell. *Trends in cell biology* **1999**, *9* (2), 48–52.

(11) Gadella Jr, T. W.; Jovin, T. M.; Clegg, R. M. Fluorescence Lifetime Imaging Microscopy (FLIM): Spatial Resolution of Microstructures on the Nanosecond Time Scale. *Biophysical chemistry* **1993**, *48* (2), 221–239.

(12) Magde, D.; Elson, E.; Webb, W. W. Thermodynamic Fluctuations in a Reacting System—Measurement by Fluorescence Correlation Spectroscopy. *Physical review letters* **1972**, *29* (11), 705.

(13) Rigler, R.; Elson, E. S. *Fluorescence Correlation Spectroscopy: Theory and Applications*; Schäfer, F. P., Toennies, J. P., Zinth, W., Series Eds.; Springer Series in Chemical Physics; Springer Berlin Heidelberg: Berlin, Heidelberg, 2001; Vol. 65. https://doi.org/10.1007/978-3-642-59542-4.

(14) Krichevsky, O.; Bonnet, G. Fluorescence Correlation Spectroscopy: The Technique and Its Applications. *Reports on Progress in Physics* **2002**, *65* (2), 251.

(15) Böhmer, M.; Wahl, M.; Rahn, H.-J.; Erdmann, R.; Enderlein, J. Time-Resolved Fluorescence Correlation Spectroscopy. *Chemical Physics Letters* **2002**, *353* (5), 439–445. https://doi.org/10.1016/S0009-2614(02)00044-1.

(16) Ghosh, A.; Isbaner, S.; Veiga-Gutiérrez, M.; Gregor, I.; Enderlein, J.; Karedla, N. Quantifying Microsecond Transition Times Using Fluorescence Lifetime Correlation Spectroscopy. *J. Phys. Chem. Lett.* **2017**, *8* (24), 6022–6028. https://doi.org/10.1021/acs.jpclett.7b02707.

(17) Ghosh, A.; Karedla, N.; Thiele, J. C.; Gregor, I.; Enderlein, J. Fluorescence Lifetime Correlation Spectroscopy: Basics and Applications. *Methods* **2018**, *140–141*, 32–39. https://doi.org/10.1016/j.ymeth.2018.02.009.

(18) Basché, T.; Moerner, W. E.; Orrit, M.; Talon, H. Photon Antibunching in the Fluorescence of a Single Dye Molecule Trapped in a Solid. *Physical review letters* **1992**, *69* (10), 1516.

(19) Schedlbauer, J.; Wilhelm, P.; Grabenhorst, L.; Federl, M. E.; Lalkens, B.; Hinderer, F.; Scherf, U.; Höger, S.; Tinnefeld, P.; Bange, S.; Vogelsang, J.; Lupton, J. M. Ultrafast Single-Molecule Fluorescence Measured by Femtosecond Double-Pulse Excitation Photon Antibunching. *Nano Lett.* **2020**, acs.nanolett.9b04354. https://doi.org/10.1021/acs.nanolett.9b04354.

(20) Press, D.; Götzinger, S.; Reitzenstein, S.; Hofmann, C.; Löffler, A.; Kamp, M.; Forchel, A.; Yamamoto, Y. Photon Antibunching from a Single Quantum-Dot-Microcavity System in the Strong Coupling Regime. *Phys. Rev. Lett.* **2007**, *98* (11), 117402. https://doi.org/10.1103/PhysRevLett.98.117402.

(21) Orrit, M.; Bernard, J. Single Pentacene Molecules Detected by Fluorescence Excitation in a P-Terphenyl Crystal. *Phys. Rev. Lett.* **1990**, *65* (21), 2716–2719. https://doi.org/10.1103/PhysRevLett.65.2716.

(22) Moerner, W. E.; Kador, L. Optical Detection and Spectroscopy of Single Molecules in a Solid. *Phys. Rev. Lett.* **1989**, *62* (21), 2535–2538. https://doi.org/10.1103/PhysRevLett.62.2535.

(23) Kapusta, P.; Wahl, M.; Erdmann (eds.), R. *Advanced Photon Counting: Applications, Methods, Instrumentation*, 1st ed.; Springer Series on Fluorescence 15; Springer International Publishing, 2015.

(24) Eid, J. S.; Müller, J. D.; Gratton, E. Data Acquisition Card for Fluctuation Correlation Spectroscopy Allowing Full Access to the Detected Photon Sequence. *Review of Scientific Instruments* **2000**, *71* (2), 361–368. https://doi.org/10.1063/1.1150208.

(25) Felekyan, S.; Kühnemuth, R.; Kudryavtsev, V.; Sandhagen, C.; Becker, W.; Seidel, C. a. M. Full Correlation from Picoseconds to Seconds by Time-Resolved and Time-Correlated Single Photon Detection. *Review of Scientific Instruments* **2005**, *76* (8), 083104. https://doi.org/10.1063/1.1946088.

(26) Magatti, D.; Ferri, F. 25 Ns Software Correlator for Photon and Fluorescence Correlation Spectroscopy. *Review of Scientific Instruments* **2003**, *74* (2), 1135–1144. https://doi.org/10.1063/1.1525876.

(27) Enderlein, J.; Gregor, I. Using Fluorescence Lifetime for Discriminating Detector Afterpulsing in Fluorescence-Correlation Spectroscopy. *Review of Scientific Instruments* **2005**, *76* (3), 033102. https://doi.org/10.1063/1.1863399.

(28) Gaertner, S.; Weinfurter, H.; Kurtsiefer, C. Fast and Compact Multichannel Photon Coincidence Unit for Quantum Information Processing. *Review of Scientific Instruments* **2005**, *76* (12), 123108. https://doi.org/10.1063/1.2149007.

(29) Chizhik, A. I.; Chizhik, A. M.; Khoptyar, D.; Bär, S.; Meixner, A. J.; Enderlein, J. Probing the Radiative Transition of Single Molecules with a Tunable Microresonator. *Nano Lett.* **2011**, *11* (4), 1700–1703. https://doi.org/10.1021/nl200215v.

(30) Piatkowski, L.; Schanbacher, C.; Wackenhut, F.; Jamrozik, A.; Meixner, A. J.; Waluk, J. Nature of Large Temporal Fluctuations of Hydrogen Transfer Rates in Single Molecules. *J. Phys. Chem. Lett.* **2018**, *9* (6), 1211–1215. https://doi.org/10.1021/acs.jpclett.8b00299.

(31) Ashraf, I.; Konrad, A.; Lokstein, H.; Skandary, S.; Metzger, M.; Djouda, J. M.; Maurer, T.; Adam, P. M.; Meixner, A. J.; Brecht, M. Temperature Dependence of Metal-Enhanced Fluorescence of Photosystem I from Thermosynechococcus Elongatus. *Nanoscale* **2017**, *9* (12), 4196–4204. https://doi.org/10.1039/C6NR08762K.

(32) Rust, M. J.; Bates, M.; Zhuang, X. Sub-Diffraction-Limit Imaging by Stochastic Optical Reconstruction Microscopy (STORM). *Nature methods* **2006**, *3* (10), 793–796.

(33) Betzig, E.; Patterson, G. H.; Sougrat, R.; Lindwasser, O. W.; Olenych, S.; Bonifacino, J. S.; Davidson, M. W.; Lippincott-Schwartz, J.; Hess, H. F. Imaging Intracellular Fluorescent Proteins at Nanometer Resolution. *Science* **2006**, *313* (5793), 1642–1645.

(34) Hess, S. T.; Girirajan, T. P.; Mason, M. D. Ultra-High Resolution Imaging by Fluorescence Photoactivation Localization Microscopy. *Biophysical journal* **2006**, *91* (11), 4258–4272.

(35) Dickson, R. M.; Norris, D. J.; Tzeng, Y.-L.; Moerner, W. E. Three-Dimensional Imaging of Single Molecules Solvated in Pores of Poly(Acrylamide) Gels. *Science* **1996**, *274* (5289), 966–968. https://doi.org/10.1126/science.274.5289.966.

(36) Lu, H. P.; Xie, X. S. Single-Molecule Spectral Fluctuations at Room Temperature. *Nature* **1997**, *385* (6612), 143–146. https://doi.org/10.1038/385143a0.

(37) Veerman, J. A.; Garcia-Parajo, M. F.; Kuipers, L.; van Hulst, N. F. Time-Varying Triplet State Lifetimes of Single Molecules. *Phys. Rev. Lett.* **1999**, *83* (11), 2155–2158. https://doi.org/10.1103/PhysRevLett.83.2155.

(38) Wennmalm, S.; Edman, L.; Rigler, R. Conformational Fluctuations in Single DNA Molecules. *Proceedings of the National Academy of Sciences* **1997**, *94* (20), 10641–10646. https://doi.org/10.1073/pnas.94.20.10641.

(39) Dew, S. K.; Stepanova (auth.), M.; Stepanova, M.; Dew (eds.), S. *Nanofabrication: Techniques and Principles*, 1st ed.; Springer-Verlag Wien, 2012.

(40) Tseng, A. A.; Tseng, A. A. *Nanofabrication: Fundamentals and Applications*; World Scientific Publishing Company, 2008.

(41) Mohammad, M. A.; Muhammad, M.; Dew, S. K.; Stepanova, M. Fundamentals of Electron Beam Exposure and Development. In *Nanofabrication*; Stepanova, M., Dew, S., Eds.; Springer Vienna: Vienna, 2012; pp 11–41. https://doi.org/10.1007/978-3-7091-0424-8_2.

(42) Meystre, P.; Sargent, M. *Elements of Quantum Optics*, 4th ed.; Springer, 2007.

(43) Scully, M. O.; Zubairy, M. S. *Quantum Optics*; Cambridge University Press, 1997.

(44) Walther, H.; Varcoe, B. T. H.; Englert, B.-G.; Becker, T. Cavity Quantum Electrodynamics. *Rep. Prog. Phys.* **2006**, *69* (5), 1325–1382. https://doi.org/10.1088/0034-4885/69/5/R02.

(45) Purcell, E. M. Spontaneous Emission Probabilities at Radio Frequencies. *Phys. Rev.* **1946**, *69*, 681–681.

(46) Reithmaier, J. P.; Sęk, G.; Löffler, A.; Hofmann, C.; Kuhn, S.; Reitzenstein, S.; Keldysh, L. V.; Kulakovskii, V. D.; Reinecke, T. L.; Forchel, A. Strong Coupling in a Single Quantum Dot–Semiconductor Microcavity System. *Nature* **2004**, *432* (7014), 197. https://doi.org/10.1038/nature02969.

(47) Sun, L.; Chen, Z.; Ren, Q.; Yu, K.; Bai, L.; Zhou, W.; Xiong, H.; Zhu, Z. Q.; Shen, X. Direct Observation of Whispering Gallery Mode Polaritons and Their Dispersion in a ZnO Tapered Microcavity. *Phys. Rev. Lett.* **2008**, *100* (15), 156403. https://doi.org/10.1103/PhysRevLett.100.156403.

(48) Yoshie, T.; Scherer, A.; Hendrickson, J.; Khitrova, G.; Gibbs, H. M.; Rupper, G.; Ell, C.; Shchekin, O. B.; Deppe, D. G. Vacuum Rabi Splitting with a Single Quantum Dot in a Photonic Crystal Nanocavity. *Nature* **2004**, *432* (7014), 200–203. https://doi.org/10.1038/nature03119.

(49) Thompson, R. J.; Rempe, G.; Kimble, H. J. Observation of Normal-Mode Splitting for an Atom in an Optical Cavity. *Physical Review Letters* **1992**, *68* (8), 1132–1135. https://doi.org/10.1103/PhysRevLett.68.1132.

(50) Deng, H.; Haug, H.; Yamamoto, Y. Exciton-Polariton Bose-Einstein Condensation. *Rev. Mod. Phys.* **2010**, *82* (2), 1489–1537. https://doi.org/10.1103/RevModPhys.82.1489.

(51) Byrnes, T.; Kim, N. Y.; Yamamoto, Y. Exciton–Polariton Condensates. *Nature Phys* **2014**, *10* (11), 803–813. https://doi.org/10.1038/nphys3143.

(52) Dovzhenko, D. S.; Ryabchuk, S. V.; Rakovich, Y.; Nabiev, I. Light–Matter Interaction in the Strong Coupling Regime: Configurations, Conditions, Applications. *Nanoscale* **2018**. https://doi.org/10.1039/C7NR06917K.

(53) Hertzog, M.; Wang, M.; Mony, J.; Börjesson, K. Strong Light–Matter Interactions: A New Direction within Chemistry. *Chem. Soc. Rev.* **2019**, *48* (3), 937–961. https://doi.org/10.1039/C8CS00193F.

(54) Coles, D. M.; Somaschi, N.; Michetti, P.; Clark, C.; Lagoudakis, P. G.; Savvidis, P. G.; Lidzey, D. G. Polariton-Mediated Energy Transfer between Organic Dyes in a Strongly Coupled Optical Microcavity. *Nature Mater* **2014**, *13* (7), 712–719. https://doi.org/10.1038/nmat3950.

(55) Coles, D. M.; Michetti, P.; Clark, C.; Tsoi, W. C.; Adawi, A. M.; Kim, J.-S.; Lidzey, D. G. Vibrationally Assisted Polariton-Relaxation Processes in Strongly Coupled Organic-Semiconductor Microcavities. *Advanced Functional Materials* **2011**, *21* (19), 3691–3696. https://doi.org/10.1002/adfm.201100756.

(56) Coles, D. M.; Grant, R. T.; Lidzey, D. G.; Clark, C.; Lagoudakis, P. G. Imaging the Polariton Relaxation Bottleneck in Strongly Coupled Organic Semiconductor Microcavities. *Phys. Rev. B* **2013**, *88* (12), 121303. https://doi.org/10.1103/PhysRevB.88.121303.

(57) Schwartz, T.; Hutchison, J. A.; Genet, C.; Ebbesen, T. W. Reversible Switching of Ultrastrong Light-Molecule Coupling. *Physical Review Letters* **2011**, *106* (19). https://doi.org/10.1103/PhysRevLett.106.196405.

(58) Shalabney, A.; George, J.; Hutchison, J.; Pupillo, G.; Genet, C.; Ebbesen, T. W. Coherent Coupling of Molecular Resonators with a Microcavity Mode. *Nature Communications* **2015**, *6*, 5981. https://doi.org/10.1038/ncomms6981.

(59) Thomas, A.; George, J.; Shalabney, A.; Dryzhakov, M.; Varma, S. J.; Moran, J.; Chervy, T.; Zhong, X.; Devaux, E.; Genet, C.; Hutchison, J. A.; Ebbesen, T. W. Ground-State Chemical Reactivity under Vibrational Coupling to the Vacuum Electromagnetic Field. *Angewandte Chemie International Edition* **2016**, *55* (38), 11462–11466. https://doi.org/10.1002/anie.201605504.

(60) Zhong, X.; Chervy, T.; Zhang, L.; Thomas, A.; George, J.; Genet, C.; Hutchison, J. A.; Ebbesen, T. W. Energy Transfer between Spatially Separated Entangled Molecules. *Angewandte Chemie International Edition* **2017**, *56* (31), 9034–9038. https://doi.org/10.1002/anie.201703539.

(61) Kéna-Cohen, S.; Forrest, S. R. Room-Temperature Polariton Lasing in an Organic Single-Crystal Microcavity. *Nature Photon* **2010**, *4* (6), 371–375. https://doi.org/10.1038/nphoton.2010.86.

(62) Lerario, G.; Fieramosca, A.; Barachati, F.; Ballarini, D.; Daskalakis, K. S.; Dominici, L.; De Giorgi, M.; Maier, S. A.; Gigli, G.; Kéna-Cohen, S.; Sanvitto, D. Room-Temperature Superfluidity in a Polariton Condensate. *Nature Phys* **2017**, *13* (9), 837–841. https://doi.org/10.1038/nphys4147.

(63) Plumhof, J. D.; Stöferle, T.; Mai, L.; Scherf, U.; Mahrt, R. F. Room-Temperature Bose–Einstein Condensation of Cavity Exciton–Polaritons in a Polymer. *Nature Materials* **2014**, *13* (3), 247–252. https://doi.org/10.1038/nmat3825.

(64) Chizhik, A.; Schleifenbaum, F.; Gutbrod, R.; Chizhik, A.; Khoptyar, D.; Meixner, A. J.; Enderlein, J. Tuning the Fluorescence Emission Spectra of a Single Molecule with a Variable Optical Subwavelength Metal Microcavity. *Phys. Rev. Lett.* **2009**, *102* (7), 073002. https://doi.org/10.1103/PhysRevLett.102.073002.

(65) Steiner, M.; Schleifenbaum, F.; Stupperich, C.; Virgilio Failla, A.; Hartschuh, A.; Meixner, A. J. Microcavity-Controlled Single-Molecule Fluorescence. *ChemPhysChem* **2005**, *6* (10), 2190–2196. https://doi.org/10.1002/cphc.200500108.

(66) Wang, D.; Kelkar, H.; Martin-Cano, D.; Utikal, T.; Götzinger, S.; Sandoghdar, V. Coherent Coupling of a Single Molecule to a Scanning Fabry-Perot Microcavity. *Physical Review X* **2017**, *7* (2). https://doi.org/10.1103/PhysRevX.7.021014.

(67) Konrad, A.; Metzger, M.; Kern, A. M.; Brecht, M.; Meixner, A. J. Controlling the Dynamics of Förster Resonance Energy Transfer inside a Tunable Sub-Wavelength Fabry–Pérot-Resonator. *Nanoscale* **2015**, *7* (22), 10204–10209.

(68) Wang, D.; Kelkar, H.; Martin-Cano, D.; Rattenbacher, D.; Shkarin, A.; Utikal, T.; Götzinger, S.; Sandoghdar, V. Turning a Molecule into a Coherent Two-Level Quantum System. *Nat. Phys.* **2019**, *15* (5), 483–489. https://doi.org/10.1038/s41567-019-0436-5.

(69) Chikkaraddy, R.; Nijs, B. de; Benz, F.; Barrow, S. J.; Scherman, O. A.; Rosta, E.; Demetriadou, A.; Fox, P.; Hess, O.; Baumberg, J. J. Single-Molecule Strong Coupling at Room Temperature in Plasmonic Nanocavities. *Nature* **2016**, *535* (7610), 127. https://doi.org/10.1038/nature17974.

(70) Maier, S. A. *Plasmonics: Fundamentals and Applications*; Springer Science & Business Media, 2007.

(71) Hayashi, S.; Okamoto, T. Plasmonics: Visit the Past to Know the Future. *Journal of Physics D: Applied Physics* **2012**, *45* (43), 433001. https://doi.org/10.1088/0022-3727/45/43/433001.

(72) Le Ru, E.; Etchegoin, P. *Principles of Surface-Enhanced Raman Spectroscopy: And Related Plasmonic Effects*; Elsevier, 2008.

(73) Kneipp, K.; Wang, Y.; Kneipp, H.; Perelman, L. T.; Itzkan, I.; Dasari, R. R.; Feld, M. S. Single Molecule Detection Using Surface-Enhanced Raman Scattering (SERS). *Physical review letters* **1997**, *78* (9), 1667.

(74) Nie, S. Probing Single Molecules and Single Nanoparticles by Surface-Enhanced Raman Scattering. *Science* **1997**, *275* (5303), 1102–1106. https://doi.org/10.1126/science.275.5303.1102.

(75) Törmä, P.; Barnes, W. L. Strong Coupling between Surface Plasmon Polaritons and Emitters: A Review. *Reports on Progress in Physics* **2015**, *78* (1), 013901.

(76) Anger, P.; Bharadwaj, P.; Novotny, L. Enhancement and Quenching of Single-Molecule Fluorescence. *Phys. Rev. Lett.* **2006**, *96* (11), 113002. https://doi.org/10.1103/PhysRevLett.96.113002.

(77) Kühn, S.; Håkanson, U.; Rogobete, L.; Sandoghdar, V. Enhancement of Single-Molecule Fluorescence Using a Gold Nanoparticle as an Optical Nanoantenna. *Physical Review Letters* **2006**, *97* (1), 017402. https://doi.org/10.1103/PhysRevLett.97.017402.

(78) Khaywah, M. Y.; Jradi, S.; Louarn, G.; Lacroute, Y.; Toufaily, J.; Hamieh, T.; Adam, P.-M. Ultrastable, Uniform, Reproducible, and Highly Sensitive Bimetallic Nanoparticles as Reliable Large Scale SERS Substrates. *J. Phys. Chem. C* **2015**, *119* (46), 26091–26100. https://doi.org/10.1021/acs.jpcc.5b04914.

(79) Jia, K.; Bijeon, J.-L.; Adam, P.-M.; Ionescu, R. E. Large Scale Fabrication of Gold Nano-Structured Substrates Via High Temperature Annealing and Their Direct Use for the LSPR Detection of Atrazine. *Plasmonics* **2013**, *8* (1), 143–151. https://doi.org/10.1007/s11468-012-9444-3.

(80) Novotny, L.; Hecht, B. *Principles of Nano-Optics*, 2nd ed.; Cambridge University Press, 2012.

(81) Züchner, T.; Failla, A. V.; Meixner, A. J. Light Microscopy with Doughnut Modes: A Concept to Detect, Characterize, and Manipulate Individual Nanoobjects. *Angewandte Chemie International Edition* **2011**, *50* (23), 5274–5293. https://doi.org/10.1002/anie.201005845.

(82) Novotny, L.; Beversluis, M. R.; Youngworth, K. S.; Brown, T. G. Longitudinal Field Modes Probed by Single Molecules. *Phys. Rev. Lett.* **2001**, *86* (23), 5251–5254. https://doi.org/10.1103/PhysRevLett.86.5251.

(83) Dorn, R.; Quabis, S.; Leuchs, G. Sharper Focus for a Radially Polarized Light Beam. *Phys. Rev. Lett.* **2003**, *91* (23), 233901. https://doi.org/10.1103/PhysRevLett.91.233901.

(84) Wackenhut, F.; Virgilio Failla, A.; Züchner, T.; Steiner, M.; Meixner, A. J. Three-Dimensional Photoluminescence Mapping and Emission Anisotropy of Single Gold Nanorods. *Applied Physics Letters* **2012**, *100* (26), 263102. https://doi.org/10.1063/1.4729152.

(85) Carmichael, H. J.; Walls, D. F. Proposal for the Measurement of the Resonant Stark Effect by Photon Correlation Techniques. *Journal of Physics B: Atomic and Molecular Physics* **1976**, *9* (4), L43.

(86) Kitson, S. C.; Jonsson, P.; Rarity, J. G.; Tapster, P. R. Intensity Fluctuation Spectroscopy of Small Numbers of Dye Molecules in a Microcavity. *Physical Review A* **1998**, *58* (1), 620–627. https://doi.org/10.1103/PhysRevA.58.620.

(87) Brown, R. H.; Twiss, R. Q. Correlation between Photons in Two Coherent Beams of Light. *Nature* **1956**, *177* (4497), 27–29. https://doi.org/10.1038/177027a0.

(88) Marian, C. M. Spin–Orbit Coupling and Intersystem Crossing in Molecules. *WIREs Computational Molecular Science* **2012**, *2* (2), 187–203. https://doi.org/10.1002/wcms.83.

(89) Raman, C. V.; Krishnan, K. S. The Negative Absorption of Radiation. *Nature* **1928**, *122* (3062), 12–13. https://doi.org/10.1038/122012b0.

(90) Kasha, M. Characterization of Electronic Transitions in Complex Molecules. *Discussions of the Faraday society* **1950**, *9*, 14–19.

(91) Harbecke, B. Coherent and Incoherent Reflection and Transmission of Multilayer Structures. *Appl. Phys. B* **1986**, *39* (3), 165–170. https://doi.org/10.1007/BF00697414.

(92) Mie, G. Beiträge zur Optik trüber Medien, speziell kolloidaler Metallösungen. *Annalen der Physik* **1908**, *330* (3), 377–445. https://doi.org/10.1002/andp.19083300302.

(93) Jackson, J. D. *Classical Electrodynamics*; Wiley, 1999.

(94) Sun, G.; Khurgin, J. B.; Soref, R. A. Practical Enhancement of Photoluminescence by Metal Nanoparticles. *Applied Physics Letters* **2009**, *94* (10), 101103. https://doi.org/10.1063/1.3097025.

(95) Khurgin, J. B.; Sun, G. Enhancement of Optical Properties of Nanoscaled Objects by Metal Nanoparticles. *Journal of the Optical Society of America B* **2009**, *26* (12), B83. https://doi.org/10.1364/JOSAB.26.000B83.

(96) Sun, G.; Khurgin, J. B. Comparative Study of Field Enhancement between Isolated and Coupled Metal Nanoparticles: An Analytical Approach. *Appl. Phys. Lett.* **2010**, *97* (26), 263110. https://doi.org/10.1063/1.3532101.

(97) Maier, S. A. Plasmonic Field Enhancement and SERS in the Effective Mode Volume Picture. *Opt. Express, OE* **2006**, *14* (5), 1957–1964. https://doi.org/10.1364/OE.14.001957.

(98) Griffiths, D. J. *Introduction to Electrodynamics*; Cambridge University Press, 2017.

(99) Sun, G.; Khurgin, J. B. Theory of Optical Emission Enhancement by Coupled Metal Nanoparticles: An Analytical Approach. *Applied Physics Letters* **2011**, *98* (11), 113116. https://doi.org/10.1063/1.3565170.

(100) Sun, G.; Khurgin, J. B.; Bratkovsky, A. Coupled-Mode Theory of Field Enhancement in Complex Metal Nanostructures. *Physical Review B* **2011**, *84* (4). https://doi.org/10.1103/PhysRevB.84.045415.

(101) Haus, H. *Waves and Fields in Optoelectronics*; Prentice-Hall, 1984.

(102) García de Abajo, F. J. Nonlocal Effects in the Plasmons of Strongly Interacting Nanoparticles, Dimers, and Waveguides. *J. Phys. Chem. C* **2008**, *112* (46), 17983–17987. https://doi.org/10.1021/jp807345h.

(103) Li, K.; Stockman, M. I.; Bergman, D. J. Self-Similar Chain of Metal Nanospheres as an Efficient Nanolens. *Phys. Rev. Lett.* **2003**, *91* (22), 227402. https://doi.org/10.1103/PhysRevLett.91.227402.

(104) Stalder, M.; Schadt, M. Linearly Polarized Light with Axial Symmetry Generated by Liquid-Crystal Polarization Converters. *Opt. Lett., OL* **1996**, *21* (23), 1948–1950. https://doi.org/10.1364/OL.21.001948.

(105) Falk, H. From the Photosensitizer Hypericin to the Photoreceptor Stentorin— The Chemistry of Phenanthroperylene Quinones. *Angewandte Chemie International Edition* **1999**, *38* (21), 3116–3136. https://doi.org/10.1002/(SICI)1521-3773(19991102)38:21<3116::AID-ANIE3116>3.0.CO;2-S.

(106) Lajos, G.; Jancura, D.; Miskovsky, P.; García-Ramos, J. V.; Sanchez-Cortes, S. Surface-Enhanced Fluorescence and Raman Scattering Study of Antitumoral Drug Hypericin: An Effect of Aggregation and Self-Spacing Depending on PH. *The Journal of Physical Chemistry C* **2008**, *112* (33), 12974–12980. https://doi.org/10.1021/jp8034117.

(107) Wynn, J. L.; Cotton, T. M. Spectroscopic Properties of Hypericin in Solution and at Surfaces. *The Journal of Physical Chemistry* **1995**, *99* (12), 4317–4323. https://doi.org/10.1021/j100012a063.

(108) Goodman, J. W. *Introduction to Fourier Optics*, 3rd ed.; Roberts and Co., 2005.

(109) Semin, D. J.; Lo, A.; Roark, S. E.; Skodje, R. T.; Rowlen, K. L. Time‐dependent Morphology Changes in Thin Silver Films on Mica: A Scaling Analysis of Atomic Force Microscopy Results. *The Journal of Chemical Physics* **1996**, *105* (13), 5542–5551. https://doi.org/10.1063/1.472375.

(110) Zheng, C. *Nanofabrication: Principles, Capabilities and Limits*; Springer, 2008.

(111) Kubin, A.; Wierrani, F.; Burner, U.; Alth, G.; Grunberger, W. Hypericin - The Facts About a Controversial Agent. *Current Pharmaceutical Design* **2005**, *11* (2), 233–253. https://doi.org/10.2174/1381612053382287.

(112) Agostinis, P.; Vantieghem, A.; Merlevede, W.; de Witte, P. A. M. Hypericin in Cancer Treatment: More Light on the Way. *The International Journal of Biochemistry & Cell Biology* **2002**, *34* (3), 221–241. https://doi.org/10.1016/S1357-2725(01)00126-1.

(113) Davids, L. M.; Kleemann, B.; Kacerovská, D.; Pizinger, K.; Kidson, S. H. Hypericin Phototoxicity Induces Different Modes of Cell Death in Melanoma and Human Skin Cells. *Journal of Photochemistry and Photobiology B: Biology* **2008**, *91* (2–3), 67–76. https://doi.org/10.1016/j.jphotobiol.2008.01.011.

(114) Ritz, R.; Scheidle, C.; Noell, S.; Roser, F.; Schenk, M.; Dietz, K.; Strauss, W. S. In Vitro Comparison of Hypericin and 5-Aminolevulinic Acid-Derived Protoporphyrin IX for Photodynamic Inactivation of Medulloblastoma Cells. *PLoS One* **2012**, *7* (12). https://doi.org/10.1371/journal.pone.0051974.

(115) Ritz, R.; Müller, M.; Weller, M.; Dietz, K.; Kuci, S.; Roser, F.; Tatagiba, M. Hypericin: A Promising Fluorescence Marker for Differentiating between Glioblastoma and Neurons in Vitro. *Int J Oncol* **2005**, *27* (6), 1543–1549. https://doi.org/10.3892/ijo.27.6.1543.

(116) Darmanyan, A. P.; Jenks, W. S.; Eloy, D.; Jardon, P. Quenching of Excited Triplet State Hypericin with Energy Acceptors and Donors and Acceptors of Electrons. *The Journal of Physical Chemistry B* **1999**, *103* (17), 3323–3331. https://doi.org/10.1021/jp984030o.

(117) Jancura, D.; Sánchez-cortés, S.; Kocisova, E.; Tinti, A.; Miskovsky, P.; Bertoluzza, A. Surface-Enhanced Resonance Raman Spectroscopy of Hypericin and Emodin on Silver Colloids: SERRS and NIR FTSERS Study. *Biospectroscopy* **1995**, *1* (4), 265–273. https://doi.org/10.1002/bspy.350010405.

(118) Raser, L. N.; Kolaczkowski, S. V.; Cotton, T. M. Resonance Raman and Surface-Enhanced Resonance Raman Spectroscopy of Hypericin. *Photochemistry and Photobiology* **1992**, *56* (2), 157–162. https://doi.org/10.1111/j.1751-1097.1992.tb02142.x.

(119) Yamazaki, T.; Ohta, N.; Yamazaki, I.; Song, P. S. Excited-State Properties of Hypericin: Electronic Spectra and Fluorescence Decay Kinetics. *The Journal of Physical Chemistry* **1993**, *97* (30), 7870–7875. https://doi.org/10.1021/j100132a013.

(120) English, D. S.; Das, K.; Ashby, K. D.; Park, J.; Petrich, J. W.; Castner, E. W. Confirmation of Excited-State Proton Transfer and Ground-State Heterogeneity in Hypericin by Fluorescence Upconversion. *Journal of the American Chemical Society* **1997**, *119* (48), 11585–11590. https://doi.org/10.1021/ja9721071.

(121) English, D. S.; Zhang, W.; Kraus, G. A.; Petrich, J. W. Excited-State Photophysics of Hypericin and Its Hexamethoxy Analog: Intramolecular Proton Transfer as a Nonradiative Process in Hypericin. *Journal of the American Chemical Society* **1997**, *119* (13), 2980–2986. https://doi.org/10.1021/ja962476h.

(122) Arabei, S. M.; Galaup, J. P.; Jardon, P. Analysis of the Site Selected Fluorescence and the Phosphorescence Spectrum of Hypericin in Ethanol. *Chemical Physics Letters* **1997**, *270* (1–2), 31–36. https://doi.org/10.1016/S0009-2614(97)00338-2.

(123) Angerhofer, A.; Falk, H.; Meyer, J.; Schoppel, G. Lowest Excited Triplet States of Hypericin and Isohypericin. *Journal of Photochemistry and Photobiology B: Biology* **1993**, *20* (2–3), 133–137. https://doi.org/10.1016/1011-1344(93)80142-V.

(124) Brecht, M.; Studier, H.; Radics, V.; Nieder, J. B.; Bittl, R. Spectral Diffusion Induced by Proton Dynamics in Pigment−Protein Complexes. *Journal of the American Chemical Society* **2008**, *130* (51), 17487–17493. https://doi.org/10.1021/ja806216p.

(125) Nieder, J. B.; Brecht, M.; Bittl, R. Dynamic Intracomplex Heterogeneity of Phytochrome. *Journal of the American Chemical Society* **2009**, *131* (1), 69–71. https://doi.org/10.1021/ja8058292.

(126) Nieder, J. B.; Bittl, R.; Brecht, M. Fluorescence Studies into the Effect of Plasmonic Interactions on Protein Function. *Angewandte Chemie International Edition* **2010**, *49* (52), 10217–10220.

(127) Moerner, W. E.; Fromm, D. P. Methods of Single-Molecule Fluorescence Spectroscopy and Microscopy. *Review of Scientific instruments* **2003**, *74* (8), 3597–3619.

(128) Stracke, F.; Blum, C.; Becker, S.; Müllen, K.; Meixner, A. J. Intrinsic Conformer Jumps Observed by Single Molecule Spectroscopy in Real Time. *Chemical Physics Letters* **2000**, *325* (1–3), 196–202. https://doi.org/10.1016/S0009-2614(00)00633-3.

(129) Piwoński, H.; Stupperich, C.; Hartschuh, A.; Sepioł, J.; Meixner, A.; Waluk, J. Imaging of Tautomerism in a Single Molecule. *J. Am. Chem. Soc.* **2005**, *127* (15), 5302–5303. https://doi.org/10.1021/ja043265c.

(130) Chizhik, A. M.; Jäger, R.; Chizhik, A. I.; Bär, S.; Mack, H.-G.; Sackrow, M.; Stanciu, C.; Lyubimtsev, A.; Hanack, M.; Meixner, A. J. Optical Imaging of Excited-State Tautomerization in Single Molecules. *Phys. Chem. Chem. Phys.* **2011**, *13* (5), 1722. https://doi.org/10.1039/c0cp02228d.

(131) Vosgröne, T.; Meixner, A. J. Surface- and Resonance-Enhanced Micro-Raman Spectroscopy of Xanthene Dyes: From the Ensemble to Single Molecules. *ChemPhysChem* **2005**, *6* (1), 154–163. https://doi.org/10.1002/cphc.200400395.

(132) Liu, Q.; Wackenhut, F.; Hauler, O.; Scholz, M.; zur Oven-Krockhaus, S.; Ritz, R.; Adam, P.-M.; Brecht, M.; Meixner, A. J. Hypericin: Single Molecule Spectroscopy of an Active Natural Drug. *J. Phys. Chem. A* **2020**, *124* (12), 2497–2504. https://doi.org/10.1021/acs.jpca.9b11532.

(133) Panzer, O.; Göhde, W.; Fischer, U. C.; Fuchs, H.; Müllen, K. Influence of Oxygen on Single Molecule Blinking. *Advanced Materials* **1998**, *10* (17), 1469–1472. https://doi.org/10.1002/(SICI)1521-4095(199812)10:17<1469::AID-ADMA1469>3.0.CO;2-O.

(134) Zondervan, R.; Kulzer, F.; Orlinskii, S. B.; Orrit, M. Photoblinking of Rhodamine 6G in Poly(Vinyl Alcohol): Radical Dark State Formed through the Triplet. *The Journal of Physical Chemistry A* **2003**, *107* (35), 6770–6776. https://doi.org/10.1021/jp034723r.

(135) Stracke, F.; Blum, C.; Becker, S.; Müllen, K.; Meixner, A. J. Correlation of Emission Intensity and Spectral Diffusion in Room Temperature Single-Molecule Spectroscopy. *ChemPhysChem* **2005**, *6* (7), 1242–1246. https://doi.org/10.1002/cphc.200400436.

(136) Freeman, D.; Frolow, F.; Kapinus, E.; Lavie, D.; Lavie, G.; Meruelo, D.; Mazur, Y. Acidic Properties of Hypericin and Its Octahydroxy Analogue in the Ground and Excited States. *J. Chem. Soc., Chem. Commun.* **1994**, No. 7, 891. https://doi.org/10.1039/c39940000891.

(137) Etzlstorfer, C.; Falk, H.; Müller, N.; Schmitzberger, W.; Wagner, U. G. Tautomerism and Stereochemistry of Hypericin: Force Field, NMR, and X-Ray Crystallographic Investigations. *Monatsh Chem* **1993**, *124* (6), 751–761. https://doi.org/10.1007/BF00817311.

(138) Gillan, M. J. Quantum-Classical Crossover of the Transition Rate in the Damped Double Well. *J. Phys. C: Solid State Phys.* **1987**, *20* (24), 3621–3641. https://doi.org/10.1088/0022-3719/20/24/005.

(139) Chizhik, A. M.; Jäger, R.; Chizhik, A. I.; Bär, S.; Mack, H.-G.; Sackrow, M.; Stanciu, C.; Lyubimtsev, A.; Hanack, M.; Meixner, A. J. Optical Imaging of Excited-State Tautomerization in Single Molecules. *Phys. Chem. Chem. Phys.* **2011**, *13* (5), 1722. https://doi.org/10.1039/c0cp02228d.

(140) Spinicelli, P.; Buil, S.; Quélin, X.; Mahler, B.; Dubertret, B.; Hermier, J.-P. Bright and Grey States in CdSe-CdS Nanocrystals Exhibiting Strongly Reduced Blinking. *Phys. Rev. Lett.* **2009**, *102* (13), 136801. https://doi.org/10.1103/PhysRevLett.102.136801.

(141) Biss, D. P.; Brown, T. G. Cylindrical Vector Beam Focusing through a Dielectric Interface. *Opt. Express* **2001**, *9* (10), 490. https://doi.org/10.1364/OE.9.000490.

(142) Youngworth, K. S.; Brown, T. G. Focusing of High Numerical Aperture Cylindrical-Vector Beams. *Optics Express* **2000**, *7* (2), 77. https://doi.org/10.1364/OE.7.000077.

(143) Cheng, P. L. A Spherical Rotation Coordinate System for the Description of Three-Dimensional Joint Rotations. *Annals of Biomedical Engineering* **2000**, *28* (11), 1381–1392. https://doi.org/10.1114/1.1326030.

(144) Chen, Y.; Müller, J. D.; Ruan, Q.; Gratton, E. Molecular Brightness Characterization of EGFP In Vivo by Fluorescence Fluctuation Spectroscopy. *Biophysical Journal* **2002**, *82* (1), 133–144. https://doi.org/10.1016/S0006-3495(02)75380-0.

(145) Aragón, S. R.; Pecora, R. Fluorescence Correlation Spectroscopy as a Probe of Molecular Dynamics. *The Journal of Chemical Physics* **1976**, *64* (4), 1791–1803. https://doi.org/10.1063/1.432357.

(146) Widengren, J.; Mets, U.; Rigler, R. Fluorescence Correlation Spectroscopy of Triplet States in Solution: A Theoretical and Experimental Study. *J. Phys. Chem.* **1995**, *99* (36), 13368–13379. https://doi.org/10.1021/j100036a009.

(147) König, I.; Zarrine-Afsar, A.; Aznauryan, M.; Soranno, A.; Wunderlich, B.; Dingfelder, F.; Stüber, J. C.; Plückthun, A.; Nettels, D.; Schuler, B. Single-Molecule Spectroscopy of Protein Conformational Dynamics in Live Eukaryotic Cells. *Nature Methods* **2015**, *12* (8), 773–779. https://doi.org/10.1038/nmeth.3475.

(148) Verberk, R.; Orrit, M. Photon Statistics in the Fluorescence of Single Molecules and Nanocrystals: Correlation Functions versus Distributions of on- and off-Times. *The Journal of Chemical Physics* **2003**, *119* (4), 2214–2222. https://doi.org/10.1063/1.1582848.

(149) Verberk, R.; van Oijen, A. M.; Orrit, M. Simple Model for the Power-Law Blinking of Single Semiconductor Nanocrystals. *Phys. Rev. B* **2002**, *66* (23), 233202. https://doi.org/10.1103/PhysRevB.66.233202.

(150) Shlesinger, M. F. Fractal Time in Condensed Matter. *FRACTAL TIME* 22.

(151) Shlesinger, M. F. Electron Scavenging in Glasses. *The Journal of Chemical Physics* **1979**, *70* (11), 4813–4818. https://doi.org/10.1063/1.437370.

(152) Wohland, T.; Rigler, R.; Vogel, H. The Standard Deviation in Fluorescence Correlation Spectroscopy. *Biophysical Journal* **2001**, *80* (6), 2987–2999. https://doi.org/10.1016/S0006-3495(01)76264-9.

(153) Friedrich, J.; Vogel, J.; Windhager, W.; Dörr, F. Deuterium Isotope Effect in the Radiative Triplet Decay of Heavy Atom Substituted Aromatic Molecules. *Zeitschrift für Naturforschung A* **1976**, *31* (1), 61–70. https://doi.org/10.1515/zna-1976-0108.

(154) Watts, R. J.; Strickler, S. J. Deuterium Isotope Effects on the Lifetime of the Phosphorescent Triplet State of Naphthalene. *The Journal of Chemical Physics* **1968**, *49* (9), 3867–3871. https://doi.org/10.1063/1.1670691.

(155) Lin, S. H.; Bersohn, R. Effect of Partial Deuteration and Temperature on Triplet‐State Lifetimes. *The Journal of Chemical Physics* **1968**, *48* (6), 2732–2736. https://doi.org/10.1063/1.1669507.

(156) Ross, S. M. *Stochastic Processes*; Wiley, 1996.

(157) Wasshuber, C. About Single-Electron Devices and Circuits, 1997.

(158) Fehr, M. J.; McCloskey, M. A.; Petrich, J. W. Light-Induced Acidification by the Antiviral Agent Hypericin. *J. Am. Chem. Soc.* **1995**, *117* (6), 1833–1836. https://doi.org/10.1021/ja00111a024.

(159) Michaeli, A.; Regev, A.; Mazur, Y.; Feitelson, J.; Levanon, H. Triplet-State Reactions of Hypericin: Time-Resolved Laser Photolysis and Electron Paramagnetic Resonance Spectroscopy. *The Journal of Physical Chemistry* **1993**, *97* (36), 9154–9160.

(160) Yokoyama, H.; Nishi, K.; Anan, T.; Yamada, H.; Brorson, S. D.; Ippen, E. P. Enhanced Spontaneous Emission from GaAs Quantum Wells in Monolithic Microcavities. *Appl. Phys. Lett.* **1990**, *57* (26), 2814–2816. https://doi.org/10.1063/1.103771.

(161) Suzuki, M.; Yokoyama, H.; Brorson, S. D.; Ippen, E. P. Observation of Spontaneous Emission Lifetime Change of Dye‐containing Langmuir–Blodgett Films in Optical Microcavities. *Appl. Phys. Lett.* **1991**, *58* (10), 998–1000. https://doi.org/10.1063/1.104388.

(162) Vredenberg, A. M.; Hunt, N. E. J.; Schubert, E. F.; Jacobson, D. C.; Poate, J. M.; Zydzik, G. J. Controlled Atomic Spontaneous Emission from Er 3 + in a Transparent Si/ SiO 2 Microcavity. *Phys. Rev. Lett.* **1993**, *71* (4), 517–520. https://doi.org/10.1103/PhysRevLett.71.517.

(163) Santori, C.; Fattal, D.; Vučković, J.; Solomon, G. S.; Yamamoto, Y. Indistinguishable Photons from a Single-Photon Device. *Nature* **2002**, *419* (6907), 594–597. https://doi.org/10.1038/nature01086.

(164) Chizhik, A. I.; Chizhik, A. M.; Kern, A. M.; Schmidt, T.; Potrick, K.; Huisken, F.; Meixner, A. J. Measurement of Vibrational Modes in Single SiO 2 Nanoparticles Using a Tunable Metal Resonator with Optical Subwavelength Dimensions. *Phys. Rev. Lett.* **2012**, *109* (22), 223902. https://doi.org/10.1103/PhysRevLett.109.223902.

(165) Faraon, A.; Barclay, P. E.; Santori, C.; Fu, K.-M. C.; Beausoleil, R. G. Resonant Enhancement of the Zero-Phonon Emission from a Colour Centre in a Diamond Cavity. *Nature Photon* **2011**, *5* (5), 301–305. https://doi.org/10.1038/nphoton.2011.52.

(166) Kaupp, H.; Hümmer, T.; Mader, M.; Schlederer, B.; Benedikter, J.; Haeusser, P.; Chang, H.-C.; Fedder, H.; Hänsch, T. W.; Hunger, D. Purcell-Enhanced Single-Photon Emission from Nitrogen-Vacancy Centers Coupled to a Tunable Microcavity. *Phys. Rev. Applied* **2016**, *6* (5), 054010. https://doi.org/10.1103/PhysRevApplied.6.054010.

(167) Bjork, G. On the Spontaneous Lifetime Change in an Ideal Planar Microcavity-Transition from a Mode Continuum to Quantized Modes. *IEEE journal of quantum electronics* **1994**, *30* (10), 2314–2318.

(168) Khoptyar, D.; Gutbrod, R.; Chizhik, A.; Enderlein, J.; Schleifenbaum, F.; Steiner, M.; Meixner, A. J. Tight Focusing of Laser Beams in a λ/2-Microcavity. *Optics Express* **2008**, *16* (13), 9907. https://doi.org/10.1364/OE.16.009907.

(169) Chizhik, A. I.; Gregor, I.; Schleifenbaum, F.; Müller, C. B.; Röling, C.; Meixner, A. J.; Enderlein, J. Electrodynamic Coupling of Electric Dipole Emitters to a Fluctuating Mode Density within a Nanocavity. *Phys. Rev. Lett.* **2012**, *108* (16), 163002. https://doi.org/10.1103/PhysRevLett.108.163002.

(170) Falk, H.; Meyer, J. On the Homo- and Heteroassociation of Hypericin. *Monatsh Chem* **1994**, *125* (6–7), 753–762. https://doi.org/10.1007/BF01277637.

(171) Miškovský, P.; Jancura, D.; Sánchez-Cortés, S.; Kočišová, E.; Chinsky, L. Antiretrovirally Active Drug Hypericin Binds the IIA Subdomain of Human Serum Albumin: Resonance Raman and Surface-Enhanced Raman Spectroscopy Study. *Journal of the American Chemical Society* **1998**, *120* (25), 6374–6379. https://doi.org/10.1021/ja974233a.

(172) Creighton, J. A. Surface Raman Electromagnetic Enhancement Factors for Molecules at the Surface of Small Isolated Metal Spheres: The Determination of Adsorbate Orientation from Sers Relative Intensities. *Surface Science* **1983**, *124* (1), 209–219. https://doi.org/10.1016/0039-6028(83)90345-X.

(173) Michetti, P.; La Rocca, G. C. Simulation of J-Aggregate Microcavity Photoluminescence. *Phys. Rev. B* **2008**, *77* (19), 195301. https://doi.org/10.1103/PhysRevB.77.195301.

(174) Michetti, P.; La Rocca, G. C. Exciton-Phonon Scattering and Photoexcitation Dynamics in $J$-Aggregate Microcavities. *Phys. Rev. B* **2009**, *79* (3), 035325. https://doi.org/10.1103/PhysRevB.79.035325.

(175) Kim, S.; Zhang, B.; Wang, Z.; Fischer, J.; Brodbeck, S.; Kamp, M.; Schneider, C.; Höfling, S.; Deng, H. Coherent Polariton Laser. *Phys. Rev. X* **2016**, *6* (1), 011026. https://doi.org/10.1103/PhysRevX.6.011026.

(176) Frisk Kockum, A.; Miranowicz, A.; De Liberato, S.; Savasta, S.; Nori, F. Ultrastrong Coupling between Light and Matter. *Nat Rev Phys* **2019**, *1* (1), 19–40. https://doi.org/10.1038/s42254-018-0006-2.

(177) Forn-Díaz, P.; Lamata, L.; Rico, E.; Kono, J.; Solano, E. Ultrastrong Coupling Regimes of Light-Matter Interaction. *Rev. Mod. Phys.* **2019**, *91* (2), 025005. https://doi.org/10.1103/RevModPhys.91.025005.

(178) Lidzey, D. G.; Fox, A. M.; Rahn, M. D.; Skolnick, M. S.; Agranovich, V. M.; Walker, S. Experimental Study of Light Emission from Strongly Coupled Organic Semiconductor Microcavities Following Nonresonant Laser Excitation. *Phys. Rev. B* **2002**, *65* (19), 195312. https://doi.org/10.1103/PhysRevB.65.195312.

(179) Lidzey, D. G.; Bradley, D. D. C.; Virgili, T.; Armitage, A.; Skolnick, M. S.; Walker, S. Room Temperature Polariton Emission from Strongly Coupled Organic Semiconductor Microcavities. *Physical Review Letters* **1999**, *82* (16), 3316–3319. https://doi.org/10.1103/PhysRevLett.82.3316.

(180) Agranovich, V. M.; Litinskaia, M.; Lidzey, D. G. Cavity Polaritons in Microcavities Containing Disordered Organic Semiconductors. *Physical Review B* **2003**, *67* (8). https://doi.org/10.1103/PhysRevB.67.085311.

(181) Tassone, F.; Piermarocchi, C.; Savona, V.; Quattropani, A.; Schwendimann, P. Bottleneck Effects in the Relaxation and Photoluminescence of Microcavity Polaritons. *Physical Review B* **1997**, *56* (12), 7554–7563. https://doi.org/10.1103/PhysRevB.56.7554.

(182) Akselrod, G. M.; Argyropoulos, C.; Hoang, T. B.; Ciracì, C.; Fang, C.; Huang, J.; Smith, D. R.; Mikkelsen, M. H. Probing the Mechanisms of Large Purcell Enhancement in Plasmonic Nanoantennas. *Nature Photonics* **2014**, *8* (11), 835–840. https://doi.org/10.1038/nphoton.2014.228.

(183) Kinkhabwala, A.; Yu, Z.; Fan, S.; Avlasevich, Y.; Müllen, K.; Moerner, W. E. Large Single-Molecule Fluorescence Enhancements Produced by a Bowtie Nanoantenna. *Nat Photon* **2009**, *3* (11), 654–657. https://doi.org/10.1038/nphoton.2009.187.

(184) Viste, P.; Plain, J.; Jaffiol, R.; Vial, A.; Adam, P. M.; Royer, P. Enhancement and Quenching Regimes in Metal−Semiconductor Hybrid Optical Nanosources. *ACS Nano* **2010**, *4* (2), 759–764. https://doi.org/10.1021/nn901294d.

(185) Tame, M. S.; McEnery, K. R.; Özdemir, Ş. K.; Lee, J.; Maier, S. A.; Kim, M. S. Quantum Plasmonics. *Nature Phys* **2013**, *9* (6), 329–340. https://doi.org/10.1038/nphys2615.

(186) Esteban, R.; Borisov, A. G.; Nordlander, P.; Aizpurua, J. Bridging Quantum and Classical Plasmonics with a Quantum-Corrected Model. *Nat Commun* **2012**, *3* (1), 825. https://doi.org/10.1038/ncomms1806.

(187) Halas, N. J.; Lal, S.; Chang, W.-S.; Link, S.; Nordlander, P. Plasmons in Strongly Coupled Metallic Nanostructures. *Chemical Reviews* **2011**, *111* (6), 3913–3961. https://doi.org/10.1021/cr200061k.

(188) Song, B.; Jiang, Z.; Liu, Z.; Wang, Y.; Liu, F.; Cronin, S. B.; Yang, H.; Meng, D.; Chen, B.; Hu, P.; Schwartzberg, A. M.; Cabrini, S.; Haas, S.; Wu, W. Probing the Mechanisms of Strong Fluorescence Enhancement in Plasmonic Nanogaps with Sub-Nanometer Precision. *ACS Nano* **2020**, acsnano.0c01973. https://doi.org/10.1021/acsnano.0c01973.

(189) Ashraf, I.; Skandary, S.; Khaywah, M.; Metzger, M.; Meixner, A.; Adam, P.; Brecht, M. Effects of Irregular Bimetallic Nanostructures on the Optical Properties of Photosystem I from Thermosynechococcus Elongatus. *Photonics* **2015**, *2* (3), 838.

(190) Papageorgiou, G. C.; Govindjee. *Chlorophyll a Fluorescence: A Signature of Photosynthesis*; Springer Science & Business Media, 2007.

(191) Wydrzynski, T.; Satoh, K. *Photosystem II: The Light-Driven Water:Plastoquinone Oxidoreductase*; Springer Science & Business Media, 2006.

(192) McEvoy, J. P.; Brudvig, G. W. Water-Splitting Chemistry of Photosystem II. *Chem. Rev.* **2006**, *106* (11), 4455–4483. https://doi.org/10.1021/cr0204294.

(193) Shen, J.-R. The Structure of Photosystem II and the Mechanism of Water Oxidation in Photosynthesis. *Annual Review of Plant Biology* **2015**, *66* (1), 23–48. https://doi.org/10.1146/annurev-arplant-050312-120129.

(194) Nelson, N.; Yocum, C. F. Structure and Function of Photosystems I and Ii. *Annual Review of Plant Biology* **2006**, *57* (1), 521–565. https://doi.org/10.1146/annurev.arplant.57.032905.105350.

(195) Guskov, A.; Kern, J.; Gabdulkhakov, A.; Broser, M.; Zouni, A.; Saenger, W. Cyanobacterial Photosystem II at 2.9-Å Resolution and the Role of Quinones, Lipids, Channels and Chloride. *Nature Structural & Molecular Biology* **2009**, *16* (3), 334–342. https://doi.org/10.1038/nsmb.1559.

(196) Loll, B.; Kern, J.; Saenger, W.; Zouni, A.; Biesiadka, J. Towards Complete Cofactor Arrangement in the 3.0 Å Resolution Structure of Photosystem II. *Nature* **2005**, *438* (7070), 1040–1044. https://doi.org/10.1038/nature04224.

(197) Brecht, M.; Skandary, S.; Hellmich, J.; Glöckner, C.; Konrad, A.; Hussels, M.; Meixner, A. J.; Zouni, A.; Schlodder, E. Spectroscopic Properties of Photosystem II Core Complexes from Thermosynechococcus Elongatus Revealed by Single-Molecule Experiments. *Biochimica et Biophysica Acta (BBA)-Bioenergetics* **2014**, *1837* (6), 773–781.

(198) Czechowski, N.; Lokstein, H.; Kowalska, D.; Ashraf, K.; Cogdell, R. J.; Mackowski, S.; E., D.; C., M. A.; T., N.; A., K. T.; J., F.; A., L. S.; M., van V. F. C. J.; N., R. D.; M., M.; I., G.

D. Large Plasmonic Fluorescence Enhancement of Cyanobacterial Photosystem I Coupled to Silver Island Films. *Applied Physics Letters* **2014**, *105* (4), 043701. https://doi.org/10.1063/1.4891856.

(199) Bohren, C. F.; Huffman, D. R. *Absorption and Scattering of Light by Small Particles*; John Wiley & Sons, 2008.

(200) Kern, J.; Loll, B.; Lüneberg, C.; DiFiore, D.; Biesiadka, J.; Irrgang, K.-D.; Zouni, A. Purification, Characterisation and Crystallisation of Photosystem II from Thermosynechococcus Elongatus Cultivated in a New Type of Photobioreactor. *Biochimica et Biophysica Acta (BBA) - Bioenergetics* **2005**, *1706* (1–2), 147–157. https://doi.org/10.1016/j.bbabio.2004.10.007.

(201) Hussels, M.; Konrad, A.; Brecht, M. Confocal Sample-Scanning Microscope for Single-Molecule Spectroscopy and Microscopy with Fast Sample Exchange at Cryogenic Temperatures. *Review of Scientific Instruments* **2012**, *83* (12), 123706.

(202) Brecht, M.; Radics, V.; Nieder, J. B.; Bittl, R. Protein Dynamics-Induced Variation of Excitation Energy Transfer Pathways. *PNAS* **2009**, *106* (29), 11857–11861. https://doi.org/10.1073/pnas.0903586106.

(203) Skandary, S.; Hussels, M.; Konrad, A.; Renger, T.; Müh, F.; Bommer, M.; Zouni, A.; Meixner, A. J.; Brecht, M. Variation of Exciton-Vibrational Coupling in Photosystem II Core Complexes from *Thermosynechococcus Elongatus* As Revealed by Single-Molecule Spectroscopy. *The Journal of Physical Chemistry B* **2015**, *119* (11), 4203–4210. https://doi.org/10.1021/jp510631x.

(204) Krausz, E.; Hughes, J. L.; Smith, P. J.; Pace, R. J.; Årsköld, S. P. Assignment of the Low-Temperature Fluorescence in Oxygen-Evolving Photosystem II. *Photosynthesis Research* **2005**, *84* (1–3), 193–199. https://doi.org/10.1007/s11120-004-7078-9.

(205) Shibata, Y.; Nishi, S.; Kawakami, K.; Shen, J.-R.; Renger, T. Photosystem II Does Not Possess a Simple Excitation Energy Funnel: Time-Resolved Fluorescence Spectroscopy Meets Theory. *J. Am. Chem. Soc.* **2013**, *135* (18), 6903–6914. https://doi.org/10.1021/ja312586p.

(206) Brokmann, X.; Coolen, L.; Dahan, M.; Hermier, J. P. Measurement of the Radiative and Nonradiative Decay Rates of Single CdSe Nanocrystals through a Controlled Modification of Their Spontaneous Emission. *Phys. Rev. Lett.* **2004**, *93* (10), 107403. https://doi.org/10.1103/PhysRevLett.93.107403.

(207) Buchler, B. C.; Kalkbrenner, T.; Hettich, C.; Sandoghdar, V. Measuring the Quantum Efficiency of the Optical Emission of Single Radiating Dipoles Using a Scanning Mirror. *Phys. Rev. Lett.* **2005**, *95* (6), 063003. https://doi.org/10.1103/PhysRevLett.95.063003.

(208) Acuna, G. P.; Bucher, M.; Stein, I. H.; Steinhauer, C.; Kuzyk, A.; Holzmeister, P.; Schreiber, R.; Moroz, A.; Stefani, F. D.; Liedl, T.; Simmel, F. C.; Tinnefeld, P. Distance Dependence of Single-Fluorophore Quenching by Gold Nanoparticles Studied on DNA Origami. *ACS Nano* **2012**, *6* (4), 3189–3195. https://doi.org/10.1021/nn2050483.

(209) Holzmeister, P.; Pibiri, E.; Schmied, J. J.; Sen, T.; Acuna, G. P.; Tinnefeld, P. Quantum Yield and Excitation Rate of Single Molecules Close to Metallic Nanostructures. *Nature Communications* **2014**, *5* (1). https://doi.org/10.1038/ncomms6356.

(210) Ruhlandt, D.; Andresen, M.; Jensen, N.; Gregor, I.; Jakobs, S.; Enderlein, J.; Chizhik, A. I. Absolute Quantum Yield Measurements of Fluorescent Proteins Using a Plasmonic Nanocavity. *Commun Biol* **2020**, *3* (1), 627. https://doi.org/10.1038/s42003-020-01316-2.

(211) Chizhik, A. I.; Gregor, I.; Enderlein, J. Quantum Yield Measurement in a Multicolor Chromophore Solution Using a Nanocavity. *Nano Lett.* **2013**, *13* (3), 1348–1351. https://doi.org/10.1021/nl400313z.

(212) Kongsuwan, N.; Demetriadou, A.; Chikkaraddy, R.; Benz, F.; Turek, V. A.; Keyser, U. F.; Baumberg, J. J.; Hess, O. Suppressed Quenching and Strong-Coupling of Purcell-Enhanced Single-Molecule Emission in Plasmonic Nanocavities. *ACS Photonics* **2018**, *5* (1), 186–191. https://doi.org/10.1021/acsphotonics.7b00668.

(213) Kaminska, I.; Vietz, C.; Cuartero-González, Á.; Tinnefeld, P.; Fernández-Domínguez, A. I.; Acuna, G. P. Strong Plasmonic Enhancement of Single Molecule Photostability in Silver Dimer Optical Antennas. *Nanophotonics* **2018**, *7* (3), 643–649. https://doi.org/10.1515/nanoph-2017-0081.

(214) Pellegrotti, J. V.; Acuna, G. P.; Puchkova, A.; Holzmeister, P.; Gietl, A.; Lalkens, B.; Stefani, F. D.; Tinnefeld, P. Controlled Reduction of Photobleaching in DNA Origami–Gold Nanoparticle Hybrids. *Nano Letters* **2014**, *14* (5), 2831–2836. https://doi.org/10.1021/nl500841n.

(215) Zhang, D.; Wang, X.; Braun, K.; Egelhaaf, H.-J.; Fleischer, M.; Hennemann, L.; Hintz, H.; Stanciu, C.; Brabec, C. J.; Kern, D. P.; Meixner, A. J. Parabolic Mirror-Assisted Tip-Enhanced Spectroscopic Imaging for Non-Transparent Materials: Parabolic Mirror Assisted Spectroscopic Imaging of Non-Transparent Materials. *J. Raman Spectrosc.* **2009**, *40* (10), 1371–1376. https://doi.org/10.1002/jrs.2411.

(216) Wang, X.; Broch, K.; Scholz, R.; Schreiber, F.; Meixner, A. J.; Zhang, D. Topography-Correlated Confocal Raman Microscopy with Cylindrical Vector Beams for Probing Nanoscale Structural Order. *J. Phys. Chem. Lett.* **2014**, *5* (7), 1048–1054. https://doi.org/10.1021/jz500061y.

(217) Tserkezis, C.; Mortensen, N. A.; Wubs, M. How Nonlocal Damping Reduces Plasmon-Enhanced Fluorescence in Ultranarrow Gaps. *Physical Review B* **2017**, *96* (8). https://doi.org/10.1103/PhysRevB.96.085413.

(218) David, C.; García de Abajo, F. J. Spatial Nonlocality in the Optical Response of Metal Nanoparticles. *The Journal of Physical Chemistry C* **2011**, *115* (40), 19470–19475.

(219) McMahon, J. M.; Gray, S. K.; Schatz, G. C. Nonlocal Optical Response of Metal Nanostructures with Arbitrary Shape. *Phys. Rev. Lett.* **2009**, *103* (9), 097403. https://doi.org/10.1103/PhysRevLett.103.097403.

(220) Yang, Y.; Gu, C.; Li, J. Sub‐5 Nm Metal Nanogaps: Physical Properties, Fabrication Methods, and Device Applications. *Small* **2019**, *15* (5), 1804177. https://doi.org/10.1002/smll.201804177.

(221) Zuloaga, J.; Prodan, E.; Nordlander, P. Quantum Description of the Plasmon Resonances of a Nanoparticle Dimer. *Nano Lett.* **2009**, *9* (2), 887–891. https://doi.org/10.1021/nl803811g.

(222) Savage, K. J.; Hawkeye, M. M.; Esteban, R.; Borisov, A. G.; Aizpurua, J.; Baumberg, J. J. Revealing the Quantum Regime in Tunnelling Plasmonics. *Nature* **2012**, *491* (7425), 574–577. https://doi.org/10.1038/nature11653.

(223) Reynaud, S. La fluorescence de résonance : Etude par la méthode de l'atome habillé. *Ann. Phys.* **1983**, *8*, 315–370. https://doi.org/10.1051/anphys/198308080315.

# Appendix A

## A.1 Calculation of rotation matrix R

TD-DFT yield the orientation of the transition dipole moment in the molecular coordinate system **xyz**, while images are acquired in the image coordinate system **XYZ**. The rotation matrix **R** between the two coordinate systems is defined as:

$$\begin{bmatrix} X \\ Y \\ Z \end{bmatrix} = R \begin{bmatrix} x \\ y \\ z \end{bmatrix}. \tag{A-1}$$

From DFT calculations, we have obtained the three-dimensional orientation of the transition dipole moments of the four tautomers $\mathbf{d_1, d_2, d_3, d_4}$ defined in the molecular coordinate system **xyz**. From the experimental patterns in different confocal images, we are able to determine the three-dimensional orientation of the transition dipole moments $\mathbf{D_1, D_2, D_3, D_4}$ in the image coordinate system **XYZ** for a particular single molecule. At first, the tautomerization state of the single molecule is unknown in the individual images, but the relative orientations of transition dipole moments $\mathbf{D_1, D_2, D_3, D_4}$ can be obtained from the image series. We assume the three dimensional orientation of $\mathbf{D_1}$ is already obtained from image fitting. However, without a priori information about the relationship between $\mathbf{d_1, d_2, d_3, d_4}$ and $\mathbf{D_1, D_2, D_3, D_4}$, we obtain four different rotation matrix $\mathbf{R_1, R_2, R_3, R_4}$, by solving the following equation:

$$\boldsymbol{D_1} = \boldsymbol{R d}_i, i = 1, \dots, 4. \tag{A-2}$$

This yields four different sets of dipole orientations in **XYZ**, which are $\mathbf{R_1(d_1, d_2, d_3, d_4)}$, $\mathbf{R_2(d_1, d_2, d_3, d_4)}$, $\mathbf{R_3(d_1, d_2, d_3, d_4)}$, $\mathbf{R_4(d_1, d_2, d_3, d_4)}$. Comparing with $\mathbf{D_1, D_2, D_3, D_4}$, we can determine the correct rotation matrix **R** and identify the tautomerization state in the individual experimental scan images.

# Appendix B

## B.1 Intensity autocorrelation function

Fluorescence intensity fluctuations of single molecule contains important information, such as molecular diffusion, singlet-triplet interactions, tautomerization and conformational transition. Fluorescence Correlation Spectroscopy (FCS) gives a quantitative picture to discuss the origin of the intensity fluctuations and the information with different timescale can be extracted from the correlation function.

Here, the statistics property of the photons emitted by a single molecule are discussed by looking at the correlation function. The detailed analysis can be found in reference [148].

A single molecule intensity time trace *I(t)* in Time-Tagged Time-Resolved confocal experiment can be understood as a delay distribution *C(τ)*, where *t* is total time and $\tau$ is time delay between two photons. The normalized correlation function can be written as:

$$g^2(\tau) = \frac{\langle I(t)I(t+\tau)\rangle}{\langle I(t)\rangle^2}. \tag{B-1}$$

$g^2(\tau)$ is related to the conditional probability density G($t$+$\tau$ | $t$) (it can be noted as G($\tau$) for short) by

$$g^2(\tau) = \frac{G(\tau)}{\langle I(t)\rangle}. \tag{B-2}$$

G($\tau$) is the probability to observe a photon at time $t$+$\tau$ after one was detected at the time point $t$. This photon can be the first, second, etc. after the initial photon is detected as indicated in Figure Append B-1. Hence, G($\tau$) can be expressed as the convolution products of the probability density *C(τ)*:

$$G(\tau) = C(\tau) + \int_0^\tau C(\tau-\alpha)C(\alpha)d\alpha + \cdots. \tag{B-3}$$

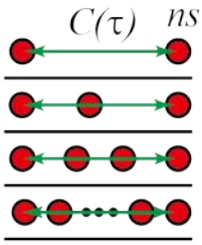


Figure Append B-1 Diagram of photon events with a delay distribution *C(τ)*. The conditional probability density G(*t*+τ | *t*) can be calculated as the convolution products of the probability density *C(τ)*.

As already derived by Reynaud[148,223], convolutions are replaced by simple products of the Laplace transforms,

$$g(s) = \frac{c(s)}{1 - c(s)}, \tag{B-4}$$

g(s) and c(s) are the Laplace transforms of G(τ) and *C*(τ).

With the simple formula of g(s) and c(s), G(τ) is determined with knowing *C(τ)*, or Vice Versa. Let's consider two simple case, a Poisson light source with $C(\tau) = ae^{-a\tau}$ and a Sub-Poisson light source with $C(\tau) = A(e^{-A\tau} - e^{-b\tau})$, which give the correlation functions as $G(\tau) = a$ and $G(\tau) = A(1 - e^{-b\tau})$, respectively. The correlation function of Poissonian light source has a constant probability of detection any other photon after the first one, while Sub-Poisson light source gives the antibunching behaviors as shown in Figure Append B-2.

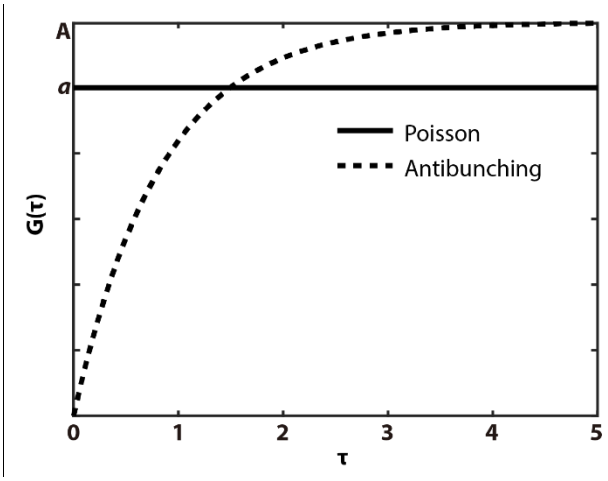


Figure Append B-2 Autocorrelation function of a Poisson light source with $C(\tau) = ae^{-a\tau}$ and a Sub-Poisson light source with $C(\tau) = A(e^{-A\tau} - e^{-b\tau})$.

Now considering a simple molecule, which can continuously cycle between singlet state and triplet state. $\varepsilon_1$ is the probability of the transition from the singlet state to the triplet state after absorb/emit a photon; and $\varepsilon_2$ is the probability of that the triplet state to the singlet state. The lifetime of triplet state is very different from singlet state. The delays between consecutive photons can be described by two single exponential distributions $C_1(\tau) = a_1 e^{-a_1\tau}$ and $C_2(\tau) = a_2 e^{-a_2\tau}$ (sketched in Figure Append B-3).

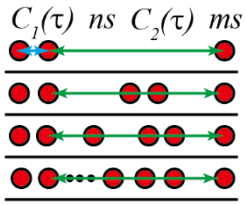


Figure Append B-3 Diagram of photon events with two delay distributions $C_1(\tau)$ at nanosecond scale and $C_2(\tau)$ at millisecond scale.

After some derivations[148], the correlation function can be written as:

$$g = \frac{1}{s}\frac{(w_1 a_1 + w_2 a_2)s + a_1 a_2(\varepsilon_1 + \varepsilon_2)}{s + a_1\varepsilon_1 + a_2\varepsilon_2}, \tag{B-5}$$

with $w_i = \varepsilon_i/(\varepsilon_1+\varepsilon_2)$.

Considering at very short time range, e.g. nanosecond range, $\varepsilon_1 \sim 0$ and $\varepsilon_2 \sim 0$, then $g \cong \frac{w_1 a_1 + w_2 a_2}{s}$, and $G(\tau) \cong w_1 a_1 + w_2 a_2$. For simplicity, we have assumed $C_1(\tau)$ as single exponential i.e. a Poisson light source. If Sub-Poisson distribution is used, antibunching will show up.

Another case is at longer timescale, e.g. millisecond, which is triplet lifetime range. We have $\varepsilon_1 \sim 0$ and $\varepsilon_2 \sim 1$, then $g \cong \frac{1}{s}\frac{w_1 a_1 s + a_1 a_2}{s + a_2}$, and $G(\tau) \cong w_1 a_1 e^{-a_2\tau} + a_1(1 - e^{-a_2\tau})$. This is the well-known result for FCS of triplet states[146].

Noting there is no coupling term of $C_1(\tau)$ and $C_2(\tau)$ in the correlation function. It is due to two delay distributions are in very different timescales. If assuming the third delay term $C_3(\tau) = a_3 e^{-a_3\tau}$ exist in even longer timescale (Figure Append B-4)), one can easily introduce it into the correlation function to get $G(\tau) \cong 1 + Ae^{-a_2\tau} + Be^{-a_3\tau}$. Two example correlation functions with double and triple delay distributions are plotted below in Figure Append B-4 c) (to be consistent with the literatures[8,14], we use $g^2(\tau) = G(\tau) - 1$).

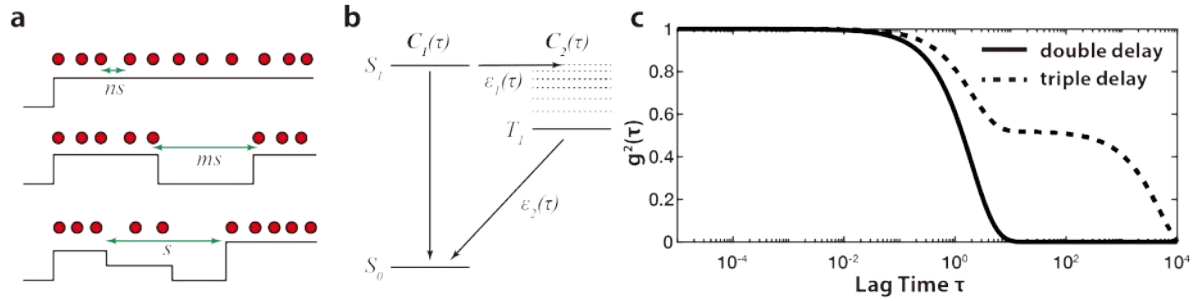


Figure Append B-4 a) Sketch of different delay distributions. b) Jablonski diagram showing the intersystem crossing from the singlet to the triplet state and the relaxation to ground state. c) Two example correlation functions with double and triple delay distributions.

There might be several delay distributions in the same timescales, for example, triplet lifetime could vary over time[37]. A linear superposition of several exponential decays including different delay and their coupling terms can be easily written into a single stretched exponential function[150,151] since

$$e^{-t^{\beta}} = \int_0^{\infty} du\, \rho(u) e^{-t/u}. \tag{B-6}$$

The mean lifetime gives

$$\langle \tau \rangle \equiv \int_0^{\infty} d\tau\, e^{-\left(\frac{\tau}{\tau_K}\right)^{\beta}} = \frac{\tau_K}{\beta}\Gamma\left(\frac{1}{\beta}\right), \tag{B-7}$$

where $\Gamma$ is the gamma function. For exponential decay, $\tau = \tau_K$ is recovered.

Overall, if there are different molecule dynamics in three different timescale, a correlation function can be fitted by

$$G(\tau) \cong 1 + Ae^{-\left(\frac{\tau}{\tau_1}\right)^{\beta_1}} + Be^{-\left(\frac{\tau}{\tau_2}\right)^{\beta_2}}. \tag{B-8}$$

The shortest timescale dynamics have been considered as constant since the electronic dead-time of a typical Time Correlated Single Photon Counting (TCSPC) device is in the range of tens nanoseconds.

We can rewrite (B-8) to be consistent with the literatures:

$$g^2(\tau) = G(\tau) - 1 \cong Ae^{-\left(\frac{t}{\tau_1}\right)^{\beta_1}} + Be^{-\left(\frac{t}{\tau_2}\right)^{\beta_2}}. \tag{B-9}$$

It is worth to mention that the normalized correlation function is invariable under a global change of detection quantum yield[148]. Therefore, we can have robust correlation function even at low signal intensity.

# Appendix C Résumé de la Thèse en Français

## C.1 Introduction

Depuis la première fois que Stokes utilise le mot *fluorescence* pour décrire l'émission de lumière suite à l'absorption de la lumière, de nombreux efforts ont été faits pour développer les méthodes expérimentales et les compréhensions théoriques de la fluorescence. Historiquement, la fluorescence et la phosphorescence ne sont pas distinguées jusqu'à ce que Lewis et Kasha prouvent que l'état phosphorescent est l'état triplet.

Avec les progrès des sources de lumière laser et des détecteurs de photons, la spectroscopie de fluorescence est devenue un outil d'enquête très réussi avec une sensibilité élevée. À la demande des sciences analytiques, matérielles et biologiques, les expériences de molécule unique basées sur la fluorescence sont en plein essor après la première détection d'une seule molécule dans une expérience basée sur l'absorption optique.

L'électrodynamique quantique (QED) bien établie a décrit comment la lumière et la matière interagissent et prédit de nombreux phénomènes. L'un des principaux défis pour manifester la théorie quantique dans le «monde réel», l'interaction d'un photon unique et d'une seule excitation électronique, est très faible. Une approche efficace consiste à confiner la lumière et l'excitation électronique dans une cavité de haute finesse. Lorsque l'interaction entre l'émetteur et le champ de cavité augmente, un régime de couplage dit fort peut être obtenu, dans lequel l'énergie est échangée de manière cohérente entre l'émetteur et le champ de mode de cavité.

La microcavité de type Fabry-Pérot (F-P) formée de deux réflecteurs de Bragg distribués (DBR) ou même de simples miroirs métalliques à espacement sous-longueur d'onde est une excellente alternative. De fortes interactions lumière-matière ont été démontrées dans une microcavité de type F-P avec de nombreux systèmes émetteurs différents à température ambiante et dans des conditions ambiantes. Bien qu'un fort couplage à température ambiante d'un seul émetteur ne soit pas encore réalisé dans une cavité F-P, la nanocavité plasmonique réalise une division de Rabi de 90 meV pour des molécules simples de bleu de méthylène à température ambiante et dans les conditions ambiantes. Les avantages sont dus à la localisation extrême et à la vitesse de décomposition rapide du plasmon de particules dans la nanocavité. La propriété évanescente du SPR le long d'une interface nanoparticulaire normale assure la localisation d'un champ électrique et donne lieu à une amélioration significative du champ proche. La diffusion Raman améliorée en surface (SERS) est l'une des applications les plus spectaculaires qui profitent de l'amélioration de grand champ de plasmonique et

ont été enregistrées sur un régime de molécule unique. L'amélioration de la fluorescence d'une seule molécule à proximité de nanoparticules plasmoniques a également été étudiée expérimentalement et théoriquement.

Les expériences présentées dans cette thèse utilisent l'accordabilité de la résonance et l'installation de fabrication de microcavités de type F-P et de nanocavités plasmoniques pour explorer une interaction lumière-matière efficace vers le régime de molécule unique. Les variations du taux d'émission spontanée d'une seule molécule d'hypéricine sont mesurées dans une microcavité F-P accordable. L'impact du mode cavité sur le taux de tautomérisation est également étudié.

Afin de profiter de la grande amélioration du champ proche des nanocavités plasmoniques pour une interaction efficace, un défi majeur consiste à aligner un seul émetteur au voisinage du 'hot spot'. Nous utilisons une approche de recuit thermique rapide sur film d'or, ce qui crée beaucoup des 'hot spot', de sorte que les émetteurs distribués clairsemés pourraient facilement se localiser dans une position préférée. Un protocole d'optimisation du multiplexage basé sur la nanocavité plasmonique vers une fluorescence améliorée à une seule molécule est développé.

La thèse est organisée comme suit. Tout d'abord, il y a un aperçu du contexte théorique général de l'interaction de la lumière et de la matière au chapitre 2. Le chapitre 3 décrit les techniques expérimentales associées. Les propriétés des émetteurs quantiques uniques sont caractérisées au chapitre 4. L'interaction de la cavité et des émetteurs quantiques est démontrée au chapitre 5. Une stratégie d'optimisation rapide basée sur la nanocavité plasmonique vers la fluorescence améliorée d'un seul photosystème II est présentée dans le chapitre 6 suivant Le dernier chapitre 7 donne un résumé de la thèse et un aperçu des expériences futures possibles.

## C.2 Fondements théoriques

### C.2.1 Un émetteur quantique

Un émetteur quantique est un système émetteur dominé par les lois de la mécanique quantique. Dans l'approximation dipolaire, l'hamiltonien du champ de rayonnement $\boldsymbol{E}$ avec un atome à un électron dans l'image d'interaction est donné par:

$$\Upsilon = \hbar g\left(\sigma_{+} a e^{i\Delta t} + a^{\dagger}\sigma_{-} e^{-i\Delta t}\right), \tag{1}$$

avec $\Delta = \omega_0 - \omega$. En résolvant l'équation de Schrödinger dépendant du temps, on obtient l'inversion de population, id est la différence entre la population à l'état excité et à l'état fondamental:

$$W(t) = \sum_n \left[ \left| c_{a,n-1}(t) \right|^2 - \left| c_{b,n}(t) \right|^2 \right]. \tag{2}$$

Dans une limite de champ faible, en supposant que le nombre de photons $n = 1$. Si le champ est en résonance avec l'atome et que l'atome est initialement dans l'état fondamental $|b, 2\rangle$, soit $c_{a,0}(0) = 0$, $c_{b,1}(0) = 1$ et $\Delta = 0$, alors l'inversion oscille d'avant en arrière entre -1 et 1 avec la fréquence de Rabi $\Omega_n$. Ce phénomène est appelé oscillation de Rabi qui est reproduit ici pour un système à deux niveaux résonnant avec un champ monomode.

### C.2.1.1 Émission spontanée

Dans la théorie semi-classique, l'émission spontanée s'ajoute phénoménologiquement. Afin d'aborder correctement l'émission spontanée, un continuum de modes dans toutes les directions, décrivant l'espace libre, doit être pris en compte. Sous l'approximation de Weisskopf-Wigner, on obtient la dérivée temporelle de l'amplitude de probabilité $c_a(t)$,

$$\dot{c}_a(t) = -\frac{\Gamma}{2} c_a(t), \tag{3}$$

où la constante de désintégration est,

$$\Gamma = \frac{1}{4\pi\epsilon_0} \frac{4\omega^3 \wp_{ab}^2}{3\hbar c^3}. \tag{4}$$

Une solution de l'équation (3) révèle la population à l'état excité comme:

$$\rho_{aa} \equiv |c_a(t)|^2 = exp(-\Gamma t). \tag{5}$$

Cela indique qu'un atome excité se désintègre de façon exponentielle avec la durée de vie

$$\tau = 1/\Gamma. \tag{6}$$

### C.2.1.2 Excitation de l'émetteur

Dans ce qui suit, nous dérivons la probabilité d'excitation d'un photon unique d'un système atomique constitué d'un état inférieur $|b\rangle$ et d'un ensemble d'états excités $|a_j\rangle$ en considérant l'interaction avec la lumière polarisée linéairement. La probabilité de trouver l'atome dans l'état excité$|a_j\rangle$ est obtenue en calculant la valeur d'espérance de l'opérateur de projection $|a_j\rangle\langle a_j|$. En

supposant que $\hat{\wp}_{a_j b}$ est indépendant de $j$, nous obtenons la probabilité d'exciter l'atome à n'importe quel état excite $|a_j\rangle$

$$P(t) = \kappa \hat{\wp}^2 \int_0^t dt_1 \left\langle i \middle| E^{(-)}(\boldsymbol{r}, t_1) + E^{(+)}(\boldsymbol{r}, t_1) \middle| i \right\rangle, \tag{7}$$

où$\kappa$ est constant. Normalement, on s'intéresse au taux d'excitation $\gamma_{exc}$ pour un champ stationnaire qui peut s'écrire:

$$\gamma_{exc} \propto |\hat{\wp} \cdot \boldsymbol{E}|^2. \tag{8}$$

C'est la même chose que l'équation de la règle d'or de Fermi.

### C.2.1.3 Diagrammes d'excitation dans les champs focaux de faisceaux laser polarisés radialement/azimutalement

Contrairement à un faisceau laser gaussien polarisé linéaire, qui est le mode Hermite-Gaussien (HG) d'ordre le plus bas, une combinaison de modes HG d'ordre supérieur peut décrire un faisceau laser polarisé radialement/azimutalement où la polarisation du faisceau varie dans l'espace.

Les champs focaux formés avec des faisceaux laser d'excitation avec polarisation APDM et RPDM sont utilisés pour surveiller l'orientation du TDM moléculaire. Dans le foyer, le champ électrique de l'APDM n'est polarisé que transversalement dans le plan **X-Y** (dans le plan), tandis que le champ de RPDM contient à la fois des polarisations transversales (dans le plan) et longitudinales (hors plan). Tous les motifs acquis avec l'APDM ont une forme à double lobé, où l'orientation du motif indique directement l'orientation du TDM dans le plan **X-Y**. L'excitation avec le RPDM conduit à des motifs allant du double lobe asymétrique en forme de point aux formes symétriques.

### C.2.1.4 Antibunching

Les propriétés statistiques de la lumière dans le régime quantique, qui sont souvent étudiées via la fonction de corrélation des photons, se comportent différemment que dans le régime classique. La fonction de corrélation la plus souvent utilisée est la fonction de corrélation du second ordre, qui est définie comme la probabilité conjointe de photo-détection, qui peut être comprise comme la probabilité de détecter un photon au temps $t+\tau$ après en avoir détecté un au moment $t$ . Carmichael et Walls ont discuté du comportement anti-poinçonnage exact d'un seul atome à deux niveaux sous excitation par résonance. Kitson et coll. fourni une analyse de $g^2(\tau)$ pour un nombre différent

d'émetteurs sous excitation en utilisant une approche semi-classique, ce qui donne un résultat pour $N$ molécules avec un taux de décroissance de fluorescence $\gamma$:

$$g^2(\tau) = 1 - \frac{1}{N} e^{-|\gamma\tau|}. \tag{9}$$

### C.2.1.5 Molécule fluorescente organique

Dans cette section, nous exposerons les caractéristiques générales et les principes importants du processus d'excitation et d'émission de molécules fluorescentes constituées de plusieurs atomes dits molécules polyatomiques. Les fonctions d'ondes électroniques des molécules polyatomiques sont appelées orbitales moléculaires et sont construites à partir des orbitales atomiques respectives et peuvent s'étendre sur toute la molécule.

En ignorant le couplage spin-orbite, la fonction d'onde de la molécule peut être séparée en partie spatiale $\psi_0(\boldsymbol{r})$ et en partie spin $\chi_0(\boldsymbol{s})$. Compte tenu de la fonction d'onde symétrique de l'état singulet et de la fonction d'onde antisymétrique de l'état triplet, on peut conclure que la transition électronique entre l'état singulet et l'état triplet est interdite. Si le couplage spin-orbite est invoqué, le croisement intersystème (ISC), se référant à la transition non radiative entre deux états électroniques de multiplicité différente, est possible comme un événement rare. A titre d'exemple, un colorant fluorescent typique possède une durée de vie de fluorescence de plusieurs nanosecondes et une durée de vie de phosphorescence de plusieurs millisecondes.

La diffusion inélastique de photons optiques avec des états vibrationnels d'une molécule est appelée diffusion Raman, du nom du scientifique indien C.V. Raman. Dans ce processus, le photon perd ou gagne de l'énergie vibratoire, appelée respectivement diffusion Stokes Raman ou anti-Stokes Raman.

Une transition qui implique des changements simultanés des états électroniques et des états vibrationnels est une transition vibronique. Le principe de Franck-Condon explique qu'une transition vibronique est plus susceptible de se produire, si les deux fonctions d'onde vibrationnelle ont un plus grand chevauchement. Une conséquence directe du principe de Franck-Condon est la règle de Kasha, qui stipule que '*the emitting level of a given multiplicity is the lowest excited level of that multiplicity*'.

## C.2.2 Résonateur optique

### C.2.2.1 Microcavité Fabry – Pérot

Une microcavité Fabry – Pérot, constituée de deux miroirs parallèles, est l'une des configurations de résonateur optique les plus simples. La réflexion permet une interférence constructive et

destructrice. Pour une cavité remplie d'un milieu d'indice de réfraction $n$, la condition de résonance nécessite que la composante du vecteur d'onde $k_\perp = k\cos\theta$ perpendiculaire à la surface du miroir remplisse:

$$k_\perp \times 2L = 2m\pi. \tag{10}$$

Ici, $m$ est un entier positif, $\theta$ est l'angle d'incidence.

Le facteur de qualité (ou facteur Q) est défini comme le rapport de l'énergie stockée à l'intérieur de la cavité à l'énergie perdue par cycle d'oscillation du champ électromagnétique. La forme de ligne du mode de résonance est donnée par un Lorentzien:

$$L_l(\omega) = \frac{\gamma/2\pi}{(\omega-\omega_c)^2 + \gamma^2/4}, \tag{11}$$

Où$\gamma$ est le taux d'amortissement qui définit la largeur de raie $\delta\omega_c = \gamma$ et le temps de stockage d'énergie est $\tau_c = 1/\gamma$.

La finesse de la cavité est un autre paramètre important pour caractériser une cavité F-P et est définie comme le rapport de la séparation de fréquence entre les modes de résonance successifs$\Delta\omega_c$ à la largeur de raie $\delta\omega_c$.

### C.2.2.2 Nanocavité plasmonique

En approximation quasi-statique, les modes propres des particules sphériques de métal noble de rayon proche ou inférieur à la longueur d'onde de la lumière incidente satisfont l'équation de Laplace $\nabla^2\Phi = 0$ pour le potentiel scalaire $\Phi$ en l'absence de charges externes. En raison de la propriété de localisation, la résonance est appelée résonance plasmonique de surface localisée (LSPR). Si une nanosphère est placée dans un champ électrique externe uniforme, seul le mode dipolaire ($l = 1$) doit être considéré, et la condition de résonance donnée par la condition aux limites:

$$\varepsilon_M(\omega_1) + 2\varepsilon_D(\omega_1) = 0. \tag{12}$$

Il s'agit de la condition de Fröhlich et le mode associé fait généralement référence au plasmon de surface localisé d'une nanosphère. La fréquence de résonance peut être déterminée à l'aide du modèle Drude pour la fonction diélectrique métallique.

Dans ce qui suit, nous présentons un modèle analytique développé par Khurgin et Sun. Le modèle est basé sur la méthode du volume efficace mise au point par Maier et permet d'optimiser les structures pour les plus grandes améliorations possibles sur le terrain. Le volume effectif du $l$ème mode est

défini comme $U_l = 1/4\varepsilon_0\varepsilon_D E_{max,l}^2 V_{eff,l}$. Lors de l'introduction de $V_{eff,l}$, la densité effective d'états dans le mode est:

$$\rho_l(\omega, d) = L_l(\omega)\frac{(1 + d/a)^{-2l-4}}{V_{eff,l}}. \tag{13}$$

Le premier terme $L_l(\omega) = \frac{\gamma_l/2\pi}{(\omega-\omega_l)^2+\gamma_l^2/4}$, qui décrit la distribution des modes sur la fréquence, est le facteur de largeur de raie de Lorentzian normalisé en fonction du taux de décroissance $\gamma_l$ de le mode, et le second terme décrit la distribution spatiale du mode.

## C.2.3 Interaction du mode cavité et de l'émetteur

### C.2.3.1 Couplage faible

Nous analysons d'abord le taux de désintégration de l'émetteur faiblement interagi avec le mode cavité. Le taux d'émission spontanée d'un émetteur en espace libre est proportionnel à la densité d'états $D(\omega)$, il est intuitif de remplacer $D(\omega)$ par la densité d'états dans la cavité, ce qui donne le taux de décroissance:

$$\Gamma_c = 2\pi\langle g^2(\omega)\rangle D_c(\omega). \tag{14}$$

Pour une situation de résonance ($\Delta = \omega - \omega_c = 0$), cela donne :

$$\Gamma_c = \Gamma Q\left(\frac{2\pi c^3}{V\omega^3}\right). \tag{15}$$

Présentation du facteur Purcell $F$,

$$F = \frac{\Gamma_c}{\Gamma} = 3Q\left(\frac{2\pi c^3}{V\omega^3}\right) = \frac{3Q\lambda^3}{4\pi^2 V}. \tag{16}$$

Ainsi, le taux d'émission spontanée peut être amélioré ou inhibé par le facteur de Purcell $F$.

### C.2.3.2 Couplage solide

Trouvons ensuite les états propres du système en utilisant une base vectorielle où état excité$|a, n\rangle = \binom{1}{0}$ et état fondamental $|b, n+1\rangle = \binom{0}{1}$. Afin de calculer les états propres d'énergie, l'hamiltonien peut être écrit comme $H = \sum_n H_n$, où $H_n$ est l'hamiltonien de n état photonique:

$$H_n = \hbar\omega\left(n+\frac{1}{2}\right)\begin{pmatrix}1 & 0\\ 0 & 1\end{pmatrix} + \frac{\hbar}{2}\begin{pmatrix}-\Delta & 2g\sqrt{n+1}\\ 2g\sqrt{n+1} & \Delta\end{pmatrix}. \quad (17)$$

Après diagonalisation on obtient les états propres correspondants (dits états habillés):

$$\begin{aligned}|1n\rangle &= -\sin\theta_n|a,n\rangle + \cos\theta_n\,|b,n+1\rangle\\ |2n\rangle &= \cos\theta_n\,|a,n\rangle + \sin\theta_n\,|b,n+1\rangle\end{aligned}', \quad (18)$$

dans lequel, $\sin\theta_n = \frac{2g\sqrt{n+1}}{\sqrt{\left(\sqrt{\Delta^2+4g^2(n+1)}-\Delta\right)^2+4g^2(n+1)}}$ et $\cos\theta_n = \sqrt{1-\sin^2\theta_n}$.

Lorsque le mode de cavité et l'émetteur sont en résonance, c'est-à-dire $\Delta = 0$, les états propres du système sont une superposition de l'état fondamental et de l'état excité, c'est-à-dire un hybride d'exciton d'émetteur et de photon de cavité. La différence entre les énergies propres indique une division dans le spectre, qui est due à un échange cohérent d'énergie entre deux systèmes. Ce phénomène est appelé couplage fort.

### C.2.3.3 Le modèle classique tient compte de l'amortissement dans la microcavité

Bien que la description quantique soit obligatoire pour un système microscopique, un modèle classique est souvent suffisant pour une description quantitative des résultats expérimentaux. Par conséquent, une description classique du couplage fort entre une microcavité F-P et des émetteurs, où un émetteur classique est traité comme un oscillateur lorentzien avec le taux d'amortissement $\gamma$, est introduite. La permittivité$\varepsilon(\omega)$ est obtenue comme:

$$\varepsilon(\omega) = 1 + \frac{A}{\omega_0^2 - \omega^2 - i\gamma\omega}, \quad (19)$$

où$A = \frac{Ne^2}{V\varepsilon_0 m}$ force d'oscillation des caractères. $N/\mathrm{V}$ est la densité de l'émetteur, $m$ est la masse d'un électron et $\omega_0$ est la fréquence de résonance. La dispersion de la cavité est maintenant:

$$\kappa^2 = \omega^2\left(1 + \frac{A}{\omega_0^2 - \omega^2 - i\gamma\omega}\right). \quad (20)$$

Le moment a été mis à l'échelle à $\kappa = c\left(k_\parallel + \frac{\pi}{L}\right)$. En supposant $\omega \approx \omega_0$, alors $\kappa + \omega \approx 2\omega_0$ et $\omega_0 + \omega \approx 2\omega_0$. La dispersion devient:

$$(\kappa - \omega)(\omega_0 - \omega - i\gamma/2) = \frac{A}{4}. \tag{21}$$

A la résonance, la division de deux modes normaux est

$$\Omega = \sqrt{A - \frac{\gamma^2}{4}}, \tag{22}$$

c'est-à-dire que l'amortissement diminue la division en mode normal. Si l'amortissement peut être ignoré ($\gamma = 0$), le découpage de mode ($\Omega = \sqrt{A} \propto \sqrt{\frac{N}{V}}$) est proportionnel à la densité de l'émetteur, qui est également déduite des descriptions semi-classiques et entièrement quantiques.

### C.2.3.4 Théorie des modes couplés de l'amélioration des émissions par nanocavité

Dans cette section, nous introduisons une théorie de modèle couplé analytique pour optimiser les nanostructures plasmoniques afin d'avoir les plus grandes améliorations d'émissions possibles, qui sont déterminées ensemble par l'amélioration de l'excitation et l'amélioration du rendement quantique, c'est-à-dire $F = F_{exc}F_{em}$ . En supposant que le TDM de l'émetteur $\hat{\wp}$ n'est pas altéré par l'environnement, l'amélioration de l'excitation peut être écrite comme:

$$F_{exc} = \gamma_{exc}/\gamma_{exc}^0 \propto |\hat{\wp} \cdot \boldsymbol{E}|^2/|\hat{\wp} \cdot \boldsymbol{E_0}|^2, \tag{23}$$

où $\gamma_{exc}^0$ et $\boldsymbol{E_0}$ sont respectivement le taux d'excitation et le champ électrique sans nanostructure. L'amélioration du rendement quantique est donnée par

$$F_{em} = \eta_{all}/\eta_{rad}, \tag{24}$$

dans laquelle $\eta_{all}$ est le rendement d'émission de l'émetteur en présence de nanostructure et $\eta_{rad}$ est le rendement quantique initial.

Un grand avantage de la nanostructure plasmonique est l'amélioration du champ proche fournie par LSPR. On considère une configuration de deux nanosphères d'or de rayon $a_1$ et $a_2$, qui sont indexées par 1 et 2 comme le montre la Figure R C-1 a). Un émetteur est placé entre les deux avec la polarisation du moment dipolaire le long de la ligne de connexion entre les centres des deux sphères. La distance entre les centres de l'émetteur et de la sphère est $r_1$ et $r_2$, respectivement.

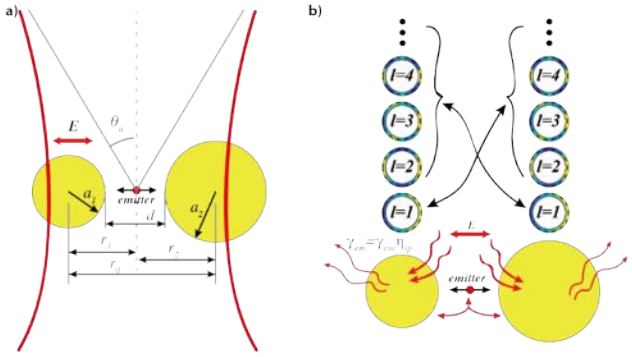


Figure R C-1 Illustration a) d'un émetteur placé en ligne avec deux nanosphères d'or qui sont éclairées par un faisceau laser gaussien. La polarisation du champ électrique se fait le long de la ligne de connexion des deux sphères ainsi que de l'orientation du TDM de l'émetteur. b) couplage du mode dipolaire et des modes d'ordre supérieur. Le champ électrique est couplé dans le mode dipolaire puis interagit avec des modes d'ordre supérieur d'une autre sphère, puis l'émetteur est excité. L'émission de l'émetteur est également couplée aux modes dipolaires, puis rayonnante ou couplée à des modes d'ordre supérieur ultérieurement.

La configuration à deux sphères, où le mode dipolaire d'une sphère est couplé aux modes d'ordre supérieur d'une autre, pourrait fournir une amélioration de champ supplémentaire (esquissé sur la Figure R C-1 b)). En l'absence de nanosphères, la puissance $|s_+|^2$ portée par l'onde incidente possédant un champ électrique $E_{foc}$ dans le foyer est:

$$|s_+|^2 = \frac{\sqrt{\varepsilon_D}}{Z_0}\pi \left(\frac{w_0}{2}\right)^2 E_{foc}^2. \tag{25}$$

Et $Z_0$ est l'impédance de l'espace libre. $w_0$ est le rayon du faisceau à la taille. On peut écrire les équations de taux d'amplitude $A_l = \sqrt{U_l} = \sqrt{\frac{1}{4}\varepsilon_0\varepsilon_D V_{eff,l}}E_{max,l}$ pour le processus d'excitation. À l'état stationnaire, c'est-à-dire $\frac{dA_l}{dt} = 0$, on peut relier $E_{max,1}^{(n)}$ et $E_{foc}$,

$$\boldsymbol{M}\begin{pmatrix} E_{max,1}^{(1)} \\ E_{max,1}^{(2)} \end{pmatrix} = \frac{\omega}{\sqrt{2}}\begin{pmatrix} E_{foc} \\ E_{foc} \end{pmatrix}. \tag{26}$$

Le champ électrique à l'emplacement de l'émetteur est:

$$\begin{aligned} E(r_1) = E_{max,1}^{(1)}\left(\frac{a_1}{r_1}\right)^3 + E_{max,1}^{(1)}\sum_{l=2}^{\infty}\frac{\omega_{1l}\kappa_{1l}^{(mn)}}{(\omega-\omega_l)+i\frac{\gamma}{2}}\frac{l+1}{2}\left(\frac{a_1}{a_2}\right)^{\frac{3}{2}}\left(\frac{a_2}{r_2}\right)^{l+1} \\ + E_{max,1}^{(2)}\left(\frac{a_2}{r_2}\right)^3 + E_{max,1}^{(2)}\sum_{l=2}^{\infty}\frac{\omega_{1l}\kappa_{1l}^{(mn)}}{(\omega-\omega_l)+i\frac{\gamma}{2}}\frac{l+1}{2}\left(\frac{a_2}{a_1}\right)^{\frac{3}{2}}\left(\frac{a_1}{r_1}\right)^{l+1}. \end{aligned} \tag{27}$$

Le facteur d'amélioration du champ, qui est le rapport entre le champ résolu et le champ en l'absence de nanosphères, est donné par:

$$F_{field} = \left|\frac{E(r_1)}{E_{foc}}\right|. \tag{28}$$

Dans ce qui suit, nous discutons de l'amélioration du rendement quantique en introduisant l'émetteur dans les équations de débit. De la même manière que précédemment, les équations de taux s'écrit:

$$\begin{aligned}
\frac{dA_1^{(m)}}{dt} &= i(\omega-\omega_1)A_1^{(m)} - i\sum_{l=1}^{\infty}\omega_{1l}\kappa_{1l}^{(mn)}A_l^{(n)} - \frac{1}{2}\gamma_1^{(m)}A_1^{(m)} - \frac{1}{2}\sqrt{\gamma_{rad}^{(m)}\gamma_{rad}^{(n)}}A_1^{(n)} - i\omega_{1B}\kappa_1^{(m)}B \\
\frac{dA_l^{(m)}}{dt} &= i(\omega-\omega_l)A_l^{(m)} - i\omega_{1l}\kappa_{1l}^{(nm)}A_1^{(n)} - \frac{1}{2}\gamma_l^{(m)}A_l^{(m)} - i\omega_{1B}\kappa_l^{(m)}B,\ \ l\geq 2 \\
\frac{dB}{dt} &= \frac{\sqrt{\gamma_m P}}{2} - \frac{1}{2}\gamma_m B - i\sum_{l=1}^{\infty}\omega_{lB}(\kappa_l^{(1)}A_l^{(1)} + \kappa_l^{(2)}A_l^{(2)})
\end{aligned} \tag{29}$$

où$\omega_{1B} = \sqrt{\omega\omega_l}$ et $\omega_{1l} = \sqrt{\omega_1\omega_l}$ sont une fréquence réduite. L'équation de vitesse pour l'émetteur contient un terme d'excitation avec une puissance de pompage *P* (obtenue par un processus réciproque) qui excite l'émetteur avec un taux de décroissance $\gamma_m = \tau_{rad}^{-1} + \tau_{nrad}^{-1}$. Le terme de super-radiance $\frac{1}{2}\sqrt{\gamma_{rad}^{(m)}\gamma_{rad}^{(n)}}A_1^{(n)}$ qui rend compte du caractère cohérent de l'émission par dipôles, ainsi que du terme de couplage entre les modes émetteur et plasmonique sont inclus avec une constante de couplage $\kappa_l^{(m)}$,

$$\kappa_l^{(m)} = \left(\frac{a_0}{r_m}\right)^{\frac{3}{2}}\left(\frac{a_m}{r_m}\right)^{l+\frac{1}{2}}\left(1+\left(\frac{a_m}{r_m}\right)^2\frac{2(l+1)}{2l+3}\right). \tag{30}$$

$r_m$ est l'écart entre l'émetteur et la sphère avec $m = 1{,}2$. Et $a_0 = \frac{\hat{\wp}}{e}$, dans lequel $\hat{\wp}$ est le TDM de l'émetteur, est un rayon caractéristique de l'émetteur. Pour une molécule fluorescente générale, le TDM est d'environ $0{\sim}10\ Debye$, c'est-à-dire $a_0 \approx 0{\sim}0.02\ nm$.

La puissance rayonnante du système $P_{all} = P_{emitter} + P_{SP}$ et la puissance d'excitation *P* peuvent être résolues. Puis analyser l'amélioration du rendement quantique $F_{em} = \eta_{all}/\eta_{rad}$. Ici, $\eta_{all} = P_{all}/P$ est le rendement d'émission du système couplé. Le rendement quantique de l'émetteur est $\eta_{rad} = 1/(\tau_{rad}\gamma_m)$. Donc,

,

$$F_{em} = \frac{\eta_{all}}{\eta_{rad}} = \frac{1 + \left|\sqrt{\gamma_{rad}^{(1)}\tau_{rad}}T_1^{(1)} + \sqrt{\gamma_{rad}^{(2)}\tau_{rad}}T_1^{(2)}\right|^2 \omega_{lB}^2}{\left|1 - 2\sum_{l=1}^{\infty}\omega_{lB}^2(\kappa_l^{(1)}T_1^{(1)} + \kappa_l^{(2)}T_1^{(2)})/\gamma_m\right|^2}. \quad (31)$$

Cette équation peut être utilisée pour tout émetteur placé entre deux nanosphères. Lorsque la distance de l'écart diminue, $\boldsymbol{\kappa}^{(m)}$ et $\kappa_l^{(2)}$ augmentent, mais le dénominateur augmente plus rapidement que le numérateur puisque seul $\boldsymbol{\kappa}^{(m)}$ est contenu dans le numérateur. Par conséquent, l'efficacité des émissions $\eta_{all}$ diminuera éventuellement.

## C.3 Installations expérimentales et préparation d'échantillons

### C.3.1 Microscope à balayage confocal combiné avec des modes laser d'ordre supérieur

Toutes les mesures optiques de ce travail sont effectuées sur un microscope confocal à balayage maison. Un schéma de l'installation est représenté sur la Figure R C-2 qui comprend trois parties principales.

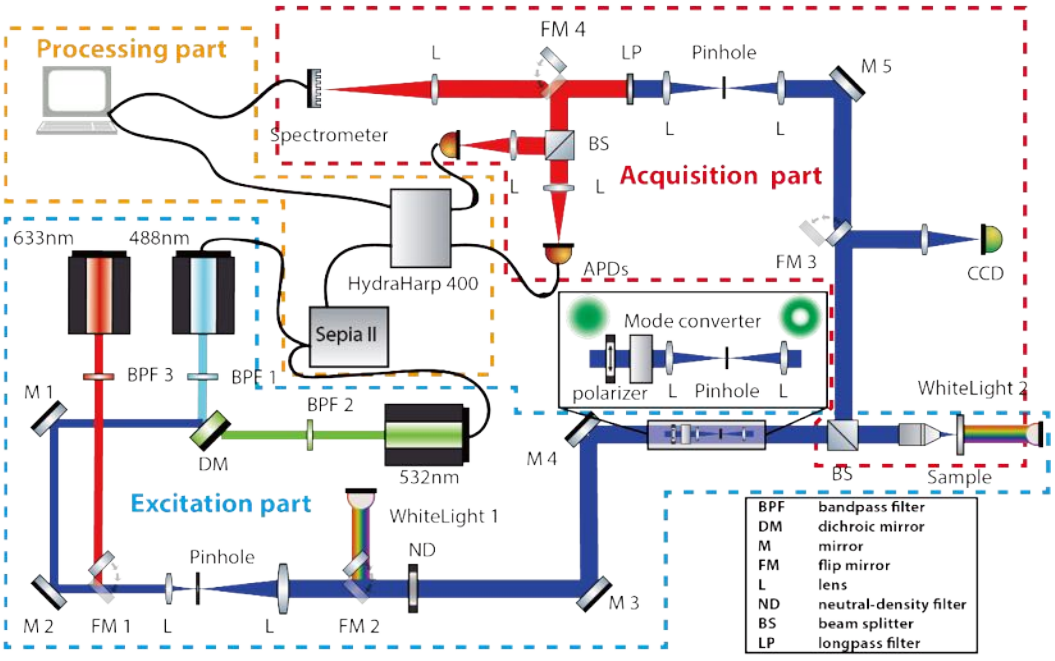


Figure R C-2 Dessin schématique du montage expérimental. L'encart est le diagramme du convertisseur de mode, qui peut être introduit dans le chemin optique si le mode anneau est nécessaire. Les lignes pointillées identifient trois parties de la configuration: la partie d'excitation, la partie d'acquisition et la partie de traitement. Composants optiques modifiés

à partir de ComponentLibrary créé par Alexander Franzen.

Comme indiqué par la ligne en pointillé cyan, la partie d'excitation contient trois lasers différents (1. $\lambda = 488\,nm$, pulsed, D-C-485, PicoQuant; 2. $\lambda = 530\,nm$, pulsed/CW, LDH-P-FA-530L, PicoQuant; 3. $\lambda = 633\,nm$, CW, XXX, XXX) qui sont couplés dans le même chemin optique. Les faisceaux laser sont étendus avant d'être envoyés à l'objectif. Une unité de conversion de mode, comprenant un polariseur linéaire, un convertisseur de mode (convertisseur de polarisation, ARCoptix), un système de télescope et un trou d'épingle ($d = 15\,\mu m$), peut être introduite dans le chemin optique si le mode anneau est demandé.

Les faisceaux gaussiens / RPDM / APDM traversent un séparateur de faisceau non polarisant 50:50 et sont focalisés sur l'échantillon via une lentille d'objectif. Deux objectifs différents sont utilisés pour des expériences spécifiques: un objectif à immersion dans l'huile (NA = 1.46, 63×, Carl Zeiss) pour les expériences liées à une seule molécule et un objectif à air (NA = 0.6, 40×, Edmund Optics) pour les expériences de couplage fort. L'échantillon est fixé avec des aimants sur une platine piézo-électrique à balayage (P-527.3CL, Physik Instrumente).

Le signal de fluorescence est collecté par la même lentille d'objectif et envoyé soit au spectromètre (SP-2500i, Princeton Instruments) soit à deux photodiodes à avalanche (APDs, SPCM-AQR-14, PerkinElmer) via un séparateur de faisceau 50/50. Les APD sont connectés à un module de comptage de photons uniques corrélé dans le temps (TCSPC, HydraHarp 400, PicoQuant). Les données collectées liées au TCSPC sont traitées à l'aide de SymPhoTime 64 (PicoQuant). Les images de spectre et d'intensité de balayage sont traitées à l'aide de scripts Matlab auto-écrits.

## C.3.2 Préparation d'échantillons moléculaires

Les lamelles (22 mm × 22 mm, thickness 150 μm, Carl Roth) sont nettoyées dans une solution d'acide chromosulfurique pendant 4 heures, puis rincées à l'eau triplement distillée et enfin séchées sous flux d'azote.

L'hypericine (Burg-Apotheke, Königstein) est dissoute dans l'éthanol (Uvasol, Merck) et diluée à une certaine concentration pour une utilisation ultérieure. Le poly (alcool vinylique) (PVA, Sigma-Aldrich) est dissous dans de l'eau triplement distillée, et 2 μL de solution d'hypéricine sont ajoutés à 2 wt. % de solution PVA pour obtenir la concentration requise. Pour les expériences de deutération, l'hypéricine est dissoute dans du méthanol-$d_4$ (99% d'atome D, Sigma-Aldrich) pour l'échange H/D. De plus, le solvant du PVA est changé en oxyde de deutérium (99% d'atome D, Sigma-Aldrich). Toutes les solutions sont stockées au réfrigérateur pour minimiser le blanchiment des molécules.

Pour les mesures de molécule unique, 5 μL de solution d'hypéricine/éthanol sont ajoutés directement sur une lamelle de verre nettoyée ou 20 μL de la solution d'hypéricine/PVA $10^{-9}$ M sont enduits par rotation (6k rpm, 30 s) sur la lamelle. La même quantité de solution d'hypéricine/PVA $10^{-9}$ M est enduite par rotation sur le miroir plat pour la mesure en microcavité. Pour une expérience de couplage fort, TDBC (FEW Chemicals) est dissous dans de l'eau triplement distillée subit une auto-organisation pour former une molécule de colorant J-agrégats puis dispersé dans 2 wt. % Matrice PVA. 100 μL de solution aqueuse TDBC/PVA sont injectés dans la cavité. La solution aqueuse peut préserver les états de J-agrégat et réduire les émissions des monomères, tandis que le PVA peut empêcher l'eau de se dessécher.

### C.3.3 Microcavité accordable

La microcavité accordable utilisée dans ce travail consiste en un miroir plat et un miroir incurvé qui sont assemblés dans un système de cage pour former la cavité. Le miroir incurvé peut être approché vers le miroir plat par un actionneur piézo (Polaris® Kinematic Mirror Mounts KC1-T-PZ, Thorlabs). Le miroir plat est préparé en évaporant (Edwards EB3, $10^{-6}$ mbar, 0.1 nm/s) 1 nm de chrome, comme couche d'adhérence, et 30 nm d'argent en séquence sur une lamelle nettoyée. Le miroir incurvé est une lentille plan-convexe (f = 50 mm, rayon de courbure 25.8 mm, Thorlabs) avec 1 nm de chrome et 50 nm d'argent évaporé en convexité. De plus, de la silice à 50 nm est évaporée au-dessus des couches d'argent des deux miroirs, servant d'entretoise pour éviter la trempe de la molécule sur le film d'argent et pour protéger les deux miroirs des dommages mécaniques. Le signal de fluorescence est collecté du côté du miroir plat, permettant une couche d'argent plus épaisse sur le miroir incurvé. L'échantillon de molécule est introduit sur le dessus du miroir plat.

Afin d'obtenir des spectres de réflexion résolus en angle, une lentille tubulaire est placée devant le spectromètre pour former un système 4f. Un trou d'épingle est utilisé pour éliminer la lumière parasite, et la dispersion dans *k*-espace est obtenue par imagerie du plan de Fourier de l'image de la cavité sur le CCD du spectromètre.

### C.3.4 Plasmonic nanocavity

Deux types de nanocavités plasmoniques sont utilisées dans ce travail. Pour les expériences SERS à molécule unique, le substrat est préparé par évaporation (Edwards EB3, $10^{-6}$ mbar, 0.1 nm/s) une couche d'argent de 4 nm d'épaisseur sur des lamelles nettoyées, ce qui donne des nanoparticules après 12 heures de recuit à température ambiante. Sur ce film d'îlot d'argent, une gouttelette de 5 μL de solution d'éthanol d'hypéricine $10^{-10}$ M est directement ajoutée pour acquérir des spectres SERS à

molécule unique. La même quantité de solution d'éthanol d'hypéricine $10^{-6}$ M est utilisée pour acquérir des spectres SERS d'ensemble pour comparaison.

Des nanoparticules d'or non uniformes sont utilisées pour les expériences d'amélioration de la fluorescence. Dans le processus d'évaporation normal, le détecteur et le substrat de l'échantillon sont à la même hauteur ($h_0$), ce qui est beaucoup plus grande que la taille du substrat de l'échantillon ($h_0 \gg d$). Cependant, en abaissant la hauteur de l'échantillon à une valeur plus petite, un film d'épaisseur non uniforme sera obtenu. De plus, étant donné que la position du capteur est inchangée, il y aura une différence entre la lecture d'épaisseur du capteur $t_0$ et l'épaisseur réelle au centre de l'échantillon $t_c$. Dans ce travail, l'échantillon est préparé en évaporant $t_0 = 1\,nm$ d'or (Plassys MEB400, $10^{-6}$ Torr, 0.05 nm/s) avec $h_0 = 250\,mm, h = 70\,mm$ et $d = 40\,mm$. L'échantillon a une épaisseur de film variant de 2 nm à 13 nm. Afin d'obtenir des nanoparticules d'or, nous suivons une stratégie de recuit thermique rapide pour chauffer l'échantillon à 270°C pendant 30 s. L'échantillon est ensuite caractérisé au microscope électronique à balayage (FEG 8030, Hitachi).

## C.4 Caractérisation de l'émetteur quantique unique

### C.4.1 Hypericine

L'hypericine est un agent multifonctionnel dans les médicaments et les applications médicales, car elle présente une activité antidépressive, antinéoplasique, antitumorale et antivirale. Il existe de nombreuses études spectroscopiques sur les propriétés d'ensemble de l'hypéricine. Cependant, les études sur une seule molécule (SM) de l'hypéricine étaient toujours manquantes. La spectroscopie SM peut fournir une meilleure compréhension de ses propriétés photophysiques, car certains aspects, tels que l'influence de l'environnement local ou des sous-populations, sont masqués par la moyenne d'ensemble.

Dans ce travail, nous présentons des expériences SM avec l'hypéricine et montrons qu'il est possible d'étudier ses propriétés optiques, par ex. clignotement de fluorescence, durées de vie de fluorescence et statistiques de photons de fluorescence, malgré son rendement élevé en triplets de 0.5-0.7.

L'hypericine est un dérivé d'anthraquinone avec sa structure moléculaire représentée sur la Figure R C-3 a). Le spectre d'absorption (ligne bleue sur la Figure R C-3 b)) peut être grossièrement divisé en trois domaines différents, à savoir l'absorption à l'état $S_1$ entre 490 nm et 600 nm, l'absorption $S_2$ entre 400 nm et 490 nm et le triplet-triplet absorption à 510 nm. Le spectre de fluorescence

d'ensemble (ligne noire) a une symétrie miroir par rapport au spectre d'absorption avec un décalage de Stokes de ~12 nm à 603 nm. La ligne rouge de la Figure R C-3 b) affiche un exemple de spectre de fluorescence d'une seule molécule d'hypéricine montrant les mêmes bandes d'émission que le spectre d'ensemble, mais avec des rapports d'intensité différents.

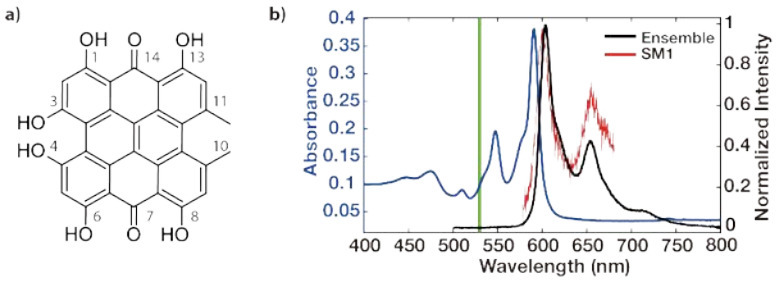


Figure R C-3 (a) Structure chimique de l'hypéricine. (b) Spectres d'absorption d'ensemble (ligne bleue) et de fluorescence (ligne noire) d'hypéricine dans l'éthanol ainsi qu'un spectre d'émission d'une seule molécule d'hypéricine (ligne rouge) sur une lamelle en verre. La longueur d'onde d'excitation est de 530 nm pour les deux spectres d'émission et est indiquée par la ligne verte.

## C.4.2 Influence de l'environnement local sur les propriétés d'émission

Deux types d'échantillons différents sont préparés afin d'étudier l'influence de l'environnement local sur des molécules d'hypéricine uniques. Les traces de temps de fluorescence sont enregistrées avec un laser à excitation pulsée $\lambda_{ex}$=530 nm (1.4 µW, 20 MHz). L'influence de l'environnement local (verre, PVA) sur le temps de survie et la dynamique de clignotement est analysée statistiquement. Le temps de survie, c'est-à-dire le temps avant qu'une photo de molécule ne blanchisse en raison de l'excitation répétée, de molécules d'hypéricine uniques est présenté sur la Figure R C-4 a)/b).

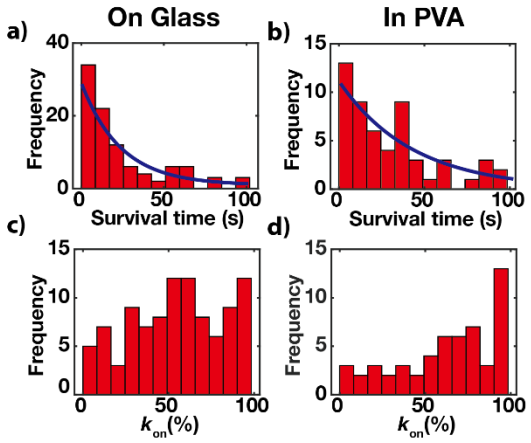


Figure R C-4 Statistiques du comportement de clignotement d'une seule molécule d'hypéricine. (a, b) montrent l'histogramme des temps de survie de molécules d'hypéricine uniques sur un substrat de verre (n=98) (a) et dans une matrice PVA (n=54) (b). La ligne bleue montre un ajustement exponentiel aux histogrammes et donne un temps de

blanchiment de 23.8 s sur le substrat en verre et de 46.6 s dans la matrice PVA. (c, d) Histogramme sur le rapport $k_{on}$ de molécules d'hypéricine uniques sur un substrat en verre (c) et dans une matrice PVA (d).

Figure R C-4 a) illustre le temps de survie de 98 molécules d'hypéricine sur un substrat en verre, tandis que les résultats présentés sur la Figure R C-4 a) sont basés sur 54 molécules d'hypéricine dans une matrice PVA. Dans les deux cas, des temps de survie allant de quelques secondes à 100 secondes. Avec une fonction exponentielle, nous déterminons un temps de survie moyen de 23.8 s sur le substrat en verre et de 46.6 s dans la matrice PVA. Les mêmes traces de temps d'intensité ont été utilisées pour étudier la dynamique de clignotement en déterminant le rapport sur $k_{on}$, c'est-à-dire le rapport entre le moment où la molécule est dans le $t_{on}$ brillant et le temps de survie $t_{surv}$. La dynamique de clignotement change lorsque l'hypéricine est intégrée dans la matrice PVA. Il est clair que la quantité de molécules d'hypéricine uniques qui ne montrent pratiquement aucun clignotement augmente avec une quantité significative de molécules ayant un $k_{on}$ proche de 100%.

La durée de vie de fluorescence moyenne en amplitude sur le substrat en verre est de 5.75 ns et 4.86 ns dans la matrice PVA. Les durées de vie de fluorescence plus courtes dans la matrice PVA conduisent à un taux de décroissance radiatif plus élevé. De plus, une durée de vie de fluorescence plus courte réduit le risque de transition vers l'état triplet; et le clignotement et le blanchiment sont réduits. Par conséquent, les résultats montrent que la matrice hôte PVA a un effet stabilisant et rend l'hypéricine plus adaptée à la spectroscopie de fluorescence au niveau d'une seule molécule.

### C.4.3 Transition de tautomérisation de l'hypéricine

De nombreuses études théoriques se sont concentrées sur l'hétérogénéité structurelle de l'hypéricine résultant de la tautomérisation, de la dé-/protonation et des équilibres conformationnels (torsion), ainsi que sur d'éventuels équilibres d'association (dimérisation), tandis que les difficultés expérimentales empêchent de clarifier les propriétés liées aux espèces et la dynamique d'équilibre sans ambiguïté dans un ensemble. Comme indiqué ci-dessus, il est possible d'observer l'hypéricine au niveau d'une seule molécule, ce qui ouvre la possibilité de discuter de la dynamique hétérogène d'une seule molécule d'hypéricine.

Il existe dix tautomères d'hypéricine, qui ne sont pas affectés par l'isomérisation conformationnelle. La nomenclature dans la littérature est utilisée pour décrire la position des groupes carbonyle, par exemple $\mathbf{Q}_{7,\,14}$ désigne le tautomère avec les groupes carbonyle en positions 7 et 14. Les quatre espèces tautomères les plus stables, ($\mathbf{Q}_{7,14}$, $\mathbf{Q}_{1,7}$, $\mathbf{Q}_{7,13}$, $\mathbf{Q}_{3,7}$), sont des tautomères avec la plus faible énergie libre. Notant que les barrières d'énergie d'activation impliquent un seul transfert de protons

dans ces tautomères sont plus grandes que l'énergie thermique $kT$ selon les calculs DFT. Par conséquent, le tunnel quantique joue un rôle dominant pour la tautomérisation de l'hypéricine.

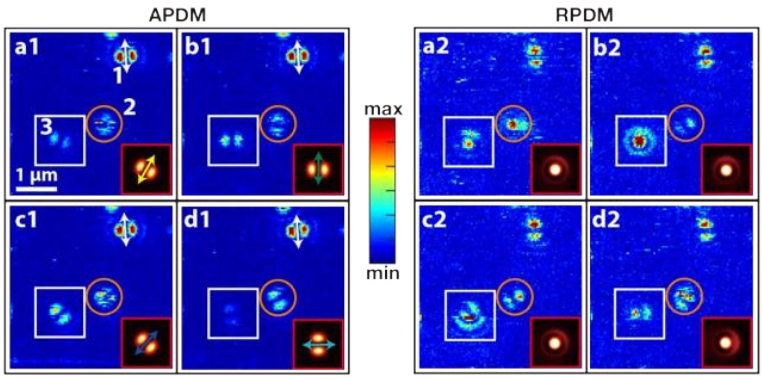


Figure R C-5 Huit images exemplaires enregistrées à la même position spatiale. La plage de balayage est de 4 μm × 4 μm (100 pixels × 100 pixels, 5 ms par pixel). (a1-d1) sont excités avec APDM et (a2-d2) sont excités avec RPDM. Les images sont disposées par paires (a1-a2, b1-b2,…) selon le dipôle de transition de la molécule. La molécule montre un changement d'orientation lors de balayages consécutifs. Les images en médaillon en carrés rouges (1.2 μm × 1.2 μm) sont des résultats de simulation.

Le changement significatif de la position du groupe carboxyle pour différents tautomères s'accompagne d'une redistribution électronique; par conséquent, le moment dipolaire de transition (TDM) électronique $S_0 \rightarrow S_1$ a une orientation différente pour les quatre tautomères. Les quatre tautomères de l'hypéricine ont une orientation différente du TDM et une transition entre ces tautomères peut être observée par un changement d'orientation du motif d'image.

Afin de vérifier que le basculement observé du TDM est provoqué par une transition de tautomérisation, des images de balayage de la même région spatiale sont acquises jusqu'au photo-blanchiment pour capturer la multiformité de l'orientation TDM. Un exemple de série d'images de la même zone spatiale est représenté sur la Figure R C-5.

Table R 1 Angle azimutal et polaire calculé

| | Molecule 3 in Figure R C-5 | | | |
|---|---|---|---|---|
| Tautomer | $Q_{7,14}$ | $Q_{1,7}$ | $Q_{3,7}$ | $Q_{7,13}$ |
| Φ | 46.8° | 89.0° | 60.2° | 0.8° |
| Θ | 167.1° | 166.0° | 167.6° | 160.0° |

Les motifs de fluorescence de trois molécules uniques peuvent être observés sur la Figure R C-5 et les images sont disposées par paires (a1-a2, b1-b2,…) selon l'orientation dipolaire de transition de la molécule 3. L'orientation du motif de la molécule 1 (flèche blanche ) est stable pendant toutes les mesures, donc cette molécule est toujours dans le même état tautomérique et sert de référence. L'orientation de la molécule 2 (cercle orange marqué) change plus rapidement que le temps

d'acquisition d'image, conduisant à une forme de motif en forme d'anneau en a1 et c1. Pour la molécule 3 (carré blanc marqué), quatre paires de modèles d'excitation différents peuvent être distinguées représentant quatre orientations TDM différentes. Ceux-ci sont cohérents avec les quatre tautomères les plus stables de l'hypéricine. L'orientation du motif à double lobe de la molécule 3 dans l'image a1 a d'abord été équipée de fonctions gaussiennes 2D en utilisant un script Matlab auto-écrit, qui donne un angle azimutal $\Phi \approx 60^{o}$. Des simulations numériques sont effectuées pour calculer une série de motifs d'image avec un angle azimutal fixe $\Phi$ et un angle polaire varié $\Theta$ sous excitation RPDM. La comparaison entre les motifs d'image simulés et l'image expérimentale de la Figure R C-5 a2 permet de déterminer l'angle polaire à $\Theta \approx 165^{o}$. Une fois que l'orientation tridimensionnelle d'un TDM est connue dans le système de coordonnées d'image **XYZ**, la matrice de rotation **R** du système de coordonnées d'image au système de coordonnées moléculaires **xyz** peut être résolue.

La matrice de rotation **R** multipliée par les orientations TDM dans le système de coordonnées moléculaires obtenu à partir du TD-DFT donne l'orientation spatiale des trois autres tautomères dans le système de coordonnées d'image. Les angles correspondants sont résumés dans le Table R 1. Les images incrustées dans les carrés rouges sont des motifs d'image respectifs calculés avec les orientations TDM du Table R 1. Veuillez noter que seul le premier motif d'image dans a1 est ajusté pour déterminer l'orientation d'un TDM . Les orientations de motif des trois autres tautomères sont purement obtenues à partir des orientations TDM relatives obtenues à partir des calculs TD-DFT. Il convient de mentionner que le motif de la molécule 3 sur la Figure R C-5 c2) est un chevauchement des tautomères $\mathbf{Q}_{7,14}$ et $\mathbf{Q}_{1,7}$. L'excellent accord entre les données expérimentales et les orientations TDM obtenues par les calculs TD-DFT confirme que le retournement observé des motifs d'image est causé par des transitions de tautomérisation; et nous pouvons identifier quel tautomère est observé dans les images individuelles.

### C.4.4 Dynamique temporelle de la transition de tautomérisation de l'hypéricine

Limité à la résolution temporelle de la méthode de balayage confocal, le balayage en mode anneau ne peut révéler la dynamique temporelle de la réorientation des TDM que sous la forme d'un retournement soudain. Cependant, la fluctuation de l'intensité de fluorescence est également évidente pendant la transition de tautomérisation, par conséquent des informations supplémentaires peuvent être extraites de la trace de temps d'intensité.

La spectroscopie de corrélation de fluorescence (FCS) donne une image quantitative pour discuter de l'origine des fluctuations d'intensité en utilisant la fonction d'autocorrélation. En fonction de la

résolution temporelle de la trace temporelle, une étude quantitative de la dynamique moléculaire allant de la nanoseconde à la seconde plage est accessible. Contrairement à un FCS standard, qui reflète l'analyse statistique des fluctuations d'équilibre, nous nous concentrons sur la fluctuation d'une seule molécule fixe (pas de rotation). La dynamique de fluctuation des microsecondes aux secondes peut être décrite par la fonction d'autocorrélation:

$$g^2(\tau) \cong Ae^{-\left(\frac{\tau}{\tau_1}\right)^{\beta_1}} + Be^{-\left(\frac{\tau}{\tau_2}\right)^{\beta_2}}, \tag{32}$$

où A et B sont des constantes donnent le rapport des fluctuations rapides et lentes. $\tau_1$ et $\tau_2$ représentent des dynamiques de fluctuations rapides et lentes, qui correspondent respectivement à l'extinction de l'état des triplets et à la tautomérisation. Les paramètres d'étirement $\beta_1$ et $\beta_2$ peuvent décrire une superposition linéaire de plusieurs désintégrations exponentielles, donnant une valeur de un s'il n'y a qu'une seule décroissance exponentielle. Les durées de vie moyennes pour les fluctuations rapides ($\langle\tau_1\rangle$) et lentes ($\langle\tau_2\rangle$) sont calculées à partir de la décroissance exponentielle étirée.

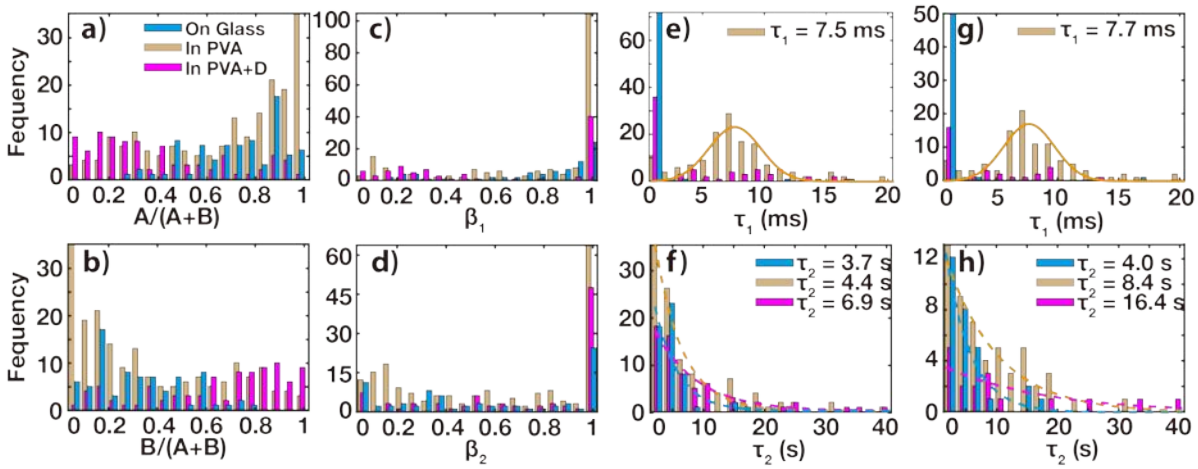


Figure R C-6 Histogrammes des paramètres dynamiques de l'hypéricine unique sur verre ($\sigma$ = 78), en PVA ($\sigma$ = 189) et deutéré en PVA ($\sigma$ = 89). a) Rapport d'amplitude de la dynamique rapide A/(A + B). b) Rapport d'amplitude de la dynamique lente B/(A + B). c) et d) Étirer les paramètres de $\beta_1$ et $\beta_2$. e) et f) Histogramme de durée de vie moyenne $\langle\tau_1\rangle$ et $\langle\tau_2\rangle$. g) et h) Histogramme de durée de vie moyenne 〈$\langle\tau_1\rangle$ et $\langle\tau_2\rangle$ en limitant $\beta_2$<0.95.

La Figure R C-6 montre les histogrammes des paramètres dynamiques pour les molécules d'hypéricine uniques sur verre ($\sigma$ = 78, bleu), en PVA ($\sigma$ = 189, orange) et deutéré en PVA ($\sigma$ = 89, magenta). De toute évidence, tant sur le verre que dans le PVA, la dynamique moléculaire est dominée par des fluctuations rapides, car le rapport d'amplitude de la dynamique rapide A/(A+B) est proche de 1. Cependant, la dynamique rapide de l'hypéricine deutérée est supprimée, entraînant une augmentation de l'amplitude rapports de la dynamique lente B/(A+B) proches de 1. Bien que le

mécanisme de suppression nécessite une discussion plus approfondie, nous donnons ici une explication possible. En raison du faible p$K_a$ (1.8), l'échange H/D est le plus susceptible de se produire au niveau des groupes hydroxyles de la baie. De plus, les transitions de tautomérisation permettent de multiples échanges H/D, ce qui peut prolonger la durée de vie de l'état du triplet jusqu'à des dizaines de fois, ainsi la dynamique rapide à l'échelle de la milliseconde est supprimée.

La plupart des paramètres d'étirement $\beta_1$ et $\beta_2$ sont égaux à 1 comme indiqué en c) et d). Il est raisonnable pour $\beta_1 = 1$ car l'extinction de l'état des triplets est la principale raison de la fluctuation rapide, tandis que $\beta_2 = 1$ indique que les molécules ne présentent pas de tautomérisation évidente ou que la diminution de la fonction d'autocorrélation est principalement due au temps de survie fini.

L'histogramme de durée de vie moyenne $\langle\tau_1\rangle$ et $\langle\tau_2\rangle$ sont présentés en e) et f). Pour les molécules sur verre, la plupart des $\langle\tau_1\rangle$ sont très courts et la moyenne $\overline{\langle\tau_1\rangle}$ = 0.10 ms est dans la plage de la durée de vie de l'état du triplet de l'hypéricine, tandis que la distribution de $\langle\tau_1\rangle$ dans le PVA est ajustée par un Fonction gaussienne avec moyenne $\overline{\langle\tau_1\rangle}$ = 7.5±1.2 ms. La durée de vie plus longue du triplet probablement due à un taux de décroissance radiatif plus rapide supprime la transition vers l'état de triplet, et moins d'oxygène dans le PVA réduit les voies de décy non radiatives possibles dans l'état de triplet. La distribution de $\langle\tau_1\rangle$ pour l'hypéricine deutérée dans le PVA est différente des deux autres situations. Ceci peut également s'expliquer par les possibles échanges H/D multiples, qui donnent lieu à la large distribution de $\langle\tau_1\rangle$ prolongés et diminuent le rapport de dynamique rapide.

g) et h) montrent l'histogramme de $\langle\tau_1\rangle$ and $\langle\tau_2\rangle$ en limitant $\beta_2$<0.95. La distribution de $\langle\tau_1\rangle$ en g) est à peine modifiée par rapport à e), tandis que les moyennes $\overline{\langle\tau_2\rangle}$ sont significativement différentes, indiquant le taux de tautomérisation de l'hypéricine ($1/\overline{\langle\tau_2\rangle}$) est modifié par le PVA matrice et échange H/D. Nous avons expliqué la tautomérisation de l'hypéricine comme tunnel quantique. L'« effet de congélation » d'une matrice polymère rigide sur le transfert de protons est déjà signalé. Et la différence de taux de tautomérisation entre l'hypéricine dans le PVA et l'hypéricine deutérée peut être attribuée à la modification de la barrière d'énergie tunnel et à la différence de masse de l'hydrogène et du deutérium.

## C.5 Couplage d'émetteurs à cavité et quantique

### C.5.1 Caractérisation de la microcavité

Pour les spectres de transmission d'une microcavité représentative utilisée dans ce travail, les fonctions lorentziennes adaptées aux spectres de transmission donnent une largeur totale à mi-maximum (FWHM) d'environ 27 nm correspondant à un Q-facteur d'environ 20.

La résonance peut également être réglée par balayage latéral dans le plan xy. Nous pouvons effectuer un calcul simple: le rayon de courbure de la lentille supérieure est de 25.8 mm, et l'étage piézo-électrique à balayage plan xy peut se déplacer en 100 μm×100 μm. Un mouvement de 100 μm partant du centre des anneaux de Newton dans le plan xy correspond à un déplacement de ~200 nm dans la direction z.

### C.5.2 Microcavité - Adaptation des propriétés d'émission de fluorescence de l'hypéricine

Pour étudier les propriétés d'émission de l'hypéricine dans une microcavité accordable, un cadre théorique pour le calcul du taux de décroissance radiatif et des spectres de fluorescence détectés est présenté dans un premier temps.

Suivant l'approche présentée par Björk attribuant les variations du taux d'émission spontanée aux fluctuations du point zéro associées à un champ électrique entrant dans la microcavité, qui peuvent être dérivées de manière classique. Le facteur de Purcell dépendant de la fréquence peut être calculé:

$$P(\omega, z) = \frac{\Gamma_{sp}(\omega)}{\Gamma_{sp0}(\omega)} = \frac{\int_0^{2\pi} d\phi \int_0^{\pi} \sin\theta \, d\theta \int_0^{\infty} \omega^2 d\omega \, \hat{\wp} \cdot \boldsymbol{\mathcal{E}}_{\boldsymbol{k}}^{c}(\theta, \phi, z)}{\int_0^{2\pi} d\phi \int_0^{\pi} \sin\theta \, d\theta \int_0^{\infty} \omega^2 d\omega \, \hat{\wp} \cdot \boldsymbol{\mathcal{E}}_{\boldsymbol{k}}}. \tag{33}$$

où $z$ est la position de la molécule à l'intérieur de la cavité.

Le spectre de fluorescence détecté$S_{real}(\omega)$ est influencé par la position des molécules excitées et l'ouverture numérique limitée de l'objectif. Par conséquent, $S_{real}(\omega)$ peut être calculé par

$$S_{real}(\omega) = P_{NA}(\omega) \times S(\omega) \tag{34}$$

où $P_{NA}(\omega)$ limite l'intégration dans l'angle de l'ouverture numérique.

L'expérience est réalisée par revêtement par centrifugation d'une couche de solution d'hypéricine / PVA $10^{-5}$ M sur le miroir plat. L'épaisseur de la cavité est réglée de 180 nm à 500 nm déterminée à partir des spectres de transmission de la cavité. La Figure R C-7 a) montre trois désintégrations de fluorescence représentatives mesurées dans la cavité, où la durée de vie de l'état excité est obtenue par ajustement d'une seule décroissance exponentielle. Une influence significative de l'épaisseur de la cavité sur la durée de vie de l'état excité peut être observée. La Figure R C-7 b) montre les résultats de la durée de vie mesurée en fonction de l'épaisseur de la cavité. La ligne noire pleine représente un

ajustement du modèle théorique aux données expérimentales. Notant que la durée de vie de l'état excité en espace libre $\tau_0$ et le rendement quantique $\eta$ sont ajustés, qui sont $\tau_0 = 4.8\,ns$ et $\eta = 13\,\%$. La durée de vie de l'état excité en espace libre est en excellent accord avec la valeur expérimentale, tandis que le rendement quantique est légèrement inférieur à celui rapporté (20±3%). Le rendement quantique plus petit peut être très probablement causé par la contribution des molécules à différentes positions $z$, ce qui est négligé dans la simulation.

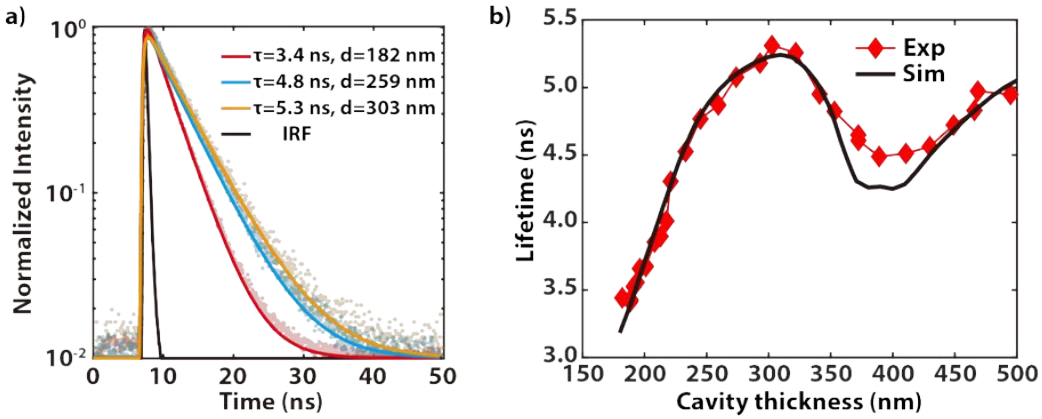


Figure R C-7 a) Décroissance de fluorescence mesurée dans la cavité. Les données expérimentales sont équipées d'une décroissance exponentielle unique. b) Durée de vie en fonction de l'épaisseur de la cavité. La ligne noire pleine représente un ajustement du modèle théorique aux données expérimentales.

### C.5.3 Nanocavité - Diffusion Raman améliorée en surface de molécule d'hypéricine unique

L'hypéricine a également été caractérisée par le SERS. Un film d'îlot d'argent est utilisé comme substrat SERS. La distribution du rayon des nanoparticules est ajustée par une fonction gaussienne avec $R = (11.93 \pm 3.66)\,nm$ . Un spectre d'extinction du substrat SERS a une résonance plasmonique de surface à 482 nm. Les spectres SERS analysés avec un script Matlab auto-écrit sont cohérents avec les valeurs rapportées dans la littérature pour l'hypéricine. La comparaison des spectres calculés par DFT avec le spectre d'ensemble expérimental suggère que les espèces neutres et déprotonées d'hypéricine sont présentes dans l'expérience d'ensemble.

Les spectres SM SERS d'hypéricine ont été acquis en utilisant les mêmes substrats SERS, mais la concentration de la solution d'hypéricine a été réduite à0.1 nM. Des images de balayage confocales enregistrées à partir de substrats purs et de substrats dopés avec une solution d'hypéricine 1.0 nM et 0.1 nM sont présentées sur la Figure R C-8 a)-c), respectivement. Deux exemples de spectres SM SERS sont représentés sur la Figure R C-8 d). En général, les mêmes pics SERS que dans le spectre d'ensemble peuvent être observés pour les SM, mais la largeur totale à la moitié du maximum des

pics est considérablement réduite car il n'y a pas de moyenne d'ensemble. Le spectre SERS représenté en d) en rouge présente de forts pics à1589 $cm^{-1}$, 1471 $cm^{-1}$ et 1299 $cm^{-1}$. Ces pics ont été attribués à la forme déprotonée de l'hypéricine. Cependant, les positions des pics en noir sont décalées vers 1610 $cm^{-1}$, 1451 $cm^{-1}$ et 1316 $cm^{-1}$, ce qui peut être attribué à la déprotonation de l'hypéricine.

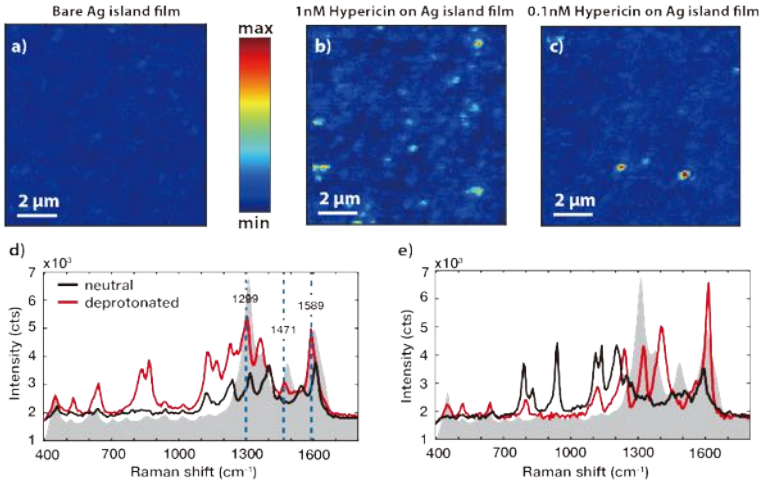


Figure R C-8 Images de balayage confocales enregistrées à partir a) de substrats purs et de substrats dopés avec b) 1.0 nM et c) solution d'hypéricine 0.1 nM d) Spectres SM SERS excités à$\lambda_{ex}$ = 530 nm. Les lignes noire et rouge montrent les spectres SM SERS de la forme neutre et déprotonée de l'hypéricine, respectivement. Les lignes pointillées bleues marquent des pics proéminents d'hypéricine déprotonée. La zone grise affiche le spectre Raman de résonance d'ensemble. e) Spectre SERS de la même SM hypericine neutre acquise à des moments différents.

Les spectres SERS présentés en e) sont obtenus à partir du même SM à des instants différents et de fortes variations d'intensité peuvent être observées entre les spectres représentés en rouge et en noir. Cela permet de déterminer l'orientation du SM par rapport à la surface. Les changements des intensités du SERS indiquent que le même SM est d'abord orienté presque parallèlement (ligne noire en e)) et se réoriente perpendiculairement ou presque perpendiculairement à la surface des nanoparticules (ligne rouge en e)). Une telle orientation perpendiculaire de l'hypéricine sur la surface de l'argent est également proposée dans les études d'ensemble SERS.

### C.5.4 Strong coupling of J-aggregated TDBC molecule and microcavity

Un J-agrégat peut être traité comme une chaîne de nombreuses molécules de colorant liées entre elles qui agissent comme un oscillateur quantique géant. Une grande force d'oscillation de la molécule est utile pour obtenir un couplage fort. Le fort couplage de molécules à un mode cavité a attiré beaucoup d'attention car il peut influencer les réactions induites par la lumière, améliorer le transfert d'énergie intermoléculaire, réaliser un laser polariton à température ambiante et la condensation Bose – Einstein. Les résultats récents ont été bien documentés dans plusieurs revues. Cette section se

concentre sur la démonstration d'un couplage fort d'une molécule de colorant J-agrégats en une microcavité accordable à température ambiante.

TDBC (5,6-dichloro-2-[[5,6-dichloro-1-ethyl-3-(4-sulphobutyl)-benzimidazol-2-ylidene]-propenyl]-1-ethyl-3-(4-sulphobutyl)-benzimidazolium hydroxide, sodium salt, inner salt, FEW Chemicals)) est un colorant cyanine qui subit une auto-organisation lorsqu'il est dissous dans l'eau pour former des J-agrégats.

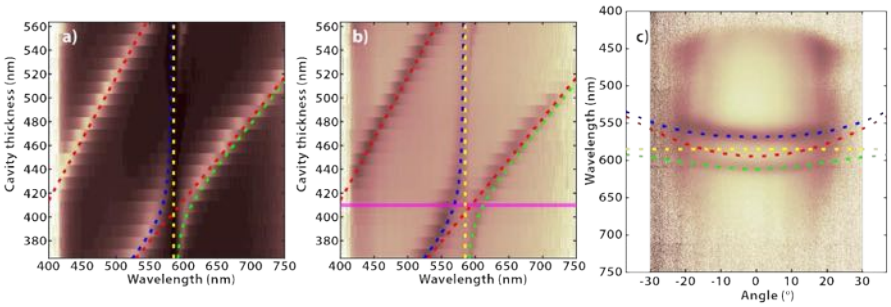


Figure R C-9 a) Spectres de transmission et b) de réflexion enregistrés à la même position pour différentes épaisseurs de cavité. c) Dispersion de réflexion dépendant de l'angle. Le spectre est enregistré à une épaisseur de cavité$d = 410\ nm$ indiquée par la ligne magenta en b). Résultats de la simulation présentés par des lignes de tirets. L'exciton moléculaire, le mode cavité, UP et LP sont tracés respectivement avec des lignes jaunes, rouges, bleues et vertes.

La Figure R C-9 a)-b) présente des spectres de transmission et de réflexion enregistrés à la même position spatiale pour différentes épaisseurs de cavité. Un anticrossing clair autour de l'exciton moléculaire (trait jaune) indique que le mode de la cavité (traits rouges) et les molécules sont couplés de manière cohérente. Les dispersions sont équipées du modèle à deux niveaux, où l'exciton moléculaire et le mode de cavité sont tracés avec des lignes jaunes et rouges sur la Figure R C-9, respectivement. Les polaritons hybrides sont représentés en bleu (UP) et en vert (LP). Le fractionnement de Rabi extrait des spectres de transmission et de réflexion sont tous deux de 150 meV.

La dispersion de réflexion dépendant de l'angle en c) est enregistrée à l'épaisseur de la cavité$d = 410\ nm$ comme indiqué par la ligne magenta en b). La dispersion dépendant de l'angle montre également une division de Rabi de $\hbar\Omega = 150$ meV. On note que l'angle maximal de collecte $\theta_{max}{\sim}20^o$ est limité par l'ouverture numérique de la lentille devant le spectromètre.

Nous avons également enregistré des spectres de fluorescence à résolution angulaire. Lorsque le mode cavité et l'exciton moléculaire sont en résonance ($\Delta{\sim}0$), les spectres de fluorescence sont élargis et seule la LP est observée. Si le désaccord est plus important ($\Delta > 0$), sauf pour LP qui suit encore les simulations, un mode de fuite émis par des molécules découplées est clairement observé.

La raison de l'absence de l'UP dans les spectres de fluorescence est déjà discutée dans la littérature. Dans un système molécule organique/microcavité fortement couplé, un laser bleu désaccordé excite la molécule à un état vibronique excité de l'état $S_1$, qui est suivi d'une relaxation rapide (plus courte que 1 ps) à l'état vibronique le plus bas. Les excitons excités s'accumulent en raison de l'effet de goulot d'étranglement, appelé réservoir d'excitons. Ils peuvent être diffusés vers le LP et l'UP dans une échelle de temps de 100 ps, ce qui est beaucoup plus long que la durée de vie du polariton (~50 fs). Par conséquent, ils ne peuvent pas conduire à une population de polaritons stable. La molécule dans l'UP peut soit émettre (~100 fs) soit être renvoyée vers le réservoir d'exciton (~50 fs). Ces processus épuisent l'UP et donc aucune émission ne peut être observée. La durée de vie du PL est plus courte que le processus de diffusion à partir du réservoir d'excitons et, par conséquent, l'émission du PL est «gelée». De plus, les excitons peuvent se détendre directement à l'état fondamental et émettre des photons (~300 ps), ce qui forme le mode de fuite.

## C.6 Multiplexage de nanocavité plasmonique vers une fluorescence améliorée d'un seul photosystème II

### C.6.1 Photosystème II

Le photosystème II (PS II) est un complexe pigment-protéine essentiel à la photosynthèse oxygénée, dans lequel les pigments (principalement la chlorophylle a (Chl a) et les molécules de caroténoïde) sont liés par un échafaudage protéique. Il existe largement dans les membranes thylacoïdes des cyanobactéries, des algues et des plantes supérieures. PS II fonctionne comme une unité de récolte légère qui oxyde l'eau et réduit la plastoquinone. La structure cristalline de PS II révèle une dimension autour de 10 nm comprenant deux protéines principales sous-unités CP43 et CP47, dans lesquelles les molécules d'antenne Chl a sont liées. Chl a absorbe la lumière et l'énergie d'excitation est transférée au centre de réaction conduisant à la séparation des charges.

Des pics prononcés dans les spectres d'absorption de PS II en solution autour de 435 nm et 674 nm sont dus à Chl a, et la bande latérale entre 450 nm et 530 nm peut être attribuée aux caroténoïdes. Le spectre de fluorescence avec le pic principal d'émission à 683 nm et la bande latérale faible autour de 740 nm est dominé par l'émission de Chl a lorsqu'il est excité avec le laser $\lambda_{ex}$=488 nm nm à température ambiante, même si les caroténoïdes sont principalement excités. Lorsque la température diminue à 160 K et que le laser d'excitation s'accorde à 665 nm, les pics d'émission sont les mêmes.

L'efficacité d'émission du PS II est extrêmement faible à température ambiante. Cependant, à basse température ou en présence d'un excès d'énergie d'excitation, plus d'énergie d'excitation est libérée

par le Chl a rouge sous forme de fluorescence, qui peut être utilisée pour analyser le transfert d'énergie dans les systèmes multichromophores.

## C.6.2 Nanoparticules d'or non uniformes

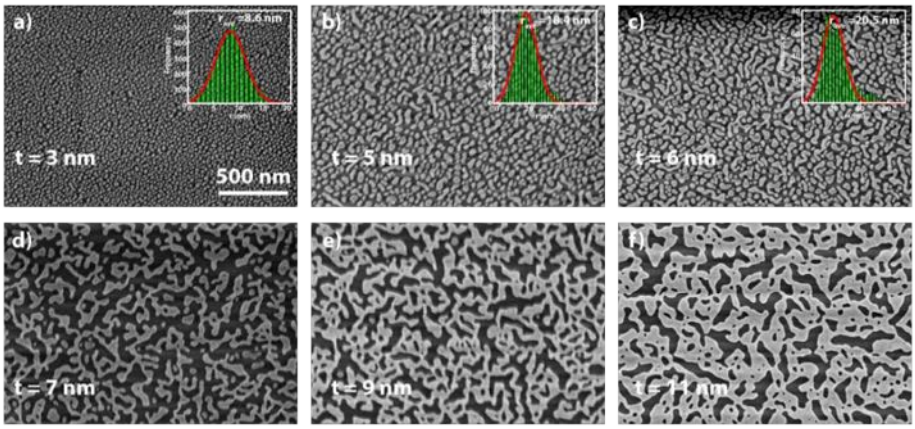


Figure R C-10 Images MEB d'un échantillon d'or non uniforme préparé à partir d'une évaporation en une étape. Les inserts en a) -c) sont la distribution du rayon des nanoparticules.

Des échantillons non uniformes représentés sur la Figure R C-10 sont préparés. La taille des nanoparticules augmente avec l'augmentation de l'épaisseur t du film d'or évaporé. Lorsque $t \leq 6\ nm$, les images MEB sont analysées avec le logiciel «ImageJ» et la distribution des rayons des nanoparticules dans l'insert de la Figure R C-10 a)-c) sont ajustées par des fonctions gaussiennes avec $R = 8.6\ nm$, $18.4\ nm$ et $20.5\ nm$, respectivement. La convergence de surface (le rapport de la zone couverte par l'or) diminue dans un premier temps, et commence à augmenter après l'obtention du film d'îlot ($t \geq 7\ nm$,) lorsque l'épaisseur continue d'augmenter.

## C.6.3 Amélioration de la fluorescence du photosystème II

Le monomère PS II de *Thermosynechococcus allongés* (*T. allongés*) sont purifiés et dilués à$10^{-9}$ M. 3 µL de la solution diluée sont pris en sandwich entre les nanoparticules d'or et une lamelle nue (deux lamelles nues pour la mesure de référence). L'échantillon est transféré dans le cryostat (T=160 K) en utilisant une construction d'échange rapide d'échantillon. Un laser d'excitation de 665 nm est utilisé pour la mesure de l'amélioration des émissions et la fluorescence est collectée après un filtre passe-long de 680 nm. Pour chaque épaisseur de film, 22 positions différentes dans une plage de 100 µm×100 µm sont sélectionnées au hasard, où 100 spectres de fluorescence (une seconde par spectre) sont acquis pour chaque position.

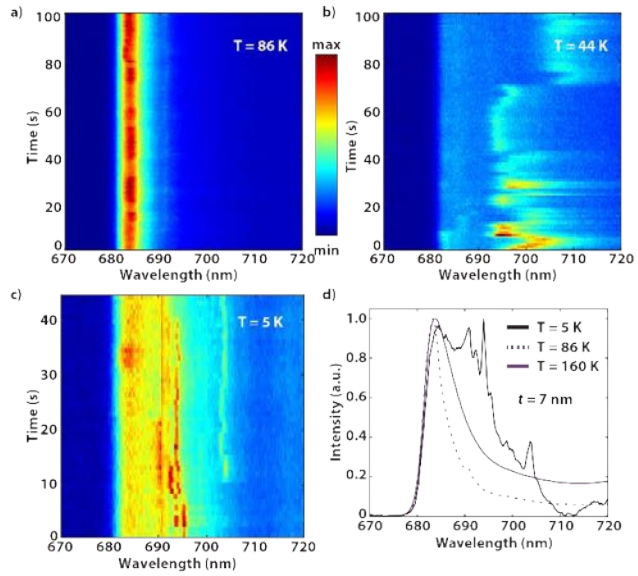


Figure R C-11 Séquence des spectres d'émission de fluorescence enregistrés en continu à a) T = 86 K, b) T = 44 K et c) T = 5 K. Le temps d'acquisition du spectre unique est de 1 s. d) Spectres moyennés enregistrés à différentes temperatures.

L'amélioration de la fluorescence est analysée en intégrant dans la gamme complète du spectre puis divisée par l'intégration du spectre sur verre. Le facteur de rehaussement maximal $F_{max} = 21.8$ est atteint à$= 7\ nm$.

Afin de confirmer que la fluorescence observée provient principalement d'un seul PS II, nous diminuons la température et les spectres mesurés à une épaisseur de film $t = 7\ nm$ pour différentes températures sont présentés sur la Figure R C-11. La FWHM des pics est significativement réduite, lorsque la température diminue à86 K (d)). Le pic d'émission est décalé vers le rouge à~695 nm pour une température T=44 K, et un clignotement clair et une diffusion spectrale indiquent que l'émission provient d'un seul PS II. Lorsque la température diminue à 5 K, des lignes nettes de phonons nuls apparaissent comme indiqué en c) et d). Le comportement complexe a été attribué à deux pools distincts de chlorophylles, F685 et F695 (Chls rouge), où le nombre se réfère au pic d'émission. À 5 K, le transfert d'énergie d'excitation des Chls rouges au centre de réaction est gelé. Par conséquent, des lignes sans phonon apparaissent aux deux longueurs d'onde. Le transfert d'énergie d'excitation de F695 est toujours gelé pour T≤77 K, tandis que F685 est éteint en raison d'un transfert d'énergie suivi d'un transfert d'électrons. À une température plus élevée, le maximum d'émission passe à une longueur d'onde plus courte en raison de l'augmentation de la population thermique d'états d'excitons plus élevés.

# C.7 Résumé et perspectives

## C.7.1 Summary and Outlook

Cette thèse porte sur la caractérisation d'une seule molécule d'hypéricine et l'interaction du mode cavité avec les molécules. L'hypericine est un médicament naturel de *l'Hypericum perforatum* (millepertuis) qui est très prometteur en médecine moderne. Il sert d'émetteur quantique unique qui présente une dynamique structurelle fascinante, telle que la dissociation, la conformation et la tautomérie, et permet l'observation de la dynamique d'une molécule unique et des impacts d'un environnement photonique.

Dans ce travail, l'utilité de la microscopie confocale à balayage, combinée à des modes laser d'ordre supérieur pour caractériser la dynamique transitoire de molécules uniques, a été démontrée. L'orientation spatiale tridimensionnelle d'une seule molécule a été déterminée, et l'état tautomérique observé dans une image de balayage spécifique peut être identifié sans ambiguïté. Des efforts supplémentaires ont été consacrés à l'analyse des propriétés temporelles de la dynamique en utilisant l'autocorrélation des photons, qui révèle l'influence distincte de l'environnement local et l'effet de deutération sur les molécules.

Le couplage entre microcavité/nanocavité et un émetteur quantique a été présenté. Le taux radiatif est modulé en accordant la résonance de la cavité; par conséquent, la densité locale des états est modifiée. Des simulations numériques, qui associent les fluctuations du point zéro au champ électrique entrant dans la microcavité, permettent de reproduire pleinement la densité locale d'états et donc de prédire la modification de l'émission spontanée. La même méthode est facilement étendue pour mesurer les taux de décroissance radiatifs et non radiatifs, ainsi que le rendement quantique intrinsèque.

Un couplage fort a été réalisé entre une microcavité et des agrégats J dans ce travail. Une tâche majeure sera d'explorer la limitation de la force de couplage d'une microcavité à faible Q-facteur et d'un seul émetteur quantique. Une méthode efficace consiste à étendre la mesure à basse température, ce qui diminue le déphasage de l'émetteur.

Une large amélioration du champ proche et une densité élevée de «points chauds» des échantillons de recuit ont permis la création de nanocavités plasmoniques, qui permettent de mesurer des SERS à une seule molécule. En outre, une stratégie d'optimisation rapide vers une amélioration optimale de la fluorescence a été validée avec PS II. La théorie des modes couplés présentée révèle l'importance

du rayon des nanoparticules et de la distance entre elles afin d'obtenir une amélioration maximale des émissions.

Une contrainte apparente de la théorie des modes couplés est que l'effet non local et les effets quantiques, tels que l'effet tunnel et le filtrage d'électrons, ne sont pas impliqués. Cependant, ceux-ci deviennent significatifs lorsque l'écart est inférieur à 5 nm. L'effet non local peut être inclus de manière appropriée dans un modèle classique, tandis que la correction plasmonique quantique peut être adoptée si nécessaire. Pour une implantation réaliste, par exemple, une pointe de sommet approchant la nanoparticule, des simulations numériques approfondies sont nécessaires pour révéler les caractéristiques de l'amélioration des émissions. Répondre à la limite de l'amélioration des émissions induite par plasmonique reste une tâche ouverte.